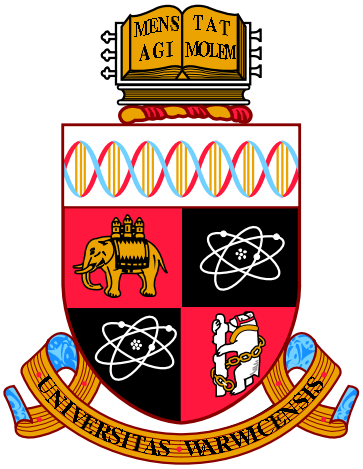

X-ray Scattering Studies of Nanostructured Patterned Arrays

by

David Stefan Greving

Thesis

Submitted to the University of Warwick

for the degree of

Doctor of Philosophy

Department of Physics

September 2020

THE UNIVERSITY OF WARWICK

Contents

Acknowledgments

Having played the most important role in the writing of this work, I begin by thanking Tom Hase and Björgvin Hjörvarsson for their trust, patience, and support of all my efforts in working on this thesis and for providing me the opportunity to conduct these studies in the first place. I have been very fortunate for always being able to rely on being welcomed with open-mindedness and the willingness to have in-depth discussions whenever facing problems I figured I was not able to solve on my own. I also owe a lot to Matts Björck for the many hours of immensely useful discussions about x-ray diffraction. These long discussions have been very enjoyable and truly inspirational. For similar reasons, thank you Bengt Lindgren for your welcoming attitude whenever I visited Uppsala, our fruitful discussions and on a personal level for the very memorable *midsommar* trip into the Swedish countryside.

A big thank you goes to Henry, for the good times doing 18-hour shifts in Brookhaven before getting lost in NYC, Björn for the good times we've had doing the slightly less intense 8-hour shifts in Warwick, and Toby for the friendly introduction of my new nickname in Uppsala. Thank you Ioan, for your kind efforts in introducing me to spin ice dynamics, despite nothing of it finally making it into this work... I hope we'll meet each other again at some board-game-night in the not-so-distant future.

Thanks a lot to David Walker and Steve Huband for all their help in the lab. Thank you Talha, for all the good days we've had in Coventry and for taking on the responsibilities that came with accepting the godparenthood of my son.

I very much recognise the unconditional love and support of my parents in every single decision I made over the years, without which I would have never made it to this point, thank you *so* much. Helping me grow as a being when times are good, and bearing with me when times are hard, I am infinitely indebted to Yara for having made that crazy decision of starting a family together.

Finally, I owe my biggest gratitude to my son Vili, for teaching me what is most important in life.

Declarations

This thesis is submitted to the University of Warwick in support of my application for the degree of Doctor of Philosophy. It has been composed by myself and has not been submitted in any previous application for any degree.

All data analysis in this thesis was performed by the author under the supervision of Dr Thomas Hase.

Abstract

X-ray resonant magnetic scattering (XRMS) has been used to investigate patterned arrays created using electron beam lithography. Diffraction from the repeating pattern has been measured close to the origin of reciprocal space. The impact of the spatial coherence of x-ray radiation is discussed in the context of reproducing rocking curves at various azimuthal rotation angles from patterned arrays of multilayered circular and elliptical islands. We show how traditional diffraction theory implicitly assumes a high coherence which has to be adapted to account for both the finite number of elements coherently illuminated by the beam and the specific experimental configurations used. This allowed a generic theoretic framework to be developed to describe the scattering from patterned arrays. The derived computational foundation is formulated in a specifically developed simulation framework, of modular code design allowing for efficient data processing, simulation, and fitting.

Utilising XRMS, and fitting the charge and magnetic scattering signals simultaneously, allowed quantitative fits to the in-plane diffraction data contained in rocking curves and the specular reflectivity from a patterned array of disk-like circular islands. The islands were spatially resolved into a three-dimensional chemical and magnetic profile revealing a core-shell structure. This structure is likely to be as a result from oxidation, affecting the surface of the islands. Simple models assuming flat disks could not reproduce the data and failed to account for the modulations in the intensity of the Bragg peaks, often by several orders of magnitude. A spatial model in which the islands were domed was developed in order to accurately reproduce the scattering data. The doming is likely to occur as a result of the prepatterning process used in sample production. The limited number of diffraction orders limits the precision of the modelling and we show how a grazing incidence small angle scattering (GISAXS) geometry can be exploited to easily and quickly obtain diffraction data over many orders, allowing a straightforward characterisation of the sample. The alternative experimental geometry is tested under laboratory conditions in which the coherence could be varied. Finally, XRMS measurements were also used in order to investigate the intra-island magnetic structure. Due to the shape anisotropy, magnetic vortex states form in the disk-like patterns. Fits of the magnetic hysteresis derived from the magnetic signal allow the structure of a magnetic vortex to be determined directly and indicate elliptical deformation of an magnetic vortex as it approaches the edge of the cylindrical host element.

Chapter 1

Overview

1.1 Thesis Structure

Within this work, characteristics of x-ray scattering of patterned arrays are explored, stressing both the similarities and differences to more established scattering theories like thin-film reflectivity and diffraction of atomic or molecular lattices. A complete framework for simulating the diffraction of patterned arrays will be developed and it will be shown how (resonant magnetic) x-ray scattering can be utilised in order to reveal peculiarities related to the x-ray coherence on microscopic length scales as well as to provide a detailed spatial model of the chemical- and magnetic structure of a patterned array.

Chapter 2 provides the fundamental theoretical groundwork concerning x-ray interaction with matter, classical x-ray reflectivity of stratified media, its connection to the current work, and the basics of diffraction of quasi two-dimensional structures.

A summary of techniques used in this work in order to fabricate patterned arrays, as well as the basics of performing laboratory- and central facility based x-ray experiments is presented in chapter 3. Further, an introduction to the differential evolution optimisation strategy is provided, forming the backbone of data fitting used in this work.

Chapter 4 focusses on how consideration of the spatial coherence of an x-ray beam becomes increasingly important on the large lateral dimensions typical of many types patterned arrays. It is shown how additional diffraction peaks are registered if the coherence of the radiation perpendicular to the scattering plane is smaller than the lattice constant of the diffracting array and how even under these ill-defined conditions valuable information may be retrieved from experimental data. It is further presented how the low-coherence conditions are in fact an extreme case

of classical diffraction theory, however necessitating a more rigorous mathematical treatment compared the (usually implicitly assumed) high coherence limiting case.

Following, chapter 5 presents an in-depth discussion of the framework developed for high resolution spatial modelling of three-dimensional patterned arrays and how these models are applied in diffraction theory. It is then shown how these techniques are used in order to perform a three-dimensional reconstruction of a patterned array consisting of domed islands utilising X-ray Resonant Magnetic Scattering (XRMS). To the author's knowledge, the accuracy in spatially resolving the (internal) chemical- and magnetic structure of the islands is unprecedented, proving how resonant x-ray scattering principally provides the sensitivity necessary for resolving three-dimensional micron sized structures on a sub-nm resolution.

Subsequently, chapter 6 shows how the previously developed theory extends to the use-case of Grazing Incidence Small Angle X-ray Scattering (GISAXS), and points out why the GISAXS geometry is believed to be the preferred method of investigating patterned arrays in future studies.

Chapter 7 then concludes with an outlook of how the developed theory extends to resolving magnetic structures that a spatial non-uniform, on the example of magnetic vortex formation on magnetically non-saturated micron-sized islands.

Finally, chapter 8 provides a conclusion and closing remarks of the thesis.

1.2 Project History

Nanotechnology[1–3] affects numerous scientific and industrial fields like the energy sector[4], medicine and drug delivery[5–7], environmental studies[8, 9], food production and agriculture[9], biosensors[10] and many more. Within solid state- and scattering physics, the last two decades have shown drastic advances in sample patterning techniques [11–17], in particular regarding lithographic patterning [18–25]. The latter opened up the research field of micron- and nano-patterned arrays, characterised by two-dimensional periodic arrays of highly uniform elements of typical structure sizes ranging from a few nm up to multiple micrometers. Essentially forming perfect supercrystals, patterned arrays provide many useful applications ranging from the fabrication of data storage devices to studying the dynamical magnetic interactions of Artificial Spin Ice (ASI).

1.2.1 Context to Scientific Literature

Lithographically patterned arrays have various use cases in both fundamental research and direct technological applications. One of the most prominent examples of

applying patterning to metallic systems is the formation of magnetic vortex states within thin nanoscopic disks. The internal magnetic state of the disk is determined by the interplay of magnetostatic interaction of the atomic spins, their total Zeeman energy, and their respective exchange interaction[26, 27]. The dominance of the magnetostatic energy for certain disk-geometries favours the formation of a magnetic vortex, being characterised by the internal atomic spins aligning locally to form closed loops within the plane of the disk[28–30]. These vortex states exhibit a two-fold degeneracy in terms of their sense of rotation, with associations regarding data storage applications emerging immediately. The latter requires control of both vortex-formation[31] as well as -detection[32] and have therefore been considered an important field of work since many years. Furthermore, apart from data storage, understanding vortex formation plays an important role in research of demagnetisation processes[33, 34] and logical magnetic circuits[35–37].

Another application of nano-patterning concerns the creation of artificial spin-ice (ASI). An ASI generally consists of a two-dimensional array of elongated magnetic rods, whose dimensions have been chosen to favour an internal single domain magnetic state, i.e. the parallel alignment of all internal atomic spins. The consequence is the formation of a mesoscopic superspin by means of superposition of the electrostatic fields of the individual atomic spins. ASI geometries include Square-[38], Kagome-[39, 40] or Shakti-lattices[41] and modifications thereof[42]. Each geometry is characterised by a periodic spatial arrangement of clusters of rods exhibiting a finite number of energetically distinct spin configurations per local cluster. The long-range structure of the lattice, though, is chosen in a way that not all neighbouring clusters are able to simultaneously adopt a low energy state, which hence leads to "spin frustration"[43, 44], as a single superspin is part of multiple local clusters. ASIs provide a highly interesting research topic, as they constitute an ideal opportunity to engineer specifically tailored systems of superspins of tunable interaction strength. This allows to gain insight into traditional atomic spin ice, spin liquids, emergent magnetic Coulomb phases, and many more by studying the temperature dependent dynamics and statistical distribution of local spin configurations on a mesoscopic length-scale[45–49].

Most research work concerning patterned arrays appears to be falling into one of two categories. The first category applies to experimental observations on a rather qualitative level, often concerning interactions at length scales exceeding the structure size of the single elements constituting the patterned array, instead of focussing on the structure of individual elements. The most prominent examples exploit X-ray Resonant Magnetic Scattering (XRMS) in order to observe the forma-

tion of magnetic Bragg peaks, often as a consequence of emergent antiferromagnetic order. Experiments have been performed on a wide variety of one-dimensional and two-dimensional gratings by means of rocking curve measurements[50, 51]. Furthermore, using SAXS geometry and an area detector, it has been possible to observe antiferromagnetic ordering of an artificial square-ice utilising the magnetic sensitivity of resonant x-ray scattering[52]. Recently published was the observation of magnetic vortices in square nanomagnets, modulating the scattered intensity captured via XRMS diffraction measured by a CCD detector upon performing a full magnetic hysteresis cycle[53].

The second category involves fitting of simulated to experimental data in order to extract quantitative information about the sample. Typically, sample models are kept as simple as possible, being often defined by not more than a handful parameters, an approach that is justified if either the sample is itself very simple, or the experimental data do not provide sufficient sensitivity in order to resolve the sample structure in higher detail. Furthermore, simple structures are often-times preferred by researchers since they are likely to allow a fully analytical treatment of the scattering process. Examples include fitting of the x-ray scattering of one-dimensional gratings, determining both the geometry of the trapezoidal cross-section of the grating[54] as well as a varying beam coherence changing with the incidence angle of the radiation[55]. Rocking curve measurements of a square patterned array of circular disks exhibited an unexpected intensity distribution, which could be resolved only after the sample model was adapted to include the unintended crowning of the circular disks having occurred as a side effect of the removal process of the photo resist used in the fabrication process of the array[56]. While the previous examples relied on an analytical description of the scattering process, a different approach consists in a fully numerical determination of diffraction data, obtained by performing the Fast Fourier Transformation (FFT) of a binary map, which is encoding only the presence or absence of an island on a spatial grid of arbitrary resolution, with the grid corresponding to a coherent sampling of the array[57].

In the context of this thesis, two major factors differ from the previously discussed cases. First, as will be discussed in depth in chapters 3 and 5, it turned out that the samples used in this work in their majority suffer from unintended doming having emerged most likely as a byproduct of using a deep pre-patterned mask, which significantly exceeded the nominal thickness of the elements. This left the nominally flat islands with a height gradient spanning about one half of the total island height ranging from the islands centre to its edges. Further, the samples were fabricated by sputter deposition of the patterned elements. The non-epitaxial

sputter deposition is believed to be the reason for obtaining a high surface roughness, likely rendering the islands susceptible to strong surface oxidation. The oxidised shell leads to a strong chemical contrast with respect to the non-oxidised core of the islands, manifesting in a measurable impact upon the scattered signal. In conclusion, this means that in contrast to what is generally desired by an experimenter, the sample structure is not simple, but rather requires a high amount of parametrisation in order to be adequately modelled.

Secondly, most of the experiments were performed at synchrotron facilities, with the associated high photon flux allowing the measurement of rocking curves at relatively high scattering angles without compromising statistical accuracy. The latter, in combination with the comparatively large lattice constants of patterned arrays allowed the measurement of high orders of diffraction peaks, implying sensitivity to high Fourier components and therefore pronouncedly spatial sensitivity to the structure of the sample. Further, the experiments presented in chapter 5 were taken under open detector conditions. This scattering geometry means that the detector accepted and integrated wavevector transfers over its whole window size, instead of reducing the acceptance by the additional introduction of slit apertures between sample and detector. As will be shown later in this work, the open detector set-up implied additional sensitivity to the Q_z component of the wavevector transfer superimposing the usual Q_x dependence of rocking curves. This left the experiment effectively a hybrid between rocking curve and off-specular reflectivity measurement, which decidedly complicated the subsequent fitting procedure. However, while using the open detector set-up arguably presents an experimental inaccuracy from the point of view of producing easily interpretable data, it nevertheless drastically increased the information density of the experiment.

These two factors, i.e. complex sample structure and high information density of the experimental data, synergised in the way of producing data which are highly sensitive to the spatial geometry of the sample, while the sample itself in its complexity required careful spatial modelling. In other words, the experiments constituted a particularly suitable use-case for exploring the capabilities of resolving the three-dimensional structure of patterned arrays by means of x-ray diffraction.

1.2.2 Finding a Framework

Using the approach of a binary sampling of the patterned array as described by Eastwood et al. [57] provides the advantage of a very straightforward sample modelling and calculation of the scattered intensity, at the cost of high computational strain if large spatial resolution is required. It leads to reasonable results if

1. The islands can be modelled adequately as being perfectly flat and contain no internal lateral structure. As pointed out by Tolan et al. [54], if the patterned structure is not flat, the quantity to be *laterally* Fourier transformed is not a simple surface-height representation of the pattern, but the (analytical) *z-component* of the Fourier transformation of the structure height.

2. The kinematical approximation of x-ray scattering is valid, i.e. no multiple scattering events, for instance as a result of substrate reflection, have to be taken into account.

3. The beam coherence is sufficient so as to render the simulated (coherently scattering) area of the sample an ergodic representation of the entire sample. If this condition is not fulfilled, additional sampling of the array has to be performed, slowing the already computationally demanding calculation down even further.

Initially following the previously described approach within this project, it quickly became clear that the resolution given by the numerical lateral grid was quickly becoming too small in order to accurately model the spatial structure of a non-flat array.

In a refined, yet still fully numerical approach, application of the convolution theorem allowed to limit the spatial grid to the dimensions of the unit cell of the patterned array, in turn providing a significantly higher lateral resolution using the same grid size. This allowed calculating the islands structure factor, which then works as a scaling factor to the diffraction peaks, with the positions of the latter being analytically determined instead of emerging as a result of the direct Fourier transformation of the binary array. A refined version of this approach has indeed been used in this thesis in order to fit the experiments performed at low spatial beam coherence presented in chapter 4.

When turning to the experimental data taken at magnetic resonance presented in chapter 5, though, it was eventually realised that the additional strain of simultaneous fitting of charge- and magnetically scattered data in connection with the high spatial sensitivity to the sample structure would quickly overburden any available computing power, which was ultimately motivating the development of the scattering framework described in section 1.3 and, in more detail, the first part of chapter 5. The decision was made to employ a semi-analytical model, that essentially consisted in dividing the sample into discrete slices, each of which corresponds to a horizontal cross-section of the structure. The chemical and magnetic structure of each slice would then be encoded by horizontally stratified annuli, each obtaining

a well defined analytical Fourier Transformation given by certain combinations of Bessel functions, similar to the approach of Lee et al. [56]. By freely choosing the slicing thickness and restricting radial increments within a given slice to chemical- or magnetic gradients of the scattering length density (SLD), this model allowed arbitrary resolution in directions both parallel and perpendicular to the sample surface, not wasting computational resources on subdividing the sample within areas of constant SLD.

Developed in this way, the framework is computationally highly efficient, taking into account the huge amount of calculations a three-dimensional micron sized structure sampled on Å-level resolution is requiring. However, the model faced its limitations when attempting the simultaneous fitting of magnetic rocking curve and reflectivity data, due to additional complications arising from interference of the scattered radiation of the pattern and unpatterned substrate. Improving the quality of the fit further did not seem worth the additional effort of introducing an even more refined sample model, after the high utility of resonant magnetic scattering for spatial characterisation of patterned arrays has arguably been proven.

It is instead believed to be more promising for future applications to switch to the GISAXS geometry as proposed in chapter 6, allowing the simultaneous extraction of sometimes dozens of diffraction peaks, providing an immense amount of experimental data of large Fourier components necessary to fit complex pattern structures.

1.3 Simulation Structure

A huge part of the work invested into the creation of this thesis has been devoted to the development of a computational framework concerning x-ray scattering of patterned arrays, which is roughly divided into three main components. The first component is given by formulation of a *modelling framework* used for defining high resolution representations of the spatial structure of patterned arrays. The second component is given by the creation of a *simulation framework* that allows the efficient and accurate computation of the way x-rays are being scattered off of patterned arrays under various experimental conditions. The third major component consists of the *fitting framework* that allows connecting the sample model and scattering simulation to match simulated- to specific experimental data. Since no publicly available software has existed to perform each of these individual tasks, one of the biggest challenges of this thesis consisted in developing of a unified framework that is able to perform each task individually and sequentially, being versatile enough to

adapt individual components if required, without compromising the functioning of the underlying larger programmatic structure.

In the broader context of this work, the specific implementation is arguably less important than the emergent structure of the general framework, which in many respects differs drastically from conventional atomic diffraction or x-ray reflectivity of stratified media. This way, any interested reader should be able to identify the relevant individual aspects of the simulation framework as well as common experimental and programmatic pitfalls. Further, this thesis also aims at developing a general appreciation for the possibilities associated with the high spatial sensitivity of x-ray diffraction of patterned arrays and presenting solutions that have empirically proven useful by the experience gained from spending hundreds of hours of refactoring of a complex code-base and increasing both the efficiency and accuracy through countless iterations until finally having arrived at the current state of the work. In other words, apart from the specific results obtained from fitting a variety of experimental data, this thesis is also aimed not just at providing a theoretical framework, but on providing a guide for any scientific researcher to create his or her own implementation of a proven concept without going through the same laborious process needed for the current structure to emerge.

The simulation code follows an object oriented design (OOD) principle[58], emphasising the encapsulation of functionality within components that are strongly isolated from the remaining code. The latter prevents rippling effects that are typically found if parts of a highly interconnected code-base have to be changed, which may cause great complications as rather drastic changes are very common when experimenting with constantly evolving models. Another advantage of highly isolated code is the easy re-use of specific components, as isolated data structures rely on no implementation details of components found elsewhere in the project.

A high level schematic of the finally used design structure is presented in Fig. 1.1, where individual objects are depicted by coloured boxes, with nested boxes representing composites of lower-level structures. The total design is separated into three fundamental columns, concerning simulation functionality, data structures, and functionality related to the fitting of simulated to experimental data. Solid arrows indicate the instantiation of a new object, while open arrows represent the referencing of an already existing object.

The individual components of the diagram seen in Fig. 1.1 can be summarised in the following way:

- All relevant experimental data are collectively stored in the `Experimental Data` module (top of middle column), which hence constitutes a pure data

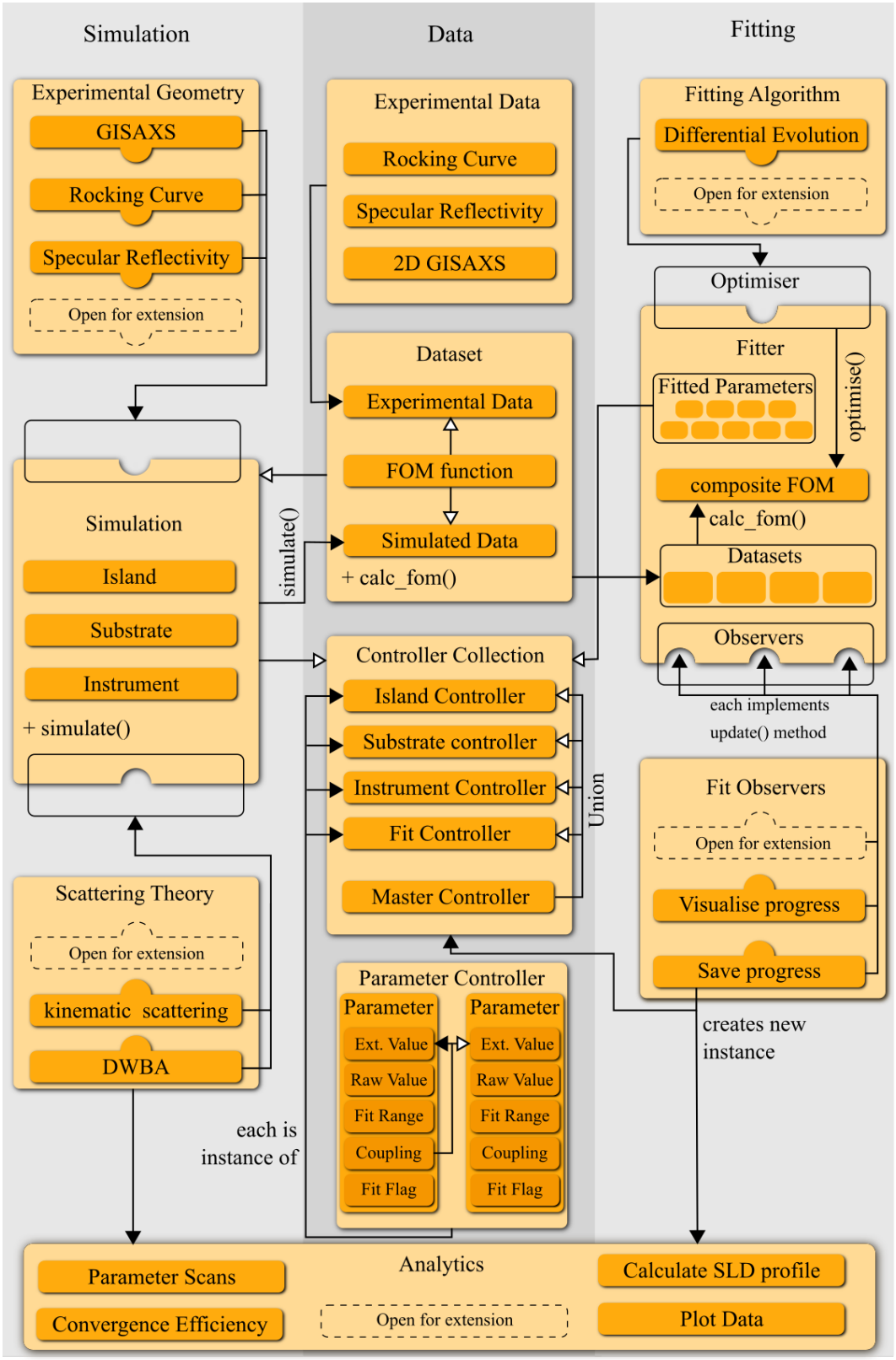

Figure 1.1: Design of the developed code.

structure, obtaining no additional functionality.

- An instance of a `parameter` class (nested within `Parameter Controller`, bottom of middle row) consists of five basic objects. The `raw value` is the quantity being varied during a fitting procedure, while the variation takes place within the limits specified by the `fit range` tuple. In contrast, the quantity exposed by the public interface of the Parameter object is the `Ext Value`, which is the external *representation* of the parameter, e.g. the value used for defining a particular sample geometry. The `Ext Value` differs from the raw value, since it is given by the output of an instance of a `Coupler` object, creating a parametric coupling to another instance of a `Parameter` class. Whether or not a parameter is considered a fitting parameter is determined by the Boolean `Fit Flag`.

  As an example, two interfaces may be coupled in a way forming a layer of unknown thickness in between them, disregarding of the actual height of the interfaces relative to, say, the substrate level. Both interface heights are represented by an instance of a `Parameter` object, for instance `Interface1` and `Interface2`. Since the physics of the composite system are intricately coupled to the absolute film thickness, it is often found to be computationally much more efficient to fit only the height of one interface and the total thickness of the respective layer, instead of fitting both interfaces independently. This corresponds to using an additive coupler on `Interface2`, adding an amount specified by the raw value off `Interface2` to the (external) interface height of `Interface1`. Apart from Additive Couplers, the most commonly used `Coupler` classes are Subtractive- and Multiplicative Couplers.

- The `Parameter Controller` is a collection of `Parameter` instances, typically defining the complete set of quantities relevant for the creation of a specific logical entity, e.g. fully describing all parameters necessary for modelling of a single island of a patterned array. It provides additional functionality like returning a list of all fitted parameters and their allowed minimum and maximum values, which are of obvious relevance for the `Fitter` object.

- The `Controller Collection` is, in a sense, the organisational centre of the code, as it represents a unified collection of all relevant information determining not only all parameter values but also the specific way all individual components work together. It contains all information relevant for creating the sample structure in the form of the `Island Controller` and `Substrate`

`Controller`, what kinds of measurements are to be simulated, specifics of the experimental set-up in form of the `Instrument Controller`, as well as the algorithmic parameters determining the dynamics of the fitting procedure given by the `Fit Controller`. The `Controller Collection` further contains the `Master Controller`, which is the union of all individual Parameter Controllers, often simplifying certain tasks.

Additionally, the `Controller Collection` provides serialisation functionality, enabling saving the Controller Collection to disk, as it is the single quantity that defines the whole set of parameters, therefore allowing recreation of particular sample- and instrumental states for subsequent analysis.

- The `Simulation` class encapsulates all functionality necessary to produce simulations of arbitrary scans through reciprocal space, by coordinating the interplay of lower level objects not shown in the diagram. Since an instance of a `Simulation` class has to reference a controller collection, it can access all information required for instantiation of `Island`, `Substrate`, and `Instrument` classes, defining the experimental conditions of the sample and measurement device. The exact kind of the simulated measurement is defined by specific `Experimental geometry` plug-ins, defining the exact coordinates in reciprocal space that have to be considered in order to simulate a particular type of scan. Another plug-in, the `Scattering Theory`, performs the calculations corresponding to the `Experimental Geometry` utilising a particular scattering theory, e.g. `kinematic approximation`, `Distorted Wave Born Approximation`, etc. The `Simulation` class is the most complex of all constituents in terms of its internal structure, since it performs both the creation of the simulated sample and the calculation of the scattered signal. By invoking it's only public method `simulate()` it returns a dictionary containing the reciprocal space coordinates and associated intensities.

- A `Dataset` object is a collection of a particular set of experimental and simulated data, the latter being created on demand, by invoking of the `simulate()` method of an associated `Simulation` object. The degree in which simulated and experimental data match is determined by a figure of merit (FOM), calculation of which is performed by a specific `FOM function` class, which has to be compatible with the return value of the `Simulation` object and the formatting of the experimental data. Hence, by invoking the public `calc_fom()` method of any instance of a `Dataset` class, a simulated signal will be created according to the current state of the respective `Parameter Controller`s, which is

in turn reduced to a single number characterising how closely the simulation matches the experimental data specific to the used FOM function.

- The `Fitter` class combines structure and the functionality required for fitting simulated to experimental data. It takes an arbitrary number of Datasets objects and requires the implementation of a `calc_fom()` method, which combines the respective individual FOMs of each Dataset to a composite FOM. The composite FOM represents the quantity then minimised by the `optimiser`. The latter takes the form of a plug-in, principally allowing different optimisers to be used, although in the context of this work only the (excellent) standard optimiser coming with the `differential_evoution`[59] module of the python `scipy.optimize` library has been used. Apart from referencing a `Controller Collection` in order to determine the fit values and boundaries, the `Fitter` class is fully ignorant of any implementations lying outside of its scope.

  Although not currently implemented, parallel processing of the `optimise()` method is highly desirable for future work, since it may drastically speed up the relatively slow optimising process. In order to use parallel processing, new simulation processes must not contain any external references in order to be be spawned independently. The latter requires the fresh instantiation of all involved objects, potentially necessitating the implementation of an additional class taking care of proper encapsulation of the required data and functionality.

- Attached to the `Fitter` is an arbitrary number of `Fit Observer` objects, that constitute callback functions to the `Optimiser` instance, being able to reference the currently best matching values of the fitting parameters according to the `FOM function`. Hence, the observers have access to all information necessary for tracing the progression of the fit, therefore allowing the observers to perform tasks like visualisation of the evolving simulations and figure of merit, keeping track of the speed of convergence of the fit, save the current state of the fitting procedure in the form of a new instance of a `Controller Collection`, etc.

- Once the fitting procedure is finished, the `Analytics` module can fully recover the state of any simulation by loading the corresponding `Controller collection`, in order to perform arbitrary visualisation of data, calculate depth profiles of the scattering length density and compare different combinations of algorithmic fitting parameters in terms of their convergence efficiency and reliability, Further, `Analytics` contain the option to perform parameter

scans, in order to explore how small changes of single parameter affect the outcome of the simulation result. All of these analytics have been proven immensely useful in the exploration and evaluation of x-ray scattering of patterned arrays, with many examples found throughout this thesis.

Chapter 2

X-Ray Scattering Theory

2.1 Basics of X-rays Interacting with Matter

2.1.1 Electromagnetic plane waves

The *electromagnetic plane wave* is arguably the simplest manifestation of electromagnetic radiation and it will be shown that plane waves, in fact, comprise the building blocks of arbitrary electromagnetic waves by means of the superposition principle[60–62]. Generally, an electromagnetic plane wave consists of oscillating electric and magnetic components, $\mathbf{E}(\mathbf{r},t)$ and $\mathbf{H}(\mathbf{r},t)$, as depicted in Fig. 2.1 and evaluated at position $\mathbf{r}$ and time t to read

$$\mathbf{E}(\mathbf{r},t) = E_0\, \mathrm{e}^{i(\mathbf{k}\cdot\mathbf{r}-\omega t)}\, \hat{\boldsymbol{\varepsilon}} \tag{2.1a}$$

$$\mathbf{H}(\mathbf{r},t) = H_0\, \mathrm{e}^{i(\mathbf{k}\cdot\mathbf{r}-\omega t)}\, \hat{\boldsymbol{\eta}}, \tag{2.1b}$$

with E_0 and H_0 being the electric and magnetic modulus field amplitudes, $\hat{\boldsymbol{\varepsilon}}$ and $\hat{\boldsymbol{\eta}}$ are the unit polarisation vectors of the respective components, and oscillatory frequency ω. The direction and wavelength of the plane wave is fully described by the wavevector

$$\mathbf{k} = \frac{2\pi}{\lambda}\hat{\mathbf{k}}. \tag{2.2}$$

Since both wave components are at all times perpendicular to each other as well as to the propagation direction of the wave they individually form transverse waves, meaning that

$$\hat{\boldsymbol{\varepsilon}}\,\hat{\boldsymbol{\eta}} = \hat{\boldsymbol{\varepsilon}}\,\hat{\mathbf{k}} = \hat{\boldsymbol{\eta}}\,\hat{\mathbf{k}} = 0. \tag{2.3}$$

Upon being exposed to electromagnetic radiation, the charge e^- and spin-

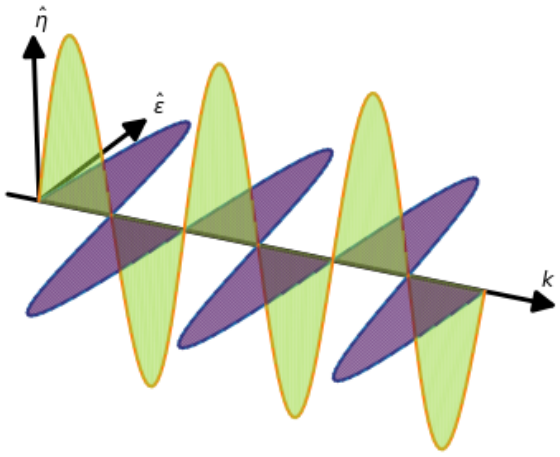

Figure 2.1: Schematic of an electromagnetic plane wave, propagating along wavevector **k**. The **E** and **H** components are always perpendicular to each other and **k**.

induced magnetic moment μ_e of an electron couples to the respective components of an electromagnetic wave via the Lorentz force[63, 64]

$$F_\mathrm{E} = \mathrm{e}^- \, \mathbf{E} = \mathrm{e}^- E_0 \, \mathrm{e}^{i(\mathbf{kr}-\omega t)} \, \hat{\boldsymbol{\varepsilon}} \tag{2.4a}$$

$$F_\mathrm{H} = \boldsymbol{\nabla}(\mu_\mathrm{e}\mathbf{H}) = i\mathbf{k}E_0\mu_\mathrm{B} \, \mathrm{e}^{i(\mathbf{kr}-\omega t)} \, \hat{\boldsymbol{\eta}}, \tag{2.4b}$$

inducing an electronic oscillation and hence the re-emittance of electromagnetic radiation by means of an accelerating charge. However, the respective forces on the electron, and hence the amplitudes of the re-emitted electric field, differ by a factor

$$\frac{F_\mathrm{E}}{F_\mathrm{H}} = \frac{\mathrm{e}^-}{k\mu_\mathrm{B}} \approx \frac{1\,\mathrm{MeV}}{E_\mathrm{xray}}, \tag{2.5}$$

which, depending on the x-ray energy E_xray ranging from roughly 0.5 keV (~ 2.5 nm) for soft- to 10 keV (~ 0.12 nm) for hard x-rays and leading to a difference of measured intensities by four to six orders of magnitude, justifying the negligence of the magnetic field component when considering x-ray scattering in most cases including the remainder of this work.

The angle of the exponential term of eq. 2.1 with the real axis in the complex plane describes the phase of the wave at any given point of space and time taking on a value from the interval $[0, 2\pi]$. Since the factor $\mathrm{e}^{-i\omega t}$ is the same for all waves considered simultaneously, it cancels out in every equation and will from now on be omitted.

X-rays in this work are treated to be mostly *monochromatic*, meaning the

incident wavefield is characterised by a single wavelength λ_0, associated with the vacuum wavevector of length

$$k_0 = |\mathbf{k}_0|. \tag{2.6}$$

Furthermore, scattering is considered to be *elastic*, implying that any scattered plane wave leaving the sample is of the same wavelength λ_0 as the incident field[65, 66], implying

$$|\mathbf{k}| = |\mathbf{k}_0|. \tag{2.7}$$

Then, the phase difference between two waves scattered by electrons located at an arbitrarily placed origin and at some location $\mathbf{r}$ can be evaluated geometrically[62] to read

$$\Delta\phi(\mathbf{r}) = (\mathbf{k_f} - \mathbf{k}_i)\mathbf{r}, \tag{2.8}$$

justifying the introduction of the fundamentally important quantity of the *wavevector transfer*

$$\mathbf{Q} = \mathbf{k_f} - \mathbf{k_i}. \tag{2.9}$$

$\mathbf{Q}$ is the quantity connecting scattering theory and experiment, since it appears in virtually all calculations and it's directional dependence of $\mathbf{k}_i$ and $\mathbf{k}_f$ translates directly into laboratory source and detector angles. The wavevector transfer, for instance, allows straightforward evaluation of the total scattered amplitude into a particular direction specified by $\mathbf{Q}$, simply by summing over (or integrating) the positions of all scatterers, comprising what will later be shown to be the *kinematical approximation*

$$A(\mathbf{Q}) = \int f(\mathbf{r})\rho^{\mathrm{num}}(\mathbf{r})\mathrm{e}^{-i\mathbf{Q}\mathbf{r}}\,\mathrm{d}\mathbf{r}, \tag{2.10}$$

where $f(\mathbf{r})$ is the *scattering length* or *scattering factor* of the atoms located within $\mathrm{d}r$ at $\mathbf{r}$, with $\rho^{\mathrm{num}}(\mathbf{r})$ being their local *atomic number density*, i.e. number of atoms per unit volume.

If the electromagnetic wave travels through a medium, the length of its wavevector $\mathbf{k}$ changes with respect to its vacuum value k_0 according to

$$|\mathbf{k}| = k = nk_0, \tag{2.11}$$

with the *refractive index* n being the proportionality constant connecting the two wavevectors[67], introduced in section 2.1.2.

As will be shown in section 2.2, when traversing the interface between two media, the component of a wavevector $\mathbf{k}$ *parallel to a flat interface* is conserved,

therefore relaxing eq. 2.7 to now read

$$\left|\mathbf{k}_{0,\parallel}\right| = \left|\mathbf{k}_{\parallel}\right| = \frac{2\pi}{\lambda}\cos\alpha \equiv k_{\parallel}, \tag{2.12}$$

with α being the angle between the sample surface and the incident radiation. The subscript $\parallel$ denotes the component of the wavevector parallel to the surface.

Since the scattering is elastic, any wavevector $\mathbf{k}$ is fully specified by two of its cartesian coordinates, which leads to the definition of the dispersion relation

$$|\mathbf{k}|^2 \equiv k_x^2 + k_y^2 + k_z^2 = n^2k^2, \tag{2.13}$$

where each component is related to the real space coordinates

$$k_x = \frac{2\pi}{x} \tag{2.14a}$$

$$k_y = \frac{2\pi}{y} \tag{2.14b}$$

$$k_z = \frac{2\pi}{z}, \tag{2.14c}$$

with $\hat{\mathbf{x}}$ and $\hat{\mathbf{y}}$ defining the sample plane and $\hat{\mathbf{z}}$ being the sample normal. Since the parallel component $\mathbf{k}_{\parallel}$ of the wavevector is always conserved, eq. 2.13 is often stated in the equivalent form

$$k_z = \pm\sqrt{n^2k^2 - \mathbf{k}_{\parallel}^{\mathbf{2}}}. \tag{2.15}$$

2.1.2 Refractive index and Scattering length density

In calculating x-ray scattering, the atomic scattering factor, refractive index and scattering length density are all closely related but distinct quantities, which only differ in their convenience in a given experimental or theoretical context.
Away from electron resonances, the *atomic scattering factor* is given by

$$f(\mathbf{Q}) = \int \rho(\mathbf{r})\mathrm{e}^{i\mathbf{Q}\mathbf{r}}\,\mathrm{d}r \tag{2.16}$$

and is the scattering amplitude of a single atom as a function of wavevector transfer $\mathbf{Q}$ from the Fourier Transformation of the spatial charge distribution $\rho(\mathbf{r})$. By convention, $f(\mathbf{Q})$ is typically implicitly considered in units of the classical electron radius r_e, given by

$$r_\mathrm{e} = \frac{e^2}{4\pi\varepsilon_0 m_\mathrm{e} c^2} \approx 2.818 \times 10^{-15}\,\mathrm{m}, \tag{2.17}$$

characterising the response of an electron upon driven oscillation by means of an

electro-magnetic wave, being defined by the fundamental quantities *electron charge* e, *electron mass* m_e, the *permittivity of free space* ε_0, and the *speed of light* c.

Since the integral over $\rho(\mathbf{r})$ equals the atomic number Z of electrons of an atom. For typical x-ray energies, small $\mathbf{Q}$ and away from electronic resonances it is essentially equivalent to $f(\mathbf{Q}) = Z$, the number of atomic electrons Z times the classical electron radius.

A more general way of expressing the scattering factor is given by

$$f = f_0(\mathbf{Q}) + f'(E) + if''(E), \tag{2.18}$$

with the Q-dependence of f_0 entering in non-forward direction as a consequence of the spatial charge distribution of electrons surrounding the atomic core, and $f'(E)$ and $f''(E)$ being the resonant dispersion correction terms[68], depending on the energy of the x-rays interacting with the atom. The real part of the dispersion correction f' deviates from zero around absorption edges, which corresponds to the x-rays being able to excite particular electronic transitions within the atoms[69–71]. The imaginary part of the dispersion correction is related to atomic absorption of individual photons and consequently increases by sharp steps every time the photon energy exceeds the energy difference of a particular electronic transition. Both, the energy dependence of real and imaginary dispersion correction terms $f'(E)$ and $f''(E)$ are plotted for the example case of Palladium in Fig. 2.2. On the wide energy range of Fig. 2.2 a) it is apparent that both correction terms tend towards zero away from electronic resonances. Fig. 2.2 a), on the other hand, presents a magnified view of the Palladium L-edge, resolving the splitting into L_I, L_II, and L_III edges.

The *refractive index* n in the x-ray regime is commonly given in the form

$$n = 1 - \delta + i\beta, \tag{2.19}$$

with the connection to the dispersion correction terms[68] given by

$$\delta = \frac{2\pi\rho^\mathrm{num} r_\mathrm{e}}{k^2}(Z + f') \tag{2.20a}$$

$$\beta = \frac{2\pi\rho^\mathrm{num} r_\mathrm{e}}{k^2} f'', \tag{2.20b}$$

where $Z \approx f_0$, is the atomic number of an atom, with the approximation being valid at small scattering angles.

Contrary to the *atomic* scattering factor, the refractive index is a *material* property in the sense that it depends on the (homogeneous) atomic number density

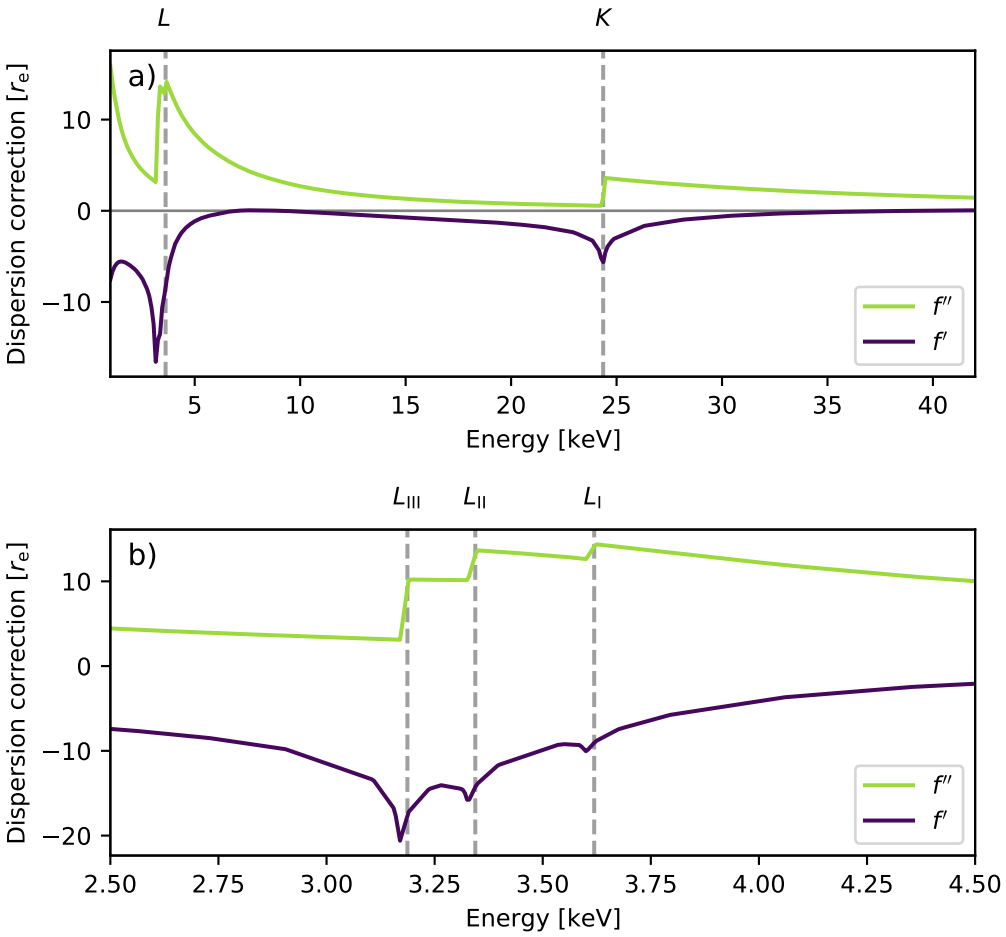

Figure 2.2: Dispersion correction of Palladium. As can be seen in panel a), real and imaginary parts of the dispersion correction are largest around resonance edges, with the L and K edge falling in the range of plotted energies. Panel b) shows a magnified view around energies close to the L edge, resolving the L_{I}, L_{II}, and L_{III} absorption edges. Data taken from [72].

averaged over the material. It is therefore sensitive to the structure of the material on length scales larger than single atoms.

Another very similar quantity is the scattering length density (SLD) of a material, which is the atomic scattering factor multiplied with the atomic number density[73, 74]. It differs from the refractive index only by a wavelength dependent factor to read

$$\mathrm{SLD} = f(E)\,\rho^{\mathrm{num}} \tag{2.21}$$

where it is again assumed that ρ_{num} can be considered locally constant. One use

case of the SLD is calculating x-ray diffraction of patterned arrays since its Fourier Transformation directly yields the form factor of an atomic distribution in the kinematical approximation via

$$A(\mathbf{Q}) = \int f(E,\mathbf{r})\rho^{\mathrm{num}}(\mathbf{r})\,\mathrm{e}^{i\mathbf{Q}\mathbf{r}}\,\mathrm{d}\mathbf{r} = \int \mathrm{SLD}(E,\mathbf{r})\,\mathrm{e}^{i\mathbf{Q}\mathbf{r}}\,\mathrm{d}\mathbf{r}. \tag{2.22}$$

The (local) SLD of a multi component material is simply the sum of the corresponding SLDs, i.e.

$$\mathrm{SLD} = \sum_\gamma \mathrm{SLD}_\gamma = \sum_\gamma f_\gamma(E,\mathbf{Q})\,\rho_\gamma^{\mathrm{num}}. \tag{2.23}$$

In many cases the material composition of an alloy is known, but calculation of the corresponding atomic number densities of each constituent might not be straightforward, which is particularly true if the growth is amorphous. In these cases the SLD can be re-expressed as a function of the mass density, which can be measured more easily or even taken from standard texts.

In order to do this, the mass density of the materials is expressed in unified atomic mass units u per unit volume. Next, a *formula unit* is defined that represents the chemical composition of the material and its weight in units of u is calculated. Dividing the mass density by the mass of the formula unit gives the *number density of formula units*. The latter can be multiplied with the total scattering length of all atoms comprising the formula unit to obtain the final SLD.

As an example, consider magnetite (Fe_3O_4) of known mass density

$$\rho^{\mathrm{mass}}_{\mathrm{Fe_3O_4}} = 5.18\,\mathrm{g\,cm^{-3}} = 3120\,\mathrm{u\,\mathring{A}^{-3}}.$$

The mass of one formula unit is

$$m_{\mathrm{Fe_3O_4}} = 3\times 55.845\mathrm{u} + 4\times 15.999\mathrm{u} = 231.531\,\mathrm{u},$$

leading to the formula unit density ("Fe_3O_4" per unit volume)

$$\rho^{\mathrm{num}}_{\mathrm{Fe_3O_4}} = \tfrac{3120}{231.531}\mathrm{\mathring{A}^{-3}} = 13.475\,\mathrm{\mathring{A}^{-3}},$$

finally yielding the total scattering length density at $E = 8.04\,\mathrm{keV}$ (Cu K-α)

$$\mathrm{SLD}_{\mathrm{Fe_3O_4}} = \rho^{\mathrm{num}}_{\mathrm{Fe_3O_4}} \times \sum_\gamma f_\gamma(E)$$

$$\approx 13.475\,\mathrm{\mathring{A}^{-3}} \times (3\times(24.74+3.19\mathrm{i})\mathrm{r_e} + 4\times(8.04+0.03\mathrm{i})\mathrm{r_e})$$

$$\approx 1433.47 + 130.57\mathrm{i}\,\mathrm{r_e}\mathrm{\mathring{A}^{-3}}.$$

Generally, calculation of the SLD from a known mass density and scattering factors f_α as well as masses m_α of all the atoms comprising one formula unit can be performed by means of

$$\mathrm{SLD}\left[\mathrm{r_e\AA^{-3}}\right] = \sum_\alpha \frac{f_\alpha\,[\mathrm{r_e}]}{m_\alpha\,[\mathrm{u}]} \quad \frac{\rho^{\mathrm{mass}}\left[\mathrm{g\,cm^{-3}}\right] 10^3}{1.660539}, \tag{2.24}$$

with α appropriately chosen to represent the chemical composition of the material. Note that eq. 2.24 holds for both atomic compounds as well as alloys of arbitrary form, e.g. $\mathrm{A_xB_{1-x}}$, in which case α takes on the fractional weights of each component.

2.1.3 Wave Polarisation

The *scattering plane* has been defined to be spanned up by the surface normal $\hat{s}$ of the sample and the component of $\mathbf{k}_i$ lying within the sample plane. When calculating resonant x-ray scattering factors it is found convenient to separate the incoming and scattered electric field amplitude into two components being parallel (π) and perpendicular (σ) to the scattering plane.

The polarisation unit vectors of the π and σ components of the electric fields of wavevector $\mathbf{k}$ are denoted $\hat{\varepsilon}_\pi$ and $\hat{\varepsilon}_\sigma$, respectively. For an incident and scattered wave of wavevectors $\mathbf{k}_i$ and $\mathbf{k}_f$ and incident and scattered angles α_i and α_f, the polarisation vectors in laboratory Cartesian coordinates $\hat{x}$, $\hat{y}$, and $\hat{z}$ can be expressed to read

$$\hat{\varepsilon}^i_\pi = \begin{pmatrix} \sin\alpha_i \\ 0 \\ \cos\alpha_i \end{pmatrix}, \qquad \hat{\varepsilon}^i_\sigma = \begin{pmatrix} 0 \\ 1 \\ 0 \end{pmatrix} \tag{2.25a}$$

$$\hat{\varepsilon}^f_\pi = \begin{pmatrix} -\sin\alpha_f \\ 0 \\ \cos\alpha_f \end{pmatrix}, \qquad \hat{\varepsilon}^f_\sigma = \begin{pmatrix} 0 \\ 1 \\ 0 \end{pmatrix} \tag{2.25b}$$

$$\tag{2.25c}$$

where the $\hat{x}$ and $\hat{y}$ span the sample plane, $\hat{x}$ lays within the scattering plane and $\hat{z} = \hat{s}$ is the surface normal (also compare Fig. 2.3).

Hence, any polarisation state is described as a linear superposition of components parallel and perpendicular to the scattering plane having a fixed phase difference $\Delta\phi = \Delta\phi_\parallel - \Delta\phi_\perp$. The two cases $\Delta\phi = 0$ and $\Delta\phi = \pm\pi/2$ correspond to the important cases of linearly, left- and right circularly polarised light, respectively.

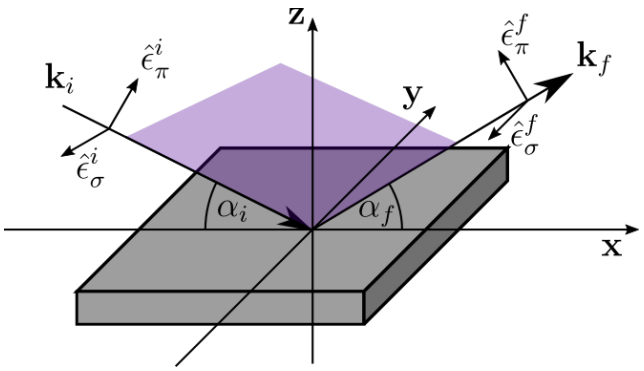

Figure 2.3: Scattering geometry discriminating polarisation states of the incident and scattered x-rays. If the scattering is limited to the scattering plane indicated in purple, the π (σ) components will always lie within (perpendicular to) the scattering plane.

For instance, π-polarised light is given by the expression

$$\mathbf{E}_{\pi pol.} = \begin{pmatrix} 1 \\ 0 \end{pmatrix} \tag{2.26}$$

and left and right circularly polarised light are expressed by

$$\mathbf{E}_{LCP} = \frac{1}{\sqrt{2}} \begin{pmatrix} 1 \\ i \end{pmatrix} \tag{2.27a}$$

$$\mathbf{E}_{RCP} = \frac{1}{\sqrt{2}} \begin{pmatrix} 1 \\ -i \end{pmatrix} \tag{2.27b}$$

where in all cases $\Delta\phi_\parallel$ has been defined to be 0 and $E_\parallel = E_\perp = 1/\sqrt{2}$, so that the modulus amplitude is normalised to 1.

2.1.4 Magnetic Scattering: A Special Case of Resonant Scattering

Magnetic scattering is usually dominated by electrical dipole (E1) transitions [70, 74, 75], and neglecting all other contributions, the *x-ray scattering factor in dipole-approximation* is given by the expression

$$f(\mathbf{Q}, E) = (\hat{\varepsilon}^f \cdot \hat{\varepsilon}^i) F^{(0)}(E) - i(\hat{\varepsilon}^f \times \hat{\varepsilon}^i) \cdot \hat{\mathbf{m}} F^{(1)}(E), + (\hat{\varepsilon}^f \cdot \hat{\mathbf{m}})(\hat{\varepsilon}^i \cdot \hat{\mathbf{m}}) F^{(2)}(E) \tag{2.28}$$

with $F^{(0)}(E)$, $F^{(1)}(E)$ and $F^{(2)}(E)$ being energy dependent constants according to the specific electronic configuration of the ion. Additionally, the magnetic dispersion correction includes a dependency on the magnetic moment $\mathbf{m}$ of an atom through

the electric dipole (E1) transition[76] as indicated in eq. 2.28. Being a resonance effect, magnetic dispersion of scattering factors is still limited in occurrence to the vicinity of absorption edges, however imposing the additional requirement of initial and excited atomic states being spin-split as is, for instance, the case for the L_{II} and L_{III} edges, but not for the L_{I} edge.

An often more convenient expression for the scattering factors can be found in matrix notation[69], explicitly considering the polarisation state of the x-rays by splitting the electrical field $\mathbf{E}$ up into π- and σ-components E_π and E_σ as discussed in section 2.1.3, to take on the form

$$f^{res.} = \boldsymbol{M}\boldsymbol{E} = \begin{pmatrix} M_{\pi\pi} & M_{\pi\sigma} \\ M_{\sigma\pi} & M_{\sigma\sigma} \end{pmatrix} \begin{pmatrix} E_\pi \\ E_\sigma \end{pmatrix}, \tag{2.29}$$

with $\boldsymbol{M}$ being a transition Matrix taking into account the particular electronic excitations of the scattering ion. In other words, computation of eq. 2.29 results in a 2-vector, specifying the π- and σ-components of the scattering amplitudes given a particular polarisation state of the incoming x-ray wavefield $\mathbf{E}$.

The four scattering channels ($\pi \to \pi, \pi \to \sigma, \sigma \to \pi, \sigma \to \sigma$) in eq. 2.29 can be expressed in terms of the respective vector products seen in eq. 2.28 using the laboratory frame for the polarisation vectors as seen in eq. 2.25. Assuming circularly polarised x-rays and small angle approximations of the trigonometric functions, we find the expression

$$f^{res.}_{dipole} = \frac{1}{\sqrt{2}} \begin{pmatrix} F^{(0)} & -iF^{(1)}m_x \\ -F^{(1)}m_x & F^{(0)} \end{pmatrix} \begin{pmatrix} 1 \\ \pm i \end{pmatrix} = \frac{1}{\sqrt{2}} \begin{pmatrix} F^{(0)} \pm F^{(1)}m_x \\ \pm i \left(F^{(0)} \pm F^{(1)}m_x\right) \end{pmatrix}. \tag{2.30}$$

Interpreting eq. 2.30 it is apparent that the terms involving $F^{(0)}$ simply contribute to the charge scattering amplitude, since they are limited – like the non-resonant charge scattering – to the $\pi \to \pi$ and $\sigma \to \sigma$ scattering channels and include no magnetic sensitivity. The magnetic terms of eq. 2.30 being proportional to $F^{(1)}$ are limited to cross-channel scattering $\pi - \sigma$ and $\sigma - \pi$, respectively.

The total scattering factor f is then given by

$$\begin{aligned} f = f_0 + f^{res.}_{dipole} &= \frac{1}{\sqrt{2}} \begin{pmatrix} f_0 + F^{(0)} & -iF^{(1)}m_x \\ -F^{(1)}m_x & f_{nonres.} + F^{(0)} \end{pmatrix} \begin{pmatrix} 1 \\ \pm i \end{pmatrix} \\ &= \begin{pmatrix} f_0 + F^{(0)} \pm F^{(1)}m_x \\ \pm i \left(f_0 + F^{(0)} \pm F^{(1)}m_x\right) \end{pmatrix}, \end{aligned} \tag{2.31}$$

where $f_0 = Zr_0$ for small scattering angles and it can be seen that $F^{(0)} = f' + if''$,

i.e. the usual resonant dispersion correction, while $F^{(1)}$ is non-zero only for x-rays of energy close to a suitable absorption edge.

Inspecting eq. 2.31 it is clear that using circularly polarised light and under the stated approximations, the scattered amplitude under resonant scattering conditions is, again, a circularly polarised electric field of the same helicity as the driving field. Depending on the beam helicity used, the charge-dependent resonant scattering amplitude is additionally either increased or reduced by an amount $F^{(1)}m_x$ proportional to the local x-component of the local magnetic moment. Note, that the same result is obtained when instead of considering a flipped beam helicity the samples magnetic moments are inverted.

The intensity of the circularly polarised scattered E-field of an arbitrary distribution of atoms is the squared modulus of the amplitude, i.e. both polarisation components contribute equally and separately. Hence, it is possible to write the total scattering factor again in the familiar form, slightly modified to include the magnetic contribution at resonance to read

$$\begin{aligned} f^{\pm} &= f_0(\mathbf{Q}) + F^{(0)} \pm F^{(1)}\hat{m}_x \\ &= f_0(\mathbf{Q}) + f'(E) + if''(E) \pm f'_{\mathrm{mag}}(E, m_x) \pm if''_{\mathrm{mag}}(E, m_x) \end{aligned} \tag{2.32}$$

where the $\pm$ sign in the magnetic correction term corresponds to either a switch of beam helicity or component within the scattering plane of the local magnetic moment m_x. The rightmost equality of eq. 2.32 stresses the fact that on resonance, the scattering factor consists of four distinct components, the real- and imaginary parts of the charge- and magnetic contributions, which generally have all to be fitted separately when a magnetic characterisation of a sample is to be done. Further, following eq. 2.20, the magnetic dispersion correction also affects the refractive index n of a magnetic material, as well as the SLD.

Fig. 2.4 shows the energy dependence of the charge- and magnetic dispersion corrections of Fe at the L-edge. The data have been found experimentally[50], by measuring the imaginary components via x-ray absorption from which the real components are calculated using the Kramers-Kronig relations[62]. Energies right below the L_{III} absorption edge are found particularly convenient for measurements of magnetic scattering: Small values of f'' imply a low fluorescence yield, which would otherwise contribute background noise to the experiment. At the same time, f'_{mag} and f''_{mag} are both relatively large, maximising the difference of the scattered intensities I^+ and I^-, measured at opposite beam helicity or sample magnetisation, following the sign convention established in eq. 2.32. Hence, the dependence of f towards the magnetisation of the sample reflects in the non-resonant scattered

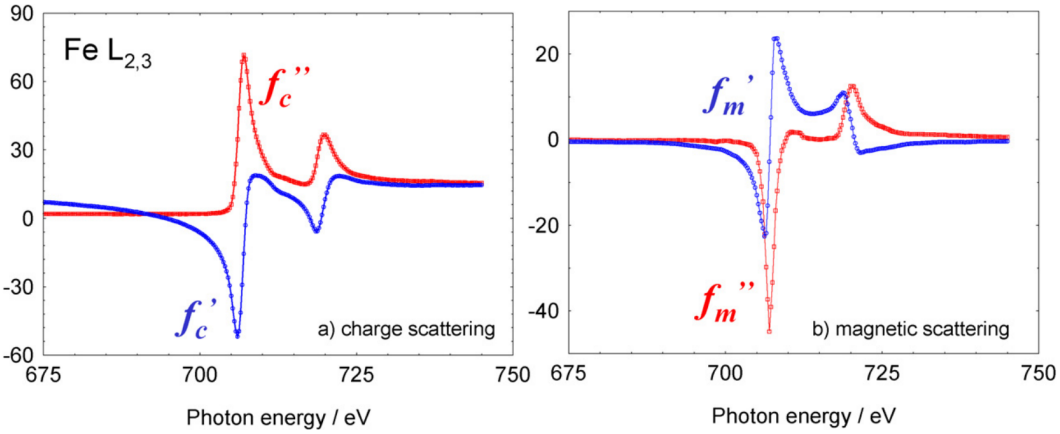

Figure 2.4: Dispersion correction of charge scattering (left) and magnetic scattering (right) of the Fe L_{II} and L_{II} absorption edges. Adapted from [50].

intensity I splitting up into two slightly different intensities I^+ and I^- at energies close to a suitable resonance edge.

The *Asymmetry Ratio*[75, 77, 78] defined by

$$A.R. = \frac{I^+ - I^-}{I^+ + I^-} \tag{2.33}$$

stresses the usually relatively small difference of two measurements $I^+ - I^-$ involving a magnetic contribution by normalising it to the sum signal $I^+ + I^-$ of the two. Since charge- and magnetic resonance corrections collectively contribute to the total dispersion correction and hence the scattering amplitude, the $A.R.$ is a charge-magnetism interference term and single components cannot directly be reconstructed from intensity measurements but have to be treated as separate parameters when fitting simulated to experimental data.

2.2 X-ray Reflectivity

When exposed to x-rays, every material interface in a layered system affects the complex-valued electromagnetic field amplitude within and above the sample. The characteristic interference phenomena affecting the reflected intensity are highly sensitive to the chemical structure of the sample. Hence, *x-ray reflectivity* (XRR) is a universal and well established tool in thin film and multilayer characterisation close to the origin of reciprocal space.

The small wave vector transfers XRR is performed at, mean that the x-rays are not sensitive to atomic structure, whose small length scales require large $\mathbf{Q}$. This

means that the sample can justifiably be modelled by a continuous distribution of scatterers, described by the refractive index n, which is known as the optical regime.

It will first be shown how an electromagnetic wave behaves at a single flat interface between two media of differing refractive index n, before generalising the result to calculate the reflectivity of a fully generic structure. It will be shown how XRR theory provides an analytical solution of the electromagnetic wave equation, which is readily extensible to a wide range of real systems investigated by x-ray scattering experiments[62, 79–83].

Intuitively, it is expected that disregarding what happens microscopically at the interface of the two media, part of the energy of the wave will penetrate from the first into the second medium, whilst some of its energy will remain in the first medium. The exact form of these new wavefields will be obtained by introducing the concepts of (amplitude and intensity) *reflectivity* and *transmittivity* and deriving *Snell's law* and the *Fresnel equations*[61, 62, 79].

In the following, indices of different media will be used either in the form of superscript or subscript. The exact choice will be made in order to maximise readability, rather than consistency and what is meant should generally be clear from context. However, if used as superscript, indices are usually used in parentheses to avoid confusion with mathematical exponents in power notation.

2.2.1 The wave equation

The starting point of the discussion will be a general electromagnetic wave of the form

$$E(\mathbf{r}) = \int E_{\mathbf{k}}\, \mathrm{e}^{i\mathbf{k}\mathbf{r}}\, \mathrm{d}^3\mathbf{k} = \int \mathrm{e}^{i\mathbf{k}_\parallel \mathbf{r}_\parallel} \left(\mathfrak{t}_{\mathbf{k}_\parallel}\, \mathrm{e}^{ik_z z} + \mathfrak{r}_{\mathbf{k}_\parallel}\, \mathrm{e}^{-ik_z z} \right) \mathrm{d}^2\mathbf{k}_\parallel, \tag{2.34}$$

and two infinite slabs of material of refractive indices n_1 and n_2 filling the half spaces $z \geq 0$ and $z < 0$ in cartesian coordinates, forming a common interface in the x-y-plane at $z = 0$ as seen in Fig. 2.5.

The two solutions of eq. 2.34 in the two media defined for $z \geq 0$ and $z < 0$ have to be connected[62, 84] at the interface $z = 0$. Demanding the boundary condition of a smooth connection of the wavefields at the interface we find

$$E^{(1)}(\mathbf{r})\Big|_{z=0} = E^{(2)}(\mathbf{r})\Big|_{z=0} \quad \text{and} \quad \frac{\partial E^{(1)}(\mathbf{r})}{\partial z}\Big|_{z=0} = \frac{\partial E^{(2)}(\mathbf{r})}{\partial z}\Big|_{z=0}, \tag{2.35}$$

where superscripts are used to indicate in which medium the waves are propagating.

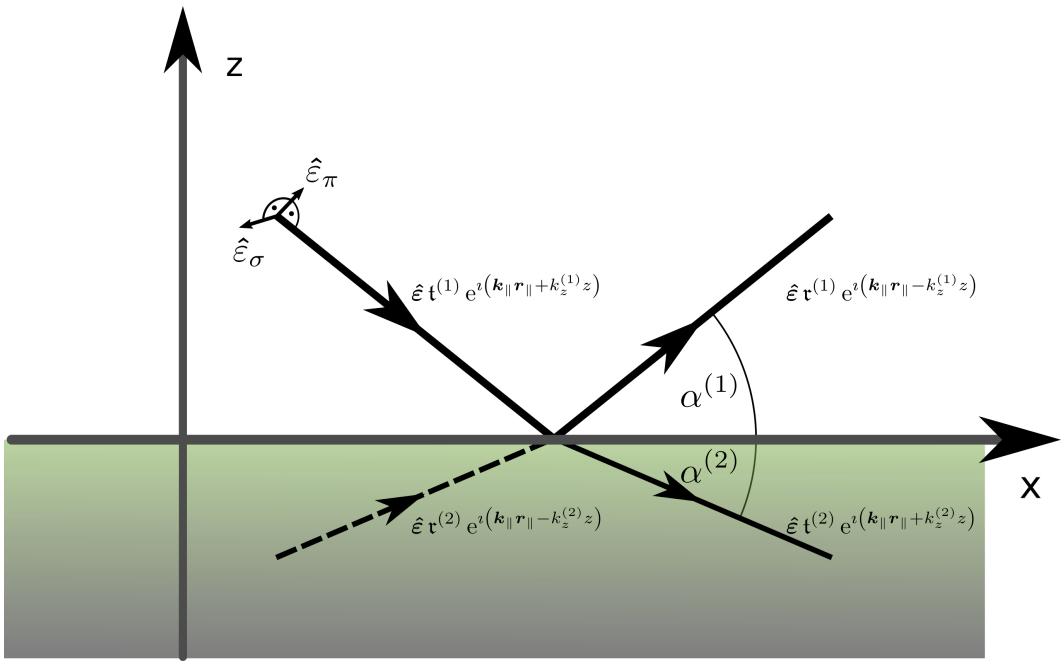

Figure 2.5: Real Space representation of the electric field at the interface of two linear, isotropic and homogeneous media. A monochromatic plane wave of wavevector $\mathbf{k^{(1)}}$ and amplitude $\mathfrak{t}^{(1)}$ excites a reflected and transmitted wavefield of identical in-plane wavevector component $\mathbf{k}_\parallel$ and amplitudes $\mathfrak{r}^{(1)}$ and $\mathfrak{t}^{(2)}$, respectively. The reflection and refraction angles $\alpha^{(1)}$ and $\alpha^{(2)}$ are connected to the refractive indices of the media $n^{(1)}$ and $n^{(2)}$ by eq. 2.39. Since electromagnetic waves are transversal, the amplitude vector will be a linear combination of the $\hat{\pi}$ and $\hat{\sigma}$ unit vectors, which are parallel and perpendicular to the scattering plane, respectively. Although part of the general solution, the amplitude $\mathfrak{r}^{(2)}$ of the reflected wave in the second medium is 0 for a single reflection process but becomes important when considering the reflectivity of multiple interfaces.

From eq. 2.34 it now follows that

$$\int \mathrm{e}^{i\mathbf{k}_\parallel^{(1)}\mathbf{r}_\parallel}\left(R_{\mathbf{k}_\parallel}^{(1)} + T_{\mathbf{k}_\parallel}^{(1)}\right)\mathrm{d}\mathbf{k}_\parallel = \int \mathrm{e}^{i\mathbf{k}_\parallel^{(2)}\mathbf{r}_\parallel}\left(R_{\mathbf{k}_\parallel}^{(2)} + T_{\mathbf{k}_\parallel}^{(2)}\right)\mathrm{d}\mathbf{k}_\parallel \tag{2.36a}$$

$$\int \mathrm{e}^{i\mathbf{k}_\parallel^{(1)}\mathbf{r}_\parallel}\left(\mathbf{k}^{(1)}\,R_{\mathbf{k}_\parallel}^{(1)} - \mathbf{k}^{(1)}\,T_{\mathbf{k}_\parallel}^{(1)}\right)\mathrm{d}\mathbf{k}_\parallel = \int \mathrm{e}^{i\mathbf{k}_\parallel^{(2)}\mathbf{r}_\parallel}\left(\mathbf{k}^{(2)}\,R_{\mathbf{k}_\parallel}^{(2)} - \mathbf{k}^{(2)}\,T_{\mathbf{k}_\parallel}^{(2)}\right)\mathrm{d}\mathbf{k}_\parallel \tag{2.36b}$$

and since eq. 2.36 a) and b) have to hold for any choice of $\mathbf{r}_\parallel$, all exponentials and the constant terms in parentheses have to equate independently from each other,

which directly leads to

$$\mathbf{k}_{\parallel}^{(1)} = \mathbf{k}_{\parallel}^{(2)} \tag{2.37a}$$

$$\mathfrak{r}_{\mathbf{k}_{\parallel}}^{(1)} + \mathfrak{t}_{\mathbf{k}_{\parallel}}^{(1)} = \mathfrak{r}_{\mathbf{k}_{\parallel}}^{(2)} + \mathfrak{t}_{\mathbf{k}_{\parallel}}^{(2)} \tag{2.37b}$$

$$k_{\parallel}^{(1)}\hat{\mathbf{k}_{\parallel}}\left(\mathfrak{r}_{\mathbf{k}_{\parallel}}^{(1)} + \mathfrak{t}_{\mathbf{k}_{\parallel}}^{(1)}\right) + k_z^{(1)}\hat{\mathbf{k}_z}\left(\mathfrak{r}_{\mathbf{k}_{\parallel}}^{(1)} - \mathfrak{t}_{\mathbf{k}_{\parallel}}^{(1)}\right) = k_{\parallel}^{(2)}\hat{\mathbf{k}_{\parallel}}\left(\mathfrak{r}_{\mathbf{k}_{\parallel}}^{(2)} + \mathfrak{t}_{\mathbf{k}_{\parallel}}^{(2)}\right) + k_z^{(2)}\hat{\mathbf{k}_z}\left(\mathfrak{r}_{\mathbf{k}_{\parallel}}^{(2)} - \mathfrak{t}_{\mathbf{k}_{\parallel}}^{(2)}\right) \tag{2.37c}$$

where eq. 2.37 a) shows that the in-plane components of $\mathbf{k}_i$ and $\mathbf{k}_f$ are conserved as pictured in Fig. 2.6. In explicit consideration of angular variables and choosing the coordinate system in a way that $\mathbf{k}_{\parallel} = \mathbf{k}_x$ eqs. 2.37 take on the form

$$n^{(1)}k\cos\alpha_i^{(1)} = n^{(1)}k\cos\alpha_f^{(1)} = n^{(2)}k\cos\alpha_i^{(2)} = n^{(2)}k\cos\alpha_f^{(2)} \tag{2.38a}$$

$$n^{(1)}k\cos\alpha^{(1)}\,\mathfrak{r}_{\alpha}^{(1)} + n^{(1)}k\cos\alpha^{(1)}\,\mathfrak{t}_{\alpha}^{(1)} = n^{(2)}k\cos\alpha^{(2)}\,\mathfrak{r}_{\alpha}^{(2)} + n^{(2)}k\cos\alpha^{(2)}\,\mathfrak{t}_{\alpha}^{(2)} \tag{2.38b}$$

$$n^{(1)}k\sin\alpha^{(1)}\,\mathfrak{r}_{\alpha}^{(1)} - n^{(1)}k\sin\alpha^{(1)}\,\mathfrak{t}_{\alpha}^{(1)} = n^{(2)}k\sin\alpha^{(2)}\,\mathfrak{r}_{\alpha}^{(2)} - n^{(2)}k\sin\alpha^{(2)}\,\mathfrak{t}_{\alpha}^{(2)}. \tag{2.38c}$$

From eq. 2.37 a) it follows that in each medium $\alpha_i = \alpha_f = \alpha$ and from eqns 2.37 b) and 2.38 b) it directly follows that

$$n^{(1)}\cos\alpha^{(1)} = n^{(2)}\cos\alpha^{(2)}. \tag{2.39}$$

Eq. 2.39 is known as *Snell's Law*, which relates the refractive indices n with the refraction angles α at the interface of two media[85, 86].

2.2.2 Fresnel Equations

We are now going to discuss the results of the previous section in the context of the problem of solving the wave equation at an interface between two media for a particular driving field in the form of a single monochromatic plane wave of wavevector k propagating in medium (1) incident at angle α on the interface of medium (2). This corresponds to considering eqns 2.34 and the following discussion for a single wave coefficient $E_{\mathbf{k}} = E_{\alpha} = E$. Hence, we specify the parameters for the refractive indices of the two media and choose a wave vector $\mathbf{k_i}$ of the incident radiation and expect to obtain values for $\alpha_2, \mathfrak{r}_1, \mathfrak{t}_2$ and $\mathfrak{r}_2$.

However, the system of linear equations 2.37 a-c (and equivalently eqns 2.38 a-c) is still underdetermined and requires specification of one additional parameter. Considering the physical interpretations of the wave components associated with $\mathfrak{r}$ and $\mathfrak{t}$ it is intuitively clear that for both media being semi-infinite in the positive and

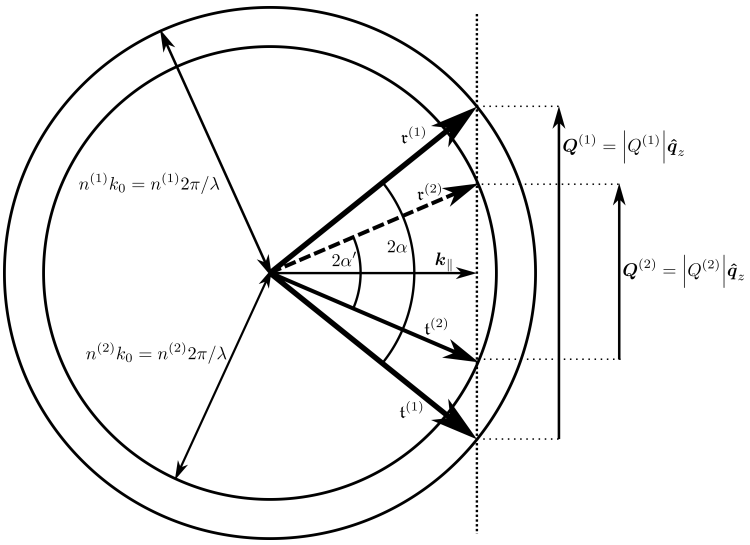

Figure 2.6: Reciprocal space representation of the scattering process. Because of the conservation of the in-plane component of the wavevector for each partial solution of the wave equation the wavevector in each medium has to terminate on the same vertical line perpendicular to $\mathbf{k}_\parallel$. The two circles represent the spheres defined by the dispersion relation $|\mathbf{k}| = nk_0$ in the upper and lower medium. As can be seen, for values $\alpha \leq \alpha_c$ it holds $\mathbf{k}_\parallel \geq n^{(2)}k_0$, leading to the formation of an evanescent wave.

negative z-directions no reflected wave component in medium (2) is then expected[61, 62, 84]. Consequently $\mathfrak{r}_2 = 0$ and all other quantities can be derived.

We define the *amplitude reflectivity* r and *amplitude transmittivity* t by

$$r \equiv \mathfrak{r}_1/\mathfrak{t}_1 \tag{2.40a}$$

$$t \equiv \mathfrak{t}_2/\mathfrak{t}_1, \tag{2.40b}$$

which corresponds to the fraction of the incident wave that gets reflected on- and transmitted through the interface, respectively. From eq. 2.37 b and the k_z component of eq. 2.37 c (eq. 2.38 c for the angular representation) we find

$$r = \frac{\sin\alpha_1 - \sin\alpha_2}{\sin\alpha_1 + \sin\alpha_2} \tag{2.41a}$$

$$t = \frac{2\sin\alpha_1}{\sin\alpha_1 + \sin\alpha_2}, \tag{2.41b}$$

which is known as the *Fresnel equations*[86]. It allows the straightforward calculation of the important quantities r and t solely from knowledge of the wavevector transfer

Q in each medium which takes on the form

$$k_z^{(2)} = \sqrt{(n_2 k)^2 - k_\parallel^2} = \sqrt{(n_2 k)^2 - (n_1 k \cos\alpha_1)^2}. \tag{2.42}$$

2.2.3 Critical angle, total reflection and limiting cases

As can be seen from eq. 2.42 c), $k_z^{(2)}$ will be fully imaginary if

$$n_2^2 < n_1^2 \cos^2\alpha_c. \tag{2.43}$$

In this case the expression for the transmitted wave takes on the form of an *evanescent wave*[62, 85, 86]

$$E_t = \mathfrak{t}\, \mathrm{e}^{i\boldsymbol{k}_\parallel \boldsymbol{r}_\parallel}\, \mathrm{e}^{-\operatorname{Im}(k_z) z}, \tag{2.44}$$

meaning that the wave is showing oscillatory behaviour along $\boldsymbol{r}_\parallel$ over the surface of the interface and gets exponentially damped with increasing penetration depth into the material.

From eq. 2.43 and the definition of the refractive index $n = 1-\delta+i\beta$, Taylor expanding the cosine and neglecting third order terms we find

$$\alpha_c \approx \sqrt{2\left(\delta^{(2)} - \delta^{(1)}\right) + 2i\left(\beta^{(2)} - \beta^{(1)}\right)}. \tag{2.45}$$

Neglecting the usually very small absorption related imaginary part of eq. 2.45 we find that the critical angle of total reflection takes on the approximate value

$$\alpha_c \approx \sqrt{2\left(\delta^{(2)} - \delta^{(1)}\right)}, \tag{2.46}$$

which, for a vacuum-matter interface, with $n^{(1)} = n_{\mathrm{vac}} = 1$ and refractive index of the material $n^{(2)} = n = 1 - \delta + i\beta$ takes on the common form $\alpha_c \approx \sqrt{2\delta}$.

To explore the limiting behaviour of reflection and refraction at low and high incident angles we consider the particular case of illuminating a vacuum-iron interface with collimated x-rays of energies slightly below and above the Fe K absorption edge at angles around α_c. The Fe K-edge is found at 7.112 keV and we limit the discussion to the two energies 7.0 keV and 7.2 keV. Strictly speaking α_c will be a function of the x-ray energy, but for the cases under consideration the approximation for both wavelengths $\delta \approx 2.6 \times 10^{-5}$ and hence $\alpha_c \approx 0.41^\circ$ will suffice.

Qualitatively, when increasing above an electronic absorption edge, the photon energy exceeds a particular electronic transition in the material, allowing a stronger photonic absorption of the material, manifesting in a sudden increase of

the extinction coefficient β being part of the refractive index $n = 1 - \delta + i\beta$.

A usual way of calculating the refractive index of a given material at a particular energy consists in looking up the (complex) scattering lengths f as well as the atomic number density ρ_{at} of the material from a standard source in order to calculate n according to eqs. 2.19 and 2.20.

The refractive indices of iron at each of the two energies is found to be

$$n_{\mathrm{Fe}}(7.0\,\mathrm{keV}) \approx 1 - 2.6 \times 10^{-5} + i\,5.6 \times 10^{-7}$$

and

$$n_{\mathrm{Fe}}(7.2\,\mathrm{keV}) \approx 1 - 2.6 \times 10^{-5} + i\,4.3 \times 10^{-6},$$

corresponding to an almost tenfold increased x-ray absorption. With

$$q^{\mathrm{vac}}/k = 2\sin\alpha \tag{2.47a}$$

$$q^{\mathrm{Fe}}/k = 2\sqrt{n^2 - \cos^2\alpha}, \tag{2.47b}$$

we obtain the angle dependent *intensity reflectivity* R and *intensity transmittivity* T defined by

$$R = rr^* \tag{2.48a}$$

$$T = tt^*. \tag{2.48b}$$

As can be seen in Fig. 2.7 a) and b) the intensity reflectivity generally starts at values close to 1 at low angles indicating the regime of total external reflection of the wave[62, 87, 88]. Around α_c the reflected intensity drops rapidly, with a lower extinction coefficient β generally meaning the drop being sharper. For angles $\alpha \gg \alpha_c$ the reflected intensity drops to very low values and from inspection of eq. 2.41 it becomes apparent that the intensity follows a power law $\propto q^{-4}$.

Apart from absorption losses, radiation which is not reflected on the interface has to be transmitted into the material, the transmitted intensity not very surprisingly acts in a way complementary to the reflected intensity as seen in Fig. 2.7 b). At very low angles below α_c, the transmitted intensity is effectively zero, because all the radiation gets reflected. Accordingly, at high angles almost all intensity of the incoming radiation gets transmitted into the material and $T \approx 1$. The evanescent wave propagating along the surface at angles around α_c may go up to as high as four times the intensity of the incident radiation. However, the evanescent wave stores energy supplied from the incident radiation but does not contribute to the energy

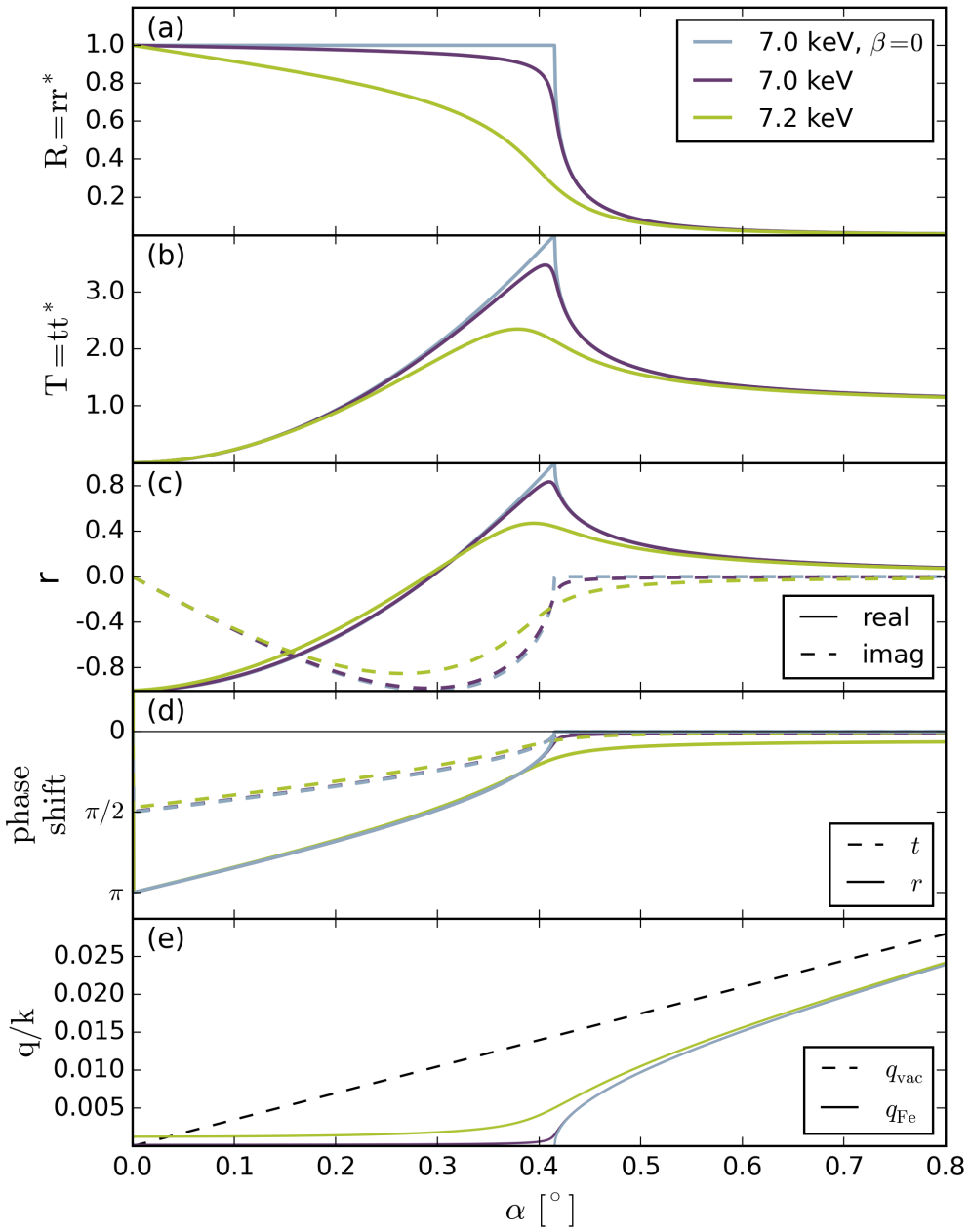

Figure 2.7: Angle dependence of refraction effects at a vacuum-iron interface below and above the Fe K-edge. a) reflected intensity, b) transmitted intensity, c) real and imaginary part of the reflected wave with respect to the incident wave of amplitude $1 + 0i$, d) phase shift of reflected and transmitted wave with respect to incident wave, e) comparison of internal and external wavevector transfer. For clarity each plot also contains a graph where the absorption coefficient β has artificially been set to zero.

flow in the (semi-infinite) system, and therefore transmitted intensities > 1 do not violate energy conservation.

It is further instructive to consider the phase dependency of the amplitude of the reflected and transmitted waves as seen in Fig. 2.7 c) and d). As α increases, the real and complex parts of amplitude reflectivity $r \equiv \mathfrak{r}^{(1)} e^{i\boldsymbol{k}^{(1)}\boldsymbol{r}} / \mathfrak{t}^{(1)} e^{i\boldsymbol{k}^{(1)}\boldsymbol{r}}$ smoothly vary in a way that its amplitude undergoes a phase shift from π to 0, meaning that the reflected wave is out-of-phase below α_c and in-phase above α_c with respect to the incoming radiation. Similarly, the transmitted wave shows a phase shift of $\pi/2$ at $\alpha = 0$ and is in-phase for $\alpha \gg \alpha_c$.

Finally, Fig. 2.7 e) compares the internal and external wavevector transfer. Around α_c the difference is largest before q_{Fe} asymptotically approaches q_{vac} for $\alpha > \alpha_c$. Figure 2.7 b) and e) together confirm the validity of the kinematic approximation for $\alpha \gg \alpha_c$, when approximating the internal wavevector transfer of a material by the easily obtainable external wavevector transfer above the sample setting the transmittivity over the whole sample equal to 1.

2.2.4 Multiple interfaces

In this section we will calculate the reflection of a plane wavefield from an arbitrary number of interfaces instead of restricting ourselves to a single interface, as is schematically presented in Fig. 2.8. The procedure as presented here basically follows that of Mikulik [84].

The illuminated sample is now modelled by a stack of N thin layers of material of refractive index $n^{(i)}$, with $n^{(0)}$ being the refractive index of vacuum and $n^{(N+1)}$ corresponding to the substrate. Furthermore, each pair of layers $n^{(i)}$ and $n^{(i+1)}$ share an interface at height $z^{(i)}$.

We can then find a generalised set of equations from eq. 2.37 b and c valid for arbitrary values of z_i to read

$$\mathfrak{r}^{(i)} e^{ik_z^{(i)} z_i} + \mathfrak{t}^{(i)} e^{-ik_z^{(i)} z_i} = \mathfrak{r}^{(i+1)} e^{ik_z^{(i+1)} z_i} + \mathfrak{t}^{(i+1)} e^{-ik_z^{(i+1)} z_i} \tag{2.49a}$$

$$k_z^{(i)} \mathfrak{r}^{(i)} e^{ik_z^{(i)} z_i} - k_z^{(i)} \mathfrak{t}^{(i)} e^{-ik_z^{(i)} z_i} = k_z^{(i+1)} \mathfrak{r}^{(i+1)} e^{ik_z^{(i+1)} z_i} - k_z^{(i+1)} \mathfrak{t}^{(i+1)} e^{-ik_z^{(i+1)} z_i}. \tag{2.49b}$$

The latter system of equations can be re-expressed using a matrix formalism to read

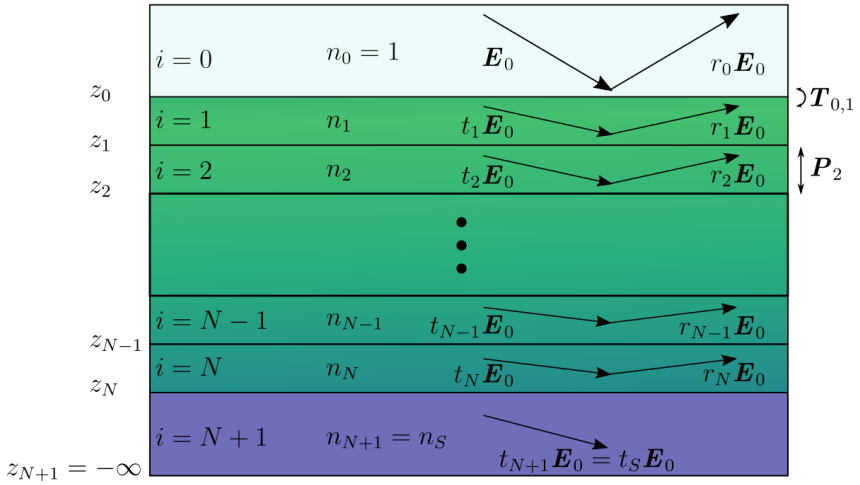

Figure 2.8: Schematic of a layered sample. Each layer consists of material of refractive index n_i. The transfer matrices $\boldsymbol{T}_{i,i+1}$ connect the wavefields at the *interfaces* located at height z_i. The propagation matrices $\boldsymbol{P_{i+1}}$ connect the phase of the wavefields within layer $i+1$, traversing the distance $\Delta_{i+1} = z_i - z_{i+1}$.

$$\boldsymbol{T}_i\,\boldsymbol{E}_i(z_i) = \mathbf{T}_{i+1}\,\boldsymbol{E}_{i+1}(z_i) \tag{2.50a}$$

$$\boldsymbol{T}_i = \begin{pmatrix} 1 & 1 \\ k_z^{(i)} & -k_z^{(i)} \end{pmatrix} \qquad \boldsymbol{T}_i^{-1} = \frac{1}{2k_z^{(i)}} \begin{pmatrix} k_z^{(i)} & 1 \\ k_z^{(i)} & -1 \end{pmatrix} \tag{2.50b}$$

$$\boldsymbol{E}_i(z_i) = \begin{pmatrix} \mathfrak{r}^{(i)} \mathrm{e}^{ik_z^{(i)} z_i} \\ \mathfrak{t}^{(i)} \mathrm{e}^{-ik_z^{(i)} z_i} \end{pmatrix} \tag{2.50c}$$

with ***interface matrix*** $\boldsymbol{T}_i$, its inverse $\boldsymbol{T}_i^{-1}$ and the ***interphase amplitude vector*** $\boldsymbol{E}_i$. In order to directly obtain an expression for $\boldsymbol{E}_i$, assuming the field amplitudes $\boldsymbol{E}_{i+1}$ are known, eq. 2.50 a can be re-arranged to read

$$\boldsymbol{E}_i(z_i) = \boldsymbol{T}_i^{-1}\boldsymbol{T}_{i+1}\,\boldsymbol{E}_{i+1} = \boldsymbol{T}_{i,i+1}\boldsymbol{E}_{i+1}(z_i), \tag{2.51}$$

where the ***Transfer Matrix*** $\boldsymbol{T}_{i,i+1}$ is given by

$$\begin{aligned} \boldsymbol{T}_{i,i+1} &= \frac{1}{2k_z^{(i)}} \begin{pmatrix} k_z^{(i)} & 1 \\ k_z^{(i)} & -1 \end{pmatrix} \begin{pmatrix} 1 & 1 \\ k_z^{(i+1)} & -k_z^{(i+1)} \end{pmatrix} \\ &= \frac{1}{k_z^{(i)}} \begin{pmatrix} k_z^{(i)} + k_z^{(i+1)} & k_z^{(i)} - k_z^{(i+1)} \\ k_z^{(i)} - k_z^{(i+1)} & k_z^{(i)} + k_z^{(i+1)} \end{pmatrix} \equiv \frac{1}{t_i} \begin{pmatrix} 1 & r_i \\ r_i & 1 \end{pmatrix} \end{aligned} \tag{2.52}$$

with r_j and t_j being the reflectivity and transmittivity amplitudes as defined in eq.

2.41.

So far, only the connection of wavefields at the interfaces have been considered, but in order to calculate the total wavefield the propagation of the electric field *within* each layer has to also be considered. Propagating from smaller to larger values of z the reflected component of the wavefield will advance in phase, while the transmitted component will recede in phase. Expressing this in matrix formulation, we find

$$\boldsymbol{E}_{i+1}(z_i) = \begin{pmatrix} \mathrm{e}^{ik_z^{(i+1)}\Delta_{i+1}} & 1 \\ 1 & \mathrm{e}^{-ik_z^{(i+1)}\Delta_{i+1}} \end{pmatrix} \begin{pmatrix} \mathfrak{r}^{(i+1)}\mathrm{e}^{ik_z^{(i+1)}z_{i+1}} \\ \mathfrak{t}^{(i+1)}\mathrm{e}^{-ik_z^{(i+1)}z_{i+1}} \end{pmatrix} = \boldsymbol{P}_{i+1}\boldsymbol{E}_i(z_{i+1}), \tag{2.53}$$

where the ***Propagation Matrix P*** connects the field amplitudes at height z_i at the *top* of layer $i+1$ to the field amplitudes at height z_{i+1} at the *bottom* of layer $i+1$. The indices of eq. 2.53 have been chosen in this way to stress that the quantity of interest is the field at height z_i.

It is now possible to connect the wavefields at the *top* of neighbouring layers i and $i+1$ by first calculating the phase-shift of the waves associated with propagating through layer $j+1$ to obtain the field at the bottom of interface j and then calculate the change of field when transferring the interface. Mathematically, this is expressed by the matrix product

$$\boldsymbol{E}_j(z_i) = \boldsymbol{T}_{i,i+1}\boldsymbol{P}_{i+1}\,\boldsymbol{E}_{i+1}(z_{i+1}). \tag{2.54}$$

To connect the fields $\boldsymbol{E}_0(z_0)$ above the sample surface to the fields in the substrate $\boldsymbol{E}_{N+1}(z_{N+1}) = \boldsymbol{E}_S(z_S)$ all intermediate layers are connected by appropriate matrices of the form of eq. 2.54

$$\begin{aligned} \boldsymbol{E}_0(z_0) &= (\boldsymbol{T}_{0,1}\boldsymbol{P}_1)\,(\boldsymbol{T}_{1,2}\boldsymbol{P}_2)\cdots(\boldsymbol{T}_{N-1,N}\boldsymbol{P}_N)\,(\boldsymbol{T}_{N,N+1}\boldsymbol{P}_{N+1})\,\boldsymbol{E}_S(z_S) \\ &= \left(\prod_{i=0}^{N}\boldsymbol{T}_{i,i+1}\boldsymbol{P}_{i+1}\right)\boldsymbol{E}_S(z_S) = \boldsymbol{M}\boldsymbol{E}_S(z_S). \end{aligned} \tag{2.55}$$

Introducing the ***Multilayer Transfer Matrix U*** and using the explicit form of the amplitude vector $\boldsymbol{E}$, eq. 2.55 reads

$$\begin{pmatrix} \mathfrak{r}^{(0)}\mathrm{e}^{ik_z^{(0)}z_0} \\ \mathfrak{t}^{(0)}\mathrm{e}^{-ik_z^{(0)}z_0} \end{pmatrix} = \boldsymbol{U}\begin{pmatrix} \mathfrak{r}^{S}\mathrm{e}^{ik_z^{S}z_S} \\ \mathfrak{t}^{S}\mathrm{e}^{-ik_z^{S}z_S} \end{pmatrix} = \begin{pmatrix} U_{11} & U_{12} \\ U_{21} & U_{22} \end{pmatrix}\begin{pmatrix} \mathfrak{r}^{S}\mathrm{e}^{ik_z^{S}z_S} \\ \mathfrak{t}^{S}\mathrm{e}^{-ik_z^{S}z_S} \end{pmatrix}, \tag{2.56}$$

where, in calculating $\boldsymbol{T}$ the propagation matrix of the substrate was defined to be $P_{N+1} = \mathbb{1}$. This is necessary because no lower interface exists within the infinitely

thick substrate, so there is no reference point to calculate the phase of the wavefield to and it is hence identified with the phase of the amplitude vector $\boldsymbol{E}_S$ within the substrate. Also, because of the lack of another interface below the substrate level z_S no reflected wave propagates within the substrate, i.e. $\mathfrak{r}^S = 0$. Therefore, from eq. 2.56 the reflectivity amplitude r_0 of the whole stack can be calculated to be

$$r_0 \equiv \frac{\mathfrak{r}^{(0)}}{\mathfrak{t}^{(0)}} = \frac{U_{12}}{U_{22}}. \tag{2.57}$$

The latter procedure suffices if one is only interested in describing the reflectivity of the sample as a whole, which generally is the only observable in a reflectivity experiment. It may be found necessary, though, that the electric field over the whole depth of the sample is required, for instance in order to utilize higher order perturbation theory. In this case, a useful approach is to keep track of the intermediate results of the matrix multiplication of eq. 2.55

$$\boldsymbol{U}_j = \prod_{i=j}^{N+1} \boldsymbol{T}_{i,i+1}\boldsymbol{P}_{i+1} \tag{2.58}$$

in order to obtain the electric field in each layer defined by

$$\boldsymbol{E}_j = \boldsymbol{U}_j \boldsymbol{E}_S \tag{2.59}$$

once the amplitude transmittivity into the substrate

$$t_S \equiv \frac{\mathfrak{t}^S}{\mathfrak{t}^{(0)}} = \frac{1}{\boldsymbol{U}_{22}} \tag{2.60}$$

has been calculated.

As an example and to recap, Fig. 2.9 shows the angle-dependent amplitude and intensity of the electric field in a sample of a single bilayer of an FeCo-Al_2O_3, each of thickness 3 nm, on a Si substrate. Panel a) shows the SLD profile of the bilayer, panels b and c (d and e) show the electric field amplitude and intensity at $\alpha_i = 2.5°$ ($\alpha_i = 15°$). It can be seen how no reflected wave exists within the substrate and how the layer and interface thicknesses are affecting the electrical field within the sample.

2.2.5 Reflectivity of a slab and Parratt's Algorithm

Calculation of the electrical field as described in the previous section provides exact results – given the resolution of the z-slicing is sufficient – but is often found

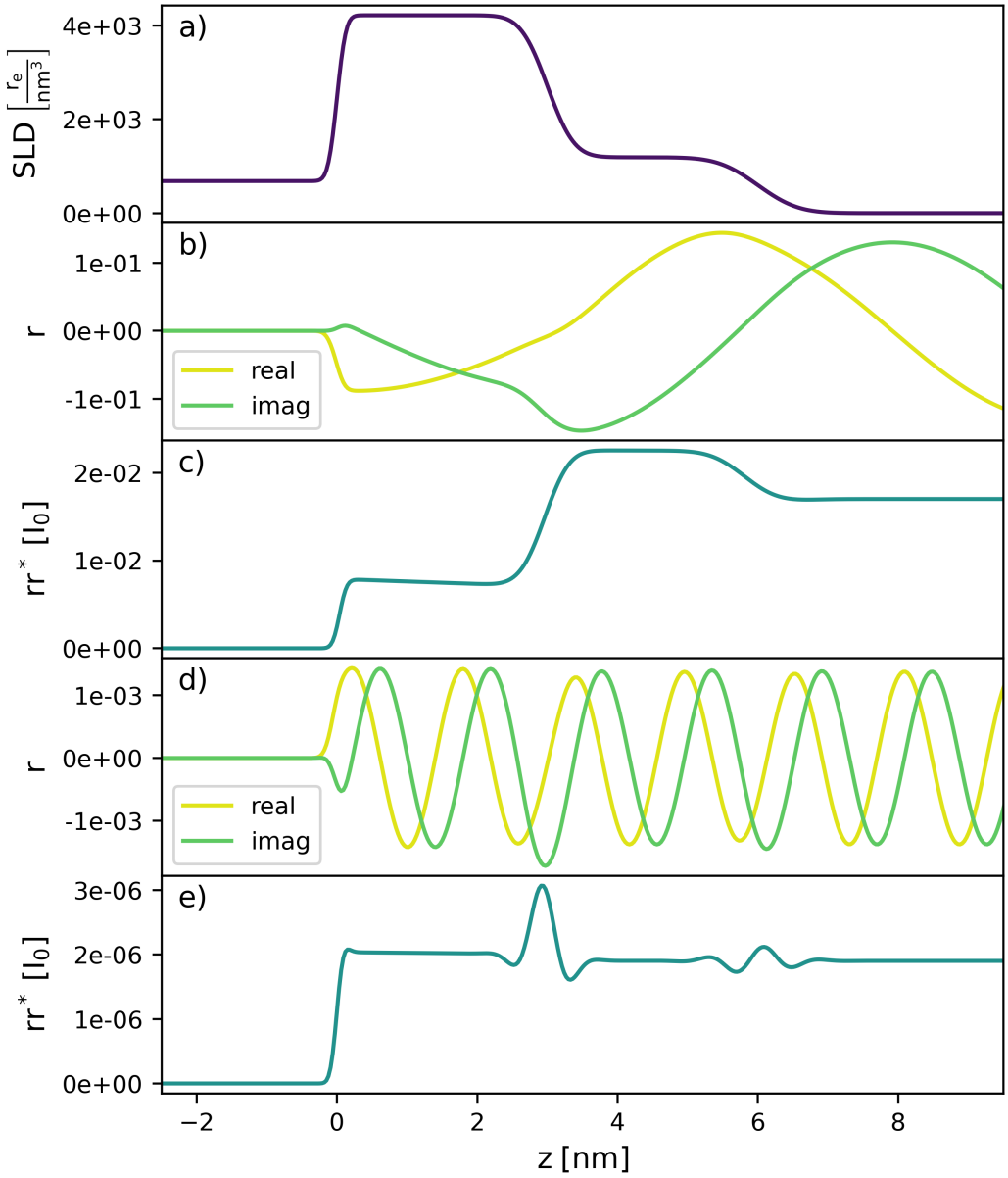

Figure 2.9: Visualisation of the scattering length density (a) of a FeCo-Al_2O_3 bilayer on a Si substrate at x-ray energy 8.04 keV. The remaining panels show the corresponding E-field and amplitude of the reflected wave at $\alpha_i = 2.5°$($\mathbf{Q}_z = 3.4\,\mathrm{nm}^{-1}$, panel b and c) and $\alpha_i = 15°$($\mathbf{Q}_z = 20.3\,\mathrm{nm}^{-1}$, panel d and e). Note that $\alpha_i = 15°$ is far beyond the grazing incidence geometry and has been chosen for demonstration purposes, only.

inefficient because of the computationally expensive matrix multiplications, which might slow a fitting process down notably. If, however, only the reflected amplitude of a sample is of interest, i.e. no differentiation in between the transmitted and reflected fields within the sample is necessary, *Parratt's recursive algorithm* provides a computationally efficient algorithm, which works for arbitrary sample profiles, the latter often not being able to be treated analytically[62, 89].

The general idea behind the algorithm is to find an exact expression of the reflectivity of a single slab and then to generalise the result to capture the reflectivity of generic sample structures. Following the previous indexing convention, let the slab of thickness d be denoted by index 1 and embedded between two semi-infinite media 0 and 2 on top and bottom, respectively. When exposed to x-ray radiation parts of the incident electrical field will be reflected on top and transmitted into the slab according to the Fresnel reflectivity and transmittivity (eqs. 2.41). However, a part of the wave transmitted into the slab is being reflected on the bottom of the slab, before being partly transmitted into medium 0 again, therefore contributing to the reflected wavefield above the slab. It is easy to see that in this way, more and more multiple reflections of ever diminishing amplitude within the slab occur, which is given by the infinite series

$$\begin{aligned} r = \;& \tilde{r}_{0,1} \\ & + \tilde{t}_{0,1}\,\tilde{t}_{1,0}\,\tilde{r}_{1,2}\,p^2 \\ & + \tilde{t}_{0,1}\,\tilde{t}_{1,0}\,\tilde{r}_{1,0}\,\tilde{r}_{1,2}^2\,p^4 \\ & + ... \end{aligned} \tag{2.61}$$

where the order of the indices indicates in which medium the wave propagates and interacts with and $p^2 = \mathrm{e}^{-ik_i d}\mathrm{e}^{ik_f d} = \mathrm{e}^{i\,q_z\,d}$ is the change of phase of the wave on traversing the slab once in both directions. Note that the notation is slightly changed so that a tilde now indicates the single reflection Fresnel reflectivity $\tilde{r}$ and transmittivity $\tilde{t}$ in order to make the differentiation from total reflectivity r including multiple reflections easier.

Eq. 2.61 is a standard geometric series, which can be evaluated and re-expressed[62], to read

$$r = \frac{\tilde{r}_{0,1} + \tilde{r}_{1,2}\,p^2}{1 + \tilde{r}_{0,1}\,\tilde{r}_{1,2}\,p^2}, \tag{2.62}$$

which allows one to calculate the total reflectivity of a slab simply from knowledge of the Fresnel reflectivities in the respective media.

In order to obtain the latter, it is noted that the wavevector transfer in

a medium is related to the (nominal) wavevector transfer in vacuum k through decomposition into a (conserved) in-plane $k_{\parallel}^{\text{medium}} = k_{\parallel}$ and out-of-plane k_z^{medium} part of the electrical field, which has to fulfil the condition

$$k = \sqrt{k^2 - k_z^2} = \sqrt{nk^2 - k_z^{\text{medium}}} = n\, k_{\text{medium}}. \tag{2.63}$$

This directly leads to

$$q_{z,j} = 2\sqrt{k^2(n^2 - 1) + k_z^2}, \tag{2.64}$$

the wavevector transfer in medium j, which in conjunction with eq. 2.41 a) allows the evaluation of eq. 2.62.

The goal of Parratt's algorithm is to slice the whole sample up into N slabs of arbitrary thickness d, with the topmost layer of the stack being identified by index 1 and the last non-identical layer of index N sitting directly on top of an infinitely thick substrate indexed $N + 1$.

In the derivation of eq. 2.62 the reflectivities $\tilde{r}_{0,1}$ and $\tilde{r}_{1,2}$ are the standard Fresnel reflectivities due to the geometry of the problem, but the equation generalises to arbitrary stacks. This means that knowledge of the Fresnel reflectivity $\tilde{r}_{j-1,j}$ and the actual reflectivity $r_{j,j+1}$ of the underlying stack allows one to calculate the reflectivity of a single slab on top of any stack of known reflectivity.

Parratt's algorithms recursively builds up the total sample reflectivity from the substrate upwards, i.e.

$$r_{j-1,j} = \frac{\tilde{r}_{j-1,j} + r_{j,j+1}p_j^2}{1 + \tilde{r}_{j-1,j}r_{j,j+1}p_j^2}, \tag{2.65}$$

where $\tilde{r}_{j-1,j}$ is the Fresnel reflectivity of the top of the iteratively built structure and $r_{j,j+1}$ is the recursively calculated reflectivity of the so-far underlying stack.

Again, the absence of a reflected wave within the substrate is exploited in order to start the iterative process, such that for calculation of the reflectivity of layer N eq. 2.62 is used, followed by calculating the reflectivity of the total stack $r_{0,1}$ by repeated application of eq. 2.65.

2.2.6 Interface Roughness

Since real interfaces between layers of material are not perfectly sharp, any calculation of x-ray reflectivity has to consider interface roughness.

Integrating the Fresnel reflectivity over infinitesimally thick slices of an ar-

bitrarily shaped interface, it can be shown that the reflectivity follows the form[62]

$$r(\mathbf{Q}) = r_{\mathrm{F}}(\mathbf{Q}) \int_{-\infty}^{\infty} \frac{\mathrm{d}f}{\mathrm{d}z} \mathrm{e}^{-iQ_z z}\, \mathrm{d}z, \tag{2.66}$$

with $f(z)$ being an interface profile function that describes the continuous transition between the nominal SLD of the two respective layers as depicted in Fig. 2.10. The derivative of the *error function* $\mathrm{erf}(x)$ is a Gaussian, i.e.

$$\frac{\mathrm{d}}{\mathrm{d}z}\mathrm{erf}(z) = \frac{2}{\sqrt{\pi}}\mathrm{e}^{-x^2}. \tag{2.67}$$

Considering the particular choice

$$f(z) = \mathrm{erf}(\frac{z - s_i}{\sqrt{2}\sigma}), \tag{2.68}$$

it follows that

$$\frac{\mathrm{d}f}{\mathrm{d}z} = \frac{1}{\sqrt{2\pi\sigma^2}}\mathrm{e}^{-\frac{z^2}{2\sigma^2}}. \tag{2.69}$$

Inserting eq. 2.69 into eq. 2.66, it follows that the reflectivity of an interface being

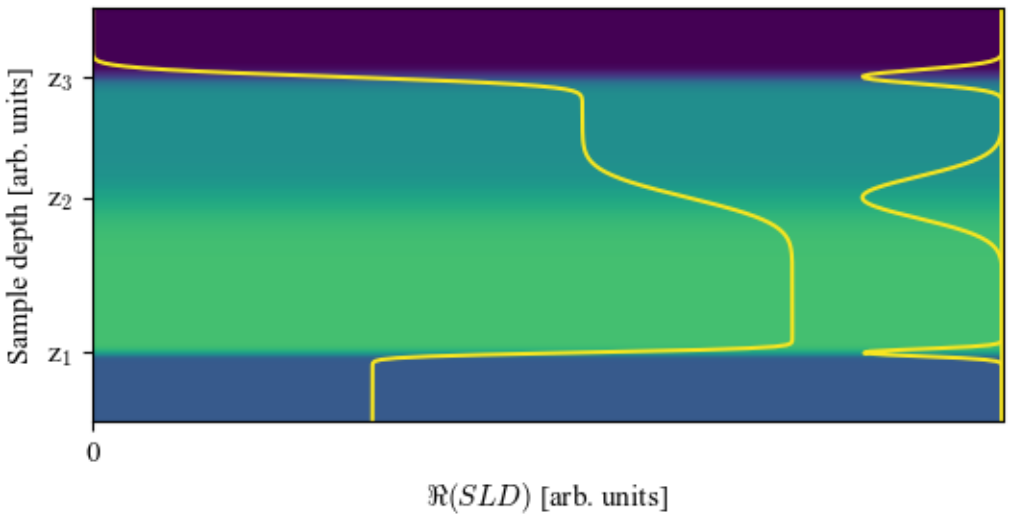

Figure 2.10: Rough interfaces in a layered system. The left line represents the SLD profile of the sample, while the Gaussians on the right hand side of the figure describe the gradient of each interface. According to eq. 2.71 wider interfaces imply lower reflected intensity at the interface.

described by an error function is given by the particularly simple expression

$$r(\mathbf{Q}) = r_{\mathrm{F}}(\mathbf{Q})\,\mathrm{e}^{-\frac{Q_z^2\sigma^2}{2}}, \tag{2.70}$$

so that the *intensity reflectivity* $R(\mathbf{Q})$ follows

$$R(\mathbf{Q}) = R_{\mathrm{F}}(\mathbf{Q})\,\mathrm{e}^{-Q_z^2\sigma^2}. \tag{2.71}$$

This result immensely simplifies calculation of x-ray reflectivity, since it provides an analytical solution to an important and common case of rough interfaces, simply stating that the reflectivity of rough interface is the Fresnel reflectivity of an perfectly flat interface, modulated by an Debye-Waller-like factor $\mathrm{e}^{-Q_z^2\sigma^2}$, which reduces reflectivity by an amount proportional to the interface width σ. meaning that the reflectivity is lower, the larger the total width of the interface is.

However, if the interface under consideration can not be reasonably described by an error function, for instance because the respective roughness of neighbouring interfaces is high enough for their profile functions to overlap, it might not be possible to find an analytical solution to the problem and the interface profile has to be solved numerically, by slicing the depth profile into slabs of finite size. Each slice is then attributed with an SLD corresponding to the desired (arbitrary) depth profile and solved by, for instance, by either of the methods discussed in sections 2.2.4 and 2.2.5.

2.3 Examples of X-ray Reflectivity

This section presents examples of x-ray reflectivity of some common sample structures and their corresponding reciprocal space characteristics. The examples are chosen to be of increasing complexity, either structurally or in the required experimental effort in determining sample properties of interest.

2.3.1 Reflectivity of a Single Slab

Even simple systems may deviate from a desired nominal structure and x-ray reflectivity often provides sufficient sensitivity to characterise a sample and validate a certain sample model. A simple example is thin film deposition onto a substrate of known material. Potentially unknown factors include the roughness on top of both the substrate and the deposited layer, as well as the question if any of the involved materials have oxidised and how thick the corresponding oxide layers are.

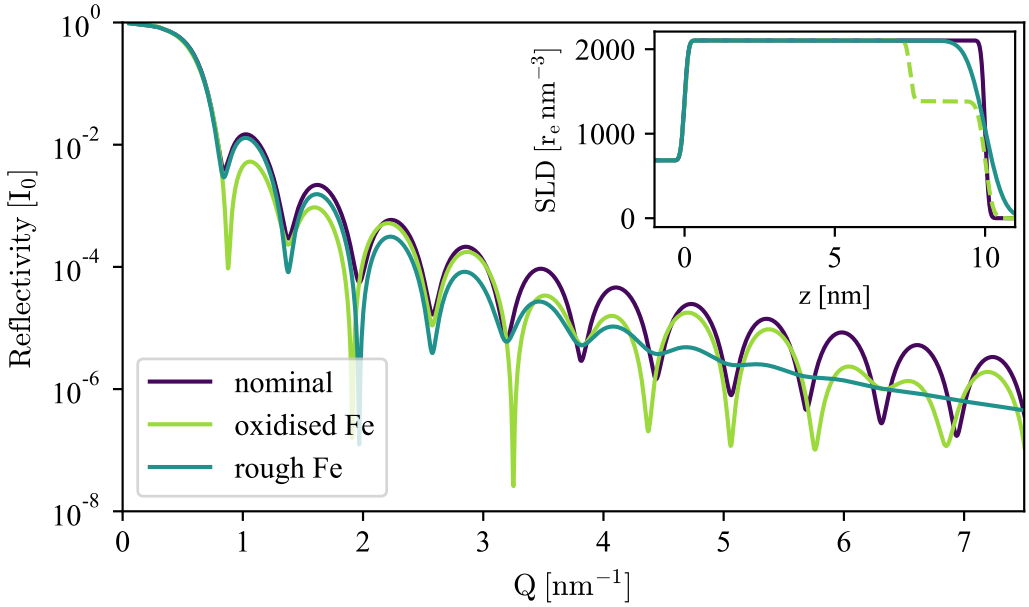

Figure 2.11: Reflectivity of a thin Fe film on a Si substrate at $E = 8.04\,\mathrm{keV}$. The nominal film thickness was 10 nm. In case of the oxidised sample the top part of the Fe layer was replaced with a 2.5 nm thick layer of Fe_3O_4. The third simulation assumed an increased surface roughness of $\sigma_{Fe} = 0.5\,\mathrm{nm}$ of the Fe layer compared to 0.1 nm in the nominal case. The inset shows the corresponding SLD profiles of all three systems.

Fortunately, all these factors affect the SLD profile and will therefore manifest in the x-ray reflectivity of the sample, which can therefore be conveniently used for structural characterisation.

Fig. 2.11 exemplifies how real space deviations affect the reciprocal space representation of the sample presenting the reflectivity and SLD profile of three similar but distinct systems. The nominal sample structure serves as a guide, and is in this case given by the simplest of the three systems, characterised by sharp interfaces and no oxidation. The calculated reflectivity of the nominal sample shows well defined oscillations over the whole angular range up to 7° or roughly $7.5\,\mathrm{nm}^{-1}$.

If the Fe layer oxidises, the top part of the scattering length density profile changes due to the altered chemical profile as can be seen in the inset of Fig. 2.11. Oxidation manifests in reciprocal space mainly by a periodical modulation of the nominal samples reflectivity. Increasing the roughness of the Fe layer on the other hand leads to a continuous dampening of the oscillation amplitude with increasing Q-values. Obviously, oxidation and increasing roughness as well as all combinations thereof, distinctly affect the samples reflectivity, and can therefore generally be

determined from an adequate model of the SLD-profile.

2.3.2 Reflectivity of a Multilayer

If the sample is organised into a superlattice, Bragg satellites corresponding to the combined thickness of the repeating component emerge in the reflectivity. Fig. 2.12 presents the simulated reflectivity of a stack of 10 repetitions of an CoFe-Al_2O_3 bilayer, each component 3 nm thick, on a Si substrate. The emerging Bragg peaks are separated by $\Delta Q = 2\pi/6\,\mathrm{nm} \approx 1.04\,\mathrm{nm}^{-1}$ corresponding to the total thickness of the bilayer. Note the intensity modulation given by the form factor of the bilayer, which significantly reduces the intensity of every second Bragg peak, because of the equal thickness of the two bilayer components. This system was also benchmarked against the known reflectivity tool *GenX* to empirically check for the validity of the slicing approach used in this work as described in section 2.2.5.

The required z-resolution of the slicing technique strongly depends on the experimental resolution and the acceptable tolerance in spatial sampling the actual SLD profile. That means that a slicing approach is only able to determine any

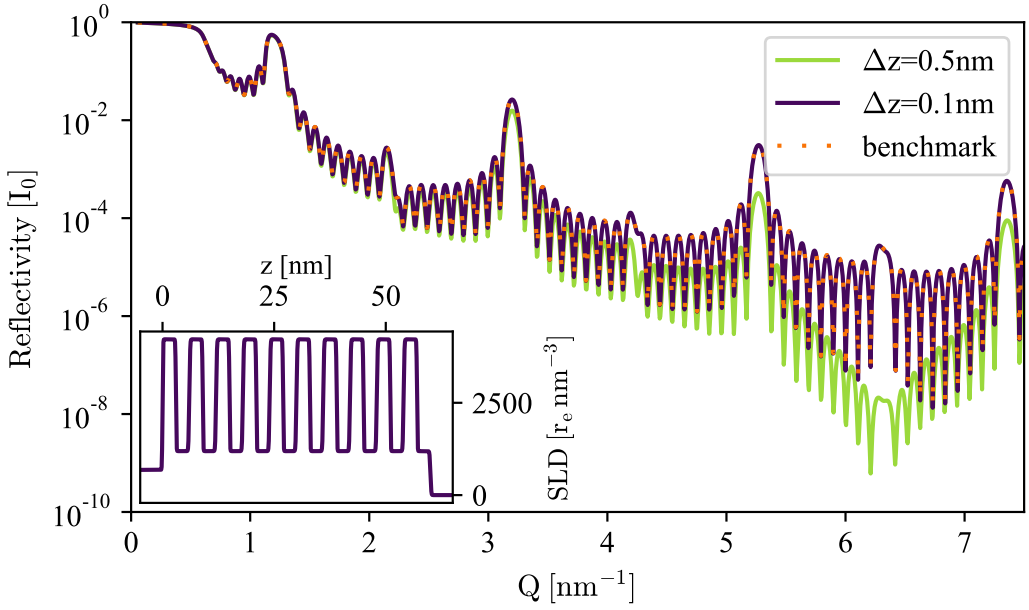

Figure 2.12: Reflectivity of 10 repetitions of a CoFe-Al_2O_3 bilayer. The main peaks correspond to the thickness of the bilayer, while in between Kiessig fringes corresponding to the total thickness of the stack are observed. The strong deviations at $\Delta z = 0.5\,\mathrm{nm}$ are due to miss sampling of the true interface structure. The inset shows the SLD profile of the sample.

interface within its z-resolution, which therefore has to be chosen appropriately. Potentially even more important is being able to determine a rough interface between two layers, since the exact transition will often strongly impact the actual experimental reflectivity.

From Fig. 2.12 it is evident that a slicing resolution of $\Delta z = 0.1\,\mathrm{nm}$ is sufficient to produce virtually perfect agreement between the exact analytical model and the slicing model. On the other hand, another simulation using a coarser resolution of $\Delta z = 0.5\,\mathrm{nm}$ is not able to produce satisfactory agreement with the analytical model, with strong deviations, particularly at high Q values. If the interface is considered to be of width 6σ, i.e. transitioning from 99% material A and 1% material B to 1% material A and 99% material B, a z-resolution of $\Delta z = 0.1\,\mathrm{nm}$ digitises the interface six times on average, which is sufficient to compete with the analytical model. The rough sampling at $\Delta z = 0.5\,\mathrm{nm}$, however, only digitises the interface once, which is the reason for the observed deviation.

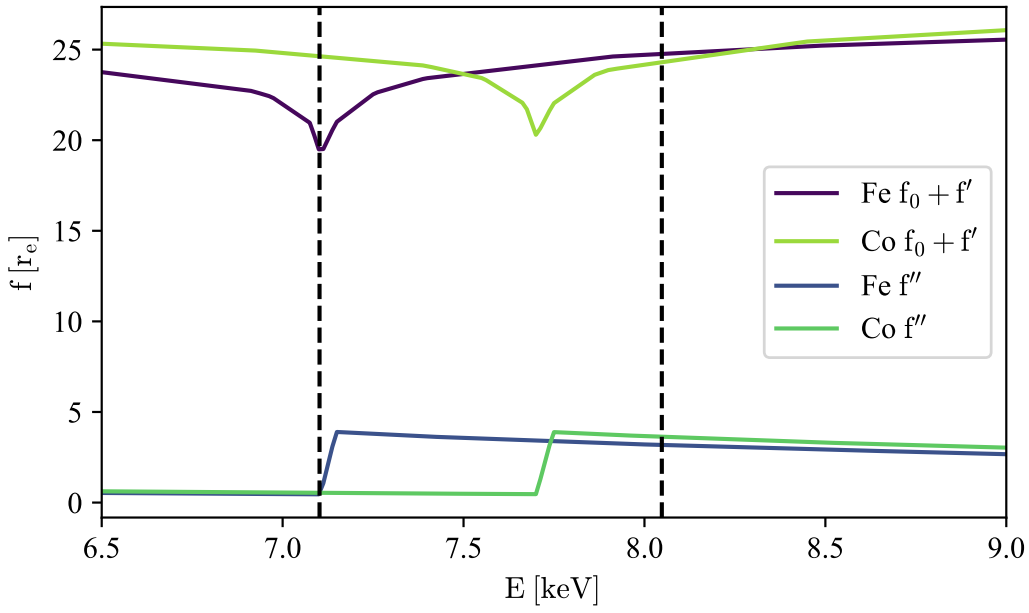

Figure 2.13: Energy dependence of the Fe and Co scattering factors. Just below the Fe K absorption edge at 7.1 keV the real part of the scattering factors show a large difference. At the Co K-α edge at 8.048 keV the difference is almost zero. Data taken from [72].

2.3.3 Resonant Multilayer

In case a sample consists of materials which only show very little contrast in their respective SLD (which is often the case for elements neighbouring each other in the periodic table), resonant scattering can be a useful tool in resolving the samples chemical structure. The latter is accomplished by tuning the x-ray energy close to a particular resonance edge of one of the materials, affecting the energy dependent dispersion correction terms f' and f'' in the expression for the scattering factor, therefore manifesting in a change of the materials SLD and hence the recovery of chemical contrast.

As an example, consider the reflectivity of a multilayer stack of 10 repetitions of an Co-Fe bilayer of thicknesses 2 nm and 4.5 nm, respectively. The atomic numbers of the two materials are 27 and 26, and hence their uncorrected scattering factors in reflectivity differ by only about 3.7 %, often too little to be resolved in the chemical structure during a non-resonant experiment.

By tuning the x-ray energy to just below the Fe K-edge, a strong negative correction term

$$f'_{\mathrm{Fe}}(E_{\mathrm{Fe-K}} - \Delta E) < 0$$

is affecting the real part of the scattering factor and and hence the SLD. Since absorption is only significantly increased *above* the absorption edge it holds that

$$f''_{\mathrm{Fe}}(E_{\mathrm{Fe-K}} - \Delta E) \ll f'_{\mathrm{Fe}}(E_{\mathrm{Fe-K}} - \Delta E)$$

and fluorescence is avoided. The latter would reduce the background intensity and therefore simplify an experimental measurement, if desired.

Fig. 2.13 shows the real- and imaginary parts of the scattering factors of Fe and Co for a range of energies covering the Fe K-edge as well as the Co K-α edge, the latter being the most commonly used x-ray energy in standard laboratory equipment and providing almost no chemical contrast between Fe and Co.

The effect of resonant scattering on the Co-Fe multilayer is presented in Fig. 2.14. The simulation taken off-resonance at $E_{\mathrm{CoK}-\alpha} = 8.048\,\mathrm{keV}$ is showing very little structure in both real- and reciprocal space. By tuning the x-ray energy to the Fe resonance, the SLD of the Fe is significantly decreased, leading to the emergence of well resolved Bragg peaks.

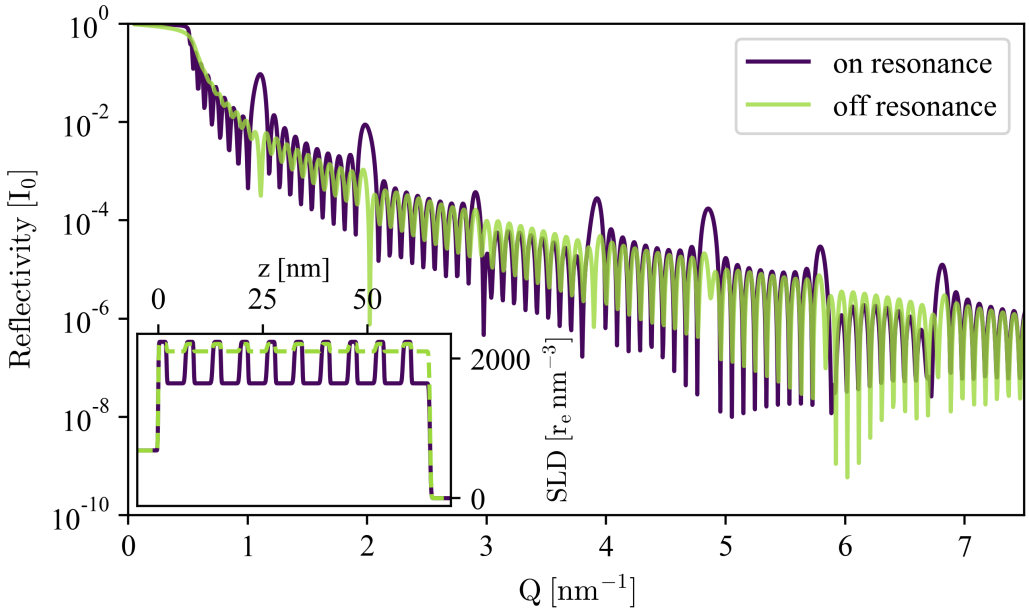

Figure 2.14: Reflectivity of 10 repetitions of an Co-Fe bilayer simulated on and off the Fe K-absorption edge. The inset shows the energy dependence of the SLD profile.

2.3.4 X-Ray Magnetic Scattering

A special case of resonant scattering occurs if the energy of polarised x-rays is tuned to magnetically sensitive absorption edges, like the L_{III} edge. At these energies, the refractive index of a magnetic material is not only affected by a large dispersion correction, but develops a coupling between the x-ray polarisation and orientation of the local magnetic moment of magnetic atoms as has been discussed in section 2.1.4.

Fig. 2.15 a) and b) show the sum signal and asymmetry ratio, calculated according to eq. 2.33, corresponding to a stratified magnetic system, consisting of a 5 nm slab of Fe, located between an semi-infinite Si substrate and a 5 nm slab of Fe_3O_4. The Fe was assumed to be fully magnetised along the direction of the incident x-ray beam and the real- and imaginary parts of the magnetic component of the scattering factor of the pure Fe were, for simplicity, defined to be 5 % and 1 %, respectively, of the corresponding non-magnetic components, i.e.

$$f'_{\mathrm{mag}} = 0.05\,(f_0(Q) + f'(E)) \tag{2.72a}$$

$$f''_{\mathrm{mag}} = 0.01\,f''(E). \tag{2.72b}$$

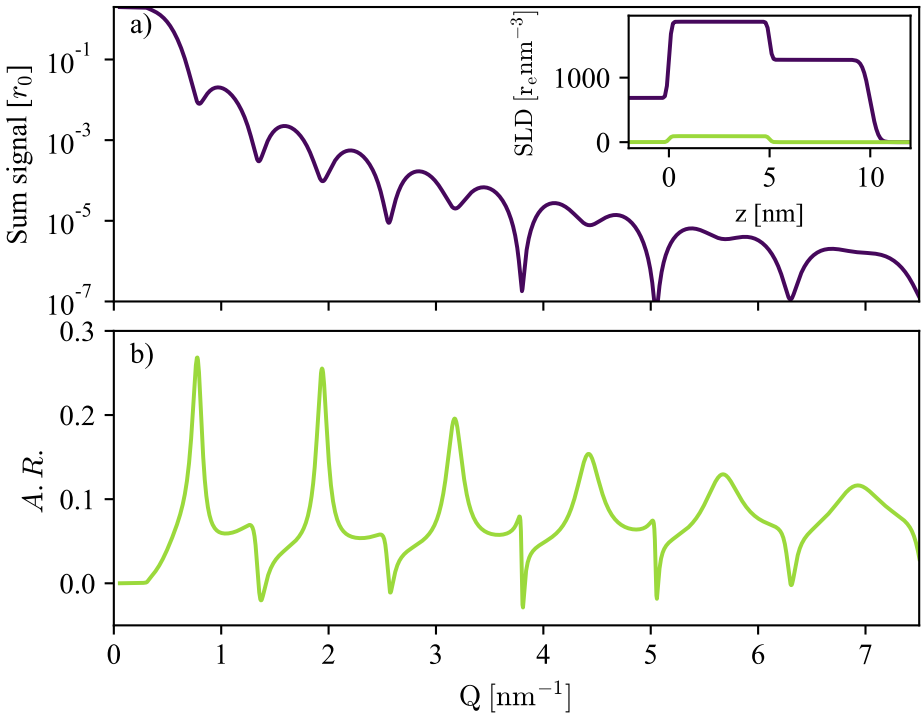

Figure 2.15: Example of the magnetically sensitive XRMS signal of an Fe-Fe_3O_4 bilayer. Panel a) and b) present the simulated sum signal and asymmetry ratio, respectively, as it would be obtained from measuring I^+ and I^-, the reflected intensities under flipping of the helicity of the circularly polarised x-rays. The inset of panel a) shows the real parts of the charge- (purple line) and magnetic (green line) SLD profiles of the underlying system.

The scattering factors of the Si and Fe_3O_4 were modelled to not obtain any magnetic components. Simultaneous fitting of both the sum signal and the asymmetry ratio then allows resolving the charge- and magnetic profile of the sample as depicted in the inset of Fig. 2.15 a).

2.4 X-Ray Diffraction of Patterned Arrays

This section will briefly summarize the fundamental aspects of diffraction of patterned arrays, i.e. of two-dimensional mesoscopic lattices. Generally, a broad body of diffraction theory exists, which can generally be quite involved both to calculate and relate to experiments[84, 90]. Applications of diffraction of patterned arrays span a wide range of topics, including Lattice imperfections and long range sample correlation [54, 91–93], short range structural characterisation [91, 92, 94, 95], coher-

ence effects [55, 95, 96], magnetic order [28, 38, 50, 75, 97, 98] and more. However, approximations such as *kinematical scattering*[62, 79] and the *two-beam approximation*[84, 90] can simplify the mathematics drastically with often still satisfactory results.

2.4.1 Motivation

In a general way, the intensity of an elastically scattered monochromatic electromagnetic wave, is given by[90]

$$I(\mathbf{Q}) = \frac{k^2 I_0}{16\pi^2 A}\left|\langle \mathbf{k}_f|\hat{\mathbf{T}}|\mathbf{k}_i\rangle\right|^2 = \frac{k^2 I_0}{16\pi^2 A}\left|\int \hat{\mathbf{T}}(r)\mathrm{e}^{-i(\mathbf{k}_f-\mathbf{k}_i)\mathbf{r}}\,\mathrm{d}^3 r\right|^2 \tag{2.73}$$

where I_0 is the intensity of the incident radiation, A is the (coherently) illuminated sample area and $\mathbf{k}_i$ and $\mathbf{k}_f$ are the incident and scattered wave vectors, respectively, both of length $|\mathbf{k}_i| = |\mathbf{k}_f| = k$. The scattering operator $\hat{\mathbf{T}}$ is given by the infinite series

$$\hat{\mathbf{T}} = \hat{\mathbf{V}} + \hat{\mathbf{V}}\hat{\mathbf{G}}_0\hat{\mathbf{V}} + \hat{\mathbf{V}}\hat{\mathbf{G}}_0\hat{\mathbf{V}}\hat{\mathbf{G}}_0\hat{\mathbf{V}} + ..., \tag{2.74}$$

where terms of order higher than zero (one) are neglected in case of kinematic approximation (Distorted Wave Born approximation). G_0 is the Green function, i.e. the free particle solution of the wave equation, which can be expressed as the superposition of plane waves to read[90]

$$G_0(\mathbf{r}-\mathbf{r}') = -\frac{i}{8\pi^2}\int \frac{\mathrm{e}^{i\mathbf{k}(\mathbf{r}-\mathbf{r}')}}{k_z}\,\mathrm{d}^2\mathbf{k}_\parallel, \tag{2.75}$$

where the in-plane wavevector component $k_\parallel \leq k$ and $k_\parallel^2 + k_z^2 = k^2$. Hence, in order to evaluate eq. 2.73 one has to find an expression for the scattering potential $\hat{\mathbf{V}}$ of the sample as will be done below.

2.4.2 Real and Reciprocal Lattice

A convenient way of describing the scattering potential $\hat{\mathbf{V}}(\mathbf{r})$ of the sample requires the decomposition of the periodic structure of a patterned array into three distinct parts. The first is the (infinite) lattice

$$\text{Ш} = \sum_{n=-\infty}^{\infty} \delta(x - n d_{\mathrm{latt}}) \tag{2.76}$$

with $n \in \mathbb{Z}$ characterising the periodicity of the array. The second is the scattering potential of the unit cell, e.g. in terms of the scattering length density

$$\hat{\mathbf{V}}_{\mathrm{uc}}(\mathbf{r}) = f(\mathbf{r})\rho^{\mathrm{num}}(\mathbf{r}),$$

which defines the repeating element. Lastly, the third component is some kind of truncation function

$$\Gamma(\mathbf{r}),$$

that takes care of the spatial finiteness of any real sample. The latter might be given either by the limited sample dimensions itself, or by the coherence of the radiation interacting with the sample as is discussed in more detail in chapter 4.

Mathematically, taking into account all three of the above components, the scattering potential of the whole "active" sample can be modelled by

$$\hat{\mathbf{V}} = \hat{\mathbf{V}}_{\mathrm{uc}} \otimes \text{Ш} \cdot \Gamma, \tag{2.77}$$

where $\otimes$ and $\cdot$ denote the convolution and multiplication operations, respectively.

A particular example is given by Fig. 2.16 a), where for simplicity a one-dimensional array was chosen. The scattering potential of the unit cell is given by

$$\hat{\mathbf{V}}_{\mathrm{uc}}(x) = \begin{cases} (a-x)/a & \text{for } 0 < x < a \\ (a+x)/a & \text{for } -a < x < 0 \\ 0 & \text{for } |x| > a, \end{cases} \tag{2.78}$$

where $a = 1/3$ has been used in the figure, while the infinite array is truncated by a box function

$$\Gamma(x) = \begin{cases} 1 & \text{if } |x| < B \\ 0 & \text{else ,} \end{cases} \tag{2.79}$$

and $B = 4.5$ has been used in Fig. 2.16.

From eq. 2.73 it is clear that the scattered intensity is given by the Fourier transformation of the scattering potential $\hat{\mathbf{V}}$. The latter can be easily performed by repeated application of the convolution theorem

$$(f \cdot g)^{\mathrm{FT}} = f^{\mathrm{FT}} \otimes g^{\mathrm{FT}} \tag{2.80a}$$

$$(f \otimes g)^{\mathrm{FT}} = f^{\mathrm{FT}} \cdot g^{\mathrm{FT}} \tag{2.80b}$$

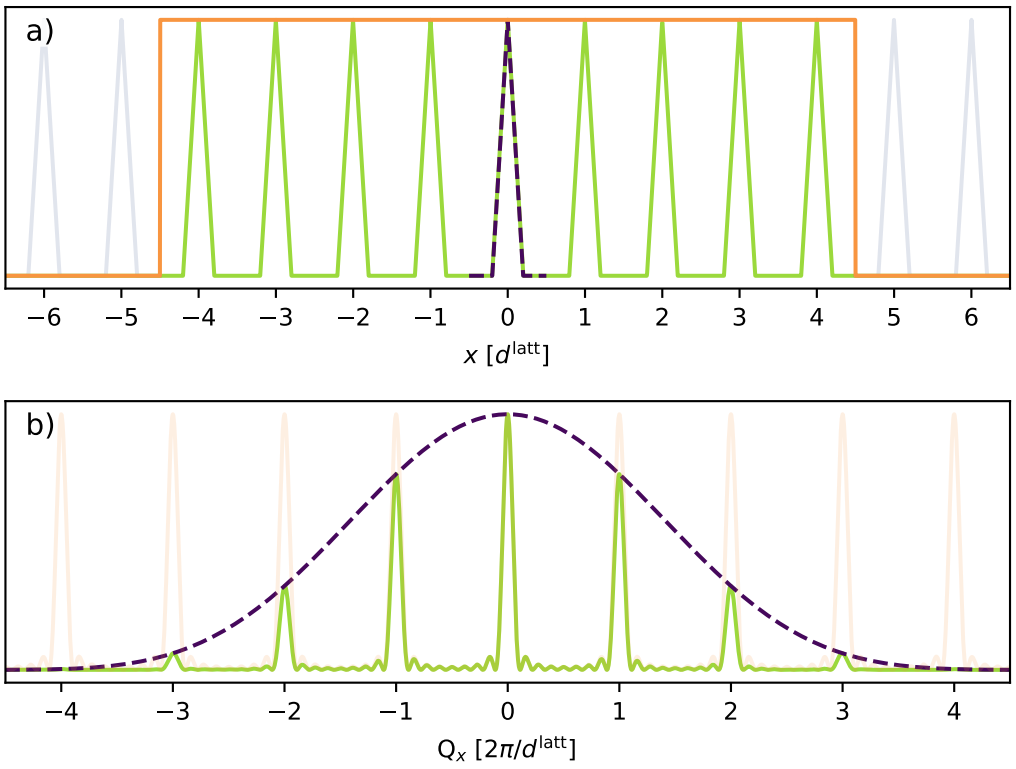

Figure 2.16: Real, panel a), and reciprocal, panel b), space of a one-dimensional array. Both lattices are finite, however the modulation of the real space lattice is given by a box-truncation of the infinite lattice, whereas the modulation of the reciprocal lattice is given by the Fourier transform $\hat{\mathbf{V}}_{\mathrm{uc}}^{\mathrm{FT}}$ of the unit cell scattering potential $\hat{\mathbf{V}}_{\mathrm{uc}}$, both depicted in dark purple. The Fourier transform of the truncation function $\Gamma(x) = \mathrm{rect}(4.5d_{\mathrm{latt}})^{\mathrm{FT}}$ is a sinc function $\Gamma^{\mathrm{FT}}(Q_x) = 9\,\mathrm{sinc}(Q_x)$, which is convolved with the reciprocal lattice, both being depicted in orange. Combined, the truncated array in panel a) turns into the modulated array in panel b) both depicted in green.

to read

$$\hat{\mathbf{V}}^{\mathrm{FT}} = \{(\hat{\mathbf{V}}_{\mathrm{uc}} \otimes \text{Ш}) \cdot \Gamma\}^{\mathrm{FT}} = (\hat{\mathbf{V}}_{\mathrm{uc}} \otimes \text{Ш})^{\mathrm{FT}} \otimes \Gamma^{\mathrm{FT}} = \hat{\mathbf{V}}_{\mathrm{uc}}^{\mathrm{FT}} \cdot \text{Ш}^{\mathrm{FT}} \otimes \Gamma^{\mathrm{FT}}. \quad (2.81)$$

With the Fourier transformation of the real space lattice being the reciprocal lattice

$$\text{Ш}(x)^{\mathrm{FT}} = \sum_{n=-\infty}^{\infty} \delta(Q_x - n\frac{2\pi}{d_{\mathrm{latt}}}) = \text{Ш}(Q_x), \quad (2.82)$$

it is apparent that eq. 2.81 represents the convolution of the reciprocal lattice with

the Fourier transform of the truncation function Γ^{FT}, *modulated* by the Fourier transform of the scattering potential of the unit cell $\hat{\mathbf{V}}^{\mathrm{FT}}$, as depicted in Fig. 2.16.

This is the basic premise to understand the scattering from a patterned array.

2.4.3 Kinematical Scattering

With respect to eq. 2.73 and for the moment restricting to kinematical scattering in the definition of $\hat{\mathbf{V}}$ in eq. 2.74, this means that the diffracted intensity of a patterned array consists of a fan of Bragg peaks distributed around diffracted wavevectors $\mathbf{k}_n$ whose component within the sample plane satisfies the Bragg condition

$$\mathbf{k}_{n,\parallel} = n\,\frac{2\pi}{d_{\mathrm{latt}}} + \mathbf{k}_{i,\parallel}, \tag{2.83}$$

and, since only elastic scattering is considered, the out-of-plane component is given by $k_{n,\perp} = \sqrt{k^2 - k_{n,\parallel}^2}$. The larger the sample area, the smaller the spread of intensity around each Bragg peak, and the scattering potential of the unit cell $\hat{\mathbf{V}}_{\mathrm{uc}}$ is encoded within the intensity modulation of the Bragg peaks, generally allowing detailed analysis of the unit cell from diffraction.

The nature of the sample and the experimental set-up determines the level of scattering processes that have to be taken into account in order to reproduce experimental data. Within the kinematical approximation only a single scattering process is considered, and hence eq. 2.74 is truncated after its first term. Limiting to a single Bragg peak, the scattered intensity is then given simply by connecting $\mathbf{k}_f$ and $\mathbf{k}_i$ by a single scattering process, obtaining the lateral wavevector transfer $Q_{\parallel} = n\,2\pi/d_{\mathrm{latt}}$ as seen by wavevector transfer Q_{tt} in Fig. 2.17 b).

Further, since the scattered wavefield consists of a fan of diffracted waves each satisfying the lateral diffraction condition, theories involving multiple scattering effects generally have to consider excitations from neighbouring Bragg peaks. However, the latter can mostly be ignored for diffraction of patterned arrays, since the coherent parts of the diffracted waves propagate mostly above the generally very thin sample structures. The latter justifies the use of the two-beam approximation, named so because only the incident and one diffracted wave are considered at any given time. One example where multiple scattering *may* play a role in diffraction of patterned arrays is *Umweganregung*, where Bragg diffraction within the underlying substrate may create significant wave fields diffracting with the array structure above[90, 99, 100].

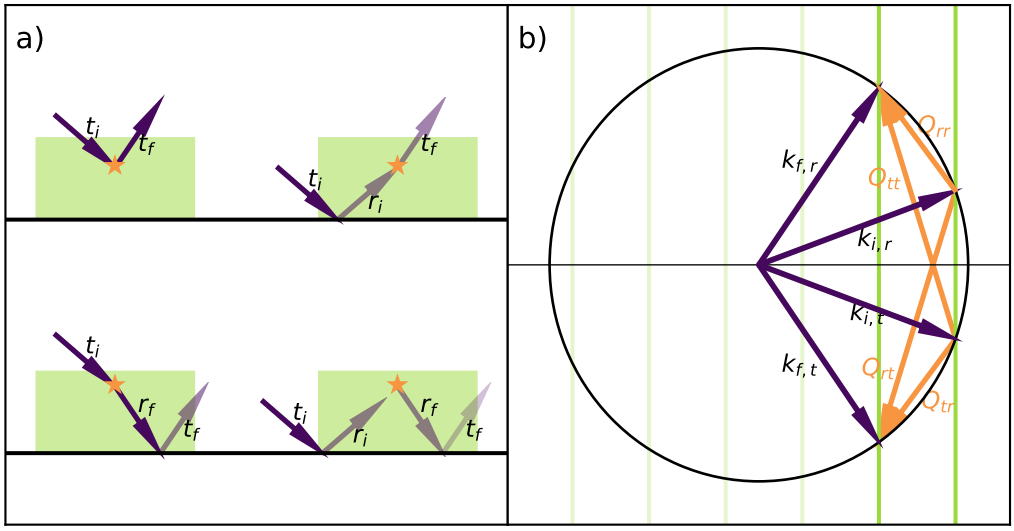

Figure 2.17: Real- and reciprocal space diffraction. Panel a) depicts four scattering processes involving intermediate states of specularly reflected waves. Within the kinematical approximation only the top left process is considered, whereas the DWBA takes all four into account. Shading of the arrows is representative of diminishing modulus of the wave field amplitudes. Panel b) shows the corresponding diffraction wavevector transfers in reciprocal space. Whenever both $\mathbf{k}_i$ and $\mathbf{k}_f$ terminate on GTRs the lateral diffraction condition is fulfilled. The orange arrows correspond to the four scattering processes considered in the DWBA on excitation of a single GTR.

2.4.4 Distorted Wave Born Approximation

Another example of multiple scattering effects concerning patterned arrays is given by the Distorted Wave Born Approximation (DWBA)[68, 90, 92]. Generally, in DWBA implementations, the scattered wavefield defined by $|\mathbf{k}_f\rangle$ is divided into an undisturbed and disturbed contribution obtained from the undisturbed and disturbed scattering potentials, $\hat{\mathbf{V}}_0$ and $\hat{\mathbf{V}}_1$, respectively. $\hat{\mathbf{V}}_0$ is chosen simple enough so that an exact analytical solution $\langle k_1|$ exists, which interacts with $\hat{\mathbf{V}}_1$, leading to

$$I(\mathbf{Q}) = \frac{k^2 I_0}{16\pi^2 A}\left|\langle \mathbf{k}_f|\hat{\mathbf{V}}|\mathbf{k_i}\rangle\right|^2 \approx \frac{k^2 I_0}{16\pi^2 A}\left|\langle \mathbf{k}_1|\hat{\mathbf{V}}_0|\mathbf{k}\rangle + \langle \mathbf{k}_f|\hat{\mathbf{V}}_1|\mathbf{k}_1\rangle\right|^2. \tag{2.84}$$

In the specific case of patterned arrays one implementation may consider replacing the periodic scattering potential $\hat{\mathbf{V}}(x, y, z)$ at height z with an average scattering potential $\bar{V}(z)$. Following section 2.2.4 this allows one to calculate the reflected and transmitted amplitudes in an imaginary stratified medium of identical average scattering length density as the real sample. Hence, additional to the direct excitation

of the Bragg peak, single reflections of either incident, $\mathbf{k}_i$, or detector beam, $\mathbf{k}_f$ or a double reflection of $\mathbf{k}_i$ and $\mathbf{k}_f$ are taken into account, as illustrated in Fig. 2.17 a). Note that in order to calculate the E-field amplitudes of transmitted and reflected field, $t_f(z)$ and $r_f(z)$, of the detector side, $\mathbf{k}_f$ has been time-inverted, i.e.

$$|\mathbf{k}_f\rangle = t_f^* \exp\{-i\mathbf{k}_f^*\mathbf{r}\} + r_f^* \exp\{i\mathbf{k}_f^*\mathbf{r}\}. \tag{2.85}$$

From the known (flat wave) solution of

$$\langle \mathbf{k}_1 | \hat{\mathbf{V}}_0 | \mathbf{k_i} \rangle$$

the matrix element of eq. 2.84 can then be expanded to read

$$\langle \mathbf{k}_f | \hat{\mathbf{V}} | \mathbf{k_i} \rangle = t_i t_f \hat{\mathbf{V}}^{\mathrm{FT}}(Q_{\mathrm{tt}}) + r_i t_f \hat{\mathbf{V}}^{\mathrm{FT}}(Q_{\mathrm{rt}}) + t_i r_f \hat{\mathbf{V}}^{\mathrm{FT}}(Q_{\mathrm{tr}}) + r_i r_f \hat{\mathbf{V}}^{\mathrm{FT}}(Q_{\mathrm{rr}}), \tag{2.86}$$

where the definition of the wavevectors as seen in Fig. 2.17 b) has been used. In other words, each term corresponds to a particular kinematical scattering event, e.g. the second term describes the kinematical scattering of an incoming wave, which has previously been specularly reflected by the sample into an outgoing wave, which is directly accepted by the detector.

However, since at angles higher than the critical angle α_c the modulus of the scattered amplitudes $r \ll 1$ drops rapidly (while $t \approx 1$), multiple scattering processes generally contribute very little intensity unless either the source or detector angle, α_i and α_i, is very small. The fourth term involves reflection of both the incident and the exiting wave, so that it usually never provides any significant contribution to the scattered intensity under experimental rocking conditions where 2θ is in the order of multiple degrees, since either r_i or r_f becomes vanishingly small.

2.4.5 Grating Truncation Rods

Finally, the fact that patterned arrays only possess lateral translational symmetry, i.e. within the sample plane, also means that only a lateral diffraction condition has to be fulfilled for $\mathbf{Q}_{\parallel}$ in order for diffraction to occur. This means that diffraction of a two-dimensional patterned array is observed along rods parallel to $\hat{Q}_z$, located at positions Q_x and Q_y according to the lateral reciprocal lattice $\text{Ш}(Q_x, Q_y)$ as seen in eq. 2.82. These rods are a direct consequence of the finiteness of the sample in $\hat{z}$ direction and can alternatively be interpreted as a result of a truncation of a three-dimensional array. Because of the latter and of the apparent similarity to crystal truncation rods[62, 68, 73, 81], diffraction rods of patterned arrays are also called

Grating Truncation Rods (GTRs)[54, 87, 101].

Since the scattering considered here is elastic, both $\mathbf{k}_i$ and $\mathbf{k}_f$ lie on the Ewald sphere, and hence intercept each GTR at a particular value of Q_z, according to the dispersion relation

$$Q^2 = Q_{\parallel}^2 + Q_z^2 = G_{\mathrm{m,n}}^2 + Q_z^2, \tag{2.87}$$

with $G_{\mathrm{m,n}}$ being a reciprocal lattice vector defined for a general real space lattice of varying pitch d_x and d_y by

$$\mathbf{G}_{\mathrm{m,n}} = m\,\frac{2\pi}{d_x}\hat{Q}_x + n\,\frac{2\pi}{d_y}\hat{Q}_y, \tag{2.88}$$

with $m, n \in \mathbb{Z}$. Separating lattice and unit cell, the structure factor $F(\mathbf{Q})$ along a given GTR obviously depends on the three-dimensional structure of the unit cell and is given by

$$F(\mathbf{G}_{m,n}, Q_z) \propto \langle k_{\mathrm{f,z}}|\hat{\mathbf{V}}_{\mathrm{uc}}|k_{\mathrm{i,z}}\rangle\,. \tag{2.89}$$

Within the kinematical approximation eq. 2.89 takes on the simple form

$$F_{\mathrm{kin}}(\mathbf{G}_{m,n}, Q_z) = \int f(\mathbf{r}_{\parallel}, z)\rho^{\mathrm{num}}(\mathbf{r}_{\parallel}, z)\exp\{-i(\mathbf{G}_{\parallel}\mathbf{r}_{\parallel} + Q_z z)\}\,\mathrm{d}^3r, \tag{2.90}$$

which is often found to be adequate in describing diffraction of patterned arrays.

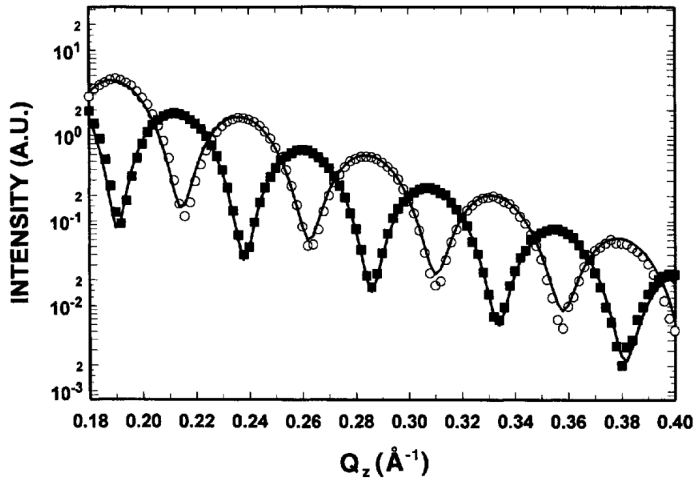

Figure 2.18: Intensity reflectivity R of the specularly reflected beam (open circles) and 1$^{\mathrm{st}}$ Q_x diffraction order peak of an one-dimensional surface grating. The asymmetric trapezoidal cross section of the grating leads to a phase shift of the periodic intensity modulations. Adapted from [55].

Within the DWBA, $F(\mathbf{Q})$ is calculated according to eq. 2.86, where the periodic scattering potential of the sample $\hat{\mathbf{V}}$ has to be replaced by the scattering potential of the unit cell $\hat{\mathbf{V}}_{\mathrm{uc}}$.

For simple (which in this case means: flat) structures, the intensity modulation along a particular GTR resembles the specular reflectivity, although generally including a phase shift of the modulation function[54, 55], an example of which can also be seen in Figs. 2.18 and 5.12, where the GTRs of each diffraction order are clearly offset from each other.

2.4.6 Diffuse Scattering

Similar to patterned arrays, correlated surface- and interface roughness gives rise to *diffuse scattering* away from the specularly reflected beam[54, 102–106]. While the highly correlated islands of a patterned array produce discrete diffraction satellites at well defined positions in reciprocal space, the (imperfectly) correlated surface- and interface roughness produces a much more continuous distribution in intensity. It can principally be found by replacing the interface height z by the height-height correlation function

$$C(x, y) = \langle h(0, 0)h(x, y)\rangle, \tag{2.91}$$

averaged over the incoherently illuminated sample, when calculating the scattered intensity. The angular brackets in eq. 2.91 represent a sample average, over all height differences separating any two points of the sample surface by the distance vector (x, y).

Correspondingly, additional to the diminishing specular reflectivity given by eq. 2.71, the emerging diffusely scattered intensity can be expressed by[62]

$$I_{\mathrm{diffuse}} \propto \frac{\mathrm{e}^{-Q_z^2\sigma^2}}{Q_z} \int \left(\mathrm{e}^{Q_z^2 C(x,y)} - 1\right) \mathrm{e}^{-i(Q_x x + Q_y y)}\, \mathrm{d}x\, \mathrm{d}y. \tag{2.92}$$

Fig. 2.19 shows the effect of structural surface roughness within the vicinity of the first Bragg peak of a 25-repetition Co-Cu multilayer, grown on silicon-nitride, resulting in the distinct separation of a very narrow Bragg peak sitting on a broad distribution of diffuse scatter.

Another example of diffuse scatter is found in the rocking curves of this work, as seen, for instance, in Fig. 5.4 a). Correlated roughness on the islands occurring on small length scales, lead to a broad distribution of diffuse intensity within reciprocal space. Particularly at the high detector angles corresponding to negative Q_x values, the wide detector acceptance integrated up a lot of diffusely scattered intensity,

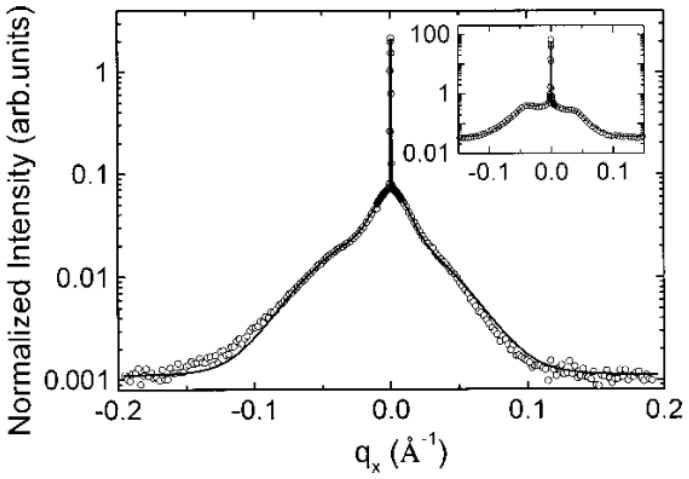

Figure 2.19: Diffuse scatter of a 25-period Co-Cu multilayer deposited on silicon nitride. The inset shows a 50-fold repetition of the same bilayer, grown on pure silicon. The solid line corresponds to a fit of the data, obtained from a superposition of two Voigt functions[107] representing sample correlation lengths. Adapted from [103].

manifesting in a wide background signal, being more distinct towards lower Q_x, which the diffraction satellites are sitting on. Since diffraction peaks and diffuse scatter are separate and distinct from each other, it has been possible to subtract the background, where the intensity distribution allowed interpolating the intensity between neighbouring diffraction peaks.

2.5 Summary

This chapter covered the theoretical foundations of x-ray scattering in general and x-ray diffraction of patterned arrays in particular. The discussion covered the relationship of the atomic scattering factors f, scattering length density SLD, and the refractive index n. Further a framework for the allowance of arbitrary polarisation of the electric field $\mathbf{E}$ of x-rays was discussed. In particular, it was shown how circular polarisation is treated within the scattering framework. The latter is one of the prerequisites of x-ray resonant magnetic scattering (XRMS), utilising the circularly polarised light of tunable energy E obtainable from modern synchrotron sources as discussed in chapter 3, therefore enabling the consideration of the distribution of local magnetic moments by simulation.

The respective scattering geometry of measurement techniques like x-ray reflectivity, rocking curves and GISAXS all possess differing requirements on the form

of the wavevector transfer $\mathbf{Q}$ in calculating the structure factor $F(\mathbf{Q})$ even when using the same underlying sample model. However, as will be seen over the course of the thesis, different scattering problems also have been found to require fundamentally different models of the sample, ranging from purely numerical summation of simple two-dimensional grids to sophisticated (semi-)analytical three-dimensional models of Å-level resolution. Furthermore, depending on the scattering geometry employing the DWBA might become necessary, significantly slowing down the simulation process.

The requirements regarding the calculation of scattering intensities are therefore found to strongly vary depending on the problem, while most of the remaining analysis, i.e. parametrisation framework and data fitting, is found to essentially be problem independent. Hence, maximising code re-usability motivated the encapsulation of the respective components seen in the leftmost column of Fig. 1.1, therefore decoupling the `Simulation` module from the remaining code base.

Chapter 3

Tools & Techniques

The focus of this section lies on the practical aspects of the work contained in this thesis such as sample creation and experimental set-ups, as well as the subsequent analysis of data, including the particularities of the fitting method applied in order to extract meaning from experimental data.

Therefore, section 3.1 will deal with nanoscopic patterning techniques in general while their practical implementation in creating the patterned arrays dealt with in this work are presented in section 3.2. The next section (3.3.2) focusses on the types of diffractometer scans performed and what the relationship between the various diffractometer angles and the wavevector transfer $\mathbf{Q}$ is. This provides the connection between experiment and scattering theory. Section 3.3.1 briefly summarizes the most important properties of modern synchrotron sources and why they are necessary for certain types of experiments. Finally, the purpose of section 3.4 is to familiarise the reader with the basic concepts of the *Differential Evolution Algorithm*, which mimics natural genetic selection in order to adapt, or fit, simulations to experimental data.

3.1 Sample Preparation

The patterned arrays presented in this work are examples of mesoscopic systems, the latter being loosely characterised by exhibiting some kind of correlation length in the order of tens of nanometres up to multiple micrometers. Often, mesoscopic systems are specifically engineered utilising various nanopatterning techniques[108–113]. The correlation lengths of these systems are then found to be of dimensions suitable for the low wavelength transfers used in grazing incidence and small angle x-ray scattering[114][68][115][116] (GISAXS and SAXS, respectively).

The structure of all samples discussed in this work can be broadly divided into their out-of-plane and in-plane components. In the case of patterned arrays in particular, the out-of-plane component is intimately related to the planar thin film deposition techniques, which are discussed in section 3.1.1. The in-plane structure of a patterned array is, in most cases, created through some kind of lithographic structuring[117][118][47], spatially truncating the out-of-plane structure into a two-dimensional array. As such, lithographic patterning is discussed in section 3.1.2.

3.1.1 Thin film deposition

Some of the most common techniques of (unpatterned) thin film deposition in nanotechnologies are *sputtering*[119–121], *molecular beam epitaxy*[122, 123] (MBE) and *spin coating*[124, 125]. Their common use is the creation of thin films[57, 126, 127] of materials, ranging from Ås up to multiple µm in thickness. In the case of sputtering and molecular beam epitaxy the mass is transferred from a material source to the sample via an intermediate vaporous state, whereas in spin coating a large quantity of material is deposited on a rapidly rotating sample and subsequently spread out into a thin film via centrifugal forces. Since no samples in this work have been prepared by MBE[128, 129], no explicit discussion will be provided at this point.

Sputtering techniques

Sputtering is an umbrella term for a plethora of similar techniques, which all follow the basic principle of transferring material from a sputtering target to be deposited on a sample. This generally happens by means of bombarding a target with highly accelerated particles of molecular size[113]. Most commonly, the incident particles are ions formed from an atmosphere of very low pressure in the order of mbar inert gases like argon, following the evacuation of the sputtering chamber to a very low base pressure in the order of 10^{-9}mbar. Acceleration of the ions onto the target material is performed by a high electrical potential difference in between anode (which might be the sample itself) and the target cathode. The kinetic energy of the incident ions is bound by the requirements that

1. it is sufficient to eject atoms or molecules out of the bulk target material
2. the remaining kinetic energy of the particles after ejection is sufficient to exhibit a mean free path through the sputtering chamber which is much larger than the target-sample distance in order to keep a sufficient particle flux onto the sample surface. The kinetic energy of the ejected particles is generally

found to be actually too high for efficient adsorption onto the sample. Therefore, the mean kinetic energy of the ejected particles is reduced by inelastic collisions with inert gas molecules, the number of which is controlled by adjusting its pressure.

Generally, a balance of parameters like gas pressure and potential difference has to be found to ensure both high deposition rates and thin film quality.

The simplest and most common form of sputtering is *direct current sputtering* (DC sputtering)[71][130], where a constant potential difference up to multiple kV is applied in between the target and source material. Any ions of inert gas atoms and free electrons are immediately accelerated either towards, or away from, the sputter target cathode. On their way, the charge carriers are triggering a chain reaction of impact ionisation of gas atoms, thereby creating a stable plasma around the target cathode which is characterised by the eponymous direct current of positive electrical charge towards the target.

Another variant of the technique is *radio frequency sputtering*[131] (RF sputtering), which – among other advantages – enables sputtering of non-conducting target materials, which would otherwise quickly lead to an agglomeration of positive charge on the target with consequences like electrical arcing and reduced sputtering rates[132, 133]. In RF-sputtering a high frequency alternating electrical field is applied in between the sputtering target and the sample. From multiple tens of kHz upwards, the relatively heavy ions are not able to follow the oscillating field any more, due to their low charge-to-mass ratio. Any electrons in the plasma, however, are still sufficiently mobile and able to follow the driving field thereby replenishing any deficient charge on the target on every field cycle. In order to overcome the apparent immobility of the inert gas ions at high frequency fields an offset voltage is applied in addition to the RF field, therefore leaving the basic working principle of a net stream of ions towards the sputtering target intact.

To improve sputtering rates even further, a magnetron may be added close to the target in a *magnetron sputtering*[98][75][134] set up. Here, electrons in the plasma are trapped close to the surface of the sputtering target by the magnetic field of the magnetron. According to the Lorentz force, the electrons take on a spiralling course along the magnetic field lines, more or less parallel to the target surface. In this way, the increased path lengths of electrons leads to drastically higher ionisation rates, therefore increasing the net ion flux towards the target and the associated sputtering rate.

In order to efficiently grow layered systems, sputtering chambers generally contain a number of sputtering targets of various materials. They are shielded from

each other with shutter doors, and can be used as required following a protocol determining the order and thickness of the desired layers. The layer thickness is usually controlled by a *quartz crystal microbalance* (QCM), which measures either the material deposition rates or the total deposited material per unit area[135]. The latter is accomplished by piezoelectric detection of the changing oscillation period of a quartz-crystal resonator, depending on the oscillators mass-increase due to the deposited material. For a reliable reading of the material deposition rate it is important that the QCM is located in close proximity to the sample within the sputtering chamber, so that the deposition rates at both locations are equal. Typical deposition rates for growing patterned arrays are in the order of $\text{Å}\,\text{s}^{-1}$.

All samples contained in this work have been created by either RF- or DC magnetron sputtering, with details about the growth process being found in Arnalds et al. [98] and Östman et al. [77].

Spin Coating

Another technique for creating thin films is *spin coating*[136][137]. Here, a liquid droplet of material is deposited onto a rapidly spinning substrate and subsequently thinned out by centrifugal forces into a thin film, removing any excess material.

This technique is obviously limited by requiring a liquid state of the initial material, which severely limits the choice of deposited material under normal laboratory conditions. Furthermore, controlling the film thickness is much less precise than in the previously discussed techniques and the lower limit of obtainable film thickness of about 100 nm is often larger than desired by an experimenter.

However, the technique's low cost and fast preparation time makes it an excellent technique for depositing electronbeam- or photoresist layers (furtherly discussed in section 3.1.2) and leaves spin coating among the most ubiquitously used techniques in nanopatterning.

3.1.2 Lateral Structure

The last section focused on the controlled creation of planar, or stratified, samples, whose structuring is basically limited to the out-of-plane direction. Patterned arrays, however, additionally to the aforementioned structure *normal* to the sample plane, obtain an additional dimension of structure *within* the sample plane, which usually manifests in form of lateral translational symmetry or at least structural long distance correlations[92, 113, 127].

Various approaches for the creation of these structures exist, most of which

can be characterised by one of either top-down[138–140] or bottom-up[137, 141, 142] patterning.

Bottom-up Approaches

The term *bottom-up* approach refers to the indirectly controlled creation of larger systems from specifically engineered building blocks, which interact in a desired way that leads to self-assembly into a desired structure[143]. Since the engineering takes place on the level of the building blocks, the approach is termed "bottom up". Bottom-up assembly generally requires less direct interference of an experimenter and is most often found to be significantly faster and cheaper than top-down approaches, because of the self assembling characteristics of the system, which necessitates little or no external intervention. However, on the flip side, the number of obtainable systems is arguably relatively low, since the processes driving the self-assembly are hard to control and can generally not be used to create arbitrary systems. Furthermore, true long range order over mesoscopic length scales can only rarely if ever be obtained and correlations of the systems are generally limited by statistical fluctuations[91].

Top-down Approaches

As opposed to bottom-up approaches *top-down patterning* works by successive reduction of an extended but simple system into a smaller system of a more complex structure[113], therefore patterning the sample from the "top down". In top-down approaches it is usually the interactions between the sample and an external patterning device that drive the assembly, rather than interactions in between the building blocks themselves as is the case for bottom-up approaches.

The very high spatial resolution modern lithography techniques provide has recently dropped to single digit nm resolution[144–146]. The ability to re-use patterning masks obtained from electron beam lithography allows the rapid sample creation using *photo-lithography*[147, 148] and *nano-imprint lithography*[149] leading to remarkably large spatial patterning dimensions of up to $\sim 10\,\mathrm{cm}^2$[77]. Because of the time consuming patterning by scanning an electron beam over the sample, mask-less patterns directly obtained via *electron beam lithography*[150, 151] (EBL) are usually smaller, typically $< 1\,\mathrm{mm}^2$. In any case, the exceptional short- and long-range accuracy obtained by any lithographic patterning techniques leads to the resulting patterned arrays to justifiably being regarded to as perfect two-dimensional supercrystals[91]. Using any lithographic technique, a chemical pattern is created

by exposing selected parts of the resist material to either light or an electron beam, thus changing the molecular structure of the exposed resist. Typically, the exposure follows either a negative or positive template of the final sample pattern.

In the *development step* the physical pattern is created, usually by application of a developer solvent to the (chemically patterned) resist. Using *positive resist*, the parts of the resist that have previously been chemically modified dissolve on contact with the developer solvent, while the chemically unmodified resist remains stable on contact with the developer. Using *negative resist* on the other hand, the resist is generally soluble within the developer solution and the chemical modification of the resists following the patterning process now stabilises the solvent with respect to the developer chemical. Using mask-less lithography (e.g. EBL) the choice of which kind of resist to use depends, amongst other factors, on whether a positively or negatively pattern requires the larger exposure area, since the electron beam has to be rastered over the whole patterning template, which can take many hours for the patterning of a micro- or even millimetre sized sample area, possibly including many millions of nano-elements.

Being a mask-less technique, EBL provides the advantage of an extremely high flexibility, as arbitrary sample structures may directly be printed to a resist layer, without requiring to first go through the mask-creation process. Further, EBL patterns usually show better results than competing lithographic techniques, both

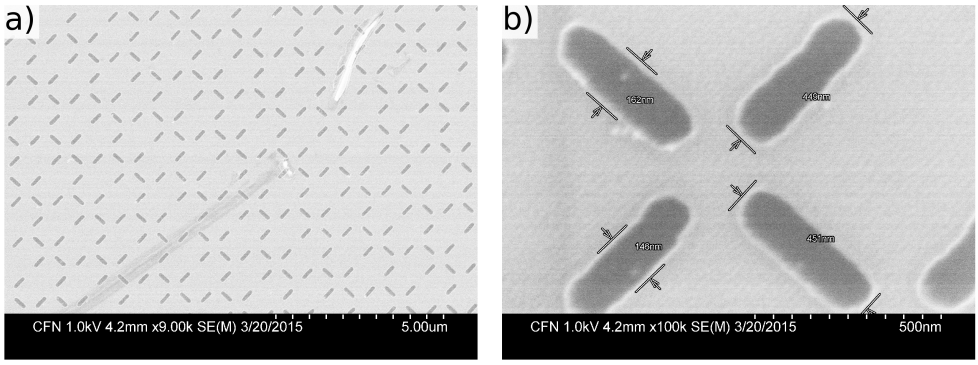

Figure 3.1: Example of patterning of narrow nano-elements into an artificial spin ice lattice. In this example a post-patterning of the sample was used, meaning that the island material has been deposited before the lithographic patterning of the sample took place. Despite impurities and scratches, the patterned array in itself is found to be virtually defect less over very large areas as can be seen in panel a). The nominal length and height of single islands almost perfectly match the specifications of 150 nm and 450 nm. Images have been captured within the authors work-group.

in terms of fewer structural defects as well as lower edge roughness[145]. Because of these advantages, EBL is the technique nowadays most often used in scientific research. Fig. 3.1 shows an example of the high degree of accuracy obtainable from electron-beam lithography.

In contrast, photo-lithography provides an advantage in sample preparation speed because of its highly parallel exposure step, which basically consists in simply irradiating the sample with light[152]. Because of the rapid patterning speed and low cost, photo-lithography is most commonly used in industrial manufacturing of nano- and microstructures.

In practice, a complex sample structure usually requires a combination of different approaches and the creation process may involve multiple steps of growing- and patterning procedures as will be shown in the example given in the next section.

3.2 Experimental Realisation of Samples in this Work

The samples presented in this work were designed by a multi-step combination of deposition methods and lithographic patterning leading to either a pre-patterning or post-patterning of the samples. The exact experimental details of sample creation are provided in the respective chapters as well as in Arnalds et al. [75] and Östman et al. [77], in all cases using pre-patterning of the arrays. For completeness, the alternative route of post-patterning samples is discussed as well. Here, only the basic principles will be compared, which are also depicted in the top- and bottom rows of Fig. 3.2.

In the case of pre-patterning the sample creation process can be broken down into five steps:

1. Application of a layer of positive resist using spin-coating.

2. Patterning of the e-beam resist through exposition to a scanning electron beam. This is the most time consuming step in the process.

3. Development of the e-beam resist, creating the patterned mask. Since a positive resist was chosen in the first step, the area exposed to the electron beam is now removed from the substrate, leaving behind a hole-pattern within the remaining resist, representing the in-plane structure of the final patterned array. (Alternatively, if nano-imprint lithography[149] is used, the patterning mask is obtained mechanically via application of a spatially moulded stamp onto a spin-coated film of silica-based sol-gel instead of chemical dissolving.)

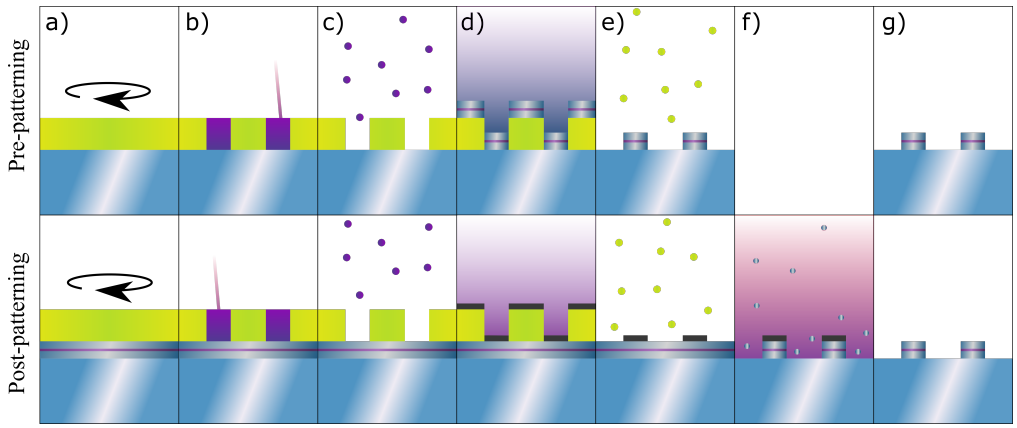

Figure 3.2: Schematic of the pre- and post-patterning processes using EBL. (a) Application of e-beam resist via spin coating, b) Chemical resist-patterning by using a focused e-beam, c) Physical resist-patterning through removal of chemically altered resist, d) sputter deposition of either the pattern material (top) or a chromium shielding (bottom), e) chemical removal of the remaining resist and attached material, f) Physical patterning of the unshielded sample material through ion-milling (postpatterning only), g) the final array is identical in both patterning processes.

4. Deposition of the pattern material by a suitable technique, e.g. magnetron sputtering. Hence, only now is the out-of-plane chemical structure of the pattern created.

5. In the last step, the remaining resist is dissolved in a lift-off process, detaching the material deposited on top of the resist from the sample, leaving behind the bare patterned array.

On the other hand, the post-patterning protocol consists of a slightly more complicated six-step process:

1. Spin-coating of positive resists onto an already grown stratified system, corresponding to the desired out-of-plane structure of the patterned array. (Preparing the thin film structure in advance, has the advantage of better control of the growth process, enabling, for instance, epitaxial growth of single crystalline structures.)

2. Patterning of the e-beam resist through exposure to a scanning electron beam.

3. Development of the e-beam resist. Being identical to step 3 of the pre-patterning approach.

4. Deposition of a shield layer, e.g. chromium, by a suitable technique, e.g. magnetron sputtering. The shield covers both the stratified sample and the remaining patterned resists.

5. Dissolving of the remaining resists. Any chromium on top of the resists is removed as well, leaving behind a chromium shielding corresponding to the lateral structure of the desired pattern.

6. Patterning of the layered sample is accomplished by ion-milling[152, 153], bombarding the sample with high energy Argon or Gallium ions. Therefore, sample material which is not protected by the chromium shield is sputtered away, hence completing the sample patterning process.

Post patterning has been used within the scope of this project for creating the artificial spin ice presented by Stopfel et al. [42]. However, since no further analysis of this system has been performed within the scope of this thesis, no further discussion is provided here.

Which of the two patterning processes is to be used depends on the desired kind of sample. Although generally possible[154, 155], if the patterned elements require epitaxial growth, usually post-patterning is favoured, since the sample growth demands a much higher spatial control of the growth process, which is much easier for stratified- than patterned media. On the other hand, pre-patterned masks are reusable, which may speed up the sample creation significantly if multiple similar arrays are to be created. However, pre-patterning is only compatible with amorphous or polycrystalline sample structures, which require less precise control over the conditions of the growth process.

What is common to all patterning processes is that the thickness of the resist layer providing the patterning mask is always significantly thicker than the final patterned structure which is mostly due to limitations regarding the lower limit of film thickness obtainable by a spin coating process. The latter might lead to problems in pre-patterned samples, since it increases the probability of shadowing effects if the incident angle of the subsequent material deposition into the mask deviates even slightly from the normal incidence to the sample plane.

Another factor to consider is the inhomogeneous energy deposition of the electron beam within the resist layer in lithographic patterning, known as the *proximity effect*[156, 157], meaning that, generally, meaning that volume within which the incident electrons deposit their kinetic energy generally exceeds the volume of the nominal scanning pattern. Fast electrons penetrating into the resist layer deposit their kinetic energy in a cascade of scattering events and are often found to

be elastically backscattered from the underlying substrate. In effect, this leads to over exposure of the resist, with the effect being more pronounced the more kinetic energy the electrons possess and the further the backscattered electrons travel back up through the resist film[158, 159]. Both of the latter is true for the higher parts of the resist layer, generally leading to overexposure being more pronounced higher up in the resist layer, resulting in patterning masks using positive resist ending up being wider at the top, potentially leading to undesired crowning effects[56]. To compensate for this overexposure, actually two layers of e-beam resist have been applied to the substrate, the lower one having a higher sensitivity to compensate for the narrower exposure width deeper down in the resist.

In fact, *crowning* has not been observed in subsequent characterisation of the pattern. However, the patterned arrays consistently exhibit *doming*, i.e. a continuous radial distribution of island height, decreasing from the island centre to the edges, an example of which is depicted in Fig. 3.3. The latter shows an AFM linescan over one patterned island of nominal radius and height of 450 nm and 10 nm, respectively. Most prominently, each island obtains a pronouncedly domed top, spanning roughly six to eight nanometres in height. Furthermore, the island's side walls do not appear to be perfectly vertical, but rather narrow down multiple tens of nanometres in width over the first 10 nm in island height.

One possible explanation of this observation is a shadowing effect of the rela-

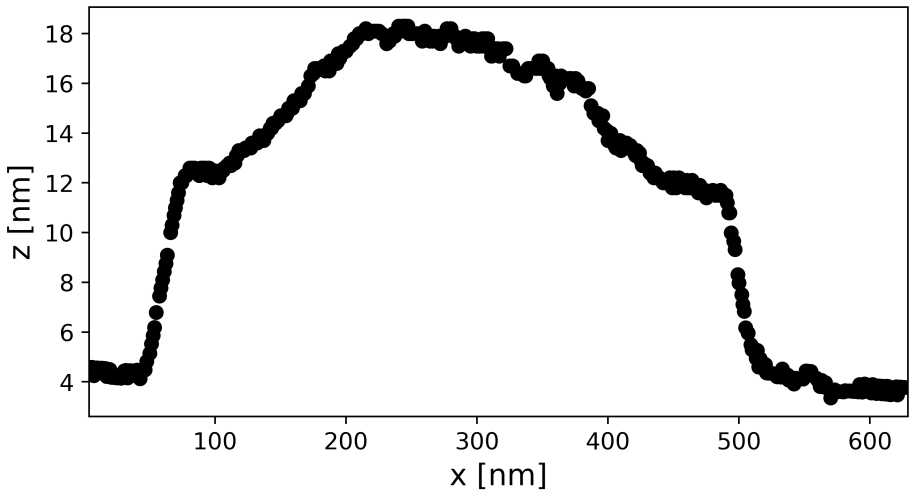

Figure 3.3: Atomic force microscopy linescan of a patterned amorphous iron palladium nanodot. The doming of the structure is clearly visible. The doming is either due to a shadowing effect of the relatively high (100 nm) patterning mask or a more dynamical redistribution of the FePd adatoms after deposition.

tively high patterning mask over the thin layer of deposited island material (100 nm vs. 10 nm) affecting the uniformity of the growth under non-perpendicular incident angles of the deposited material. However, geometric considerations show that the patterning mask would have to be significantly higher in order to account for the observed continuous radial distribution under any conceivable realistic incidence angles of deposited material. The latter, together with the fact that – as will be shown in chapter 4 – doming also occurs in the post-patterned samples, renders shadowing effects a relatively unlikely explanation for island doming. Another possible explanation is a more dynamical restructuring of the deposited material, due to adsorbent diffusion of surface atoms within the patterning holes or stress-induced deformation of the islands.

In summary, more research has to be done in order to explain the exact doming mechanism, but the possibility of doming of patterned arrays should always be considered when using disk-like island geometries, since they appear to be most susceptible to doming effects because of their rotational invariance. This is particularly true since domed structures, under certain conditions, are found to *significantly* influence the quantitative analysis of scattering experiments as will be shown in the main body of this work.

3.3 Structural Characterisation

Real space imaging techniques like scanning electron microscopy (SEM), atomic force microscopy (AFM) or magnetic force microscopy (MFM) are techniques for direct measurement of the (outer) shape and surface chemical composition of micro- and nanoscopic objects. The field of view in direct space is usually limited to a comparatively small area of a sample, making statistical statements over the whole sample difficult. Since modern lithography is able to very consistently produce patterns with remarkable accuracy, the latter is not necessarily a big problem. However, imaging techniques are usually limited to the surface of a sample, rendering any (usually much more interesting) *internal* structure fully inaccessible.

X-ray scattering solves both problems, by simultaneously (incoherently) illuminating large sample areas, providing very good statistical information. Further, because of their large penetration depth, x-ray scattering is very sensitive to the internal chemical- and (under certain conditions) magnetic structure of a sample. The remainder of this section will provide a summary of the techniques used in order to characterise a patterned array, which include the utilisation of synchrotron radiation in order to gain magnetic sensitivity, rocking- and reflectivity scans in order

to probe the in- and out-of-plane pattern structure, and finally fitting of a model to experimental data by means of the differential evolution algorithm.

3.3.1 Synchrotron Radiation

X-ray radiation for scientific applications is generally generated in laboratories, exploiting x-ray emission following ionisation, or at central facility sources, exploiting x-ray emission via accelerating electrons by magnetic fields.

In laboratory sources, energetic electrons are accelerated towards a metallic target, ionising atoms upon impact. The emitted spectrum contains Bremsstrahlung[160] as well as x-ray photons characteristic of the target material. The latter is a consequence of de-excitation along specific electronic transitions. Generally, experimental applications use these characteristic lines, since they are high in intensity and of a narrow energy bandwidth[60]. Drawbacks of laboratory sources include limited x-ray flux, high angular divergence of x-ray emittance and lack of x-ray polarisation. However, the biggest drawback is probably the inability to tune the x-ray energy to a particular value that an experiment might require, for instance in order to investigate resonant scattering phenomena.

A *synchrotron*, on the other hand, is a combination of straight and arced sections of vacuum tubes, forming a closed ring[161]. Relativistic electrons orbit the ring within the vacuum tubes, being guided by bending magnets placed within the arced sections[62]. While exposed to the magnetic field $\mathbf{B}$ of the bending magnets oriented perpendicular to the plane of the ring and in absence of any electric field the electrons experience the Lorentz force perpendicular to both their current velocity and the magnetic field[60]. The latter forces the electron on a circular path within the plane of the ring. Given the electrons charge e^- and velocity $\mathbf{v}_{\mathrm{el}}$ the Lorentz force takes on the form

$$\mathbf{F}_{\mathrm{L}} = \mathrm{e}^-(\mathbf{v}_{\mathrm{el}} \times \mathbf{B}). \tag{3.1}$$

In order to keep the electrons in orbit without touching the edges of the vacuum tube, both $\mathbf{B}$ and $\mathbf{v}_{\mathrm{el}}$ have to be tuned so as to match the angular diversions of the electrons on traversing a bending magnet to the curvature of the tube. Modern synchrotron facilities operate at bending magnet field strengths in the order of 1 T and relativistic electron energies in the GeV range[162, 163]. Since the accelerated charges lose energy on being diverted by the bending magnets, the electrons emit a narrow cone of radiation tangentially to their curved trajectory, which is found to be of angular divergence[62]

$$\Delta\alpha = \frac{1}{\gamma}, \tag{3.2}$$

with γ being the Lorentz factor. For the super-relativistic electrons in a synchrotron the Lorentz factor takes on values of $\gamma \approx 10^4$, meaning the angular divergence of the radiation is in the order of 0.1 mrad. The beam is found to be linearly polarised within the plane of the electrons' orbit and forms a continuous energy spectrum. Beamlines are located along these tangent points, enabling the utilisation of the highly energetic x-rays for scientific experiments. Naturally, the energy the electrons lose on every bending magnet has to be replaced through radio frequency cavities, having the accompanying effect of separation of the electrons into bunches[164, 165].

On stable operation, a fixed number of electron bunches transit the rings on time separations on the order of ns. Hence, a synchrotron is therefore a stroboscopic radiation source, with any beamline receiving a flash of x-rays on each bunch of electrons transitioning the associated bending magnet. Because of the continuity of the energy spectrum of the emitted radiation, it is possible to select a desired energy by using a suitable monochromator. The flux obtained in this way is orders of magnitude higher than a typical laboratory source and is capped by the quality of the vacuum within the ring and the bunch size of electrons that can be stabilised against their electrostatic repulsion[161].

Historically, x-ray production has been somewhat of a necessary byproduct of using bending magnets in order to keep electrons in a closed orbit. On the current, third generation synchrotron sources such as the ESRF, APS, Diamond etc. x-ray production for scientific applications has moved from the bending magnets, to specifically designed insertion devices within the straight sections of the ring. These devices consist of magnetic lattice arrays of a number of N alternating magnetic fields, oriented perpendicular to the plane of the ring. Hence, the electrons are forced to oscillate around their average trajectory, emitting a cone of radiation along the beamline on passing each array element. The two main types of magnetic arrays used to create synchrotron radiation are called *undulators* and *wigglers*, which vary in the maximum angular diversion that the electrons experience while traversing the array, as indicated in Figs. 3.4 and 3.5. It is convenient to define the maximum angular diversion by[62]

$$\Delta\alpha = K/\gamma = \frac{2\pi}{d_\mathrm{u}} = k_\mathrm{u} A, \tag{3.3}$$

where d_u is the spacing between the array elements, K is the maximum angular deviation from the undulator axis, and A is the amplitude modulus of the electrons' oscillating path, being smaller the higher the relativistic energy of the electrons and the smaller the magnetic field is.

It can be shown[62] that the small oscillation amplitudes of the electrons of

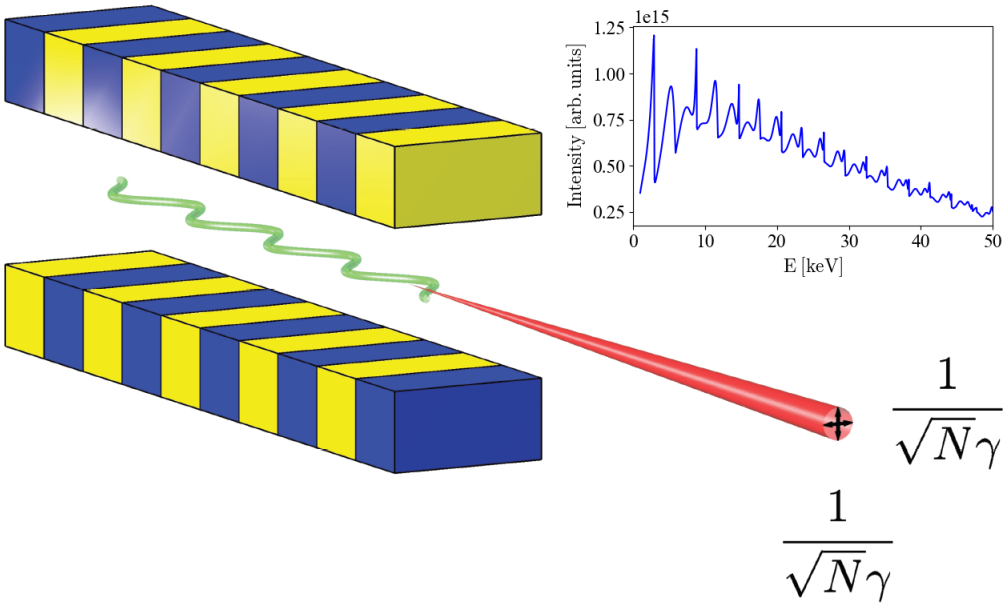

Figure 3.4: Schematic of an undulator. Electrons are diverted within the oscillating vertical magnetic fields connecting the opposite magnetic poles depicted as either blue or yellow array element. The small angular diversion of the electrons along the undulator leads to a coherent summation of amplitudes and a compression of the emitted radiation cones by a factor of $1/\sqrt{N}$ compared to a bending magnet. The inset shows the narrow energy spectrum including five harmonics calculated via the openly available XOP project[166]. Image adapted with slight alterations from [62].

an undulator, characterised by $K = 1$, lead to a compression factor of $1/\sqrt{N}$ in angular divergence as compared to the opening angle of a radiation cone emitted by a bending magnet $1/\gamma$ as indicated in Fig. 3.4, hence producing x-rays of high spatial coherence. The number of array elements is typically found to be $N \approx 50$. Undulators tune d_u in a way that the x-ray emission at all oscillations are in-phase, implying coherent summation of amplitudes, leading to a quasi-monochromatic spectrum (including harmonics) of radiation as seen in the inset of Fig. 3.4.

Wigglers are characterised by larger oscillation amplitudes, characterised by $K \approx 20$, requiring significantly larger magnetic fields compared to an undulator given the same energy of the electrons. The emission at each magnet of the array is formally identical to that of a bending magnet of the same field, but the emitted cones of radiation at each oscillation are no longer in phase with each other. Therefore, the intensity emitted by a wiggler scales by a factor of $2N$ to that of a regular bending magnet, leading to a flux spectrum identical to that of a regular bending magnet. The total radiation cone of a wiggler gets wider by a factor of K within the synchrotron plane, while maintaining its natural opening angle $1/\gamma$ perpendicular

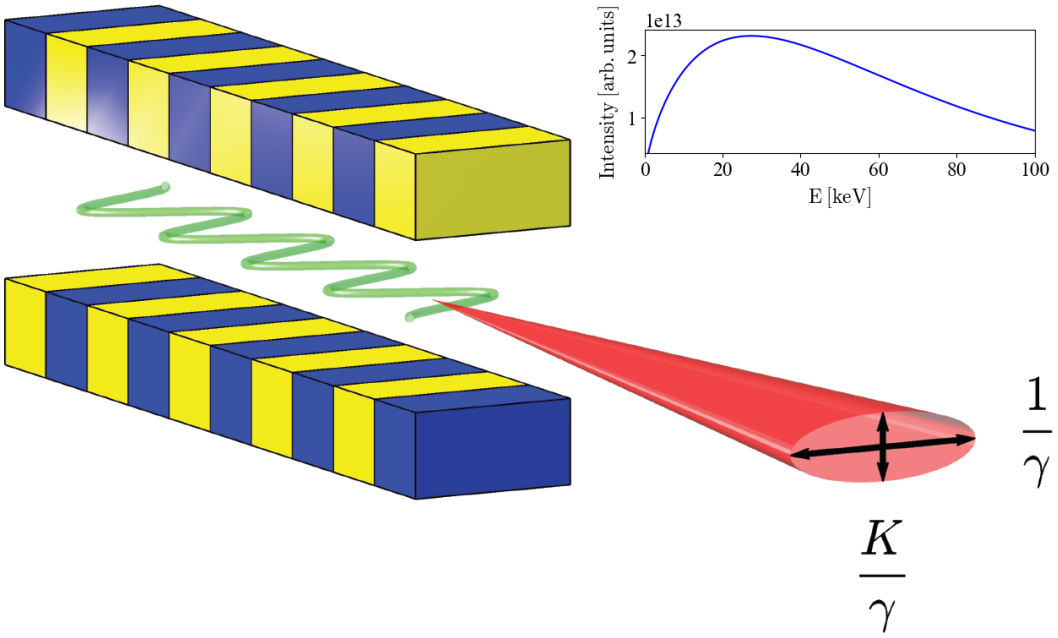

Figure 3.5: The large angular diversion in a wiggler leads to a massive increase in emitted flux at the cost of a widening of the radiation cone by a factor of K within the synchrotron plane compared to a bending magnet. The inset shows the continuous energy spectrum of a wiggler calculated via the openly available XOP project[166]. Image adapted with slight alterations from [62].

to the synchrotron plane.

A further advantage of insertion devices is that the magnetic lattice can be phase shifted resulting in beams of circular, elliptical or linear polarisation. Such "APPLE" (Advanced Planar Polarized Light Emitter) undulators are used for energies $< 1\,\mathrm{keV}$[167–169], since the tolerances on the magnetic lattice means these are only useful for soft x-ray beamlines. Recently, APPLE-Knot undulators have been developed that supply the advantage of arbitrary beam polarisation, while maintaining low on-axis heat of higher harmonics, which has been a common byproduct of low-energy x-rays at high-energy synchrotrons[170].

Beamlines

Following, a very short summary of the typical set-up of a synchrotron user-station is presented. Regarding the exact parameters of all performed experiments, the reader is referred to Procter [171] containing a more complete summary of experimental details. The multilayer samples of chapter 4 were measured on the X-22C beamline of the National Synchrotron Light Source (NSLS), using a bending magnet, while

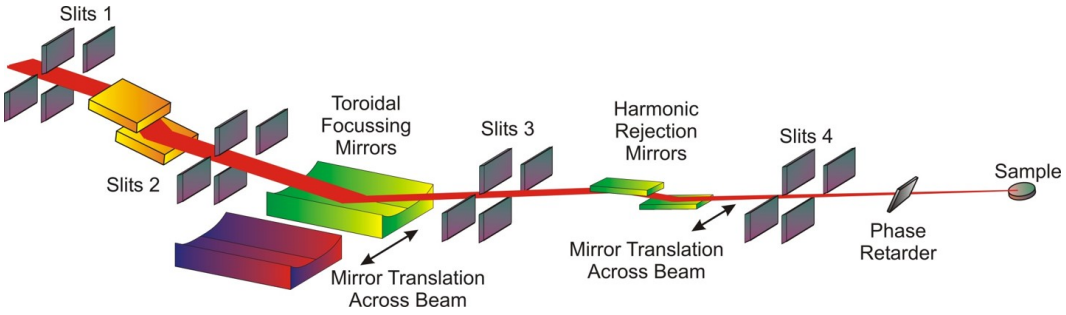

Figure 3.6: Schematic of the optical instrumentation at the user end of the XMaS beamline. Depicted in orange is the two-crystal monochromator, followed by focussing mirrors, harmonic rejection mirrors and phase retarders. All elements are connected by a pair of each of horizontal and vertical slits. Adapted from [172].

the samples of chapter 5 were measured at 4-ID-D beamline at the Advanced Photon Source (APS), using undulator radiation.

At the level of an individual beamline, the synchrotron radiation has to be processed in a few steps before being used to illuminate a sample. First, an energy dispersive monochromator[173, 174] selects a particular energy from the continuous bending magnet spectrum, or the narrow spectrum of an undulator. Typically, the monochromator is a cryogenically cooled single crystal usually made of silicon. After passing focusing mirrors[175, 176] and slits the beam is tailored further by other optical elements such as harmonic rejection mirrors[177, 178] and phase-retarders[179]. The latter are used for beamlines of "hard" energy ($> 3\,\mathrm{keV}$), where "APPLE" undulators cannot be used to directly produce circularly polarised light and the phase retarder acts essentially like a quarter wave plate converting linearly polarised- into circular- or elliptical light. A final set of slits, intensity monitors and absorbers allow the users to correct for changes in fluctuations of the incident flux over time and protect sensitive detectors. Fig. 3.6 shows a schematic of a typical synchrotron user end, including most of the optical elements discussed in the text above.

Energy selectiveness and polarisability of radiation are crucial elements in performing magnetically sensitive x-ray diffraction, which makes modern synchrotrons indispensable for investigations into magnetic patterned arrays.

3.3.2 Scans through Reciprocal Space

This section briefly summarises the relationship of the scattering geometry with the probed position in reciprocal space[62, 68, 79, 180] after the sample has been aligned with respect to a particular source of x-ray radiation. In particular, it will be shown how the wavevector transfer $\mathbf{Q}$ can be controlled by three distinct angles

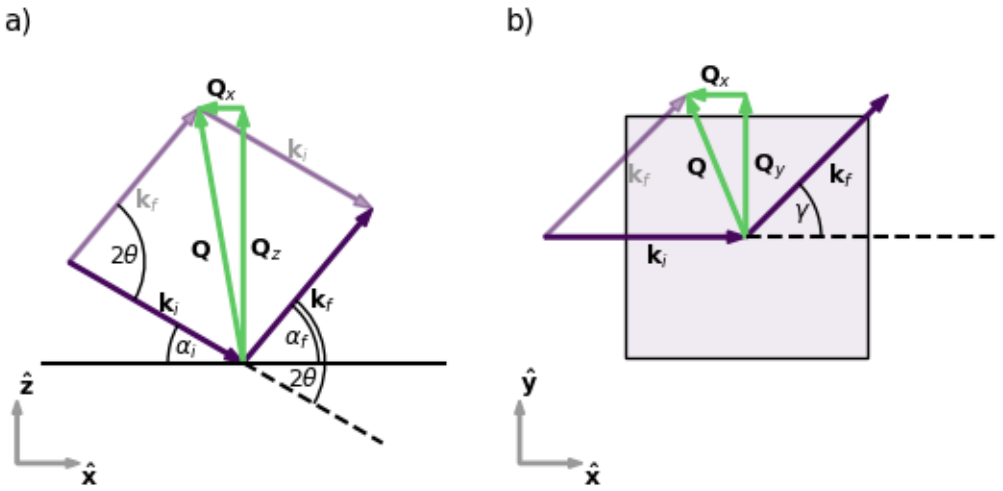

Figure 3.7: Basic diffractometer set-up. Panel a) shows the side-view from within the sample plane, panel b) shows the top-view along the sample normal. The incidence angle α_i is controlled by rotating the sample at a fixed source position around a horizontal axis perpendicular to $\mathbf{k}_i$. The exit- or detector angle α_f is controlled by the angle in between detector and source 2θ. If the detector does not lie in the scattering plane, the wavevector transfer contains a $\mathbf{Q}_y$ component that scales with the sine of γ, the detector angle in the sample plane.

of a diffractometer.

Generally, the position in reciprocal space any scattering experiment is probing is determined by the wavevector $\mathbf{k}_i$ of the incident radiation and the wavevector $\mathbf{k}_f$ of the detected wave, which both depend on the relative positions of sample, x-ray source and detector. In a usual experimental set-up the radiation is entering the sample chamber horizontally and the sample may be rotated freely within the chamber.

Figure 3.7 shows a schematic of a typical experimental set-up. The angle in between and incident radiation in the laboratory frame is called θ, whereas in the sample frame the naming convention α_i is used. Furthermore, the angle between the *source* and detector in the laboratory frame is, for historical reasons, often called 2θ, although strictly speaking the condition $2\theta = 2 \times \theta$ is valid only in the specular condition. Similarly, the angle between the *sample* and detector in the coordinate frame of the sample is given by the angle α_f. For consistency, in the following all discussion will be considering the sample frame only, although transformation of the respective coordinate systems can be easily performed by noting that $\alpha_i = 2\theta - \theta$.

If the sample frame is defined in such a way that $\hat{\mathbf{x}}$ is aligned with the projection of $\mathbf{k}_i$ onto- and the $\hat{\mathbf{z}}$ is given by outward normal of the sample plane, and restricting scattering to a plane defined by the $\hat{\mathbf{z}}$ and $\mathbf{k}_i$, the relationships

$$\mathbf{k}_i = k \begin{pmatrix} \cos\alpha_i \\ 0 \\ -\sin\alpha_i \end{pmatrix} \tag{3.4a}$$

$$\mathbf{k}_f = k \begin{pmatrix} \cos\alpha_f \\ \sin\gamma \\ \sin\alpha_f \end{pmatrix} \tag{3.4b}$$

always hold. Hence, the respective components of the wavevector transfer

$$\mathbf{Q} = \mathbf{k}_f - \mathbf{k}_i$$

are given by

$$Q_x = k\left(\cos\alpha_f \cos\gamma - \cos\alpha_i\right) \tag{3.5a}$$

$$Q_y = k\ \sin\gamma\cos\alpha_f \tag{3.5b}$$

$$Q_z = k\left(\sin\alpha_f - \sin\alpha_i\right). \tag{3.5c}$$

The condition $\gamma = 0$ defines the scattering plane, spanned up by the coordinate axes Q_x and Q_z, since traditionally most experiments were realised under this condition.

Reflectivity Measurements

Reflectivity measurements are characterized by the symmetric condition

$$\alpha_i = \alpha_f \tag{3.6a}$$

$$\gamma = 0, \tag{3.6b}$$

which means that the wavevector transfer points solely in direction $\hat{\mathbf{Q}}_z$, as can be seen in Fig. 3.7 and eqs. 3.5. Hence, this type of scan probes the out-of-plane sample structure only and is therefore particularly useful in the characterisation of stratified media, since the latter can often be considered to be purely one-dimensional structures, varying only in their depth profile of scattering length density.

From eq. 3.5 c) it is evident that the Q-resolution in a reflectivity measurement is given by

$$\mathrm{d}Q_z = 2k\ \mathrm{d}\alpha\,. \tag{3.7}$$

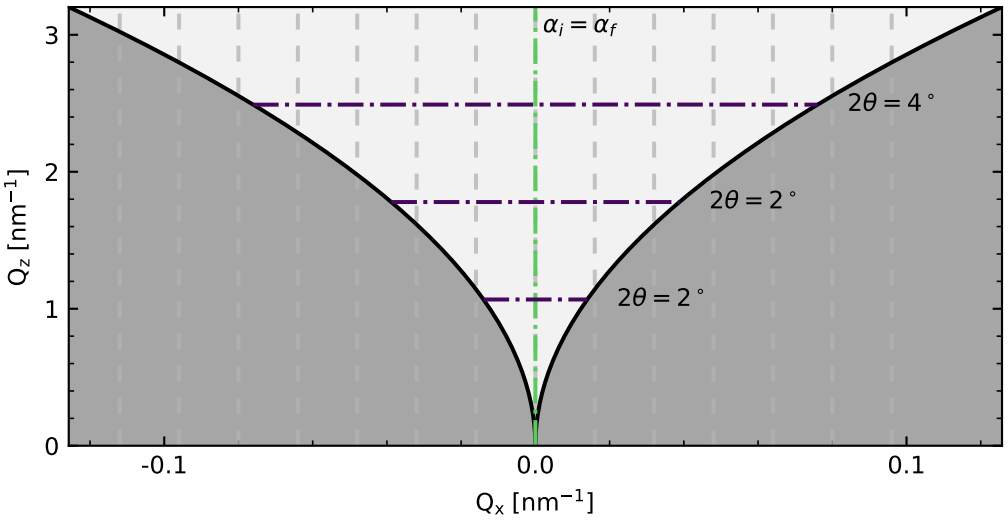

Figure 3.8: Trajectories of Q_x and Q_z scans through reciprocal space. The green line corresponds to a reflectivity measurement. Each purple lines corresponds to a different detector angle 2θ, which probes reciprocal space at constant Q_z and up to a certain maximum wavevector transfer $Q_{x,\max}$, given by eqs. 3.10. The shaded region is inaccessible since the sample would be blocking either the source or the detector and the vertical dashed lines indicate the positions of GTRs intercepted in Q_x scans.

Rocking Curves

While the trajectory of a reflectivity measurements is purely vertical, a rocking scan probes reciprocal space in a horizontal line along $\hat{\mathbf{Q}}_x$. The scan is defined by the rocking condition

$$\alpha_i + \alpha_f = 2\theta, \tag{3.8}$$

meaning the detector angle in laboratory coordinates 2θ is held constant while the sample angle θ is rocked within the range $[0^\circ, 2\theta]$. For small angles limited to the scattering plane, substituting $\alpha_f = 2\theta - \alpha_i$ and under rocking conditions eqs. 3.5 a) and c) take on the form

$$Q_x^{\text{rock}} = \frac{k\ 2\theta}{2}\,(2\alpha_i - 2\theta) \tag{3.9a}$$

$$Q_z^{\text{rock}} = 2k(\alpha_i + \alpha_f). \tag{3.9b}$$

Further, given a particular detector angle 2θ magnitude of the scanned Q_x

range and the (constant) Q_z value are given by

$$Q_{x,\max}^{\text{rock}} \approx k\frac{2\theta^2}{2} \tag{3.10a}$$

$$Q_{z,\max}^{\text{rock}} \approx k\ 2\theta. \tag{3.10b}$$

Thus, at small and grazing detector angles 2θ the scanned Q_x range in a rocking geometry is significantly lower than the probed Q_z value. By the same token, the Q_x resolution of a rocking curve is usually much better than that of a reflectivity measurement since it is given by

$$\mathrm{d}Q_x = k\ 2\theta\,\mathrm{d}\alpha\,. \tag{3.11}$$

Hence, by choosing 2θ accordingly, the Q_x range probed can be adjusted to match the in-plane periodicity of a patterned array in order to intercept a given number of grating truncation rods as indicated by the vertical dashed lines in Fig. 3.8.

For instance, in a laboratory using a standard x-ray source ($k = 40.78\,\mathrm{nm}^{-1}$) measuring a patterned array of superlattice constant of $d = 1\,\mu\mathrm{m}$ the detector has to be placed at

$$2\theta = \sqrt{\frac{2(5\frac{2\pi}{d})}{k}} \approx 2.25^\circ$$

in order to ensure that five orders of satellite peaks are being observed.

3.4 Data Fitting with Differential Evolution

After the scattered signal of the sample has been measured, the final step of structural characterisation consists of the fitting of a suitable model to the experimental data. In the context of this work, fitting of simulated to experimental data is performed via the *differential evolution algorithm*, originally invented by Storn and Price [181], and will therefore be briefly discussed in the following section. The algorithm is inspired by natural selection in biological evolution, in which the genetic material of a given population slowly changes through mutation and combination of parents.

Any individual possesses a unique genome, which encodes all of it's particular characteristics, and is a combination of the genomes of it's two parents genomes, created following certain combinatory rules. If an offspring's genome is found to lead to generally beneficial characteristics given the current environmental conditions, chances of survival, i.e. fitness, are increased. On the other hand, if recombining

the parents genomes leads to a net decrease of the individuals fitness, the probability of survival of the individual is reduced. The building blocks of a genome are single genes, which any genome consists of a fixed number of.

Recombination of the parents' genes implies that only one or the other of each of the two variants of any gene can be chosen to make it into the new genome. Generally, recombining the parents genes into a new genome might lead to an overall increase in fitness, if more often than not the more adapted gene of either parent is chosen to make it into the offspring's genome. Sometimes, however, a gene randomly mutates and is then found to not be part of either of the parents' genomes. Typically, these mutations are rare and are often limited to a only a few or even just a single gene. However, by chance mutations might lead to adaptations that neither of it's parents were capable of and might therefore prove very useful for an individual.

In the context of *differential evolution*, the counterpart to the biological genome is a vector from the D-dimensional parameter space defining an agent a_i, being identified by the running index i. The counterpart to a single gene of the genome is given by the μ^{th} parameter $a_{i,\mu}$ of the optimization problem. The fitness of a biological individual a_i corresponds to the value of an arbitrary function, called the *figure of merit*, $\text{FOM}(a_i)$, taking a single agent as an argument. In the context of data fitting the figure of merit is usually minimised as it typically is a measure of how well simulated and experimental data match.

A set of parameter vectors p_i constitutes an *original population* P comprised of a number of agents, NP, similar to a population of biological individuals. A *trial population* T of the same size NP is obtained from a linear combination of the parameters taken from a subset of agents from P, therefore mimicking biological reproduction. In this way the total population is temporarily doubled, before each trial vector t_i of T competes against an agent p_i taken from the parent population P, leading to the reduced sets $\tilde{P} \subseteq P$ and $\tilde{T} \subseteq T$. The latter is done by comparing $\text{FOM}(p_i)$ against $\text{FOM}(t_i)$, with the agent performing worse being eliminated from the population pool, therefore completing one generational cycle resulting in a new generation $g+1$ of vectors $P^{g+1} = \tilde{P}^g \cup \tilde{T}^g$, which, again, is of size NP. Note that in the following the superscript g will appear only in inter-generational contexts and is dropped otherwise for clarity.

The elimination of poorly adapted agents and promotion of well adapted ones eventually leads to a clustering of agents in volumes of the parameter space associated with a beneficial figure of merit. Subsequent generations in this way continue converging to a global optimum until the population is considered to have successfully adapted, at which point p_{best}, the population member of the lowest

figure of merit, is considered a solution to the optimisation problem. In the context of data fitting, the convergence criterion is usually defined by the deviation between simulated and experimental data falling below a predetermined cut-off limit or by the population having converged to a point that no further significant improvement is to be expected. Note that the latter typically occurs in case of a misconvergence into a local optimum, so that it cannot be considered as a criterion for a successful fit.

Probably the biggest advantage of differential evolution is that it is an example of a gradient-free algorithm. In fact, the optimization function only has to be evaluable, not requiring a closed form mathematical expression. On the other hand, the meta-heuristic character of the algorithm does not guarantee convergence to a global optimum and, in fact, misconvergence to local optima is a common problem[181]. The latter has been confirmed by this work, where highly coupled parameters and the periodic nature of complex exponentials is believed to lead to formation of many – often rather broad – minima, leading to an increased likelihood of the algorithm converging prematurely. A meta analysis of the convergence behaviour of the differential evolution algorithm for a particular geometry of patterned arrays will be presented in section 5.4.2.

Mutation and Recombination Operations

This section will begin by providing a short discussion of the most commonly used implementation of the mutation and recombination operations, as originally proposed by Storn and Price[181]. However, many variants to these basic implementations exist, each sharing common principles. Later on, a couple of these variants will be briefly touched upon, but the following basics provide a good idea of the working principles.

In order to create a member t_i of the trial population T, a mutation vector m_i is created, which is then partially recombined in its parameters $m_{i,\mu}$ with a subset of parameters $p_{i,\mu}$ taken from exactly one p_i, the latter being a unique parent vector for every trial vector. In this way t_i represents a combination of *mutated* and *parent* parameters.

Each mutant vector is created by

$$m_i = p_j + F\,(p_k - p_l), \qquad i \neq j \neq k \neq l, \tag{3.12}$$

where

$$F \in [0, 2]$$

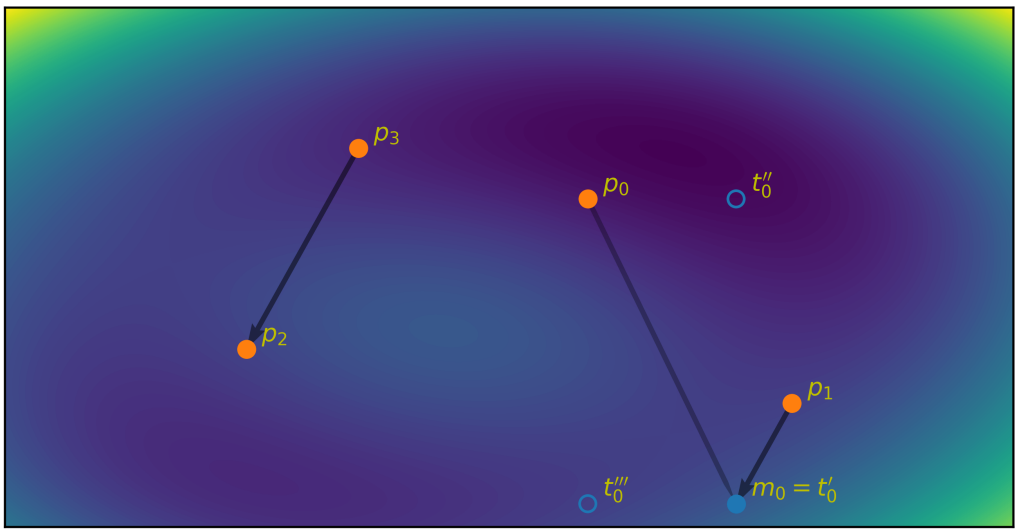

Figure 3.9: Example of mutation and recombination operations on a population of size $N = 4$. The scaled difference vector $F(p_2 - p_3)$, with $F = 0.5$, is added to base vector p_1, creating the mutant m_0. Recombination in the two-dimensional parameter space leads to the three possible trial vectors t'_0, t''_0, and t'''_0, competing against the parent vector p_0.

denotes the *differential weight* of the mutant, therefore being a scaling factor of the difference vector.

Recombination of m_i and p_i is performed for each parameter i individually, the μ^{th} parameter of t_i given by

$$t_{i\mu} = \begin{cases} m_{i\mu} & \text{if } r < CR \\ p_{i\mu} & \text{otherwise} \end{cases} \tag{3.13}$$

where

$$CR, r \in]0, 1]$$

denotes the *crossover probability* and a random number generated for every parameter μ, respectively.

Both processes are visualised in Fig. 3.9 considering the minimum number of parameter vectors, p_0, p_1, p_2, p_3, satisfying the index condition of eq. 3.12 and a single trial vector t_0. In this example, the mutant m_0 is given by a scaled difference vector $p_2 - p_3$, attached to the base vector p_1. By definition, the member of the current population p_0 competes against the trial vector t_0, which has to be one of $[t'_0, t''_0, t'''_0]$. After the recombination process, the latter generally shares at least one

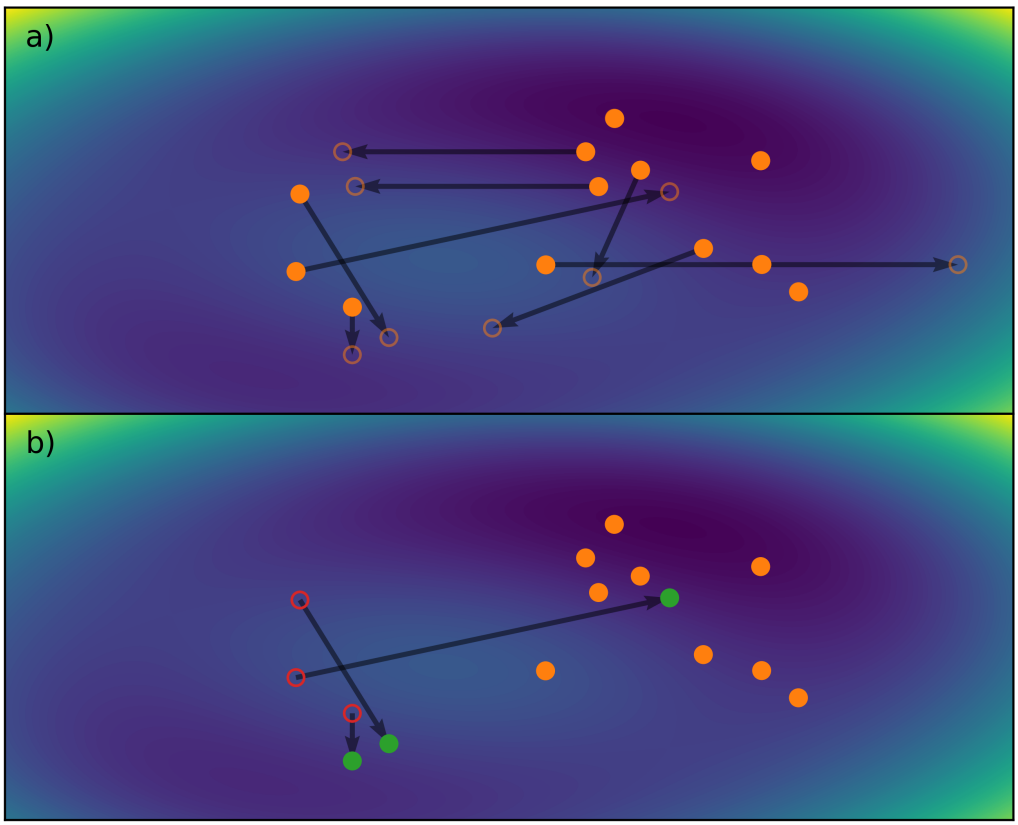

Figure 3.10: Visualisation of a single evolutionary step. Panel a) depicts a full population P^g of size $NP = 12$ by using filled circles. The trial population T^g is indicated by empty circles. Each population member p_i is associated with exactly one trial vector t_i as indicated by the arrows. Panel b) presents the new population after the generational step. Green filled circles represent trial vectors, which succeeded against their corresponding parent vectors, the latter being depicted by empty red circles. Filled orange circles represent population members that survived the comparison to their trial vectors (the latter not shown for clarity).

vector component – or gene – with m_0 and at most $N - 1 = 1$ (since the system is two-dimensional, $N = 2$) vector components with p_0. For higher dimensional parameter spaces the number of possible recombinations is 2^D and therefore the number of unique trial vectors $t_0^{(\mathrm{n})}$ will be obviously much greater.

The color coding of the surrounding figure of merit indicates that t_0'' would be promoted to next generations starting population P^{g+1}, whereas t_0' and t_0''' present no improvement over p_0, meaning the latter would remain in the population. Further, Fig. 3.10 presents a simple example of a single evolutionary step, visualising in panel a) the sets P^g and T^g as well as the new population P^{g+1} in panel b).

Variants of Differential Evolution Strategies

The exact way the trial population T is generated from the original population P is only loosely specified, and a multitude of common mutation- and recombination mechanisms exist[182–185], which are generally denoted by a string of the format "base vector/number of difference vectors/recombination scheme". Following this notation, some of the most used examples amongst the originally proposed schemes by Storn and Price include "Best1Bin", "Rand1Exp", "currentToBest1Bin", "Rand2Bin", etc. For instance, strategies starting in either "Best", or "Rand" use a base vector chosen to be either the current best or a randomly chosen vector of the original population, while strategies ending in "Bin" or "Exp" use either a binary or exponential crossover scheme, both being defined later in the text on page 82.

The **Choice of the Base Vector** in the original implementation by Storn and Price [181] regarding each trial vector t_i is that it is randomly taken from P. Alternatively, a popular variant consists in always using the best-so-far population vector p_{best} as base vector for every t_i, both being visualised in Fig. 3.11. Obviously, choosing the base vector randomly results in a much broader search radius. The latter often comes at the cost of slower convergence since much of the sampling occurs far away from the current optimum, where the probability of finding improvements is low. However, changes are that the global optimum might indeed lie far away from the currently best population member $p_best = p_0$, in which case the broader search radius helps in preventing misconvergence. Hence, eq. 3.12 actually refers to a "*Rand*/number of difference vectors/recombination scheme" strategy, whereas in case of a *Best* strategy p_j is replaced by b_{best} in eq. 3.12. It has been found[186] that for most optimisation problems commonly encountered, always choosing the best-so-far candidate significantly outperforms random choice of base-vectors.

The **Number of Difference Vectors** in the original differential evolutions implementation was taken to be one. That means that the mutant m_j is generated by adding a single difference vector $F(p_k - p_l)$ to the base vector p_{base}, as for example seen in eq. 3.12. However, the search space can be further increased by adding a *second difference vector* to the mutant. An example of the latter is the Best2Bin implementation given by

$$m_i = m_{\text{best}} + F(m_1 - m_2) + F(m_3 - m_4), \tag{3.14}$$

with $i \notin \{1, 2, 3, 4\}$.

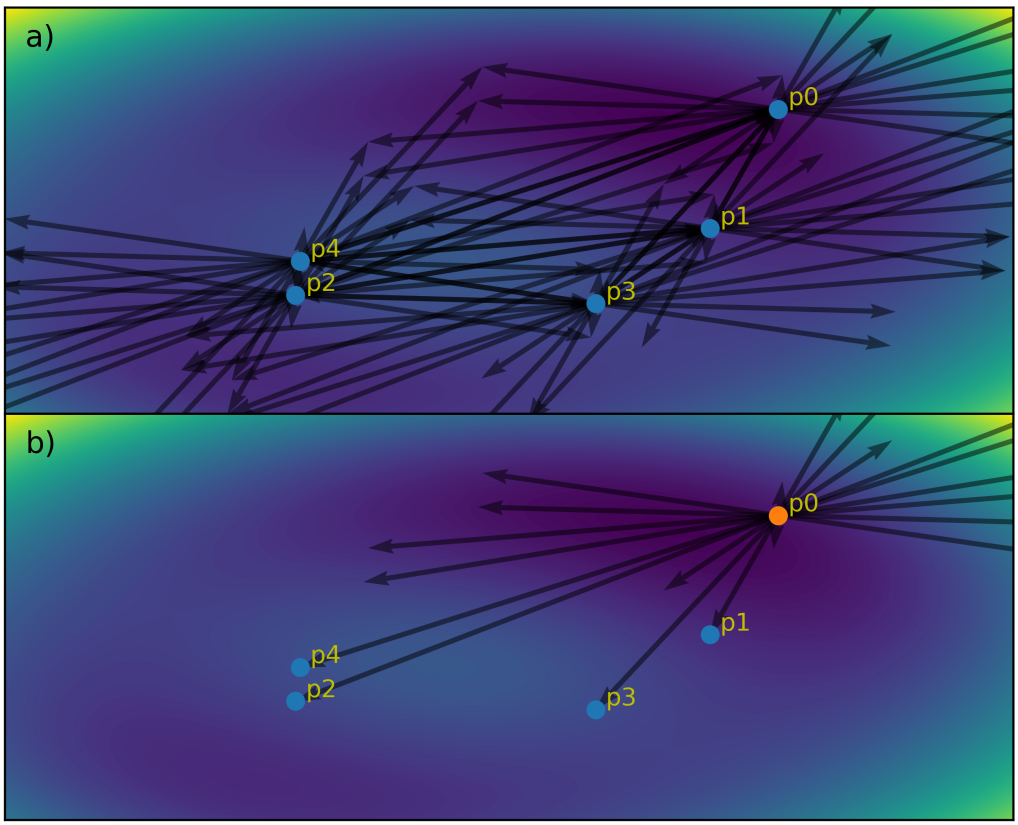

Figure 3.11: Difference in search space according to choice of base vector of population of size $NP = 5$ and $F = 1$. The search space depicted in Panel a) covers most of the parameter space since every population member may be used as a base vector for trial candidate creation. In contrast, the search space depicted in panel b) results from considering the best-so-far candidate p_0 as the only choice for a base vector and is spatially much stronger confined. Generally, the two schemes compromise robustness against optimisation speed and vice versa.

The **Crossover Scheme** determines the exact mechanism the parameters of the mutant and parent vector are being recombined. Eq. 3.13 provides an example of *binary recombination* since for each μ it is a random and independent binary choice, deciding whether the parameter is taken from the parent or mutant vector. The latter naturally leads to a binomial distribution of the number of parameters which are taken from either mutant or parent.

Another popular – and indeed the originally proposed – mechanism is *exponential crossover*, in which a randomly chosen index d acts as a starting point from where the following n parameters are taken from the mutant, whereas the remaining parameters are taken from the parent vector. The number n is again chosen accord-

ing to the crossover rate and dimensionality of the problem $n = CR\,D$. Because of its dependence on the ordering of parameter axes, exponential crossover suffers from a *representational bias*[187], which led to binomial crossover being favoured in this work.

Mutation/Recombination hybrids may improve convergence efficiency further for some problems. In these variants the base vector p_{base} may already consist of a mutated difference vector, as, for instance, in the *CurrentToBest* scheme given by $m_i = p_i + F(p_{\text{best}} - p_i) + F(p_1 - p_2)$.

In this case, instead of choosing p_{best} as a base vector, for every population member p_i a unique base vector specific (i.e. including no randomised component) to p_i is calculated, pointing from p_i in direction of p_{best}, to which a randomly chosen difference vector is added. This approach is spatially less confined compared to always choosing $b_{\text{base}} = p_{\text{best}}$, since the centre of the search is spread wider through parameter space, while at the same time ensuring a tendency towards the best-so-far individual, provided that $F < 1$.

Dithering and **Jittering**[186, 187] may introduce additional flexibility to the mutation process, somewhat alleviating problems with high sensitivity towards the (often unknown) optimal mutation rate control parameter.

In case of *dithering*, the mutation control parameter is a variable, and takes on a new random value, usually in the range $[0.5, 1]$, for every trial vector t_i. This leads to a more robust (although sometimes slower) convergence, since the momentary state of the optimisation may demand either a wide or small search radius, both of which are randomly employed. Dithering is usually denoted by subscripting the mutation control parameter, F_i, with the running population index. In other variants, the F_i was decreased linearly as the optimisation proceeded[183, 188], ensuring a wide search radius at an explorative phase at the beginning, while having a refined search radius during the exploitative phase when the population resides near the global optimum towards the end of the optimisation process.

Jittering, on the other hand, randomly varies the mutation parameter for every *parameter* of each trial vector, therefore not only rescaling the difference vector, but also rotating it since the scaling varies along each parameter axis. Jittering is usually indicated by subscripting F_μ with the running parameter index. Jittering can significantly speed up convergence by requiring fewer function evaluations of the FOM, by means of demanding a lower or similar population size compared to *dithering* or classical differential evolution, respectively. It has, however, been found to perform poorly for non-separable FOM function of highly interdependent

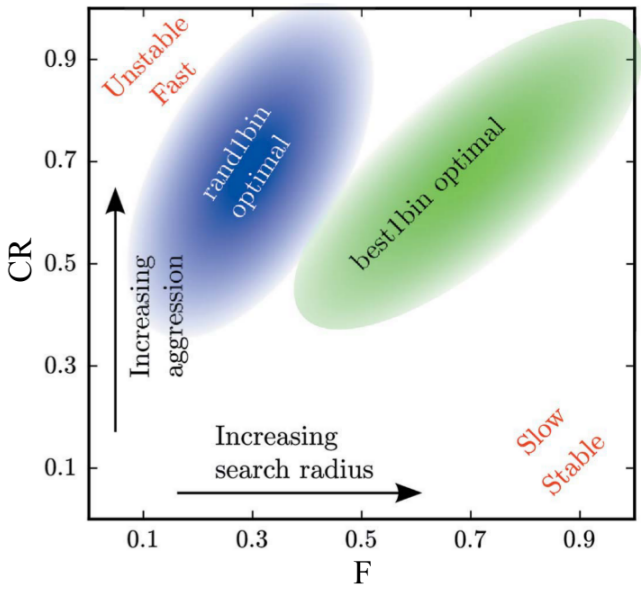

Figure 3.12: Optimal control parameters for optimisation of a 15-dimensional x-ray reflectivity problem for strategies Best1Bin and Rand1Bin. Adapted from [189].

parameters[187]. Since the latter is true for x-ray diffraction of patterned arrays, no jittering has been applied in the context of this work.

Finally, many authors give recommendations for the choice of the control parameters NP, F, and CR. In their original work, Storn and Price [181] propose the general use of values of NP between $5D$ and $10D$, depending on the dimensionality D of the parameter space. Further, they propose the use of $F \approx 0.5$, while noting that values of $F < 0.4$ and $F > 1$ are only rarely found to be effective choices. The crossover rate CR, according to Storn and Price, is not necessarily very important, and values within the range $0.1 < CR \leq 1$ may all lead to good results.

Björck [189] found that for x-ray reflectivity of layered systems of dimensionality $D = 15$, a good choice of population size is around $3D$ to $4D$ with optimal values of F and CR being shown in the two-dimensional parameter space shown in Fig. 3.12.

Das and Suganthan [186], on the other hand, argue that NP should generally lie between $3D$ and $8D$, while $0.4 < F < 0.95$, with a tendency towards the higher end of this range. They further advice $0 < CR < 0.2$ for uncoupled systems, while $0.9 < CR < 1.0$ ought to be a good choice for highly coupled parameter spaces.

More suggestions for the choice of control parameters exist[182–184, 190, 191], with the conclusions often being inconsistent if interpreted with generality. It rather appears that the optimal control parameter strongly depend on the individual

problem and general advice is not easy to give, with the likely exception that most sources agree that high crossover rates CR are strongly beneficial for problems that suffer from strong coupling of open parameters. An analysis estimating the optimal control parameters for the patterned arrays concerned with in this work will be given in section 5.4.2.

3.5 Summary

In this chapter the fundamental techniques related to investigation of patterned arrays were presented. The discussion followed the general chronology of the process of investigation, starting with the patterning of the sample, followed by the experimental measurement, and finally ending with fitting a simulated signal to the experimentally obtained data.

The first section of the chapter revolved around the patterning of micro- and nanoscopic elements, putting focus on the different processes utilised for creating the in-plane and out-of-plane structure of a sample. It was shown how the out-of-plane structure is mainly determined by the material deposition technique used, while the in-plane structure is usually obtained by some form of lithographic patterning process. Pre- and post-patterning processes refer to whether the lateral structure is imprinted on the surface before or after the material comprising the array is deposited on the sample.

Following, the specific patterning routines of all samples used in the context of this work were discussed, putting particular focus on the unintended crowning observed in the case of pre-patterned samples. The latter was identified to be the source of an interesting, yet unintended, modulation of the x-ray scattering cross section of the sample affecting a large part of the subsequent data analysis following in the coming chapters. In order to avoid unintended doming, it is advised to rather use a post-patterning process for sample creation. Post-patterning preserves the high quality of the out-of-plane chemical structure obtainable by common material deposition techniques of stratified media, which, for completeness, has been included in the discussion as well.

Section 3.3 then focussed on the characteristics of synchrotron radiation and how it is has been exploited in the context of this work. Further, it was discussed how the two main types of scans through reciprocal space used in this work, specular reflectivity and rocking curves, are used in order to gain quantitative information about the sample. While x-ray reflectivity probes the average SLD depth profile of a sample, rocking curves are sensitive to its lateral structure.

Finally, section 3.4 presented the basics of differential evolution, which comprises an optimisation strategy analogous to biological evolution. This approach allows the resolution of the chemical- and magnetic structure of a sample through a process of iterative adaptation of a series of parameters describing the physical properties of a sample in order to match simulated- to experimental data.

Chapter 4

Diffraction of Patterned Arrays in the Low X-Ray Coherence Limit

One of the distinct characteristics of nano-patterned arrays is that the typical structure size of the repeating unit often exceeds atomic length scales by multiple orders of magnitude. Typically, lithographically patterned mesocrystals obtain lattice parameters of hundreds up to thousands of nanometres as opposed to atomic crystals, whose lattice parameters are in the orders of Ångströms, leaving a factor of about 1000-10 000 between both length scales. Despite the fact that the general mathematical treatment is unaffected by the absolute length scales in a diffraction problem, the much smaller sizes of atomic lattices usually allow for certain approximations, which are often not valid in the case of patterned arrays. Generally, the determining factors for what approximations may be applied to obtain the correct solution to a diffraction problem in an efficient way depend mainly on the ratio between the (super)structure's lattice parameters, structural correlation length, total crystal size and the coherence volume of the illuminating radiation, which will be defined more precisely in the following.

In this chapter the classical solution to a diffraction problem will be reformulated mainly considering the interplay between lattice parameters and the coherence length of the radiation and it will be shown how the formalism has to be adapted to give correct results in the particular case of the beam coherence being *smaller* than the typical length scale of the array, a scenario which is rather uncommon in atomic diffraction or diffraction of one-dimensional mesostructures but can easily become important in two-dimensional patterned structures.

The theory will then be applied to the case of modelling Q_z and Q_x scans of a patterned array of a multi-element unit cell, finding that low-coherence theory has to be applied in order to be able to fit experimental data.

4.1 Theoretical and Experimental Considerations regarding coherence and resolution

4.1.1 Limits of diffracted intensity

A fully coherent radiation source like, for instance, a laser[192, 193], means that a distinct phase relationship between all points of the electromagnetic wave field exists. In this case, the phase difference $\Delta\phi$ of any two points $\mathbf{r}_1$ and $\mathbf{r}_2$ of the wave field depends only on their spatial separation $\Delta\mathbf{r}$.

If, on the other hand, the source is only partially coherent, $\mathbf{r}_1$ and $\mathbf{r}_2$ may lose this well-defined relationship and interference effects become less pronounced[96, 194]. The effect of decorrelation usually gets amplified with increasing spatial separation, meaning that the phase differences of the electromagnetic wave at the two positions are increasingly randomised the further they are separated from each other[195, 196]. Randomisation of phase differences then generally implies the reduction of averaged sums of amplitudes and hence the disappearance of interference effects[197].

Typical x-ray sources are in fact only partially coherent[96, 198], meaning that generally only a limited part of the sample will scatter coherently. The coherently scattering part of the sample is then given by the *coherence volume*[83, 91] over which a certain phase correlation of the incident wave field was maintained. The exact shape of the coherently scattering volume generally depends on the type of source and experimental geometry, but will in many cases be modelled adequately by an ellipsoid[198].

Since stratified media can generally be considered ergodic, their laterally averaged SLD profile is identical to their local depth profile at any given sample position. Hence, the effectively one-dimensional nature of these systems requires x-rays to be phase coherent only along the sample normal at any surface position. These conditions are usually fulfilled and implicitly assumed in performing, for instance, reflectivity measurements.

In atomic crystallography, the Å-level length scale of atomic lattices is the reason that a diffraction experiment can be carried out without explicit consideration of source coherence, as coherent illumination of a sufficiently large sample

volume is considered implicitly in common diffraction techniques, meaning all relevant (statistical) sample properties are covered[62].

Generally, the electric field amplitude of an x-ray beam decorrelates between two points in space because of either finite beam divergence or imperfect monochromaticity[55, 198]. Conversely, this means that *any* point in space (including any point of the sample) is surrounded by a finite coherence volume, over which at least a partial phase correlation of the electric field is retained[91]. Hence, every part of the sample contributes a coherently scattered amplitude, which is the coherent superposition of the waves scattered by its surrounding area, each point of which is weighted by the locally retained amount of phase correlation. In this way, coherently scattered amplitudes corresponding to every point on the sample surface are then integrated up *incoherently* over the entire sample, i.e. added by *intensity*.

In x-ray diffraction, the thickness of a scattering structure is usually so small that decorrelation of the wave field can safely be neglected in this direction, since the penetration depth of the radiation is usually less than the coherence length perpendicular to the sample surface. Instead of referring to a coherence *volume* it may then be adequate to refer to the *coherence area* of a sample, which is to emphasize that the decorrelation of the wave field mainly happens within the sample plane. Sometimes the coherence area is more specifically referred to by the term *coherence ellipse*, which is due to the fact that, for reasons discussed in section 4.1.2, the coherence area is found to be elongated along the projection of the incident beam onto the sample surface[198].

The measured intensity in a diffraction experiment is typically considered in reciprocal space as a function of the wavevector transfer $\mathbf{Q} = (Q_x, Q_y, Q_z)$, which is the conjugate variable of the real space positional vector $\mathbf{r} = (x, y, z)$. The mathematical formalism connecting real- to reciprocal space under Fraunhofer diffraction conditions[57, 96, 199] and considering the classical scattering from electrons as given by the Fourier transformation of the scattering length density (SLD) in real space, within the coherence area. The mathematical treatment of the problem can often be significantly simplified by describing the sample and its coherently scattering area in terms of multiplications and convolutions of objects which are easier to describe separately than the complete system all at once, as was introduced in section 2.4.

From the discussion so far, it is clear that in order to be able to describe a diffraction phenomenon, knowledge of the phase relation between scattering objects is critical. However, these phase relations are not exclusively restricted to decorrelation of the electrical field only. Spatial decorrelation of the physical *structure* of

a periodic system may lead to similar effects as limited coherence of radiation[75, 102, 180]. In this case it is the probability of the *presence* of a scatterer separated by $\Delta\mathbf{r}$ relative to $\mathbf{r}$ that determines the strength of interference, rather than the probability of phase alignment of the E-field at the two positions.

Mathematically, the effects of decorrelation of the electric field amplitude and of structural decorrelation of the scattering structure are identical and the type of decorrelation occurring at smaller length scales is usually the dominant one. In any case, the *correlation length* ξ is the average distance over which amplitudes instead of intensities are added and it is given by the smaller of the beam coherence length or the structural correlation length of the sample.

In the case of patterned arrays obtained from electron beam lithography the structural correlation can be safely assumed to be much larger than the typical x-ray coherence length. However, many examples exist where the outcome of a diffraction experiment is governed by sample properties. For instance, self-assembled nanoparticles often form grains of perfect hexagonal order, but are separated by grain boundaries effectively randomising the lattice orientation of neighbouring grains[116, 137]. The typical grain size is often found to be of only tens to hundreds of nanometres in diameter, which is very likely to be smaller than the coherence length of any impinging radiation. Another example is the investigation of magnetic correlations within artificial spin ice[42], which potentially span only a very short distance.

4.1.2 Coherence of Radiation and Resolution in Reciprocal Space

Finite beam coherence is a result of the gradual dephasing of x-ray wave trains in space, which are for now visualised by restricting to only the real part of a complex wave to read[194]

$$A(k) = P(k)\ \mathrm{Re}(\mathrm{e}^{-i(kx+\Delta\phi)}) = P(k)\ \cos(kx + \Delta\phi). \tag{4.1}$$

Depending on the properties of the beam, each wavetrain is associated with a spectral Power coefficient $P(k)$, which represents the amplitude of a wave train of wavevector k. Wave trains which share a distinct phase relation $\Delta\phi$ at a particular point in space will dephase as a result of a misfit Δk with respect to their mean wavevector modulus $k_0 = |\boldsymbol{k}_0|$.

Fig. 4.1 a) shows a schematic of the amplitudes of a series of wave trains following the (Gaussian) Power spectrum

$$P(k) \propto \exp(-\frac{(k-k_0)^2}{2\sigma_k^2}), \tag{4.2}$$

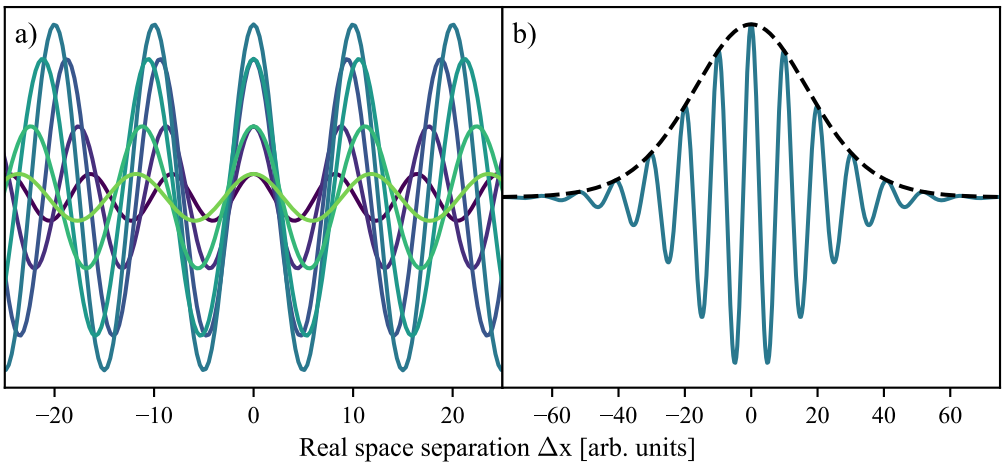

Figure 4.1: Real space dephasing of plane waves in dependence of varying wavenumbers k and amplitude $\exp\left(\frac{-(k-k_0)^2}{2\sigma_k}\right)$. In panel a) all waves are in phase at point separation point $x = 0$ and will gradually lose their phase relation with increasing $|x|$. The solid line in panel b) shows the normalised integral over all k as a function of real space separation x. With increasing $|x|$ the integral gets progressively smaller as the sign of the waves starts fluctuating more and more. The dashed line represents the amount of phase correlation and represents the coherence function Γ of the radiation.

which all share the same phase at the origin of the x-axis, with the variance σ_k^2 determining the spread of k around k_0. This implies that the amplitudes of waves decrease if they are stronger misaligned with k_0. It is evident that at a larger distance from the origin the phase alignment of all wavetrains gets progressively worse until all waves effectively inhibit a random phase for large separation Δx.

Integrating the wave trains over all k

$$\Gamma(x) = \int \exp\left\{-\frac{(k-k_0)^2}{2\sigma_k^2}\right\} \mathrm{Re}(\exp\{-i(kx+\Delta\phi)\})\,\mathrm{d}k \tag{4.3}$$

results in the solid curve of Fig. 4.1 b), which effectively accounts for addition of all plane waves being of phase ϕ at a distinct point in space and obeying the power spectrum given by equation 4.3. As can be seen in Fig. 4.1 b), the coherent summation leads to an oscillating function, where the diminishing maxima are indicative of the dephasing of increasingly distant wave peaks.

In case of a complex wave $P(k)\,\mathrm{e}^{-ikx}$ integration over all k and restricting to the modulus of the result leads to the dashed curve of Fig. 4.1 b). A spread in the wavevector modulus Δk determines the phase decorrelation – and hence the

coherence length of the radiation, which is identified as $\xi = \frac{1}{\sigma_k}$ in the following – as a function of real space separation Δx around an arbitrarily chosen point. Therefore, small values of σ_k imply a large coherence length ξ in real space, and vice versa.

A variance in Δk *along a particular direction* is not exclusively limited to a spread in the wavelength of the radiation, but may as well – and often more importantly – be the result of a diverging beam. In the latter case, it is more precise to use the notation $\Delta\mathbf{k}$, indicating the vector characteristic of $\mathbf{k}$ and that decorrelation of the radiation is a result of projecting wavevectors $\mathbf{k} = \mathbf{k}_0 + \Delta\mathbf{k}$ of identical modulus k but differing directions onto the nominal direction $\mathbf{k}_0$.

The spectral purity $\Delta\lambda/\lambda$ of the beam determines the coherence of the radiation *parallel* to its propagation direction and is hence called *longitudinal coherence* or *temporal coherence*. Two points along a given ray of the beam will be illuminated coherently only if their separation is less then the length it takes for the radiation to decorrelate due to imperfections of the monochromaticity of the beam. Identifying the longitudinal coherence $\xi_{\mathrm{t},0}$ of the radiation along a given angle α as the Gaussian standard deviation σ_λ we find [90]

$$\xi_{\mathrm{t},0} \approx \frac{\lambda}{2}\frac{\lambda}{\Delta\lambda}. \tag{4.4}$$

In a typical experiment using a silicon single crystal monochromator typical values of the spectral purity are in the order $\Delta\lambda/\lambda \approx 10^{-4}$[62, 200], which means that for soft x-rays of $\lambda \approx 0.5\,\mathrm{nm}$ the longitudinal coherence length of the x-ray beam is in the order $\xi_{\mathrm{t},0} \approx 10^3\mathrm{nm}$.

The second contribution affecting the beam coherence is the dephasing of wave trains *perpendicular* to $\boldsymbol{k}$ due to an angular divergence $\Delta\alpha$ of the beam, which is named the *lateral coherence* or *spatial coherence* and is given by[55, 198]

$$\xi_{\mathrm{s},0} \approx \frac{\lambda}{2\Delta\alpha}. \tag{4.5}$$

Typical values for the beam divergence are in the order $\Delta\alpha \approx 10^{-3}\mathrm{mrad}$[68, 75, 80, 179], which results in spatial correlation of a typical x-ray beam of about $\xi \gtrsim 10^3\mathrm{nm}$

The quantities of interest in a scattering experiment are, however, the projections of $\xi_{\mathrm{t},0}$ and $\xi_{\mathrm{s},0}$ onto the sample surface, which are consequently given by

$$\xi_{\mathrm{t}} = \frac{\xi_{\mathrm{t},0}}{\cos\alpha} \tag{4.6}$$

and

$$\xi_{\mathrm{s}} = \frac{\xi_{\mathrm{s},0}}{\sin\alpha}. \tag{4.7}$$

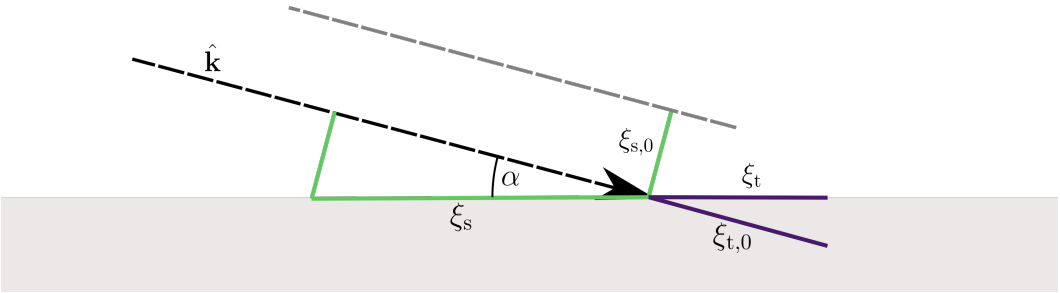

Figure 4.2: Projections of the temporal- and lateral coherence lengths, ξ_t and ξ_s, onto the sample surface. Because of the $1/\sin\alpha$ dependence, under grazing incidence geometry the total coherence length will be strongly dominated by the lateral coherence length ξ_s.

As can be seen from eq. 4.7 and Fig. 4.2, ξ_s can become very large for a grazing incidence geometry and hence this term often dominates the coherence area on a sample, while ξ_t will generally be of the same order of the lattice pitch of the samples discussed in this chapter. The inverse sine of the incident angle α_i and its effect on ξ_s is found to be the main reason for the high ellipticity of the coherence area.

It should be noted that not only the radiation *source* determines the amount of coherence in a scattering experiment, but eqs. 4.4 - 4.7 equally hold for the *detector* geometry. This can easily be understood when interpreting the coherence area of a sample as the distance on a sample over which a (random) fixed phase relation emitted from two points on the sample will be maintained until the radiation reaches the detector.

In total, the projected beam coherence onto the sample surface is given by[55, 198, 201]

$$\begin{aligned}\xi_{\text{total}} &= \xi_{\text{s,source}} + \xi_{\text{s,detector}} + \xi_{\text{t,source}} + \xi_{\text{t,detector}} \\ &\approx \frac{\lambda}{2}\left(\frac{1}{\Delta\alpha_i \sin\alpha_i} + \frac{1}{\Delta\alpha_f \sin\alpha_f}\right) + \frac{\lambda^2}{2\Delta\lambda}\left(\frac{1}{\cos\alpha_i} + \frac{1}{\cos\alpha_f}\right)\end{aligned} \tag{4.8}$$

Applying Gaussian superposition to each coherence component leads to an effective width of the coherence area of

$$\sigma_{\text{total}} = \sqrt{\left(\frac{\sigma_{\text{s,source}}}{\sin\alpha_i}\right)^2 + \left(\frac{\sigma_{\text{s,detector}}}{\sin\alpha_f}\right)^2 + \left(\frac{\sigma_{\text{t,source}}}{\cos\alpha_i}\right)^2 + \left(\frac{\sigma_{\text{t,detector}}}{\cos\alpha_f}\right)^2} \tag{4.9}$$

along the impinging beam direction.

Note that in grazing incidence geometry, where the angles are of the order of one degree or less, the $1/\sin\alpha$ dependence of the lateral coherence component

usually dominates and is strictly a function of $\alpha_{i,f}$, meaning that the coherence area on the sample varies as a function of the relative positions of source and detector. Although reasonable estimates for $\Delta\lambda/\lambda$ and the divergence of the incoming beam from the known optical elements in the beamline can be made, they should be determined separately for each instrument used. The effect of changing instrumental parameters upon the beam coherence will be discussed in more detail in chapter 6.

4.1.3 Detector Resolution in Reciprocal Space

As was shown in the previous section, the coherently scattering area of a sample depends on the spectral purity of the radiation and the divergence of the incident and scattered radiation. However, in order to describe the measured intensity in a scattering experiment it is necessary to consider the *resolution* of the detector.

The detector resolution describes the area in reciprocal space a given detector integrates over and depends on the scattering angles (or, equivalently, wave vectors) the detector accepts at a given nominal detector angle α_f. In other words, a detector of a given angular acceptance will simultaneously be exposed to a range of wave vector transfers $\boldsymbol{Q} = (\boldsymbol{k}_f + \Delta\boldsymbol{k}_f) - (\boldsymbol{k_i} + \Delta\boldsymbol{k}_i)$, over which it is integrating, therefore limiting its resolution. In this definition $\Delta\boldsymbol{k}_{i,f}$ represents a vector distribution perpendicular to the source and detector beams $\boldsymbol{k}_{i,f}$.

The resolution element is intrinsically a three-dimensional object in reciprocal space and later on in this section the importance of the detector integrating perpendicular to the scattering plane (along ν as seen in Fig. 3.7) will be discussed in detail. The latter leads to a finite (and in fact often very considerable) width of the resolution element in Q_y. However, the extent of the detector resolution in Q_y does not change with varying angles α_i and α_f and will therefore not be concerned in detail in this section, but it should be remembered that the following discussion implicitly assumes the integration over a more or less (depending on the detector size and slit geometry) wide Q_y range.

Mathematically, in a diffraction experiment, the measured intensity is the convolution of the probed reciprocal space and the detector resolution function[55, 80, 198, 201]

$$R(\Delta\alpha_i, \Delta\alpha_f).$$

The resolution function, however, is given by the convolution of wave vector spreads $\Delta\boldsymbol{k}_i$ and $\Delta\boldsymbol{k}_f$ of the source and detector beams[90, 198]. Since usually[62] $\Delta\lambda/\lambda \ll \Delta\alpha/\alpha$ it is justified to neglect non-monochromaticity of the beam. Assuming Gaussian beams for both source and detector, the resolution function R as

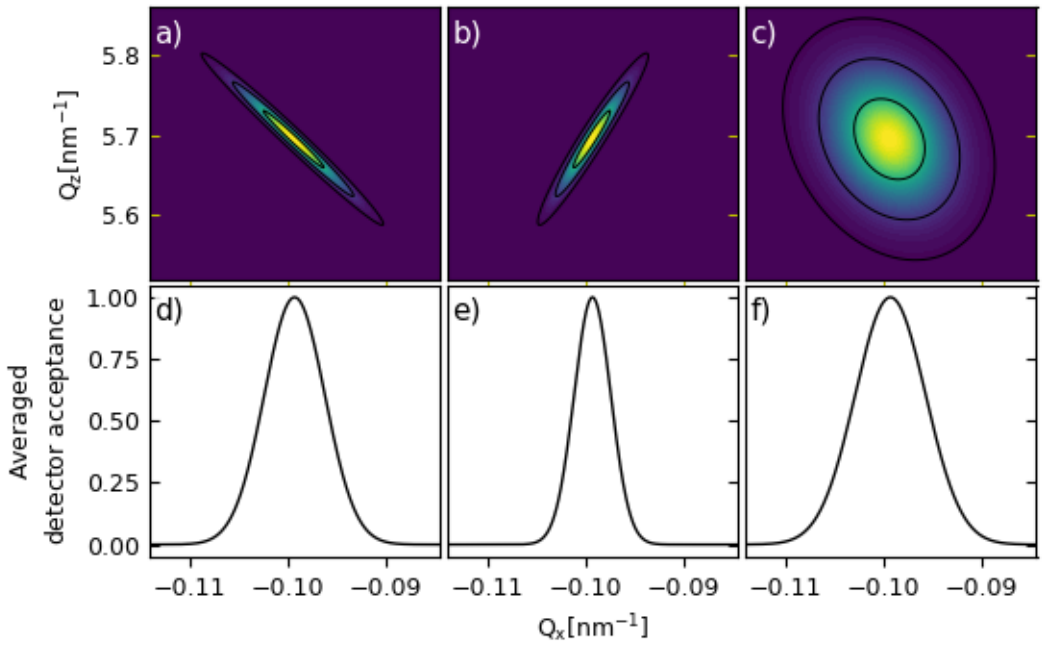

Figure 4.3: Resolution elements in reciprocal space probed by a diffractometer as a function of beam divergences on the source- and detector side of the experiment. The beam divergences were assumed to be of the form a Gaussian standard deviation. Values used were, panel a): $\Delta\alpha_i = 0.005°, \Delta\alpha_f = 0.05°$, panel b): $\Delta\alpha_i = 0.05°, \Delta\alpha_f = 0.005°$, panel c): $\Delta\alpha_i = 0.05°, \Delta\alpha_f = 0.05°$. Panels d) - f) show the projection of the resolution elements onto the Q_x axis.

a function of angular divergence $\Delta\alpha_i = \sigma_i$ and $\Delta\alpha_f = \sigma_f$ (representing standard deviations) of the incident and detected beam is given by

$$R(\Delta\alpha_i, \Delta\alpha_f) = \left(\exp\left(-\frac{(\alpha_i - \alpha_{i,0})^2}{2\Delta\alpha_i^2}\right) k \sin\Delta\alpha_i\right) \otimes \left(\exp\left(-\frac{(\alpha_f - \alpha_{f,0})^2}{2\Delta\alpha_f^2}\right) k \sin\Delta\alpha_f\right). \quad (4.10)$$

The three upper panels of Fig. 4.3 show resolution elements corresponding to a typical rocking scan of patterned arrays as performed in this thesis, assuming a detector angle $2\theta = 8°$. All the plots in Fig. 4.3 are calculated at $\alpha_i = 3°$ and $\alpha_f = 5°$ but assume varying angular divergence for the incident and exit beams. The resolution elements of panels a) to c) in Fig. 4.3 correspond to the cases $\Delta\alpha_i < \Delta\alpha_f$, $\Delta\alpha_i > \Delta\alpha_f$ and $\Delta\alpha_i \approx \Delta\alpha_f$. Fig. 4.3 d) to f) shows an approximate projection onto the Q_x-axis of the respective resolution elements obtained from a Gaussian

superposition of $\Delta\boldsymbol{k}_i$ and $\Delta\boldsymbol{k}_f$ which for the Q_x- and Q_z-directions read

$$\Delta Q_x = k\sqrt{\Delta\alpha_i^2 \sin^2\alpha_i + \Delta\alpha_f^2 \sin^2\alpha_f} \tag{4.11a}$$

$$\Delta Q_z = k\sqrt{\Delta\alpha_i^2 \cos^2\alpha_i + \Delta\alpha_f^2 \cos^2\alpha_f}. \tag{4.11b}$$

It is often convenient to simplify the problem of resolution convolution to a one-dimensional case by using eq. 4.11 a) as the resolution function. The latter is justified if the rate of change of intensity in reciprocal space over ΔQ_x is much greater than the change over ΔQ_z. The latter is often the case for grating truncation rods found in off-specular diffraction, which (after convolution with R) show a Gaussian profile along Q_x depending on the scattering correlation length but can be considered constant in intensity over the Q_z range the detector is integrating over[54, 87, 101].

If, however, the detector acceptance $\Delta\alpha_f$ is wide and the detector acceptance window intercepts the GTR at considerably differing Q_z values, then the convolution of the whole resolution element is required (using eqs. 4.11 a and b), taking into account the variation of intensity along the GTR. The latter quickly gets computationally expensive when confronted with the task of fitting experimental data. This is particularly true for an open detector set-up, where no exit slit is present in front of the detector. This is a problem discussed in more detail in Chapter 5.

A related phenomenon often witnessed in off-specular diffraction experiments is an angle sensitivity of the satellite peak width, which most often manifests in the form of peak broadening with increasing detector angle $\alpha_f = 2\theta - \alpha_i$, which might be confused for a reduction of beam coherence leaving to similar effects. The reason, however, is the inclination of the detector resolution element in combination with a large angular detector acceptance $\Delta\alpha_f$ as seen in Fig. 4.4. The latter can also be seen from inspection of eq. 4.11 a) in the limit $\Delta\alpha_i < \Delta\alpha_f$. At low detector angles, the total acceptance of the detector effectively consists of a vertical sheet in reciprocal space, leading to progressively worse resolution as the detector angle α_f increases and, equivalently, Q_x decreases.

In the simplified case of considering the Q_x projection of the resolution element only, the intensity at position $Q_{x,0}$ in reciprocal space defined by a particular set of nominal source and detector angles α_i and α_f, respectively, is given by the integral of the squared amplitude over the detector acceptance

$$I(Q_{x,0}) = \int_{-\infty}^{\infty} A(Q_x)A^*(Q_x)\,\mathrm{d}Q_x, \tag{4.12}$$

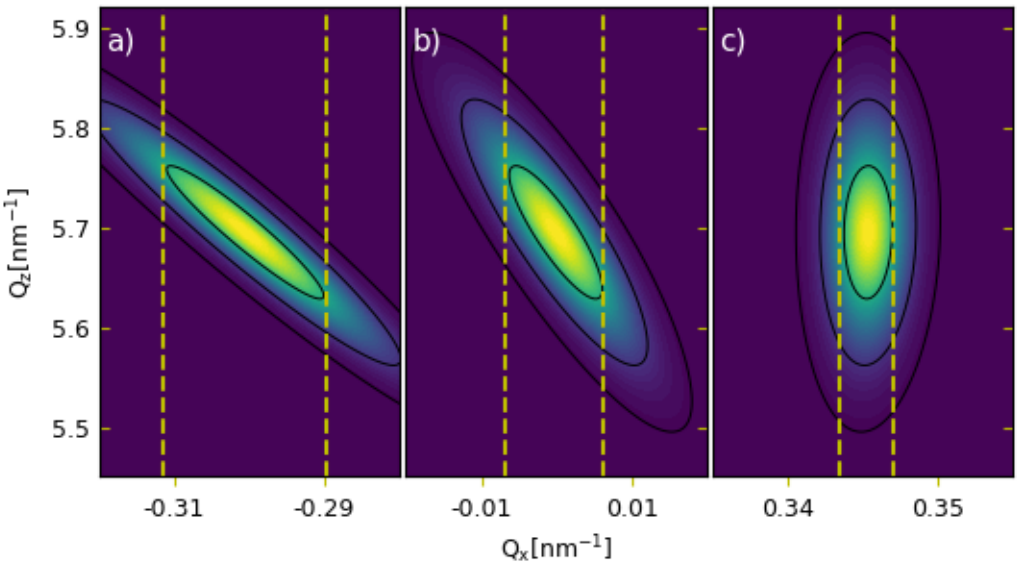

Figure 4.4: Angle dependency of resolution elements at fixed beam divergences $\Delta\alpha_i = 0.025°, \Delta\alpha_f = 0.09°$ on a rocking geometry $\alpha_f = 2\theta - \alpha_i$ with fixed angle $2\theta = 8°$. Going from left to right, the panels represent detector angles α_f =7°, 4° and 0.5°. As can be seen, larger values of α_f lead to a wider detector acceptance in Q_x, which often leads to a visible broadening of satellite peaks at low Q_x values.

where the amplitude is given by

$$A(Q_x) = \exp\left(-\frac{(Q_x - Q_{x,0})^2}{2\Delta Q_{x,0}^2}\right) A(Q_x^{\mathrm{GTR}}, Q_z) \left(\frac{1}{\tilde{\xi}\sqrt{2\pi}} \exp\left(-\frac{(Q_x - Q_x^{\mathrm{GTR}})^2}{2\tilde{\xi}^2}\right)\right), \tag{4.13}$$

with $\tilde{\xi} = \xi_{\mathrm{total}}^{-1}$ being the Gaussian width of the coherence function in reciprocal space under a particular experimental set-up. Eq. 4.13 is the product of the detector resolution function

$$R(\Delta Q_x = \sigma_{\mathrm{Det.}}, Q_x) = \exp\left(-\frac{(Q_x - Q_{x,0})^2}{2\Delta Q_{x,0}^2}\right) \tag{4.14}$$

and a grating truncation rod[54, 65, 101]

$$A_{\mathrm{GTR}}(\tilde{\xi}, Q_x) = \frac{1}{\tilde{\xi}\sqrt{2\pi}} \exp\left(-\frac{(Q_x - Q_x^{\mathrm{GTR}})^2}{2\tilde{\xi}^2}\right) A(Q_x^{\mathrm{GTR}}, Q_z), \tag{4.15}$$

where the amplitude of the GTR over its full width has been approximated by its value at the nominal lattice position Q_x^{GTR} and the nominal Q_z-value of the detector under diffraction condition with the particular GTR (as defined in section 2.4). Note

that this simplification, which is also known as the two-beam approximation[90, 202, 203], is valid only if the beam coherence is sufficiently large so that no two GTRs are broadened such that their amplitudes significantly overlap in reciprocal space. Low coherence conditions and broad GTRs will, in fact, comprise a large part of the remaining chapter.

Inserting eq. 4.13 into eq. 4.12 leads to

$$I^{\mathrm{GTR}}(Q_{x,0}) = \frac{\left|A(Q_x^{\mathrm{GTR}}, Q_z)\right|^2}{2\sqrt{\pi}\tilde{\xi}} \frac{\Delta Q_{x,0}}{\sqrt{\Delta Q_{x,0}^2 + \tilde{\xi}^2}} \exp\left(-\frac{(Q_{x,0} - Q_x^{\mathrm{GTR}})^2}{\Delta Q_{x,0}^2 + \tilde{\xi}^2}\right), \quad (4.16)$$

which is the general expression for the integrated intensity of a GTR over a given detector acceptance. Inspecting eq. 4.16, it becomes apparent that $I(Q_{x,0})$ tends to zero if the nominal detector position $Q_{x,0}$ in reciprocal space is far away from the GTR located at Q_x^{GTR}.

Furthermore, as a sanity check, we check eq. 4.16 with respect to the classical case of high beam coherence. We find that, as it should, the scattered intensity is proportional to both the squared structure factor $\left|A(Q_x^{\mathrm{GTR}}, Q_z)\right|^2$ and the real space coherence length $\xi = \tilde{\xi}^{-1}$ if $Q_{x,0} \approx Q_x^{\mathrm{GTR}}$ and the high coherence condition $\tilde{\xi} \ll \Delta Q_{x,0}$ is fulfilled, i.e. if the length in reciprocal space probed by the detector is broader than the coherence function in reciprocal space. Eq. 4.16 then simplifies to a more familiar form

$$I^{\mathrm{GTR}}(Q_{x,0}) = \xi \frac{\left|A(Q_x^{\mathrm{GTR}}, Q_z)\right|^2}{2\sqrt{\pi}} \exp\left(-\frac{(Q_{x,0} - Q_x^{\mathrm{GTR}})^2}{\Delta Q_{x,0}^2}\right), \quad (4.17)$$

Finally, in an open detector set-up or when the slit width of the detector is large the resolution function is not described well by a Gaussian. Instead, an often better approximation is given by a rectangular window function, accepting all wave vectors within the solid angle given by the geometry of the detector equally. In this case the first exponential in eq. 4.13 is replaced by 1 and the integration limits in eq. 4.12 are replaced by the Q_x values corresponding to the upper and lower detector edges so that the open detector analogue to eq. 4.16 now reads

$$I(Q_{x,0})_{\substack{\text{open} \\ \text{detector}}} = \frac{\left|A(Q_x^{\mathrm{GTR}}, Q_z)\right|^2 \tilde{\xi}\sqrt{\pi}}{2} \left(\mathrm{erf}\left(\frac{Q_x^{\mathrm{GTR}} - Q_{x,1}}{\tilde{\xi}}\right) - \mathrm{erf}\left(\frac{Q_x^{\mathrm{GTR}} - Q_{x,2}}{\tilde{\xi}}\right)\right), \quad (4.18)$$

where erf denotes the Gauss error function.

4.1.4 The Limiting Case of Very Low Coherence

In many cases of x-ray diffraction – and particularly in the case of diffracting atomic lattices – the coherence length of the radiation can safely be assumed to be much larger than any significant periodicity of the diffracting structure. All photons scattered within a coherence ellipse centred arbitrarily at point $\mathbf{r}_{\parallel,\mathrm{c}}$ on the illuminated surface of the sample contribute a coherent superposition of electric field amplitudes $A(\mathbf{r},\mathbf{Q})$ at a given detector position corresponding to wave vector transfer $\mathbf{Q}$. The *total* measured intensity I then is the incoherent sum or integral

$$I = \int A(\mathbf{r},\mathbf{Q})A^*(\mathbf{r},\mathbf{Q})\,\mathrm{d}\mathbf{r}_{\parallel,\mathrm{c}} \tag{4.19}$$

taken over all possible centre positions $\mathbf{r}_{\parallel,\mathrm{c}}$ within the (incoherently) illuminated area.

Since in the high coherence limit the coherently scattering area is large, it can be safely assumed to represent an ergodic subset of the whole sample. Hence, the scattered amplitude of both coherence ellipses seen in Fig. 4.5 is effectively independent of the centre position $\mathbf{r}_{\parallel,\mathrm{c}} = (x_\mathrm{c}, y_\mathrm{c})$. Consequently, the incoherent integral of eq. 4.19 will effectively contribute only a scaling factor and can generally be neglected if the illumination of the sample is homogeneous and absolute intensities are not required.

However, if $\xi/d_\mathrm{latt} \lesssim 1$, i.e. the coherence of the radiation is of the order of,

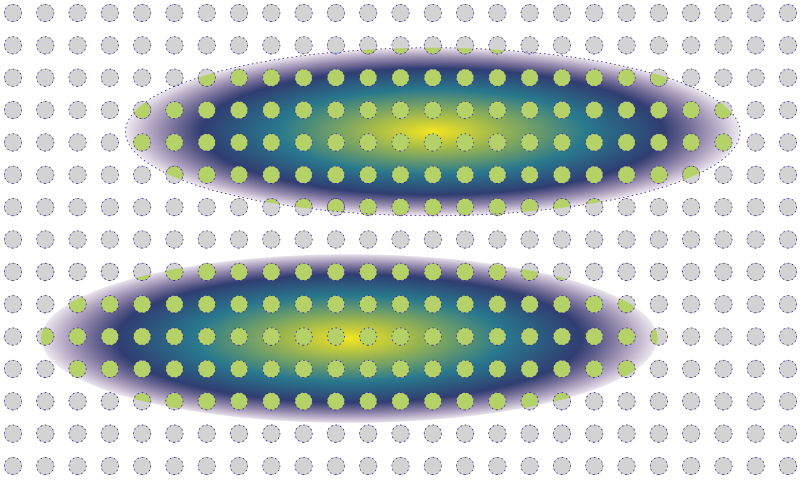

Figure 4.5: Coherence areas in the limit of large beam coherence. The part of sample probed by a large coherence ellipse looks effectively identical and can therefore be considered ergodic, irrespective of exactly where the coherence ellipse is centred on the sample.

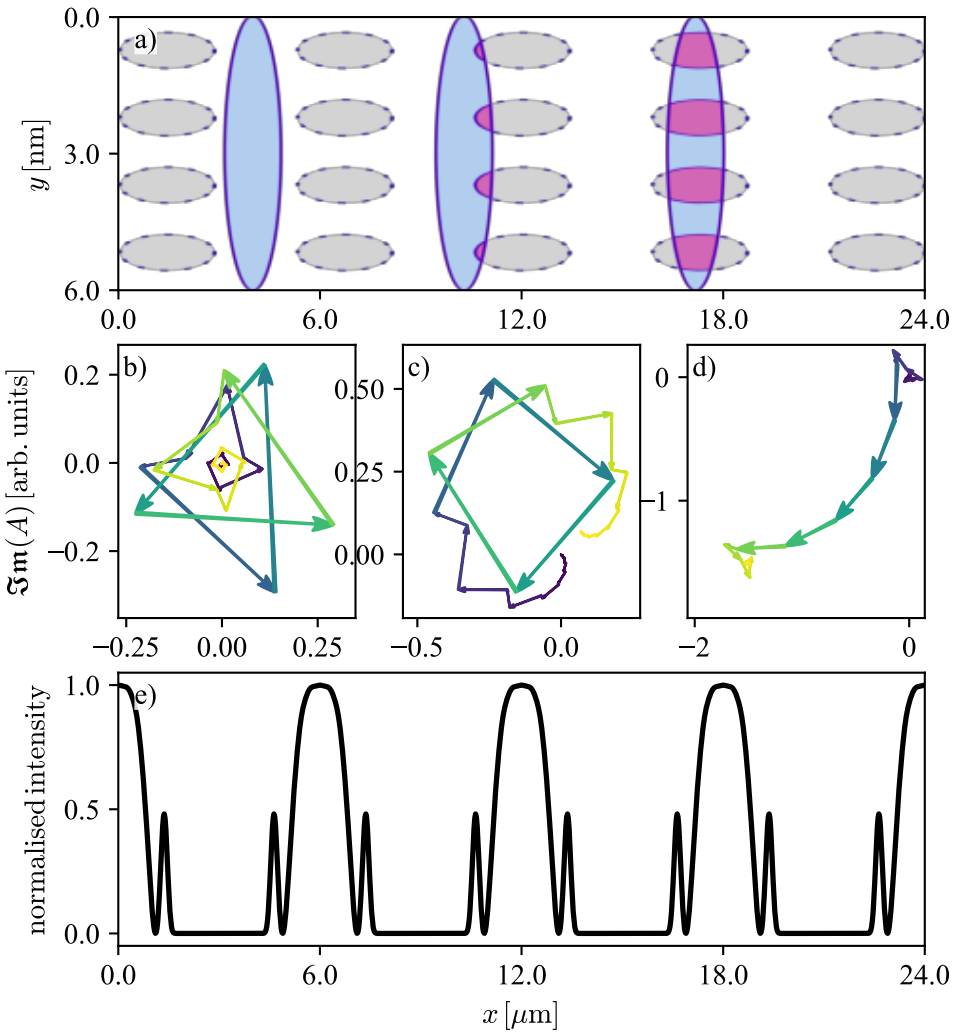

Figure 4.6: Effects of small beam coherence. Panel a) visualises coherence areas in the limit of small beam coherence. If the beam coherence along the short axis of the coherence ellipse is less than the width of the superstructures unit cell, the coherently illuminated sample area can not be considered ergodic and the diffracted signal will in general vary depending on where the coherence ellipse is placed on the sample. The scattered amplitude from coherent summation of GTRs at fixed value of $\mathbf{Q}$ is shown in panels b) - d). Panel e) shows the scattered intensity as a function of y-position of centre of the (narrow) coherence ellipse.

or less than the lattice periodicity, the exact localisation of the coherence ellipse *does* matter. This is sketched in Fig. 4.6 a), where the blue areas represent individual coherence ellipses, which extend far to the top and bottom beyond the figure because of the extreme ratio of ξ_t and ξ_s being typical in the small angle geometry.

The coherence ellipses are identical apart from a translation Δy along $\hat{\mathbf{y}}$. They are aligned with a lattice vector, and longer than multiple lattice constants but narrower than a single lattice constant. This means they either probe multiple elements along the principle lattice direction (here $\hat{\mathbf{y}}$) or are located right between the rows, missing all elements on the way. Whether the coherence ellipse is located *between* the rows or *on top* of multiple elements determines whether x-ray diffraction occurs and is solely determined by Δy. The latter translation becomes a single additional phase factor $\mathrm{e}^{-i\,\Delta y Q_y}$ in reciprocal space.

The large coherence along the incident beam direction means the reciprocal coherence ellipse (which by means of convolution with the reciprocal lattice comprises the reciprocal space representation of the coherently sensed sample) extends over less than a single lattice spacing, which may lead to classical Bragg satellites if the diffraction condition $Q_x = n\ 2\pi/d_{\mathrm{latt}}$ is met. However, because of the poor coherence *perpendicular* to the scattering plane (here along $\hat{\mathbf{y}}$), the reciprocal lattice points along $\hat{\mathbf{Q}}_y$ extend over many reciprocal lattice spacing and consequently overlap with each other. This means that if the diffraction condition is met the coherent amplitude in the two-beam approximation is in fact a sum over lattice points of a single row along Q_y, each obtaining a Gaussian weight according to the distance of their corresponding lattice point from the detected wave vector transfer Q_y. In order for the diffracted intensity to vanish because the coherence ellipse is located in between rows of elements, the coherent lattice sum has to average out towards zero, so that no net amplitude emerges, despite of the scattering amplitude of each individual lattice point being finite, as will be shown shortly in eq. 4.21.

Qualitatively, this is depicted in Fig. 4.6 b), where the real and imaginary part of each amplitude is visualised in the complex plane. Neglecting GTRs, which are separated by more than $3\tilde{\xi}$ from $\mathbf{Q}$, yellow and blue arrows represent the most distant lattice points in negative and positive Q_y direction, respectively. Two connected arrows represent neighbouring lattice points, and after traversing all probed lattice points, the final amplitude ends up very close to the origin, as is expected for a coherence ellipse effectively "missing" all patterned structures. By translating the coherence ellipse so that the pattern is probed only partially, each amplitudes phase is slightly altered so the final amplitude ends up to be small, but finite, as depicted in panel c). Finally, if the coherence ellipse is located right in the centre of the patterned islands, most of the amplitude phases are aligned within the complex plane, leading to a strong coherent amplitude, as shown in panel d). Scanning over the sample along $\hat{\mathbf{y}}$, the scattered intensity periodically shows distinct maxima when the coherence ellipse hits a row of patterned islands as seen in Fig. 4.6 e).

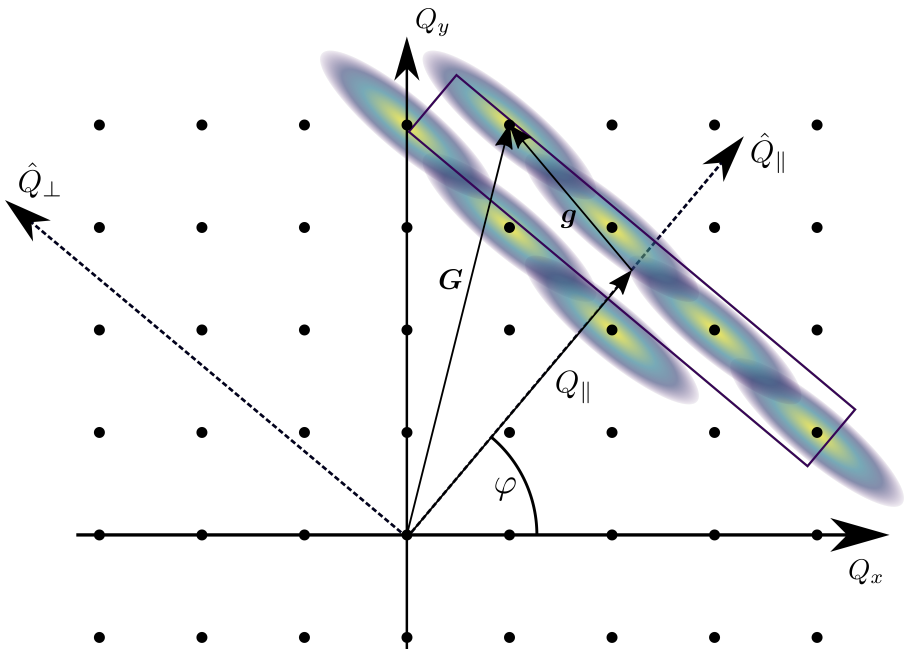

Figure 4.7: Reciprocal space and resolution function (depicted by the rectangular box) in the low-coherence limit. The GTRs located at the reciprocal lattice points are broadened up by the poor coherence in the direction $Q_\perp$ perpendicular to the scattering plane. Addition of amplitudes instead of intensities is required whenever two or more GTRs overlap.

Fig. 4.7 shows a sketch of the relevant features of a square reciprocal lattice and the detector resolution function – now in the $Q_x - Q_y$-plane – under conditions of low beam coherence. Two coordinate systems have been utilised: The *sample space* coordinate systems is defined by the Q_x and Q_y axes aligned with the principal reciprocal lattice vectors, hence all lattice points are found at integer multiples of $2\pi/d_{\mathrm{latt}}$ in Q_x and Q_y, respectively. The *instrumental* coordinate system is rotated at an angle ϕ with respect to the sample space, attributing an azimuthal rotation of the sample, misaligning $\mathbf{k}_{i,\parallel}$ and $\mathbf{R}_1$, the first real space lattice vector. The detector resolution element moves through reciprocal space along the $\mathbf{Q}_\parallel$ axis of the instrumental coordinate system, as is depicted by the rectangular box centred at $\mathbf{Q}_\parallel$.

The schematic exemplifies four key features of x-ray diffraction:

1. The inclined rectangle represents the resolution element under the assumption of a narrow slit perpendicular to the scattering plane and placed in front of the detector. It is centred at position $\mathbf{Q}_\parallel = k\,(\cos\alpha_f - \cos\alpha_i)$. The resolution element is wide in direction of $\mathbf{Q}_\perp$ because the angular acceptance along the

slit is restricted by the detector window only. The measured intensity at the nominal detector position then is the incoherent integral over the squared amplitudes over the whole resolution element. The inclination angle of the resolution element correspond to an azimuthal rotation of the sample, rotating the resolution element with respect to the lattice vectors of the sample.

2. The dots represent the reciprocal lattice of the sample, which equivalently can be thought of as a horizontal cut through the GTRs of the two dimensional supercrystal. Each lattice point is associated with a distinct phase and amplitude depending on the exact charge distribution within the unit cell of the array and the wave vector transfer $\mathbf{Q}$. Depending on the geometry of the experimental set-up each GTR will be intercepted at a particular value of Q_z, which generally leads to a modulation of the measured intensities.

   For a rocking scan of the sample, the interception value of the nominal wave vector transfer is a constant given by $Q_{\mathrm{z,rock}} = 2k \sin 2\theta/2$. If the dimension ΔQ_z of the resolution element is small enough, the variation in amplitude along the GTR is low enough that it can be considered constant when integrating over ΔQ_z. Under these conditions the integration in Q_z contributes only a scaling factor to the scattered intensity and can often be ignored.

3. Because of the finite beam coherence, the reciprocal lattice is convoluted with the coherence function, represented in this example by a two dimensional Gaussian function. Because of the $\sin^{-1}\alpha$ dependence of the lateral coherence length $\xi_{\|}$ within the scattering plane, the coherence element is narrow in direction of $\mathbf{Q}_{\|}$. The component of the beam coherence perpendicular to the scattering plane, however, depends mainly on the perpendicular divergence of the incoming radiation and may be found to fall below the unit cell dimensions of typical patterned arrays.

   Under these circumstances the convolution of reciprocal lattice and coherence functions transforms GTRs from scattering *rods* into scattering *sheets*, which may interfere with sheets associated with neighbouring lattice points. Perhaps surprisingly, this means that under conditions of low beam coherence the scattering amplitude will generally be the coherent sum of the densely packed neighbouring lattice points of the often µm-pitched patterned arrays which are contributing to a particular wave vector transfer $\mathbf{Q}$. Contrary to that, under conditions of large coherence, the separation of narrowly defined GTRs leads to at most one reciprocal lattice point contributing to the scattered intensity at any given value of $\mathbf{Q}$.

It is probably noteworthy that, because it is the Fourier transform of the real-space coherence ellipse, each coherence function in reciprocal space has a strict dependence on the centre position of the coherence ellipse and is therefore proportional to $\exp\left(-i\mathbf{r}_{\parallel}\mathbf{Q}_{\parallel}\right)$. This phase factor can usually be ignored, since it cancels when squaring the scattering amplitude of a single GTR. However, since in the low coherence case multiple distinct amplitudes of neighbouring GTRs interfere, the corresponding phase factor for each GTR has to be explicitly taken into account when calculating the overall amplitude and hence intensity. For clarity, in Fig. 4.7 the convolution of reciprocal lattice and the coherence function has been performed for the lattice points overlapping with the resolution function, only.

4. Finally, because of the narrow size of the detector slit within the scattering plane, the resolution function can be approximated by a Gaussian distribution along $\mathbf{Q}_{\parallel}$. Hence, the amplitude of each GTR is modified by a factor $\exp\left(-\frac{g_{\parallel}^2}{2\tilde{\xi}_{\parallel}^2}\right)$, where $\mathbf{g}$ is the vector connecting the nominal detector position and a particular reciprocal lattice point located at $\mathbf{G}$. The components of $\mathbf{g}$ parallel and perpendicular to $\mathbf{Q}_{\parallel}$ can be easily found in the instrumental coordinate system expressed by its components in sample coordinate system to read

$$g_{\parallel} = g_x \sin\phi - g_y \cos\phi \tag{4.20a}$$

$$g_{\perp} = g_x \cos\phi + g_y \sin\phi. \tag{4.20b}$$

The above considerations describe the general case of low-coherence diffraction. In reality, the parallel beam coherence is generally so much larger than the coherence perpendicular to the scattering plane that it is often justified to approximate the two-dimensional coherence function by a one-dimensional function, which significantly simplifies the mathematical treatment and lowers the computational effort. The latter is accomplished by treating any one GTR as a one-dimensional function when convolving with the detector resolution function R.

Combining the above considerations with eq. 4.15 assuming a Gaussian profile for the one-dimensional coherence function one can readily derive the *general*

diffraction equations at low perpendicular beam coherence to read

$$A(Q_\parallel, Q_\perp) = \sum_{g_\perp} A(\mathbf{G})\, \frac{\xi_\parallel}{\sqrt{2\pi}} \exp\left(-\frac{(Q_\parallel - g_\parallel)^2 \xi_\parallel^2}{2}\right) \frac{\xi_\perp}{\sqrt{2\pi}} \exp\left(-\frac{(Q_\perp - g_\perp)^2 \xi_\perp^2}{2}\right) \exp\Big(i\, r_\perp (Q_\perp - g_\perp)\Big) \tag{4.21a}$$

$$I(Q_\parallel) \propto \iint A(Q_\parallel, Q_\perp) A^*(Q_\parallel, Q_\perp)\, \mathrm{d}r_\perp\, \mathrm{d}Q_\perp. \tag{4.21b}$$

Eq. 4.21 a) defines the scattering amplitude of a single coherence ellipse located arbitrarily on the sample. It is a sum over reciprocal lattice vectors whose GTRs fall within the detector resolution. Each GTR is of peak amplitude $A(\mathbf{G})$, whose amplitude at position $\mathbf{Q}$ is modulated by the two exponentials containing the coherence lengths $\xi_\parallel$ and $\xi_\perp$. Additionally, the last exponential takes care of the phase factors of all GTRs at position $\mathbf{Q}$ depending on the real space displacement $r_\perp$ of the coherence ellipse, which becomes important when multiple (broad) GTRs overlap. Parallel displacement of the coherence ellipse does not need not to be considered because of sufficient ergodicity of the coherence ellipse along its long coherence axis aligned with $\mathbf{k}_{i,\parallel}$.

Eq. 4.21 b) represents the measured intensity of the detector at the nominal wave vector transfer $Q_\parallel = k\,(\cos\alpha_f - \cos\alpha_i)$. The (incoherent) integration is performed over all the perpendicular wave vector transfers $Q_\perp$ the detector accepts as well as over all relevant perpendicular shifts $r_\perp$ of the coherence ellipse in *real space*.

Due to the large coherence within the scattering plane, integrating over $r_\parallel$ only contributes a scaling term to the intensity and can generally be neglected. The integration over $r_\perp$ can be performed in two ways: Either it has to be taken over a large enough range to provide sufficient statistical averaging to accommodate for the non-ergodicity of the sample area probed by the narrow coherence function. Alternatively, the integration can be performed over a range that reflects the periodicity of the lattice. Hence, if considering a high symmetry direction like (10), the integration may be carried out, for instance, over one lattice constant, to ensure that the coherence ellipse probes every distinct view of the sample (compare also Fig. 4.6).

4.2 Investigation of Coherence Limited Diffraction on Multi-Element Patterned Arrays

As was discussed in the previous sections, when performing x-ray diffraction on patterned samples it can easily be the case that coherence conditions of the beam have to be considered explicitly, which might usually be safely neglected for most types of samples.

In the following, the geometrical configuration of a set of samples of mesoscopic dimensions is introduced and it will be shown how a naive treatment of scattering theory breaks down in trying to reproduce the experimental diffraction pattern and how with a proper treatment of beam coherence one is able to capture the diffraction features on both a qualitative and quantitative level. Previous experiments on this set of samples have already recognised the importance of beam coherence in MOKE[98] and XRMS[75] studies, highlighting the need of a diffraction framework of patterned arrays, which explicitly contains applicability to low beam coherence. This framework was developed in the course of this thesis and will be presented in the current chapter. If not indicated differently, all results are the work of the author.

The following experiments show all of the characteristics previously discussed: The lattice pitch of the patterned arrays used is on a µm scale, requiring a low coherence treatment of scattering theory. Wide detector slits parallel to the sample surface lead to a wide resolution element in reciprocal space. Finally, by rotating each sample around its surface normal a wide range of diffraction peaks corresponding to distinct lattice planes could be resolved. It will be shown how the latter will be quantitatively reproduced considering – amongst other parameters – the beam coherence as a critical fitting parameter.

4.2.1 Sample structure

A negatively patterned resist of the structures was prepared at the Micro and Nanotechnology Centre, MNTC[204, 205], by electron beam lithography before deposition of the samples at Uppsala University. The latter was done by depositing 10 bilayers, each consisting of 3 nm thick $Co_{68}Fe_{24}Zr_8$ and 3 nm thick Al_2O_3 into the prepatterned masks. The material was deposited by magnetron sputtering and each multilayer was additionally seeded by 3 nm of Al_2O_3 adding up to a total stack height of 63 nm. The whole preparation process is described in more detail in [98].

Each final structure was a supercrystal consisting of circular islands of diameter 1.5 µm and elliptical islands of short- and long axis 1.5 µm and 4.5 µm, respec-

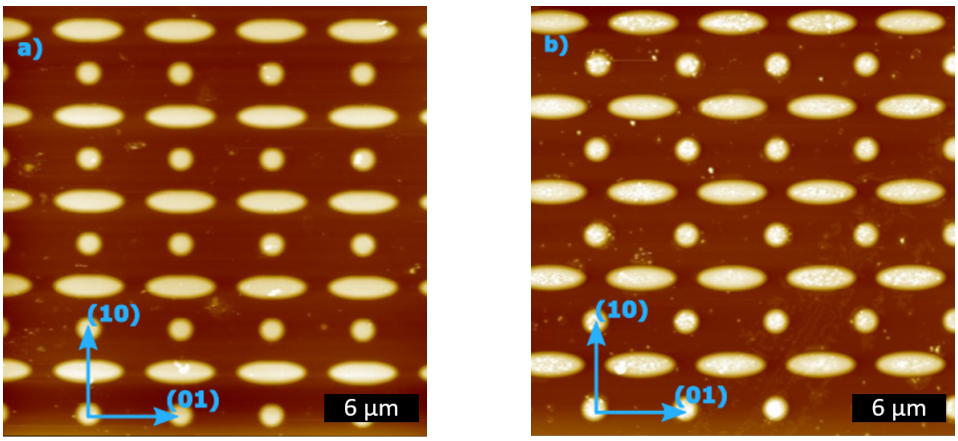

Figure 4.8: AFM image of type α (panel a) and β (panel b) patterned arrays. The α is characterised by circular and elliptical islands lining up in the (10) direction. In pattern β both sublattices are shifted by half a lattice constant in both x- and y-directions. Images also published in [98].

tively, an atomic force microscopy image can be seen in Fig. 4.8.

We will now briefly discuss the α and β configurations, which differ in the relative positioning of one circular and one elliptical island and together form the unit cells of the supercrystals. Both patterns consist of a square unit cell of lattice constant 6 µm. In the α case, the centres of the elliptical islands were placed in-line with the circular islands along the (10) direction, with the long axis pointing in the (01) direction. In the β case, the elliptical islands were shifted by half a lattice constant in the (01) direction, so that each elliptical island was centred in between four neighbouring circular islands.

In the following, a cartesian coordinate system originating in the centre of a circular island with x- and y-axis aligned with the (01) and (10) directions of the real space lattice will be used in describing the patterned arrays.

4.2.2 Experiment

For each sample a series of rocking curves as a function of azimuthal rotation angle ϕ were taken on beamline X22C at the NSLS[206]. For the α sample the beam energy was chosen to be 8.8 keV and the detector angle was set to 1.403°, corresponding to an Bragg peak of the reflectivity. For the β sample the beam energy was decreased to 6.5 keV in order to reduce the amount of x-ray fluorescence; a decision made after the α sample had been measured already, and the detector had been adjusted to stay at the Bragg peak.

For each angle ϕ the experimental set-up is sensitive to distinct sample peri-

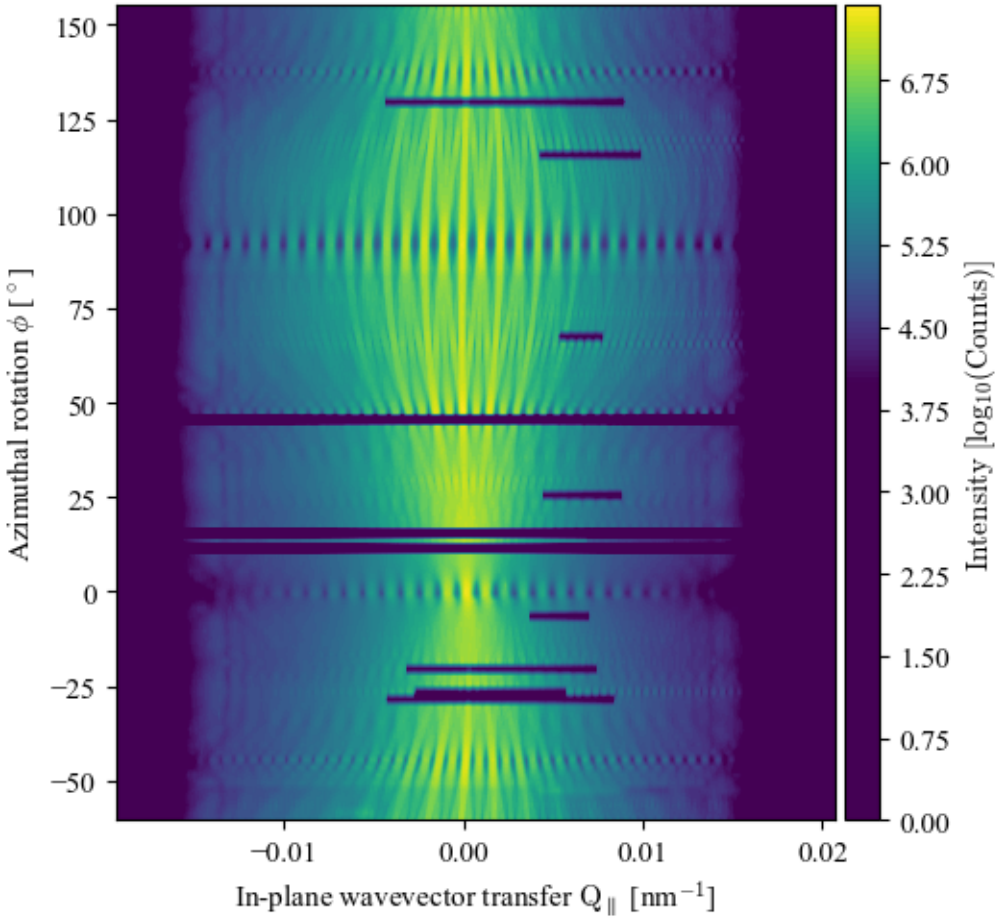

Figure 4.9: Scattered intensity of α pattern as a function of in-plane wave vector transfer $Q_{\parallel}$ and azimuthal rotation ϕ. The high symmetry directions (01) and (10) are clearly visible at $\phi = 0°$, 90° and 180°. The dark horizontal lines indicate missing data, being the result from problems with the diffractometer motors.

odicities, manifesting in the formation of Bragg peaks (or GTRs) along $Q_{\parallel}$, where, in this context, the latter again denotes the in-plane component of the wavevector transfer within the scattering plane. The GTRs are visible as continuous streaks in Figs. 4.9 and 4.10, showing a map of scattered intensity against $Q_{\parallel}$ and azimuthal sample rotation ϕ of the β pattern.

Since both pattern types sit on the same lattice, the mappings of Figs. 4.9 and 4.10 look very similar, with the main difference being the range of probed $\mathbf{Q}_{\parallel}$ because of the differing beam energy the respective measurements have been taken at, which is of course also affecting the (constant) Q_z value the rocking curves of each pattern have been measured on. The asymmetric form factor of the unit cells

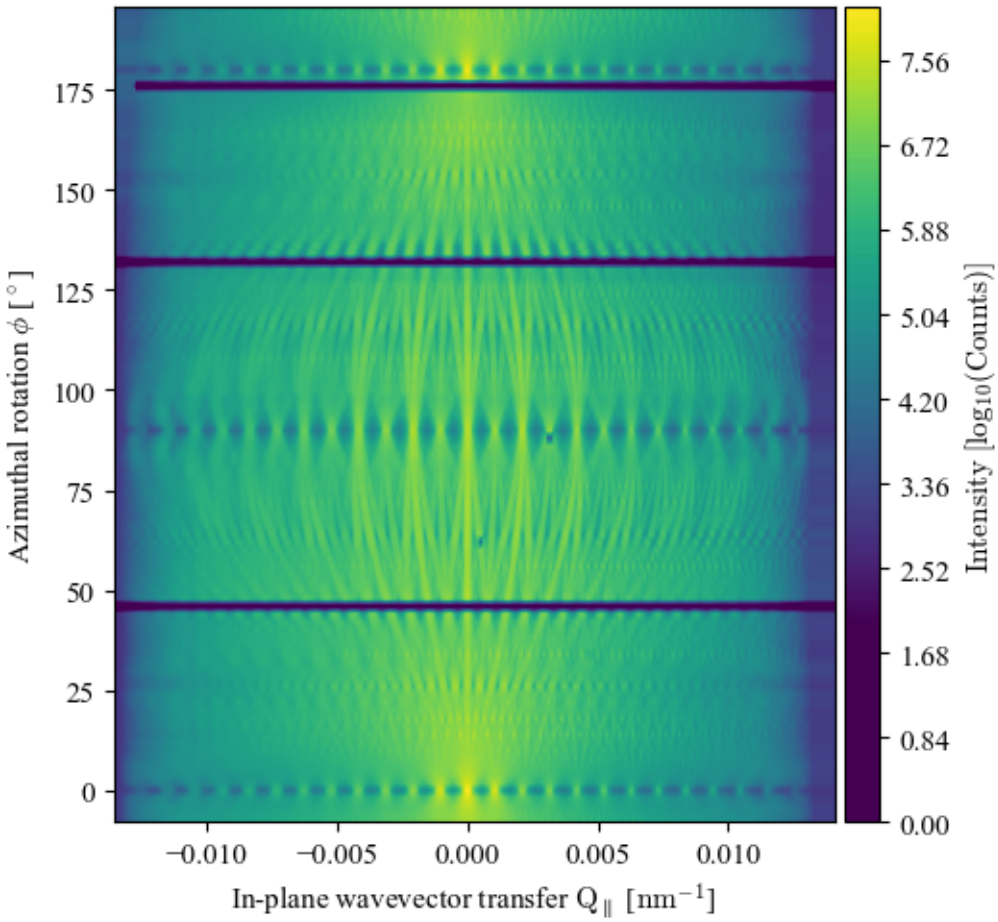

Figure 4.10: Scattered intensity of β pattern as a function of in-plane wave vector transfer $Q_{\parallel}$ and azimuthal rotation ϕ. The high symmetry directions (01) and (10) are clearly visible at $\phi = 0°$, 90° and 180°. The dark horizontal lines indicate missing data, being the result from problems with the diffractometer motors.

of both patterns clearly manifest in an asymmetry between rocking curves measured at $\phi = 0°$ along the (01)-direction and $\phi = 90°$ along (10), despite the spacing of the diffraction peaks along both direction being identical due to the rectangular nature of the real space lattice of both patterns. As the α pattern was measured at a smaller slit size determining the beam divergence $\Delta\alpha_i$, diffraction peaks along $\mathbf{Q}_{\parallel}$ are expected to be sharper compared to the β pattern, which is hard to be confirmed visually but will be subjected to the subsequent analysis by means of fitting the data.

Along high symmetry directions – most pronouncedly at $\phi = 0°$ and $\phi = 90°$, i.e. along the (10) and (01) direction of the lattice – GTRs corresponding to

the same lattice plane align, and are hence superimposed onto the same values of $\mathbf{Q}_{\parallel}$. Contrary, along ill-defined values of ϕ the GTRs of differing $\mathbf{Q}_{\perp}$ are likewise intercepted at ill-defined values of $\mathbf{Q}_{\parallel}$. Both effects can be seen in Figs. 4.11 and 4.12, respectively. From the absence of a visible background signal in the upper two panels of Figs. 4.11 and 4.12 it also becomes apparent that what appears to be a continuous background of diffuse scattering over most part of the azimuthal maps, is in fact simply the superposition of a huge number of misaligned diffraction peaks. Note that, technically, the average number of GTRs the resolution element R intercepts at any orientation in reciprocal space is more or less constant, and the apparent smaller number of peaks along high symmetry directions is merely a consequence of the GTRs aligning with- and superimposing on each other.

Each (roughly vertical) streak corresponds to a particular GTR, continuously being modified in $\mathbf{Q}_{\parallel}$, due to the ϕ-dependent interception with the detector resolution function R. The latter can be interpreted visually by inspection of the value of $\mathbf{Q}_{\parallel}$ corresponding to any reciprocal lattice point shown in Fig. 4.7 upon rotating ϕ. Once ϕ is moved away from a high symmetry direction, the GTRs along $Q_{\perp}$ do not align up with the detector resolution element any more. Because of the wide detector acceptance these additional GTRs appear to spread up away from the high symmetry directions, typically into three to five additional streaks. The latter is therefore indicative of the width of the resolution element in reciprocal space. Put differently, a narrower detector acceptance perpendicular to the scattering plane would result in less or no additional streaks at all since the resolution function would be able to accept fewer, only one or even not a single GTR at any nominal $Q_{\parallel}$. Additionally, the continuity of every single streak is potentially indicative of a low coherence set-up, in which a lack of coherence perpendicular to the scattering plane leads to formation of scattering sheets being perpendicular to $Q_{\parallel}$, which are anchored at the corresponding reciprocal lattice points. In this case, even a narrow detector acceptance would intercept multiple scattering sheets even if the corresponding reciprocal lattice points are not located within the detector resolution function.

The full lines in Figs. 4.11 and 4.12 show experimental rocking curves at selected values of ϕ for the α and β patterns. As expected, the measurements taken at $\phi = 0°$ and $\phi = 90°$ (or, equivalently, along the (10) and (01) directions) show well defined, Gaussian shaped satellite peaks at $Q_{\parallel,m} = m\,\frac{2\pi}{d} = m\,\Delta Q_x \approx m \times 0.001\,\mathrm{nm}^{-1}$ corresponding to the lattice periodicity $d_{\mathrm{latt}} = 6000\,\mathrm{nm}$ and m being integer.

The satellite peak intensity modulation is determined by the contribution

of all simultaneously probed GTRs according to eq. 4.21, which are generally more than one under low coherence conditions even for the high symmetry directions. The (kinematical) GTR structural amplitude $A(\mathbf{G})$ in eq. 4.21 can be approximated for a unit cell consisting of a spatially flat pair of a circular island of radius R centred at $\mathbf{r} = 0$ and elliptical islands of long and short axes A_x and A_y and center displacement x_{off} and y_{off} by the superposition of scaled Bessel functions of the first kind of order 1 to read[207]

$$A_{\text{GRT}}(\boldsymbol{Q}_{\parallel}) \propto R^2 J_1(RQ_{\parallel}) + A_x A_y J_1\left(\sqrt{A_x^2 Q_x^2 + A_y^2 Q_y^2}\right) \exp(-i(Q_x x_{\text{off}} + Q_y y_{\text{off}})), \tag{4.22}$$

which will be proportional to the scattering length density SLD(z) of the material as well as to

$$A_{\text{GTR}}(Q_z) \propto \frac{1 - \exp\{-ihQ_z\}}{-iQ_z}, \tag{4.23}$$

the z-component of the Fourier Transformation of the unit cell, depending on the total height h of the islands.

Note that the layered structure of the real sample has only implicitly been included in the SLD and plays no role in eq. 4.22. This is justified since the chemical profile of the islands is a function of the height over the substrate surface z only, and will hence only modulate the scattered intensity distribution along Q_z by means of forming Bragg peaks according to the multilayer periodicity of the internal structure of each island as discussed in section 2.2. The Q_x, Q_y dependency of the scattered intensity, on the other hand, is not affected apart from a proportionality constant which is implicitly considered in a scaling constant of the total intensity.

It is evident that the reduced intensity of odd ordered peaks along the (10) direction as witnessed for the α pattern presented in Fig. 4.11 b) is a result of the $d_{\text{latt}}/2$ offset of the ellipse in the (10) direction with respect to the circular island of the same unit cell as seen in Fig. 4.8. According to eq. 4.22 this corresponds to a phase shift in between the circular and elliptical island of the unit cell of

$$\exp(-iQ_y y_{\text{off}}) = \exp\Big(-i(Q_{\parallel} r_{\parallel}^{\text{off}})\Big) = \exp\left(-i\frac{m\,2\pi}{d}\frac{d}{2}\right) = \exp(-im\pi) \tag{4.24}$$

leading to destructive interference for satellites of odd order m along the $Q_{\parallel} = Q_y$ axis at $Q_{\perp} = Q_x = 0$, which corresponds to the nominal direction in reciprocal space for the scan. On the other hand, the two islands of the unit cell of the α pattern are not subjected to any spatial offset along the (01) direction. The center points of neighbouring islands along the beam in this direction are always separated exactly by d_{latt} and hence, for $Q_y = 0$, the structure factors of both circular and elliptical

islands add constructively leading to no local minima in the combined structure factor.

Interestingly, by the same argument the diffracted intensity of the β pattern does not show any signs of destructive interference, despite the predicted minima of the unit cell structure factor from eq. 4.22 for $x_{\text{off}} = y_{\text{off}} = d_{\text{latt}}/2$, according to the predicted phase shift when restricting to the scattering plane ($Q_\perp = Q_y = 0$)

$$\exp(-i(Q_x x_{\text{off}} + Q_y y_{\text{off}})) = \exp\Big(-i(Q_\parallel r_\parallel^{\text{off}} + Q_\perp r_\perp^{\text{off}})\Big) = \exp(-im\pi). \tag{4.25}$$

The latter can be explained qualitatively by considering the finite perpendicular beam coherence $\xi_\perp$ of the radiation. Inspecting Fig. 4.8, it is clear that if

$$\xi_\perp \lesssim \frac{d_{\text{latt}}}{2} = 3000\,\text{nm}$$

a coherence ellipse aligned in the (01) direction is able to only coherently illuminate rows of a single type of either ellipses or circles at any given time, therefore always experiencing the total lattice pitch d_{latt} in between coherently scattering elements. A coherence ellipse aligned along the (10) direction of the α pattern will conversely be able to coherently illuminate both types of elements aligned in any row along (10), therefore leading to destructive interference of odd ordered diffraction peaks as displayed in Fig. 4.11. However, because of the relative shift of circles and ellipses, when aligned along the (10) direction of the β pattern, the coherence ellipse will, again, be only able to coherently illuminate a single type of elements, therefore not experiencing destructive interference of circles and ellipses. Destructive interference is nevertheless implied in the calculation of the classical structure factor $F(\mathbf{Q})$, since the integration limits of eq. 2.90 span the whole unit cell, disregarding any considerations regarding beam coherence, therefore predicting a dip in intensity for odd-ordered peaks which is not observed in experiment.

Because of the projected coherence properties, the coherence ellipse will be able to extend over many unit cells in the parallel direction and be narrow in the perpendicular direction. That means that in the high symmetry (10) and (01) directions of the β pattern only a single row of elements of a single kind will be coherently illuminated simultaneously. A supplementary discussion of the experimental observations is provided by Arnalds et al. [75].

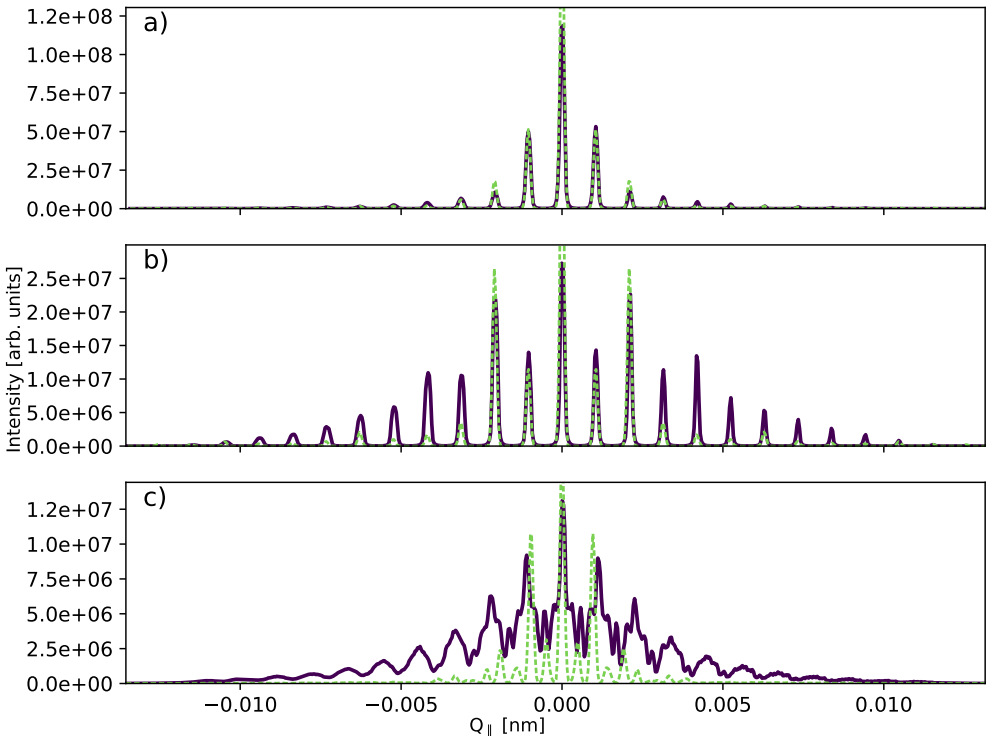

Figure 4.11: Simulated and experimentally measured rocking curves. Panels a), b), and c) show measurements along $\phi = 0°$, $90°$ and $28°$, respectively, taken on the α pattern. Solid lines show experimental data. In panel b) odd satellite orders are of reduced intensity due to destructive interference of circular and elliptical islands being lined up along the (10) direction corresponding to azimuthal rotation $\phi = 90°$. Panel c) shows the superposition of multiple GTRs being probed due to the wide detector acceptance and low perpendicular beam coherence. Dashed green lines show simulations of the experiment considering flat islands (modelled by Bessel functions of first kind of order 1) and infinite coherence along both $r_{\parallel}$ and $r_{\perp}$, leading to poor match in between experimental and simulated data.

4.2.3 Neglecting coherence effects

The dotted lines in Figs. 4.11 and 4.12 show examples of a "naïve" simulation of the scattered signal, disregarding beam coherence effects. For the simulation, the patterns have been modelled by two-dimensional circles and ellipses of SLD being unity within and zero outside of the structure. This is justified by the comparatively simple nominal sample geometry, in terms of the side walls and island tops being perfectly flat. This way, the effect of the chemical profile along the z-direction of each island towards the structure factor $F(\mathbf{Q})$ is reduced to a simple scaling factor modifying the simulated intensity.

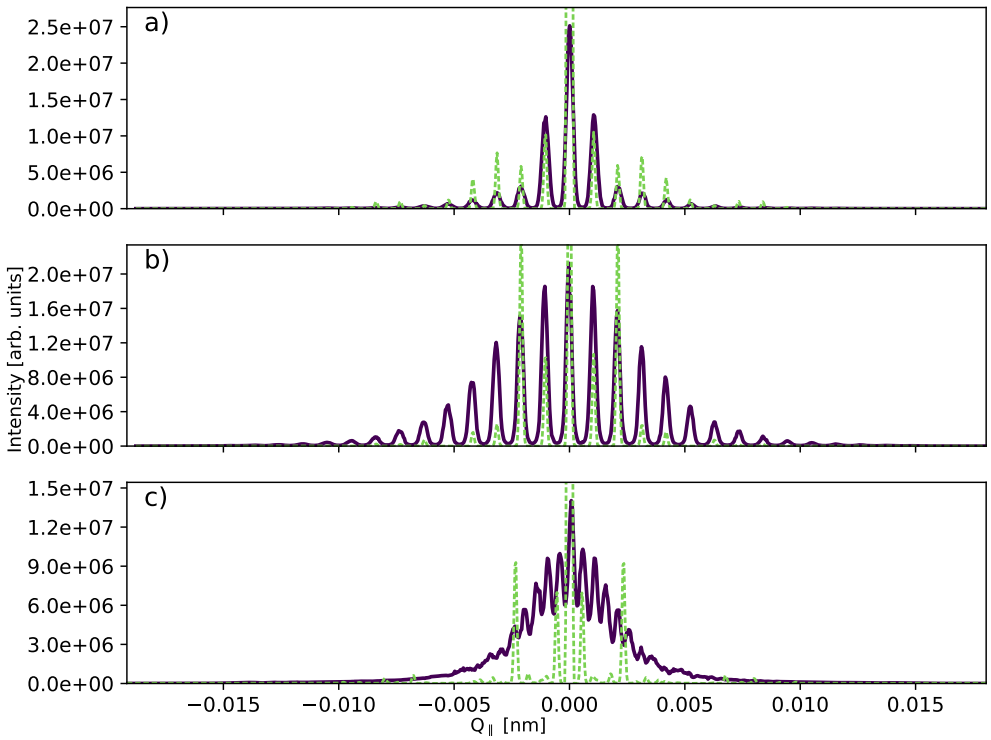

Figure 4.12: Simulated and experimentally measured rocking curves. Panels a), b), and c) show measurements along $\phi = 0°$, $90°$ and $28°$, respectively, taken on the β pattern. Solid lines represent experimental data. Note how in the experimental data in panel b) odd ordered satellite peaks in the (10) direction show no decrease in intensity, although the structural form factor $A(\mathbf{Q})$ of the unit cell of the array exhibits reduced amplitude along Q_y, since the two sublattices are shifted by a half a lattice period along y. This is a direct indication of poor perpendicular coherence under the experimental conditions, since amplitudes scattered by the circular and elliptical islands are not able to add coherently. The dashed lines represent simulated data, again leading to poor matching with experiment. Note how the simulated rocking curve of panel b) – since it was performed in the high coherence limit – *does* show reduced intensity of odd satellite orders along the (10) direction.

It is furthermore implicitly assumed that the beam coherence is infinite in both spatial directions in the sample plane. The angular detector acceptance $\Delta\alpha_f$ has been assigned empirically through trial-and-error in order to roughly match the satellite shape of the experimental observation, whereas the perpendicular angular acceptance $\Delta\nu$ of the detector was assumed to the cover the whole detector range. Finally, all curves have been scaled by normalising the $0°$ simulation of the α pattern to the first negative order Bragg satellite of the experimental data.

In eq. 4.21 a) the exponential containing the perpendicular coherence length

$\xi_\perp$ can here be dropped because the detector slit will always be able to integrate the whole GTR in $Q_\perp$. Also, the last exponential, which contains the phase information depending on the center location $\mathbf{r}_\mathrm{c}$ of the coherence ellipse, can be dropped because at any value of $\mathbf{Q}$ only a single GTR will be contributing intensity, so the phase information will eventually cancel out when multiplying the scattering amplitude with its complex conjugate. Furthermore, in eq. 4.21 b) the integration over $r_\perp$ can be dropped because of the ergodicity of the coherently illuminated part of the sample and the integration over $Q_\perp$ turns into a summation over single lattice points that are being accepted by the detector. Performing these adaptations it follows that

$$I(Q_\parallel) \propto \sum_{\mathbf{G}} \xi_\parallel^2 \exp\Big(-g_\parallel^2 \xi_\parallel^2\Big) |A(\mathbf{G})|^2, \tag{4.26}$$

where the amplitude structure factor $A(\mathbf{G})$ of the two-element unit cell according to eq. 4.22 has been used and the sum over lattice vectors $\mathbf{G}$ is taken over the extent of the resolution function R.

Comparing simulated and experimental signals in Fig. 4.11 it becomes clear that the simulation qualitatively captures the features of the measurements at $\phi = 0°$ and $\phi = 90°$, which is expected following the previous discussion, even when neglecting coherence effects. However, higher order satellite intensities are found to be much smaller than expected and the simulation completely breaks down for the example case of a rocking curve not along a high symmetry direction. The match of simulated and experimental signal for the β pattern is even worse. Because of the relative spatial dislocation in both x and y of circular and elliptical islands, the geometry is more susceptible to coherence effects, which is why the destructive interference of odd ordered peaks is observed principally in the simulation along *both* (10) and (01) directions. Again, deviation between data and model is greatest for diffraction away from a high symmetry direction, where the detector appears to capture significantly fewer GTRs because of the stricter diffraction condition in the high coherence case, again stressing the importance of considering beam coherence in diffraction of patterned arrays.

4.2.4 Simulating Low Beam Coherence

In the previous section it was seen how simulating off-specular diffraction fails if no proper treatment of the beam coherence is performed. Hence, in this section the general form of eq. 4.21 will be put to use. To this end, conditions of low perpendicular beam coherence will be assumed so as to investigate the effects of the latter towards the diffracted intensity.

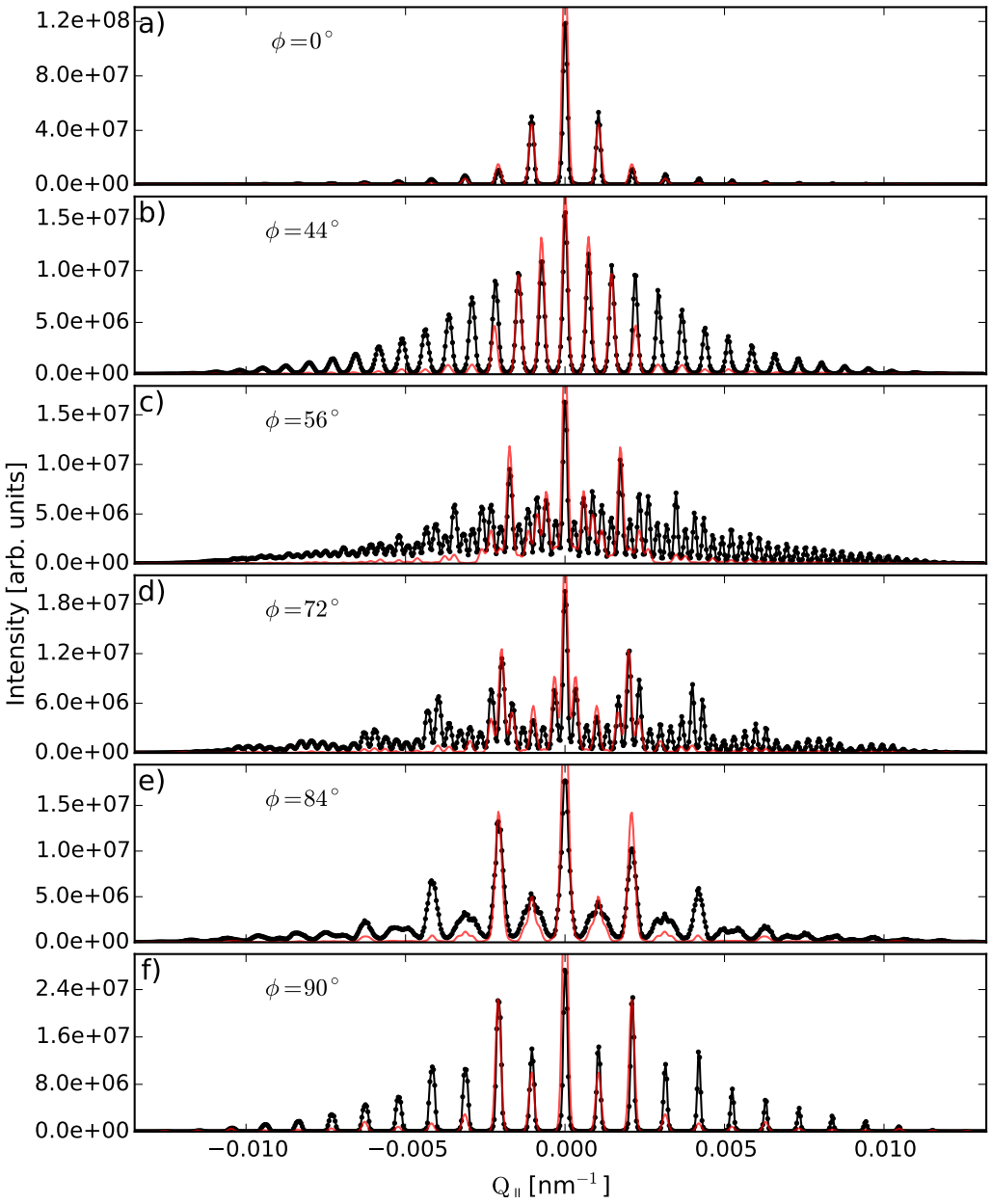

Figure 4.13: Experimental (black dotted) and simulated (red line) signal of rocking curves of α pattern at selected azimuthal rotations ϕ at beam energy 8.8 keV. Structural form factors of circular- and elliptical islands have each been calculated from a single Bessel function of first kind of order 1.

Generally, decreasing beam coherence is associated with a widening of the GTRs, centred at the reciprocal lattice points. One potential consequence is the appearance of additional peaks in the diffraction pattern, each corresponding to a single

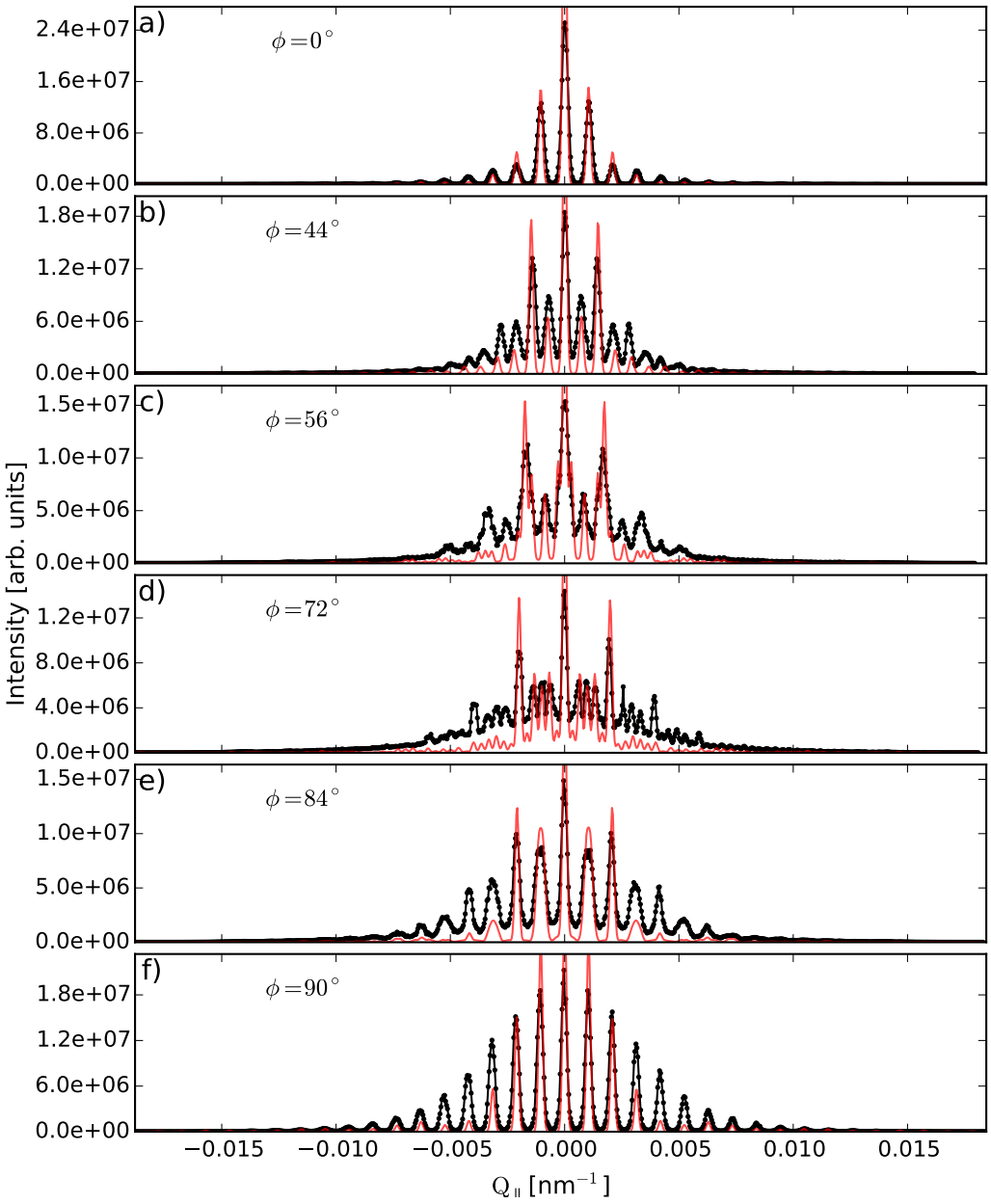

Figure 4.14: Experimental (black dotted) and simulated (red line) signal of rocking curves of β pattern at selected azimuthal rotations ϕ at beam energy 6.5255 keV. Structural form factors of circular- and elliptical islands have each been calculated from a single Bessel function of first kind of order 1.

reciprocal lattice point, which actually does not necessarily have to lie within the detector resolution function. However, the corresponding GTR, which is anchored to the lattice point, has been extremely widened due to low coherence conditions,

Parameter	Empirical Value
Parallel beam coherence [nm]	150000
Perpendicular beam coherence [nm]	750
Parallel detector acceptance [mrad]	0.166667
Perpendicular detector acceptance [mrad]	0.5

Table 4.1: Simulation parameters used in producing Figs. 4.13 and 4.14. The parallel detector acceptance is understood to be along the narrow slit dimension and represents one Gaussian standard deviation. The perpendicular detector acceptance lies along the wide detector slit dimension, effectively represents the angular acceptance of the (open) detector and represents the width of a top-hat function.

so that it is nevertheless partly intercepted by the detector resolution function. A second potential effect is the coherent amplitude modulation of overlapping GTRs. In this case, it is not sufficient for the perpendicular coherence $\xi_\perp$ to merely fall below the spatial distance of neighbouring islands, but additionally, the GTRs have to be oriented in a way that the long axis of the GTRs aligns with a reciprocal lattice plane, as is indicated in Fig. 4.7, where GTRs align and partly overlap along the (11) lattice plane.

Simulated rocking curves of both patterns are presented in Figs. 4.13 and 4.14, using reasonable simulation parameters presented in table 4.1. As can be seen both of the effects mentioned above are observed in the low-coherence simulated signal. The simulation now produces peaks at most of the positions observed in experiment.

Also, the odd ordered peaks along the (01) direction of the β pattern seen in Fig. 4.14 f) are no longer affected by the reduced structural form factor of the unit cell, which is a direct consequence of the low coherence conditions present. Similarly, because of the circles and ellipses lining up in the α case, modulation of the odd ordered satellites along (10) is still observed in Fig. 4.13, as would be expected even under low perpendicular coherence.

Apparently, the implementation of the low beam coherence appears to be able to reproduce many of the experimental features already and is a promising route to providing valuable information for both investigating beam coherence properties as well as a means of characterising sample properties under imperfect coherence conditions. However, although attempted, up to this point no proper fitting of experimental data has been successful.

The motivation for applying fits of low coherence experiments is clear, though. On the one hand, experimental set-ups often simply do not provide sufficient coherence

that neglecting the issue is feasible. Also, the complex interplay of many superpositioned GTRs – in particular at wide detector acceptance, is computationally very costly. On the other hand, the same complexity may be understood as providing a plethora of information about the investigated system; in particular rocking curves taken away from high symmetry sample directions may be sensitive to a very high number of reciprocal lattice points as well as to their superposition mediated by the beam coherence.

Coming back to the simulated data, as a general trend, satellites at large wave vector transfers are found to be systematically of intensities significantly too low relative to the experimental data. This strongly indicates that the simulation model is not able to adequately reproduce the experimental measurement, and so fitting of the experimental data cannot be expected to lead to any meaningful results under the assumptions currently used.

The fact that all peaks seen in experiment are actually present in the simulation but are found to be at too low intensities hints at the need to re-evaluate the role of the structure factor $F(\mathbf{Q})$ of the superlattice unit cell, which provides the envelope function of the Bragg peaks. It seems that the scattering amplitude of the GTRs gets underestimated systematically with increasing $\left|\mathbf{Q}_{\parallel}\right|$. Apparently, the model that has been used is not able to capture all the critical contributions in evaluating the structure factor of the patterned array.

4.2.5 A Realistic Model of the Sample Structure

In the previous sections the spatial structure of the sample was assumed to obey a number of simplifying assumptions. First, the variation of the chemical composition of each layer of the sample was assumed to be limited in the direction perpendicular to the sample plane, which in turn means that the perpendicular SLD profile merely affects the scattered intensity along Q_z, hence only acting as a scaling factor in a rocking experiment, for which $Q_z = const$ holds.

The second simplifying assumption was the constant cross section at any height z of the patterned structure. This simplified the mathematical treatment significantly, since the Fourier Transformation of the unit cell consisted of a simple product of two terms. The first is a constant phase factor given by eq. 4.23, corresponding to the nominal height h of the islands, which does affect the scattered intensity only in the form of a scaling factor and is taken care of implicitly in the final rescaling of the simulated intensity to match the experimental data. The second factor is the superposition of the Fourier transforms of a circle and an ellipse given by eq. 4.22. The apparent simplicity of this approach is tempting, and it is, in fact,

an often legitimate approximation[38, 52, 75, 98]. However, off-specular diffraction of patterned arrays is often found to be highly sensitive to even the smallest changes in the sample structure[56, 65, 83], a phenomenon which will be explored more fully in Chapter 5.

In any fitting procedure it is critically important to accurately account for any sample property, which might be affecting the scattered intensity. Only if the model of the investigated system encapsulates *all* the relevant sample properties will it correctly reproduce the scattered intensity at all wavevector transfers $\mathbf{Q}$ and the fit converges, providing sensitivity to experimental parameters. In the context of the current work, the latter means that even if deviations from the target structure may only be of secondary interest, for instance, in characterising the beam coherence, an accurate model of the spatial sample structure *is* necessary if these deviation have a strong impact on the structure factor of the unit cell.

Therefore, the very convenient analytical form factor of the array given by eqs. 4.22 and 4.23 had to be dropped in favour of a more flexible numerical evaluation, taking into account more subtle geometrical factors like sloped walls or doming of the islands. Hence, in the model finally adopted, each island was characterised by a *surface cut function*

$$S(\mathbf{r}) = h(x, y)$$

determining its total height on a finite two-dimensional grid, representing the x and y coordinates within the unit cell. The three dimensional Fourier transformation of the scattering length density is then performed by replacing each point on the real space grid by the product of its phase contributions in all three dimensions and performing a Riemann sum of these phases at particular locations in reciprocal space. The latter locations are given by all the reciprocal lattice points whose GTRs intercept the detector resolution function so as to obtain the correct phase information of overlapping GTRs. In the limit of kinematical scattering this leads to the structure factor of the unit cell

$$\begin{aligned} A(\mathbf{Q}, h(x,y)) &\approx \sum_{x,y} \frac{f\rho^{\mathrm{num}}}{-iQ_z} \left(1 - \mathrm{e}^{-ih(x,y)Q_z}\right) \mathrm{e}^{-i(Q_x x + Q_y y)} \,\mathrm{d}A \\ &\propto \sum_{x,y} \left(1 - \mathrm{e}^{-ih(x,y)Q_z}\right) \mathrm{e}^{-i(Q_x x + Q_y y)} \,\mathrm{d}A\,, \end{aligned} \quad (4.27)$$

with $f\rho^{\mathrm{num}}$ being the (constant) island scattering length density, $\mathrm{d}A$ is the area of a single grid element and the sum is taken over all grid elements contained in one unit cell. Note that the scattering length density is again considered constant over

the whole volume of the island, since it is still implicitly considered to vary along z only, so that it contributes no modulation of the GTR intensity at constant Q_z. Moreover, in the following analysis all constant factors in eq. 4.27 will be dropped and implicitly enter the scaling constant.

In the lack of any analytical model describing the deviations of the patterned islands from the target structure, the surface cut function $S(\mathbf{r})$ had to be defined in such a way so as to provide an adequate amount of flexibility in describing sloped edges and island doming caused by the deposition through a patterning mask, while keeping the number of open fitting parameters needed to create a sufficiently flexible model as low as possible. The choice was therefore made to allow the model to account for any potentially sloped sides by a double exponential function, smoothly transitioning from its saturation value at substrate level close to a saturation value representing the nominal height of the islands. Furthermore, the domed tops were modelled by a variant of a Pearson VII function, being able to reproduce a wide range of doming shapes, while ensuring a physically reasonable shape. The exact modelling procedure is described in the context of Chapter 5. For now, it suffices if the reader accepts that in the following the unit cell structure factor is modified by a more flexible and more realistic model of the spatial shape of the patterned islands. However, this comes at the cost of a computationally much more demanding evaluation of what is only an approximate solution, which is limited by the finite resolution of the real space lattice the unit cell is defined on.

Exploiting the rotational symmetry of the circular island, its surface cut function has been defined as a function of the horizontal distance to the islands centre r to read

$$S(r) = \begin{cases} \zeta h_\mathrm{n} \exp\left(\frac{r_\mathrm{t}-r}{\sigma_\mathrm{b}}\right) & \text{for } r \geq r_\mathrm{t} \\ h_\mathrm{n}\left(1-(1-\zeta)\exp\left(\frac{-(r_\mathrm{t}-r)}{\sigma_\mathrm{t}}\right)\right) & \text{for } r_\mathrm{t} > r \geq r_\mathrm{n} \\ (h_\mathrm{d}-\tilde{h}_0)\left(\frac{\eta^2}{\eta^2+r^2}\right)^M & \text{for } r_0 > r, \end{cases} \tag{4.28}$$

which is explored in more detail in eqs. 5.5 and 5.6, Fig. 5.7 and the accompanying

discussion. Eq. 4.28 includes the substitutions

$$\zeta = \sigma_{\mathrm{b}}/(\sigma_{\mathrm{b}} + \sigma_{\mathrm{t}}) \tag{4.29a}$$

$$\eta = r_0\sqrt{\frac{\kappa}{\kappa - 1}} \tag{4.29b}$$

$$\kappa = \left(\frac{b_{\mathrm{off}}}{h_{\mathrm{d}} - h_{\mathrm{n}}}\right)^{\frac{1}{M}} \tag{4.29c}$$

$$\tilde{h}_0 = h_{\mathrm{n}} - \Delta h \tag{4.29d}$$

$$r_{\mathrm{t}} = r_0 - r_{\mathrm{off}} \tag{4.29e}$$

$$r_{\mathrm{off}} = \frac{\sigma_{\mathrm{t}}}{1 - \zeta}\ln\left(\frac{t_{\mathrm{off}}}{h_{\mathrm{n}} + t_{\mathrm{off}}}\right), \tag{4.29f}$$

and the open parameters of the model are then given by the *nominal height* and *nominal radius* of the island, respectively h_{n} and r_{n}, the total *height of the doming centre* h_{d}, the *top- and bottom widths* of the sloped island sides σ_{t} and σ_{b}, the *Pearson-VII exponent* M and the two offset parameters b_{off} and t_{off}. The latter define z-offsets of the doming function and the z-value $\geq h_{\mathrm{n}}$ at which the transition from sloped sides to the domed centre function occurs, which both provides additional flexibility to the model in obtaining a wide range of generalised island structures. Defining the *transition radius* r_{t} of eq. 4.28 in this way indirectly via t_{off} has the advantage of being able to fix a range of transitioning heights in a fit more easily.

Importantly, the slightly complicated form of eq. 4.28 was chosen deliberately, so that what is believed to be the most critical parameters (like the nominal height, doming height and nominal radius) remain uncoupled from other parameters, which significantly accelerates most data fitting procedures. Inserting eq. 4.28 into eq. 4.27 and expressing the scattering amplitude of the elliptical island as a linear transformation of a translated and stretched circular island the structure factor of the patterned arrays unit cell evaluates to

$$A(\mathbf{Q})_{\mathrm{u.c.}} = A(Q, h(x,y)) + l_{\mathrm{x}}l_{\mathrm{y}}\,A\left(\tilde{Q}, h(x,y)\right)\mathrm{e}^{-i(x_{\mathrm{off}}Q_x + y_{\mathrm{off}}Q_y)}, \tag{4.30}$$

with $\tilde{Q} = \sqrt{l_{\mathrm{x}}^2Q_x^2 + l_{\mathrm{y}}^2Q_y^2}$. The first term on the right hand side of eq. 4.30 represents the circular island and the second term represents the elliptical island following a suitable real-space translation and scaling of the circular island axes by factors of l_{x} and l_{y} of the elliptical island.

Fitting of simulated to experimental data has been performed utilising the differential evolution algorithm[181] using recommended parameters [189], by min-

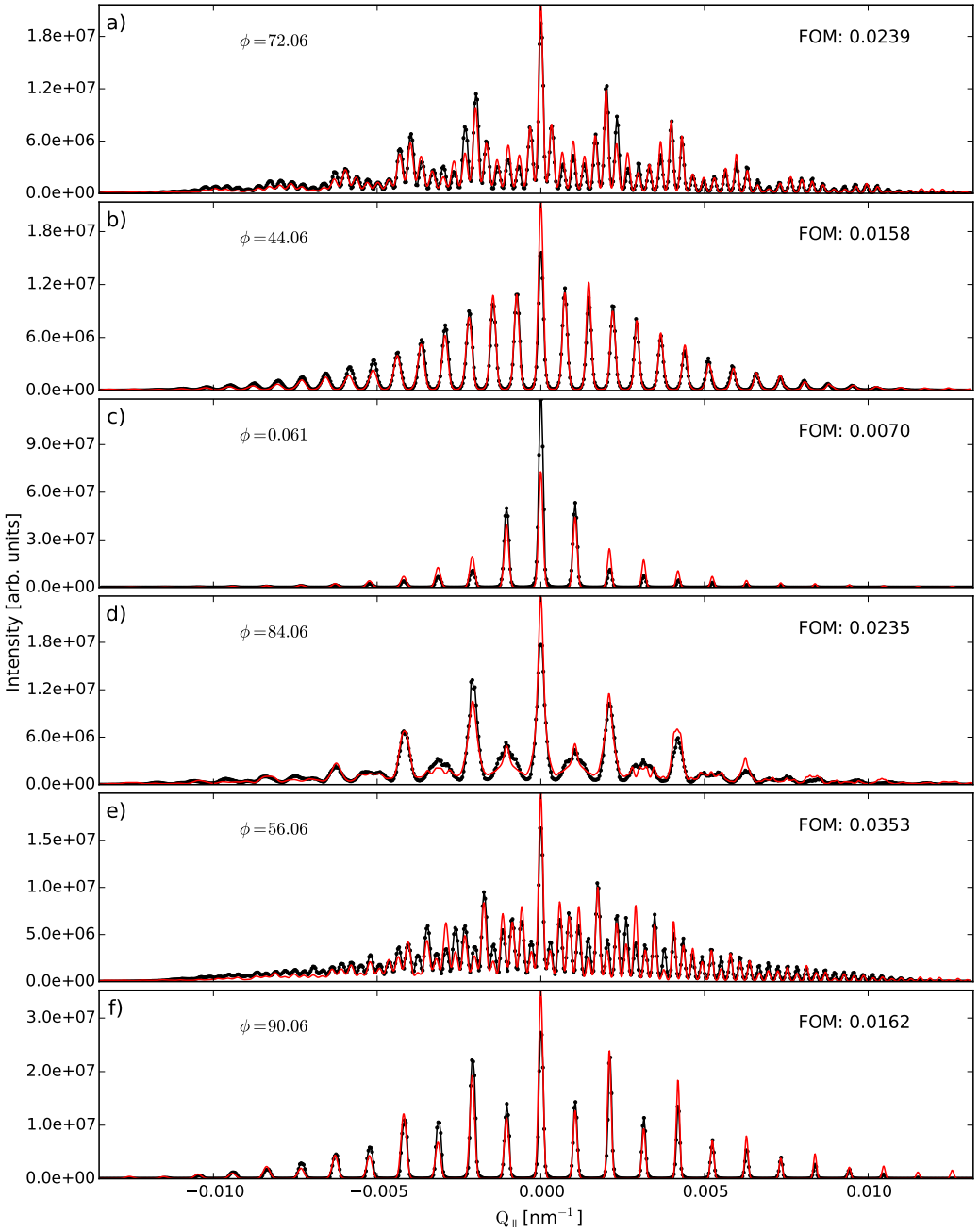

Figure 4.15: Comparison of experimental (black dotted) and simulated (red line) rocking curves of α pattern at selected azimuthal rotation ϕ. The annotated values of ϕ represent fitted parameters, which match experimental data best.

imising the figure of merit of the absolute difference of experimental and simulated data as discussed in section 3.4. The unit cell structure factor has been calculated from eqs. 4.30 and 4.27 using a grid size of 151x151 points, corresponding to a real

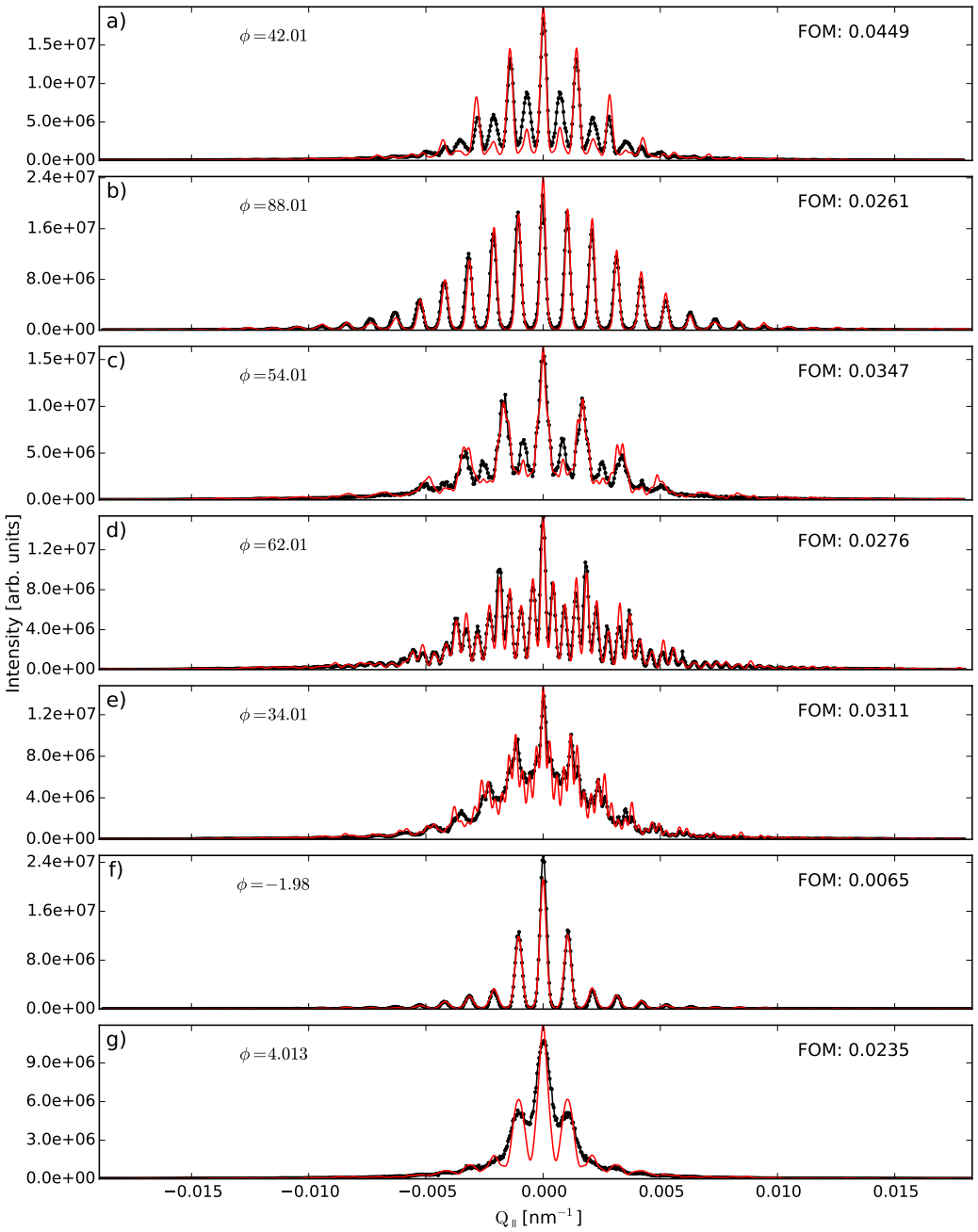

Figure 4.16: Comparison of experimental (black dotted) and simulated (red line) rocking curves of β pattern at selected azimuthal rotation ϕ. The annotated values of ϕ represent fitted parameters, which match experimental data best.

space spatial resolution of 9 nm within the sample plane used in evaluation of the structure factor of the circular islands.

For both the α and β pattern simultaneous fits of simulated to experimental

Parameter	Value [α]	Value [β]
Nominal island height h [nm]	56.6	61.7
Dome height h_d [nm]	2.2	1.4
Bottom edge slope σ_b [nm]	4.6	0.56
Top edge slope σ_t [nm]	21	23
Beam divergence $\Delta\alpha_i$ [mrad]	0.2	0.5
Parallel Detector Acceptance $\Delta\alpha_f$ [mrad]	0.11	0.2
Perpendicular beam coherence $\xi_\perp$ [nm]	230	390
Perpendicular Detector Acceptance $\Delta\phi$ [mrad]	2.5	0.73

Table 4.2: Selection of fitting parameters for the α pattern

data at seven different azimuthal angles ϕ have been performed and are presented in Figs. 4.15 and 4.16. Note that in between the experiments measuring the α and β patterns the beam energy and incident slit size has been adjusted to improve experimental conditions by reducing x-ray fluorescence and improving counting statistics via increasing incident slit width. The first experiment has been performed on the β pattern at 8.8 keV and an incident slit width of 150 µm and the second experiment, on the α pattern, has been performed at 6.5255 keV and an incident slit width of 240 µm. As a consequence, important properties determining the beam coherence have changed from one experiment to the other, making a simultaneous fit of both pattern types impossible. Furthermore, since identification of lattice directions by fine tuning of the azimuthal rotation ϕ was not possible at the time of the experiment, measurements were taken at azimuthal steps of 2°. The final identification of the actual azimuthal rotation with respect to the (10) direction was left out to subsequent analysis, meaning that after a rough identification of lattice directions by eye, the final evaluation of ϕ was performed by inclusion of a fitting parameter ϕ_off in the range 4° to 4°.

The quality of the fits is generally satisfactory, reproducing the qualitative features of the rocking curves in all cases and in many cases reproducing even subtle details. Table 4.2 presents the best fitted values of the individual fitting of the α and β patterns, while Figs. 4.17 and 4.18 presents scans of the FOM as a function of varying a single selected parameter, while keeping all remaining parameters fixed at their fitted values. This presentation highlights the impact of a particular parameter, with well defined minima usually being indicative of high model sensitivity towards that parameter.

The critical parameters determining the quality of the fits have been identified to be the beam coherence both parallel, $\xi_\parallel$, and perpendicular, $\xi_\perp$, to the scattering plane as well as the doming height h_d and nominal height h_n of the is-

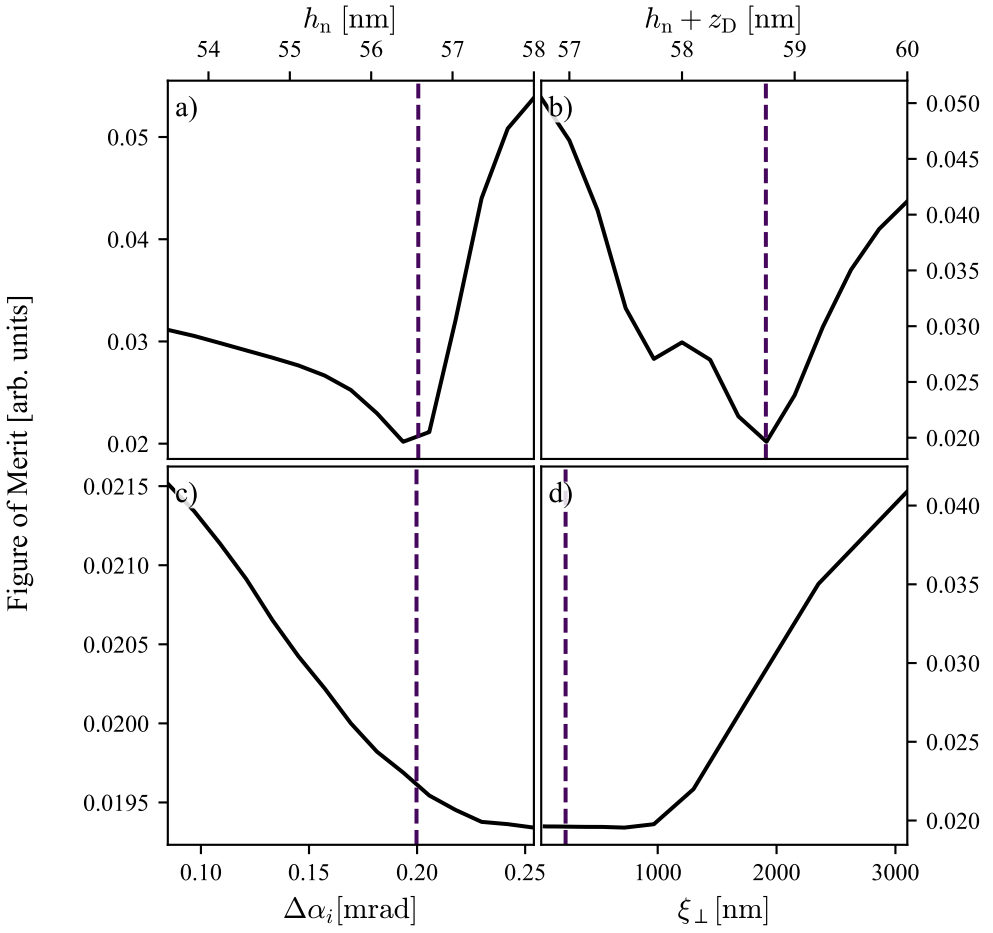

Figure 4.17: FOM scans of selected parameters for fitting the α pattern. Each panel shows a simulation's figure of merit as a function of a specific parameter, while keeping all other parameters at their best values according to the fit. The dotted line indicates the parameter's best value as obtained from the fit. Panel a) shows FOM vs. nominal height h_n (Total island height minus dome height), b) FOM vs. total island height h_d including the doming, c) FOM vs. divergence of the incident beam α_i, and d) FOM vs. perpendicular beam coherence $\xi_\perp$ of the beam.

lands. The minima of both nominal height h_n and total height including doming $h_\mathrm{d} = h_\mathrm{n} + t_\mathrm{d}$ presented in panels a) and b) of Figs. 4.17 and 4.18 coincide very well with the best fit values. In case of the α pattern, the nominal height $h_\mathrm{n} = 56.6\,\mathrm{nm}$ falls slightly short below its design value of 60 nm, while it slightly exceeds the desired value in case of the β pattern. The observed discrepancy can be interpreted as a direct consequence of the sample model; Neglecting the sloped sides, each island can be approximately decomposed into a flat and a domed part. Then, varying the

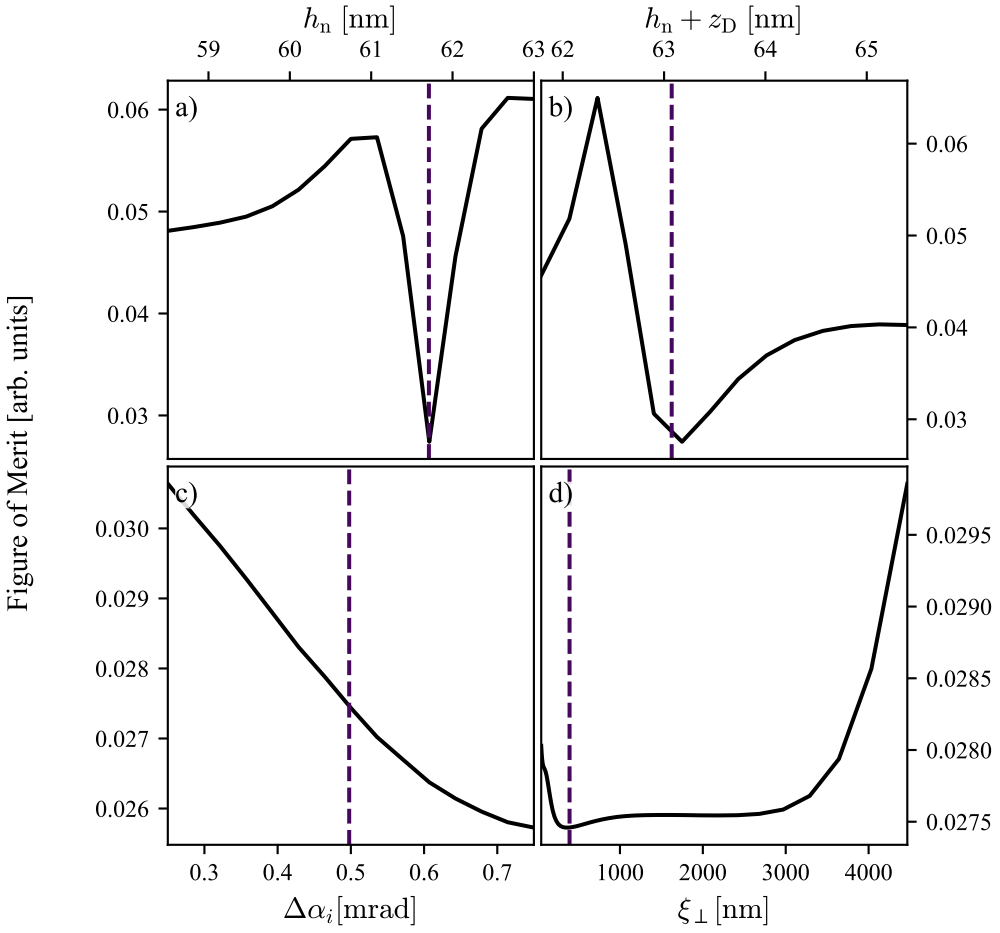

Figure 4.18: FOM scans of selected parameters for fitting the β pattern. Each panel shows a simulation's figure of merit as a function of a specific parameter, while keeping all other parameters at their best values according to the fit. The dotted line indicates the parameter's best value as obtained from the fit. Panel a) shows FOM vs. nominal height h_n (Total island height minus dome height), b) FOM vs. total island height h_d including the doming, c) FOM vs. divergence of the incident beam α_i, and d) FOM vs. perpendicular beam coherence $\xi_\perp$ of the beam.

nominal island height h_n, while maintaining the shape of the dome, will primarily affect the complex exponential term containing z in eq. 4.27. Hence, changes in h_n will mostly manifest in changes of a constant scaling factor, which is compensated for in the fit by adaptation of the global intensity scaling factor, which combines all constant factors determining the registered intensity (like incident beam flux, sample size, etc). In other words, without additional explicit consideration of the Q_z dependence of the scattering, for instance in form of a reflectivity measurement,

the nominal island height is very hard to reproduce from the rocking curves, as it merely enters the calculations as one of the many constant scaling factors of the rocking curve intensity.

The thickness of the dome t_d is found to be 2.2 nm for the α and 1.4 nm for the β pattern. Albeit only relatively small relative to the total island height, t_d plays a particularly decisive role in determining the unit cell structure factor $A(\mathbf{Q}_\mathrm{u.c.})$ and is therefore critically important when a quantitative fit of experimental data is to be obtained. The reason is that island doming boosts high frequency modulation of the form factor as will be shown in the course of chapter 5. If island doming is neglected in the modelling of the sample, the simulation will systematically underestimate high order Bragg satellites and fitting of the data becomes impossible. However, because of the similarity of the patterning processes, the doming height t_d is expected to be similar for both the α and β patterns and despite being small, the discrepancy is significant. The most likely explanation for this result is a combination of an imperfect sample model and measuring both patterns at different x-ray beam energies, the latter affecting the energy dependent scattering length density. The doming of the outer surface of the islands is expected to actually propagate through all of the stacked bi-layers as well, therefore creating additional and unique in-plane components of the structure factor of the unit cell $F(\mathbf{Q})$ within each bilayer. These additional modulations may differ in their effect in between the α and β samples, since changing the beam energy also affected the respective SLDs of the $Co_{68}Fe_{24}Zr_8$ and Al_2O_3 comprising each bilayer. As the scattering model does not include the chemical structure of the multilayer, but rather assumes the islands to be of a homogeneous SLD, the additional effects of bilayer doming are not incorporated within the used scattering model, and may reflect in independent variations of the doming thickness t_d, leading to different values matching the experimental data best, considering the imperfect sample model and differing energy dependent SLD profiles. If both measurements were taken at the same energy, the model would still be slightly off for the reasons just discussed, however, the similarity of the two patterns would likely reflect in both fits converging to an identical doming thickness t_d. The hypothesis of the doming propagating through the bilayers is further strengthened by the SLD profile of the α pattern obtained from independent fitting of the specular reflectivity presented in Fig. 4.21 of section 4.2.6, which taking into account a different sample model, being better suited for fitting Q_z scans. The SLD profile shows that the interface roughness of each bilayer increases the higher up in the stack the bilayer is. The latter is exactly how increasing the doming thickness of bilayers would reflect in the laterally averaged SLD profile of a sample, which is

what a reflectivity measurement is probing.

Figs. 4.17 c) and 4.18 c) show a parameter scan of the divergence $\Delta\alpha_i$ of the incident beam, the quantity that determines the parallel beam coherence along the long axis of the coherence ellipse. In accordance with the experimental set-up, the beam divergence increased after using a wider slit when measuring the β sample. Apart from their absolute difference, both parameter scans reveal very similar behaviour, with the best value according to the fit, curiously, being located in neither local nor global minimum, despite larger values in both cases clearly leading to a smaller figure of merit.

Direct evaluation of the parallel coherence is not straightforward, since it is generally a function of the source angle α_i and changes therefore over the probed range of $Q_\parallel$, according to

$$\xi_\parallel = \frac{\lambda}{2}\frac{1}{\Delta\alpha_i \sin\alpha_i}, \tag{4.31}$$

where the coherence has been assumed to be determined purely by the divergence of the impinging radiation, so the detector and wavelength spread according to eq. 4.8 have been neglected.

Finally, panel d) of Figs. 4.17 and 4.18 shows the relationship of fit quality and coherence perpendicular to the scattering plane $\xi_\perp$. The FOM continuously decreases with $\xi_\perp$ down to almost exactly 1 µm, below which the FOM plateaus and variation in the FOM is less drastic. This makes intuitive sense, since at a certain threshold, islands which are even slightly offset in their projection along the incident wave field, will not scatter coherently and so the scattered signal stays effectively the same when reducing the coherence even further. The best value of the α pattern, as obtained from the fit, appears more or less chosen randomly from within the range of basically constant FOM. Interestingly, in case of the β pattern, the figure of merit steeply increases for values of the perpendicular coherence $\xi_\perp \lesssim 300\,\text{nm}$. This is interpreted as a characteristic of the sample geometry, arising if perpendicular coherence $\xi_\perp$ lies within an intermediate range between the high coherence limit and vanishing perpendicular coherence. When aligned along the (10) direction, the width of the coherence ellipse has to exceed a certain threshold in order to coherently cover at least parts of both circles and ellipses. This is in contrast to the geometry of the α pattern, where the alignment of the circles and ellipses along (10) means that not such a high amount of sensitivity to the intermediate coherence length exists, since whenever an ellipse is illuminated coherently, the circles scatter coherently as well. In other words, there exists no lower limit for $\xi_\perp$ for the α pattern, below the scattering changes qualitatively because the respective island do not even partially

scatter coherently.

Figs. 4.19 and 4.20 show reproductions of the mapping of parallel wavevector transfer $Q_{\parallel}$ vs. azimuthal rotation ϕ of the α and β pattern, respectively. The full set of azimuthal rotations spanning more than 180° has been calculated according to the best parameters obtained from the fitting the limited set of rocking curves as seen in Figs. 4.15 and 4.16, leading to generally satisfying agreement between simulated and experimental data.

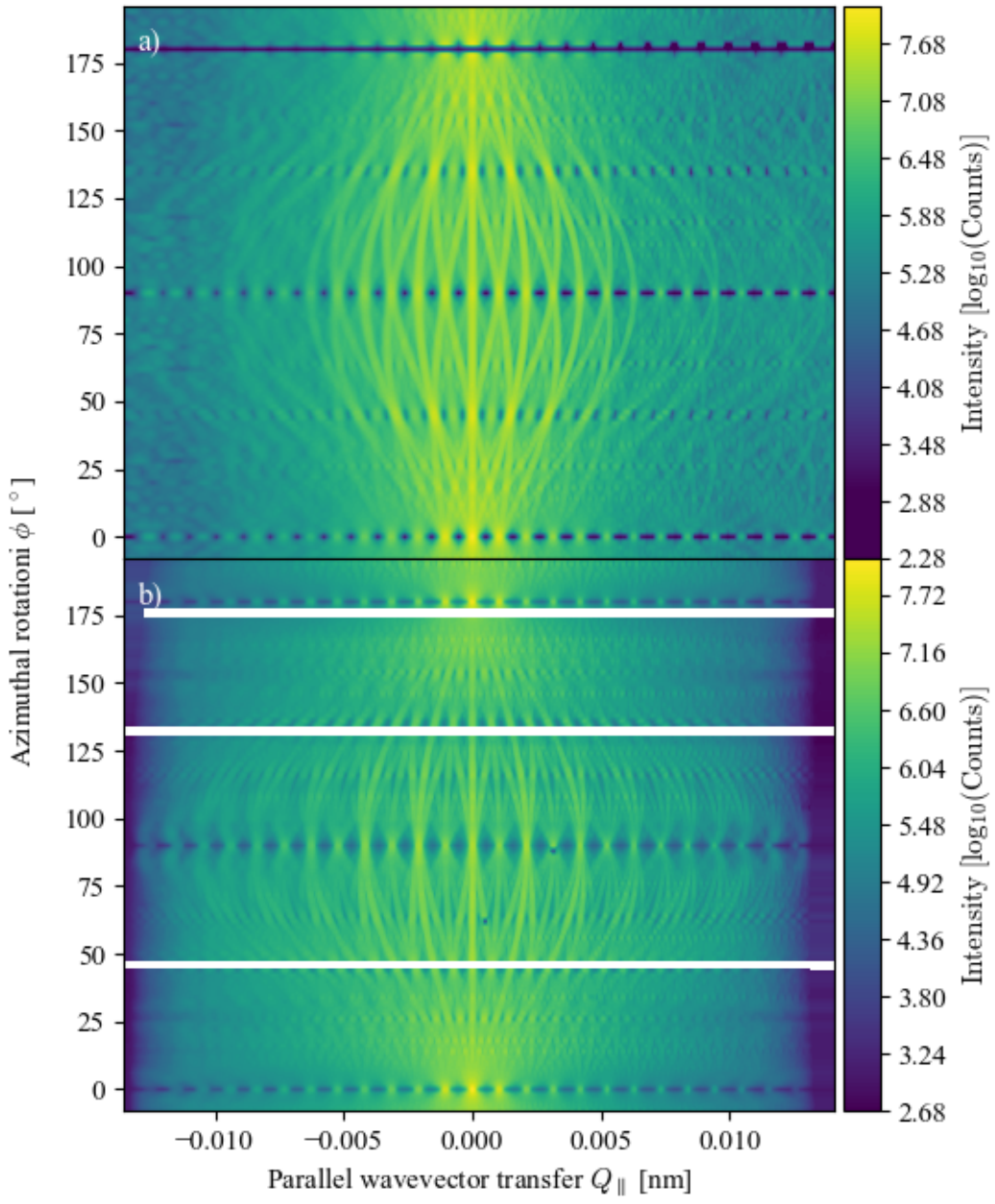

Figure 4.19: Simulation (a) and experimental data (b) of the azimuthal map of the α pattern.

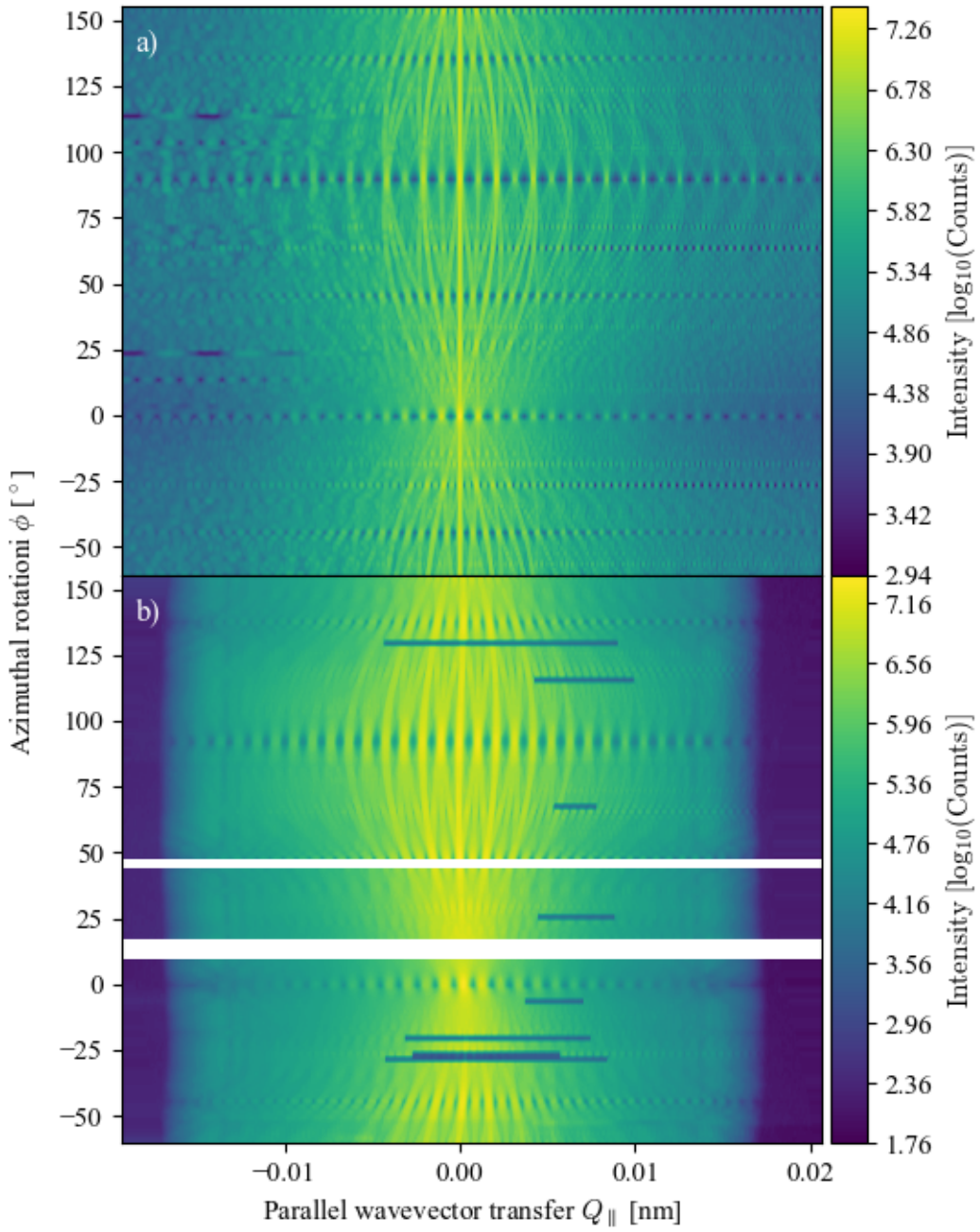

Figure 4.20: Simulation (a) and experimental data (b) of the azimuthal map of the β pattern.

4.2.6 Specular Reflectivity

In the previous section it was shown that in order to obtain a satisfactory fit to experimental data, the sample model had to be adapted to allow for deviations of the nominal sample structure in the form of island doming. Despite the doming being comparatively small (only 2.2 nm compared to about 60 nm total height) the impact on the satellite modulation was profound as can be witnessed, for instance, by comparing Figs. 4.13 and 4.15. The question now arises, in how far island doming might be affecting the specular reflectivity of the sample as well and if reflectivity measurements support the domed island model.

Because of its vertical wavevector transfer, $|\mathbf{Q}| = Q_z$, reflectivity measurements are sensitive to the averaged scattering length density along the sample normal only. That means that on the one hand any coherence projections onto the sample plane can safely be neglected. On the other hand, the temporal coherence along the beam is under all conceivable experimental conditions sufficient to coherently illuminate the sample along its very thin z-projection. Hence, three models of increasing complexity (two of which are including doming) representing the out-of-plane SLD-profile of the sample have been fitted to the experimental data in order to determine which matches the experimental observations best.

Fitting has been performed using the freely available GenX-software[208], utilising Parratt's Recursive Method, which is discussed in section 2.2.5. Although the software package was designed for fitting of continuous multilayers, the insensitivity to the in-plane chemical structure of the sample allows fitting of reflectivity curves, taking into account the spatially averaged scattering length density at height z of the sample, hence requiring the periodic nature of the multilayer to reflect in the simulated SLD profile.

All models assumed a stack of ten identical bilayers of $Co_{68}Fe_{24}Zr_8$ and Al_2O_3 as well as a seeding and terminating layer of Al_2O_3. The thickness of each sublayer was coupled by a common bilayer thickness. Each bilayer was assumed to be iden-

Parameter	FittedValue
bilayer thickness d_{bl} [nm]	6.0
thickness Co layer d_{Co} [nm]	2.7
thickness of bottom Al buffer $d_{\mathrm{Al,bottom}}$ [nm]	3.7
interface roughness σ_{CoFeZr} [nm]	0.51
interface roughness σ_{Al} [nm]	0.40

Table 4.3: Selected best fit parameters obtained from fitting of the simple model to experimental reflectivity data.

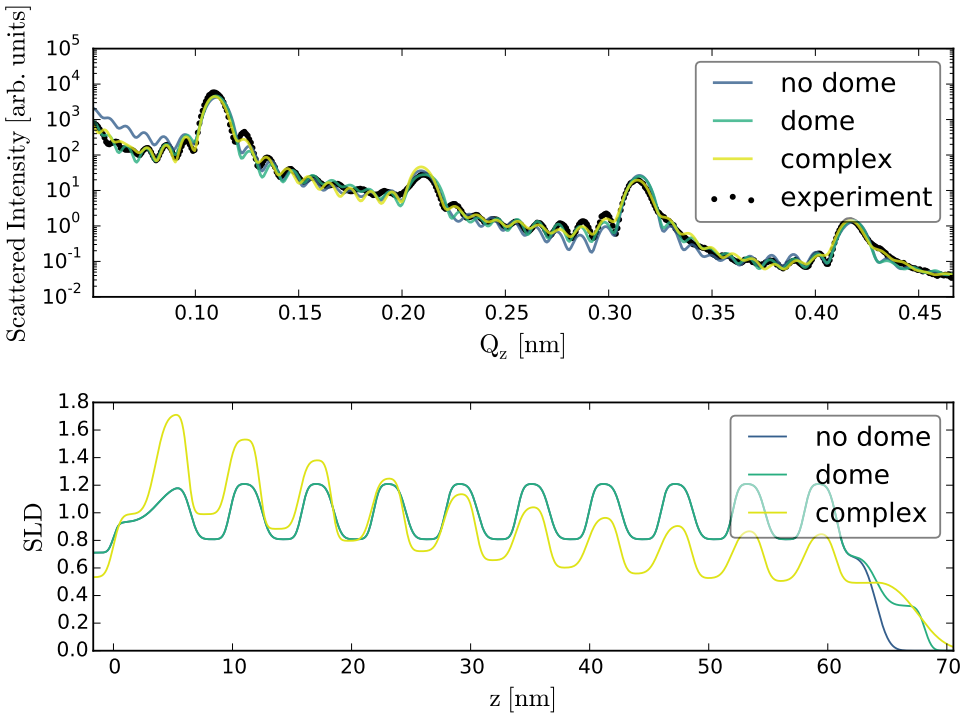

Figure 4.21: Reflected intensity (top) and SLD profile in z-direction (bottom) of the α pattern. Despite strong differences in the SLD profiles of the respective models the effect towards the reflected intensity is relatively weak.

tical with respect to its chemical profile and the open parameters of the bilayer consisted of the respective sublayer's SLD and interface roughness and the total thickness d_{BL} as well as the thickness of the $Co_{68}Fe_{24}Zr_8$ sublayer. Consequently, the thickness of the Al_2O_3 sublayer $d_{\mathrm{AlO}} = d_{\mathrm{BL}} - d_{\mathrm{Co}}$ was fully determined by the respective thickness of the two remaining layers. The most important fitting parameters using this sample model are presented in table 4.3.

The fit to experiment and corresponding SLD profile are given by the blue curves in Fig. 4.21. The fit obtained in this way is generally of satisfying quality, indicating a layer period which almost exactly matches the target bilayer thickness of 6 nm, and a thickness of the Cobalt layer $d_{\mathrm{Co}} = 2.7\,\mathrm{nm}$, implying the thickness of the aluminium layer to be $d_{\mathrm{Al}} = 3.3\,\mathrm{nm}$, both slightly deviating from their nominal thickness $d_{\mathrm{Co}}^{\mathrm{nom.}} = d_{\mathrm{Al}}^{\mathrm{nom.}} = 3\,\mathrm{nm}$. The fit further allowed the characterisation of growth parameters like the interface roughness σ_{Co} and σ_{Al}, respectively.

Nevertheless, in a second fit the SLD profile of the sample was modelled in a less restrictive way, which allowed the atomic number density ρ^{num} of each layer to depend on its lower neighbour's density. The idea here is that the model is given the

Parameter	Fitted Value
bilayer thickness d_{bl} [nm]	6.03
thickness CoFeZr layer d_{CoFeZr} [nm]	3.03
thickness bottom AlO buffer $d_{\mathrm{AlO,bottom}}$ [nm]	3.02
dome thickness h_D [nm]	3.05
CoFeZr c_0	4.48
CoFeZr c_1	-0.20
CoFeZr c_2	0.019
AlO a_0	8.32
AlO a_1	-0.38
AlO a_2	0.01
γ_2	0.76
γ_3	0.80
γ_4	0.82
γ_5	0.83
γ_6	0.86
γ_7	0.94
γ_8	0.87
γ_9	0.91
γ_{10}	0.77

Table 4.4: Selected best fit parameters obtained from fitting of the complex model to experimental reflectivity data.

possibility to reflect changes in island geometry by means of adapting the laterally averaged SLD. Hence, sloped side walls would be witnessed by a change in SLD traversing one layer to another. Hence, the density of each sublayer ρ_i for $i \geq 2$ is calculated via

$$\rho_i^{\mathrm{num}} = \gamma_i \, \rho_{i-1}^{\mathrm{num}}, \tag{4.32}$$

and the first layer's density ρ_1^{num} and γ_{2-9} are all fitted independently.

Furthermore, the interface roughness of CoFeZr and Al_2O_3 layers i were calculated via

$$\sigma_{\mathrm{CoFeZr},i} = c_0 + c_1 \, i + c_2 \, i^2 \tag{4.33a}$$

$$\sigma_{\mathrm{AlO},i} = a_0 + a_1 \, i + a_2 \, i^2, \tag{4.33b}$$

to, again, allow for a more flexible model. The motivation here was that stress induced doming of the island would have a larger effect towards the upper layers. The latter would lead to an increased average interface thickness because of the additional height variation of the interface from centre to periphery.

Finally, a top layer of thickness equal to its roughness was added to the

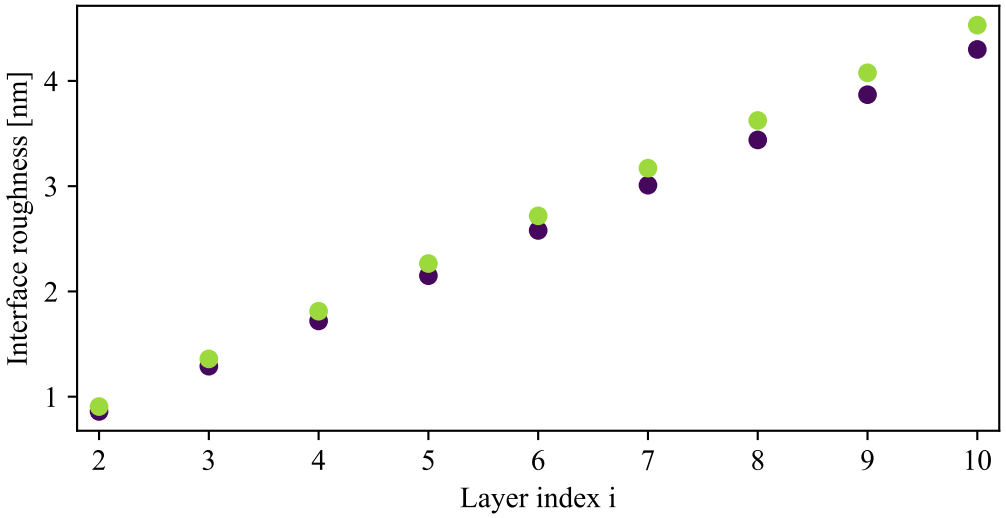

Figure 4.22: Interface roughness of the CoFeZr and Al_2O_3 interfaces as a function of bilayer i following the complex sample model. Both types of interfaces were fitted independently from each other (although within the same optimisation procedure), obeying a polynomial model of order 2, given by eq. 4.33. It is found that for both interface types the roughness appears to be increasing almost perfectly linearly with i, which is in accord with the hypothesis of non-uniform growth of the islands as a result of the pre-patterning of the sample.

model to account for sample doming. This is a rather crude approximation, leading to an error-function-like tail to the SLD profile, similar to what would be expected to be observed in case of island doming. The range of allowed values of each γ_i spanned 0.75 to 1.25, so this model assured some flexibility in between the density of neighbouring layers, without decoupling all layer density completely.

A fit and corresponding SLD profile using this model is presented by the yellow lines in Fig. 4.21 and all relevant fitting parameters are shown in table 4.4. The quality of the fit does slightly improve with respect to the simpler model (most noticeably in the direct vicinity of the Bragg peaks, although the differences are subtle), despite the SLD profile as a hole changing somewhat dramatically. It was found empirically by repeating the fitting procedure multiple times that, although the effect towards the quality of the fit is small, the SLD of higher layers is consistently drawn towards decreasing value, as can be seen by the yellow line in the bottom panel of Fig. 4.21. At the same time, the width of the Cobalt and Aluminium interfaces of bilayer i, following eq. 4.33, are systematically increasing with i, as is shown in Fig. 4.22. It can be seen that the interface width tends to linearly

increase with the bilayer index, which agrees with an non-uniform growth process of the elements, preferentially depositing material closer to the centre of the holes provided by the patterning mask. Consequently, chemical layers getting increasingly deformed the higher they are located in the bilayer stack.

Furthermore, as is the case for the simpler model, a large thickness of the topmost layer is reproducibly improving the quality of the fit, as it is seen to work as a natural continuation of the envelope function modulating the SLD profile of the bilayer stack.

To conclude, reflectivity measurements do not contradict domed island structures and in fact hint towards domed models being more adequate to reproduce the experimental observations. However, unlike to the case of Q_x scans, the exact choice of model does after all only slightly affect the simulated outcome. In fact, even physically completely unreasonable SLD profile were able to fit the experimental data somewhat satisfactory, so in this case x-ray reflectivity proved to be at most a complementing technique, very well suited to resolve the out-of-plane structure of the stratified medium, but not able to uniquely resolve the in-plane structure of a patterned array from its averaged depth profile.

4.3 Summary

In the first section of this chapter, a framework for simulating low beam coherence conditions and modelling the detector resolution function R were developed under particular consideration of micro- and nano-patterned arrays. It was shown how under low coherence conditions grating truncation rods are significantly widened, replacing spatially confined grating truncation rods with diffraction planes, due to a softening of the diffraction condition. Each diffraction plane is anchored on a reciprocal lattice point, and even if the lattice point does not lie within R, the latter might still be intersected by a finite section of the diffraction plane, therefore contributing to the detected intensity. In effect, especially when using an open detector set-up, the number of detected diffraction planes under low coherence conditions is usually much larger than the number of GTRs directly intersecting R under conditions of large beam coherence, which is precisely what has been observed in experiment.

It was further shown how the scattered intensity of a single coherence ellipse depends on its exact spatial location on the sample, and how the convolution theorem can be used in order to calculate the scattered intensity of arbitrarily small coherence areas. Further, it was discussed how the scattered intensity is calculated under the additional restriction of overlapping GTRs, requiring coherent phase summation

along the overlapping areas of neighbouring GTRs and real space translation of the coherence ellipse, both of which is usually avoided under conditions of high beam coherence.

In the second section of the chapter, a framework has been utilised in order to obtain insight about the sample structure as well as to quantify the beam coherence properties both parallel and perpendicular to the scattering plane. Two complementary sample models have been utilised in order to characterise the sample. One model, agnostic of the internal chemical structure of the sample, has been successfully utilised to reproduce rocking curves at a variety of azimuthal rotation angles of the sample, while the second model, reproducing the averaged chemical SLD depth profile, has been used in order to simulate the x-ray reflectivity of the sample. As it reduces the three-dimensional sample structure to a laterally averaged SLD, the model used in reflectivity appears too oversimplified as to provide meaningful insight into in-plane components of the sample structure. On the other hand, the model used to reproduce the rocking curves runs into problems when the sample structure significantly deviated from perfectly flat islands. However, the shortcomings of both models are well understood and form a consistent picture as to why fits deviate from experimental data. The two complementary models highlight the importance of being able to accurately model both lateral geometry as well as the three-dimensional chemical structure of patterned arrays. Further, a unified model, that allows simultaneous fitting of both rocking curves as well as specular reflectivity has been identified as highly desirable, which is, amongst others, the topic of chapter 5.

In order to fit the experimental data, the modular structure of the simulation code as shown in Fig. 1.1 was found advantageous in being able to easily switch between the respective approaches in calculating the scattering structure factor $F(\mathbf{Q})$ of the unit cells of the α and β patterns, replacing the semi-analytical approach of section 4.2.4 with the more flexible, yet computationally more demanding, fully numerical model discussed in section 4.2.5.

Chapter 5

Three dimensional Modelling of Magnetic Patterned Arrays

Chapter 4 primarily dealt with the effects of beam coherence towards the intensity registered in an experiment. For the most part, it was sufficient to utilise comparatively easy analytical expressions to model the spatial structure of the sample when developing the *low-coherence scattering framework*, only to, out of necessity, introduce a more complex model in the final sections. This chapter, on the other hand, focusses, amongst others, on the development of a generic *spatial modelling framework* of arbitrary sample structures of patterned arrays. The discussion follows the line of the whole process of fitting a particular sample of a patterned array, which turned out to require a highly non-idealised modelling framework to reproduce the experimentally observed x-ray scattering. However, the explicit implementation of the model is presented along with the general ideas of the scattering framework, so that translating the concepts to a different system is straightforward.

Despite the modelling process being time consuming and tedious, the experimentally observed sensitivity to often subtle geometrical deviations from a nominal sample structure makes diffraction of patterned arrays an excellent tool for extracting a plethora of characterising information unavailable by most other experimental techniques. This way, information about the internal magnetic state of a sample is generated, provided the energy of the incident x-ray field is tuned to a resonance edge of the sample material. Hence, this work represents the first attempt of solving both the chemical and magnetic structure by means of parametric fitting of patterned arrays consisting of islands obtaining an oxidised shell and a magnetic core. Along the way to fitting the experimental data of this specific sample, the general framework of fitting patterned arrays will be developed. This allows to easily extend

this work to a wide range of similar patterned arrays, by means of both following the discussing on common phenomena as well as providing a detailed description of the underlying mathematical and computational modelling.

However, in order to keep things simple, in this chapter only saturated magnetic states, i.e. all internal magnetic moments aligned parallel, will be considered, whereas chapter 7 extends the theory towards spatial distributions of internal magnetic moments within the scattering structure.

5.1 Experimental Observations

The samples dealt with in this section have been prepared by sputter deposition of an amorphous $Fe_{13.5}Pd_{86.5}$ alloy into a pre-patterned lithographically defined template as described in section 3.2 and Östman et al. [77] and both an SEM and AFM image of which are presented in Fig. 5.1. However, as can be seen in Figs. 5.2 and 5.3, the AFM linescans are prone to systematic readout errors, most likely related to the sharp height gradients at the island edges, since distinct spikes appear at almost every island edge along the scan direction (best seen in Fig. 5.3). These spikes are almost certainly scan artefacts, as they would otherwise break the rotational symmetry of the disks. Because of their apparent low reliability, extracting trustworthy spatial information from AFM scans of patterned arrays seems to not be easy, again stressing the importance of alternative analysis techniques.

The patterned array consisted of a two-dimensional square lattice of circular islands of radius $R = 225\,\text{nm}$, nominal height $10\,\text{nm}$ and lattice pitch $d = 513\,\text{nm}$.

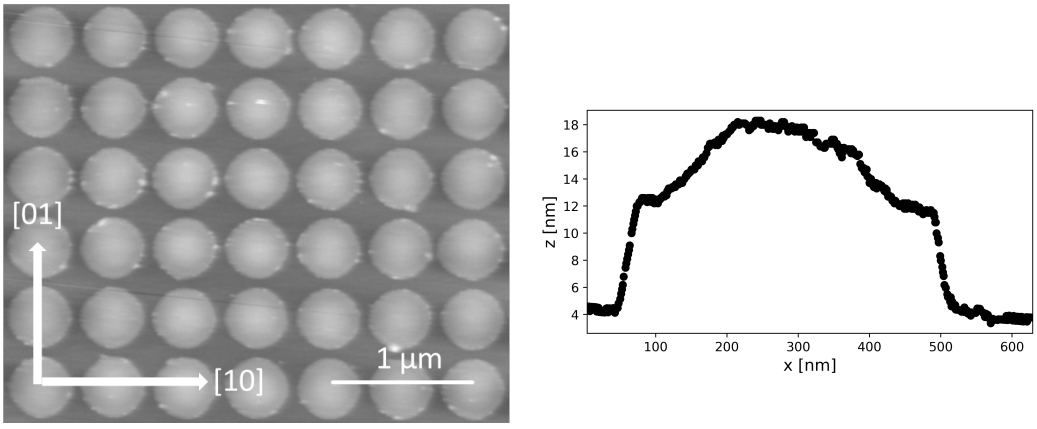

Figure 5.1: Left: SEM image of the sample, showing the high lateral conformity of the FePd patterned array studied herein. Right: A lateral AFM scan through an island centre of the same array, showing an characteristic domed top.

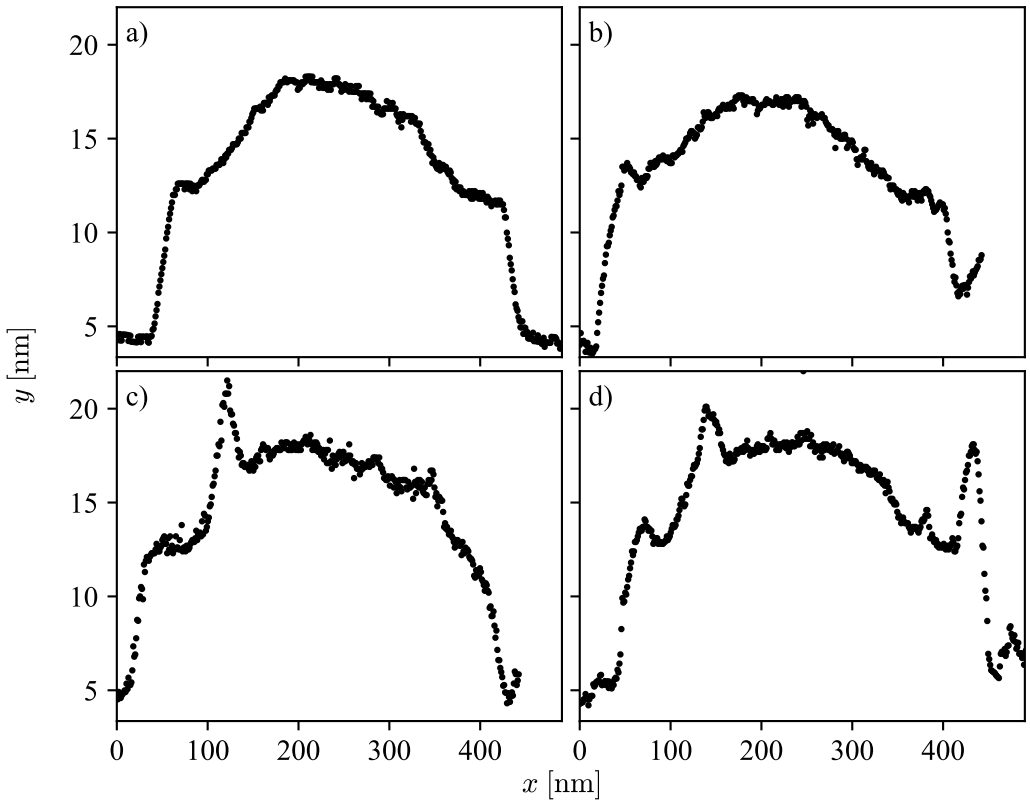

Figure 5.2: Four randomly chosen AFM linescans along individual nano disks. Although each island shows a similar doming geometry, the linescans often include sharp spikes, most likely due to problems related to large height-gradients of the sample.

Below the Curie Temperature $T_C \approx 308\,\mathrm{K}$[77] the FePd exhibits a strong magnetic response, as palladium is highly polarisable in the vicinity of the dopant iron, developing a high magnetic moment per iron atom of about 10 to 12 μ_B[209][210]. Upon being magnetised, the atomic scattering factor f of a material is altered according to the general form seen in eq. 2.31 derived in chapter 2. Under small angle conditions and using circularly polarised radiation the simpler form found in eq. 2.32 may be used, reading

$$f = f_c(Q, E) \pm f_m(E, \mathbf{Q}, m_x), \tag{5.1}$$

where f_c includes the Thomson scattering $f_0(\mathbf{Q})$ and (energy dependant) resonant correction terms $f'(E)$ and $f''(E)$ representing the *charge scattering*, f_m depends on the angle between the wavevector transfer $\mathbf{Q}$ and the local magnetic moment $\mathbf{m}$, only exhibiting maxima near appropriate resonance edges. Finally, the sign of the

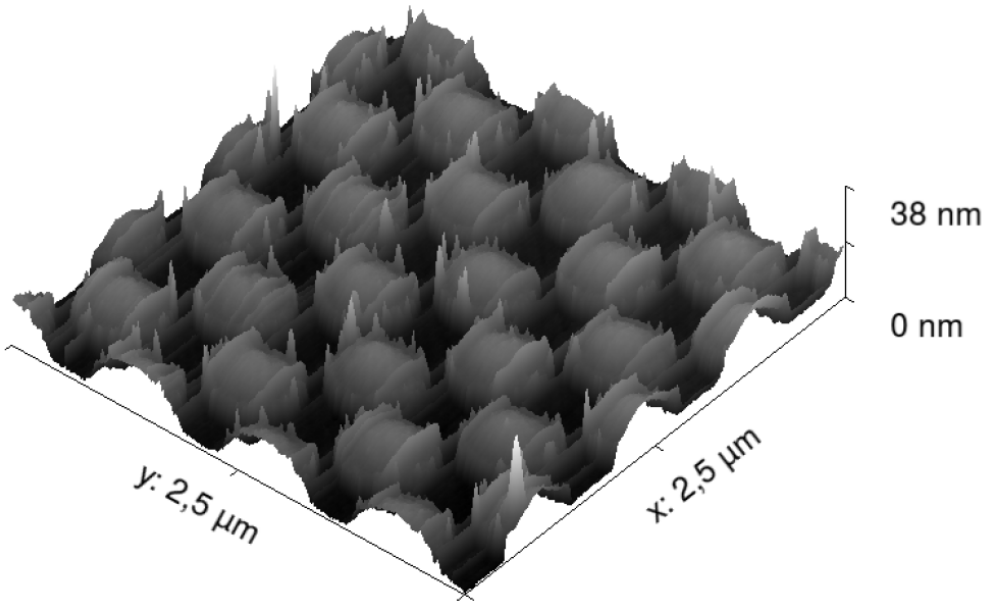

Figure 5.3: Two dimensional AFM sample profile. Spikes systematically appear at the island edges along the y-axis. As these apparent spikes violate the isotropy of individual disks (and their formation process) they are considered artefacts. Image adapted from [171].

magnetic term depends on the helicity of the circularly polarised radiation as can be seen from inspection of eq. 2.30.

X-ray Resonant Magnetic Scattering (XRMS) was then utilised to investigate magnetised patterned arrays by performing multiple experiments on the 4-ID-D beamline at the *Advanced Photon Source* (APS)[211], Chicago, Illinois. The experiments presented in this chapter were performed on two different sample temperatures, 200 K and 30 K, both well below the Curie Temperature T_C of the island material. Furthermore, an external magnetic field of 12.85 mT was applied parallel to both the sample- and scattering plane, which was sufficient to fully magnetise the islands[77]. A strong magnetic sensitivity of the incident radiation was obtained from tuning the photon energy to 3.174 keV, which is located just below the Pd L_3 edge at 3.187 keV, ensuring an increased resonant response of f', at the same time minimising the effect on f'', which would otherwise lead to enhanced fluorescence at and above the absorption edge.

Since the islands were magnetically saturated, all of the local magnetic moments $\hat{\mathbf{m}}(\mathbf{r})$ were in parallel alignment along both the scattering- and sample plane,

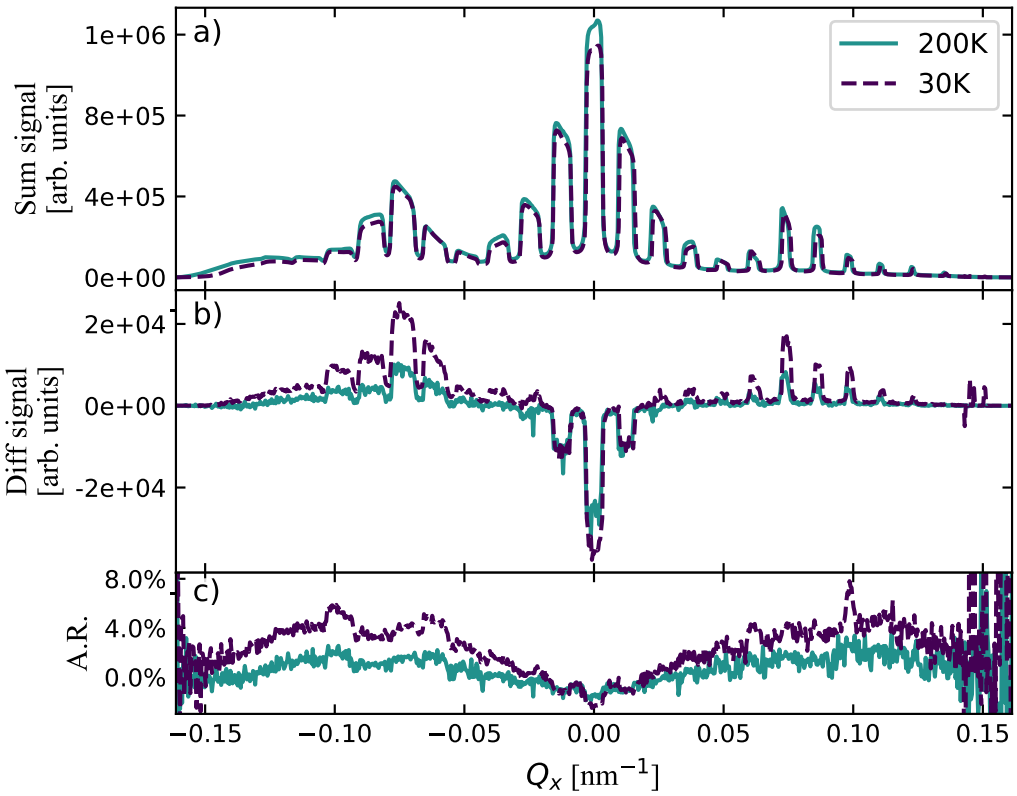

Figure 5.4: Sum, difference and asymmetry ratio obtained from rocking scans taken at $2\theta = 8.12\,°\mathrm{C}$ corresponding to $q_z = 2.27\,\mathrm{nm}$. Scans were performed at temperatures 200 K and 30 K and all data are normalised with respect to integration time per angular step. The difference signal and asymmetry ratio seen in panel b) and c) and significantly increased at the 30 K measurement, in accord with the increased bulk magnetisation of ferromagnetic material at lower temperatures.

and hence $\hat{\mathbf{m}}_x = \hat{\mathbf{x}}$, implying $m_x = 1$. Under these conditions, the local scattering factors simplify further to read

$$f^{\pm} = f_0 + F^{(0)} \pm F^{(1)}, \tag{5.2}$$

where now the explicit dependence on E and m_x has been omitted since these parameters are held constant. As can be seen, $F^{(0)} = f' + if''$ and $F^{(1)} = f'_{\mathrm{mag}} + if''_{\mathrm{mag}}$ are simply the (complex) resonant charge- and magnetic correction terms, which are often not very well defined and generally depend on the local atomic environment and electronic band structure of a material. In a typical experiment using circularly polarised x-rays, the local scattering factors $f^{\pm}$ manifest in slightly different intensities I^+ and I^-, corresponding to left- and right circular polarisation

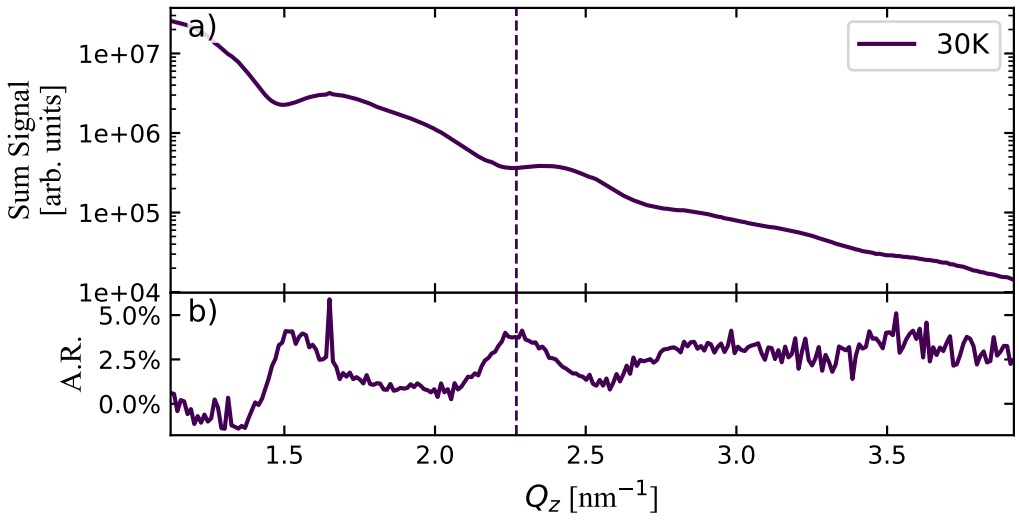

Figure 5.5: Sum signal and asymmetry ratio in reflectivity scattering geometry. Unfortunately no high temperature measurements could be performed due to time constraints at the time of the experiment. The dashed dashed line marks the q_z value the rocking curve has been performed at, thus maximising the asymmetry ratio of the specularly reflected beam.

according to the definition given by eqs. 2.27 a) and b).

Figs. 5.4 and 5.5 present a comparison of a set of quantities derived from I^+ and I^- taken respectively during rocking curve and reflectivity scans. They were obtained by swapping the beam helicity at every angular step of the diffractometer. By splitting up the scattered amplitude into charge- and magnetic parts

$$A^{\pm}(\mathbf{Q}) = A_c(\mathbf{Q}) \pm A_{\mathrm{mag}}(\mathbf{Q}) \tag{5.3a}$$

$$I = AA^* \tag{5.3b}$$

and subsequent expansion, the *sum signal*, *difference signal* and *asymmetry ratio* can be expressed by

$$I_{\mathrm{sum}} = I^+ + I^- = 2A_{\mathrm{c}}A_{\mathrm{c}}^* + 2A_{\mathrm{mag}}^*A_{\mathrm{mag}} \tag{5.4a}$$

$$I_{\mathrm{diff}} = I^+ - I^- = 2A_{\mathrm{c}}A_{\mathrm{mag}}^* + 2A_{\mathrm{c}}^*A_{\mathrm{mag}} \tag{5.4b}$$

$$A.R. = \frac{I_{\mathrm{diff}}}{I_{\mathrm{sum}}} = \frac{I^+ - I^-}{I^+ + I^-}. \tag{5.4c}$$

As can be seen in eq. 5.4 a) and b), the sum signal consists of an incoherent superposition of charge- and magnetic intensities, which is always > 0. The difference

signal, however, includes charge and magnetic mix terms, which are products of amplitudes of arbitrary phases and can therefore take on positive or negative values, which is what is being observed in Figs. 5.4 and 5.5.

From these figures a couple of observations can be made:

1. As a result of the lateral periodicity of the patterned array, the sum signal of the rocking curve presented in Fig. 5.4 a) exhibits at least 12 orders of satellite diffraction peaks located at $Q_{x,\mathrm{GTR}} = n\,\Delta Q_x = n\,\frac{2\pi}{d} = n\,0.0122\,\mathrm{nm}^{-1}$, corresponding to the nominal lattice constant $d = 513\,\mathrm{nm}$ and diffraction order $n \in \mathbb{Z}$.

   The satellites decrease in width with Q_x and despite the supposedly Gaussian beam properties, satellites look remarkably non-Gaussian, which is particularly true for orders $< +6$. The latter exhibit sloped tops both rising and falling with Q_x. As can be seen, sum signals obtained at different temperatures vary only slightly, which is consistent with the separation of charge- and magnetic intensities as seen in eq. 5.4 a) in conjunction with the modulus of the magnetic amplitude being much smaller than the modulus of the charge scatter, i.e. $|A_{\mathrm{mag}}| \ll |A_{\mathrm{c}}|$ (or, alternatively, $f_0 + F^{(0)} > F^{(1)}$), even if the material is close to its saturation magnetisation.

2. The islands of the patterned array are nominally cylindrical, and as such, their structure factor $F(\mathbf{Q})$ was expected to resemble the Fourier transformation of a circle,

$$F(\mathbf{Q}) = |2\pi R J_1(QR)|^2,$$

   with $R = 225\,\mathrm{nm}$ being the island radius and J_1 the first Bessel function of kind 1 (the constant island height not contributing to any modulation along Q_x). The latter does clearly not provide a satisfying modulation function to the experimental data as becomes obvious from comparing Figs. 5.4 a) and 5.6 b).

3. The difference signal in the rocking curve as seen in Fig. 5.4 b) expectedly reveals the formation of satellites as well. However, the charge-magnetic interference leads to a modulation of the peaks, being negative for the orders -3 to 3 and positive for the remaining. The temperature dependence leads to qualitatively similar difference signals, however, the 30 K measurements reveals a significantly increased difference signal, which is in accord with increasing island magnetisation at lower temperatures.

4. The asymmetry ratio present in Fig. 5.4 c) gives an idea of the modulating

function of the difference signal and reveals a maximum difference in intensity of sum and difference signal of about 2% for the 300 K and up to 8% for the 30 K sample.

5. The sum signal of the specularly reflected intensities shown in Fig. 5.5 a) shows no easily identifiable beating, which again is in disagreement with the relatively simple nominal sample structure. Flat islands lead to a sharp out-of-plane SLD profile of the sample, which would lead to well-defined periodic modulation in reciprocal space of period

$$\Delta Q_z = \frac{2\pi}{10\,\mathrm{nm}} = 0.63\,\mathrm{nm}^{-1},$$

at least within the sum signal. The reflected intensity actually measured, readily hints at a more complex depth profile of the sample. Together with the unexpected intensity modulation of the rocking curves, this gives clear indication that the real sample structure deviates in a very significant way from what was desired in the patterning process.

6. Finally, the asymmetry ratio of the reflectivity shows clear indication of charge-magnetic interference of up to 5% of the sum signal.

The rest of this chapter will focus on understanding these observations, using them to find an adequate way of modelling the scattering of patterned arrays and obtain information about the spatial geometry and magnetic structure of the system.

5.2 Sample Modelling

Clearly, if quantitative reproduction of experimental results is to be aspired, a model has to take into account all relevant properties of a particular sample. When, as already discussed earlier, dealing with an x-ray reflectivity measurement, it is often sufficient to model the sample in a one-dimensional way, only taking into account the SLD depth profile of the sample, since this is the only property a reflectivity measurement is sensitive to. Depending on the sample, this modelling can get arbitrarily complicated, but the problem remains essentially one-dimensional. By the same token, one cannot expect to obtain any in-plane spatial information about any sample from doing a reflectivity measurement without projecting the out-of-plane data onto a three-dimensional model of the sample, in this way *inferring* spatial information. In this way it is possible to fit the reflectivity measurement

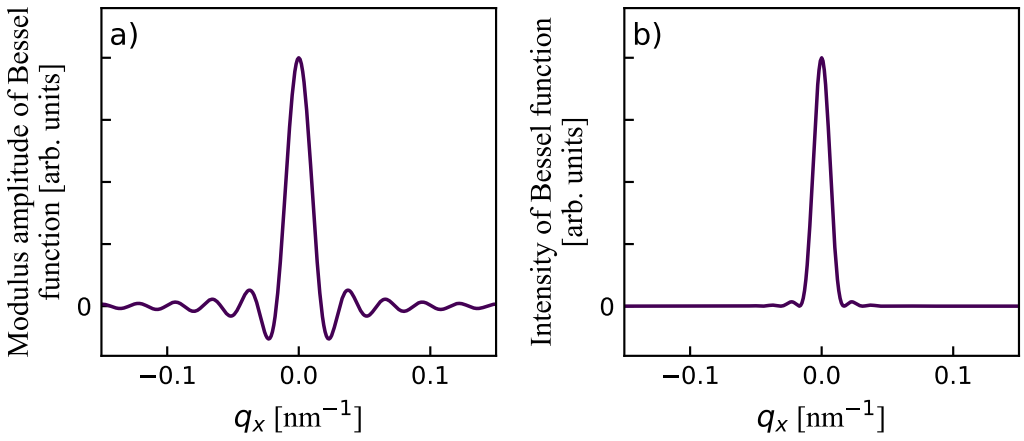

Figure 5.6: Comparison of J_1 Bessel functions being the in-plane Fourier transformations of a disk. The graph in panel a) is proportional to the scattered amplitude of a circular island of radius 225 nm. Panel b) shows the square of a), being proportional to the scattered intensity of the same disk, providing the envelope function of a patterned array of (perfectly flat) circular disks.

seen in Fig. 5.5, but reproducing the signal seen in Fig. 5.4 certainly requires a more complex three-dimensional model.

The driving task of the modelling process is answering the questions *"What properties of the real system have to be captured by the model?"* and *"How can these properties be implemented taking into account the limited processing capacity of the available data processing system?"*.

After all, the higher dimensionality (at least two dimensions are needed for a spatial model of the rotationally symmetric islands discussed in this chapter) also generally means higher computational effort, which can easily bring a modern desktop computer to its limits if immense numbers of recalculations are required, as is the case in fitting a model to experimental data. The latter is particularly true if the simulated model obtains no closed form analytical expression describing the scattering and solutions have to be found numerically.

Focussing on the first question from above, it seems reasonable for a model of the patterned array to include the possibility of some kind of doming, since peak modulation of the rocking curves did not at all meet the expectations from a flat array, and, more specifically, both AFM imaging (see Fig. 3.3) and the SLD profile obtained from reflectivity measurements indicates the presence of island doming towards its central axis. A spatial model should be versatile enough to capture a range of realistic domed structures, while requiring only as few parameters as possible to

access this set. The model being as generic as possible is important since without knowledge of the exact formation process of the dome the exact doming function is still rather unclear. After all, a spherical dome might be easy to implement and require only very few parameters to be fitted on top of the island, but this will be to no avail if the real doming is in fact not spherical *and* the scattered intensity is sensitive to the exact shape of the doming, (which it turned out to be).

In this work we chose to code the doming function using a *Pearson VII* distribution, which provides a height z as a function of radius r of the form

$$z(r) = \frac{1}{\alpha \mathrm{B}\left(m - \frac{1}{2}, \frac{1}{2}\right)} \left[1 + \left(\frac{r-\mu}{\alpha}\right)^2\right]^{-M}, \tag{5.5}$$

where $\alpha = \sigma\sqrt{2M-3}$, σ is the variance of the distribution, B is the beta function, μ is the distribution centre and $M > 3/2$ is a shape parameter controlling the kurtosis of the distribution. The distribution continuously varies from approximating a Lorentzian for low values of M to Gaussian shapes for $M \gtrsim 10$.

In modelling patterned arrays, though, choosing a slightly different form of eq. 5.5 making certain restrictions is useful. Namely, demanding that

1. The doming height above the nominal island height takes on a fixed value
2. The value of the doming function takes on the nominal island height at the edges of the island.

This way the model allows one to decouple certain key parameters of the doming function like nominal height z_n and doming height z_D, while ensuring edge continuity and smooth boundary conditions. From solving the two equations obeying the boundary conditions $z(r_n) \stackrel{!}{=} z_n$ and $z(0) \stackrel{!}{=} z_D$ a reformulation of eq. 5.5 leads to

$$z(r) = (z_D - z_0)\left(\frac{\eta^2}{\eta^2 + r^2}\right)^M + z_0 \tag{5.6a}$$

$$\eta = \frac{r_n\sqrt{\xi}}{\sqrt{\xi - 1}} \tag{5.6b}$$

$$\xi = \left(\frac{h - z_0}{z_D - z_0}\right)^{\frac{1}{M}} \tag{5.6c}$$

$$z_0 = z_n - z_{\mathrm{off}} \tag{5.6d}$$

where the beta function has cancelled out. The shape of the dome is now fully determined by the nominal island height z_n, the doming height z_D, the nominal island radius r_n, the shape parameter m and a parameter $z_{\mathrm{off}} \geq 0$, which translates

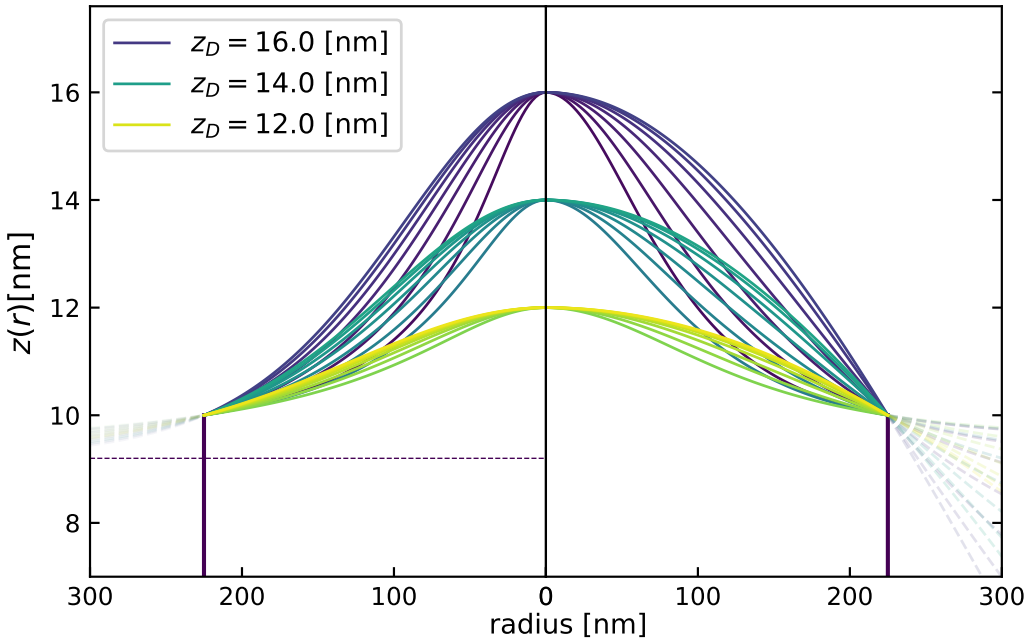

Figure 5.7: Influence of doming parameters M (left panel) and z_{off} (right panel) for boundary conditions of constant $r_{\text{n}} = 225\,\text{nm}$ and three doming heights $z_{\text{D}} = 12\,\text{nm}$, 14 nm and 16 nm, coloured yellow, blue and purple, respectively. In the left panel $z_{\text{off}} = 0.8$ (indicated by the horizontal dotted line) was held constant, while the Pearson exponent is varied covering the seven values $M = 0.70$, 0.97, 1.35, 1.87, 2.61, 3.63 and 5.04. In the right panel $M = 1.5$ is held constant and z_{off} is scanned through the values 0.5, 1.0, 2.0, 4.0, 8.0, 16.0 and 32.0.

the baseline of the Pearson VII distribution to values below z_n, while keeping the boundary conditions intact. A visualisation of eq. 5.6 is found in Fig. 5.7. Hence, the shape is determined by four open parameters, of which it has been empirically found that m may often be of only very little impact on the actual doming for physically reasonable parameter combinations. The choice of eq. 5.6 is preferred over eq. 5.5 because of looser parameter coupling, the obvious physical meaning of the parameters and the possibility of easily defining meaningful parameter limits when fitting the simulation to experimental data. After all, obscure parameter choice could easily lead to, for instance, unreasonable doming heights, evaluating unphysical sample geometries which are consequently wasting computing time and efficiency. The implicit assumption in this choice of function, however, is that any doming is symmetric. Alternatively, more general cases could be considered through a different choice of analytic function. The choice was motivated by the AFM data in Fig. 3.3 and reproduced in Fig. 5.1.

Fig. 5.7 shows a comparison of the influence of the two parameters determining the shape of the doming function m and z_{off}, respectively, at fixed boundary conditions given by r_{n}, z_{n} and z_{D}. As can be seen from the chosen example, a wide variety of different shapes continually morphing into each other can be obtained. Generally, higher sensitivity to M is obtained at low values of z_{D}, which is when the baseline of the PearsonVII function is asymptotically closer to the nominal height z_{n} of the island, so that varying the shape in between the limiting cases of Lorentzian and Gaussian actually has a strong impact upon the doming shape. By increasing the z_{off} parameter to high values relative to z_{n} the doming approaches more spherical shapes, acquiring high residual slope at the nominal island radius r_{n}. In practice, it has to be kept in mind that M and z_{off} might be effectively coupled in a way that the produced output is very similar for certain combinations or that varying a parameter in between the allowed limits does not result in a recognisable change of the doming shape for certain values of the other parameter. Again, this might slow down fitting convergence or lead to high uncertainties in fitted parameter values and must be considered an unavoidable side effect of the approach used here.

The Pearson VII function, as seen in Fig. 5.7, is hopefully sufficiently generic in order to be able to model the doming on top of the islands. The small plateaus around the edges of the island just above its nominal height as seen in Fig. 3.3, might, if real and no artefact or peculiarity of this particular island, lead to very small values of z_{off} as a result of parameter fitting. The latter, as can be seen on the right hand side of Fig. 5.7, leads to a delayed onset of the sloping, i.e. the formation of plateaus near the edges of an island. The choice to not include the plateaus explicitly within the sample model was made deliberately, since it would provide the risk of over-engineering the sample structure based on potentially inaccurate AFM measurements and would greatly limit the generality of the final sample model. Also, suspecting an (angle- and therefore position dependent) shadowing effect to be responsible for the observed doming, perfect reproduction of the exact doming shape for each island was very unlikely, implying that the *average* sample structure (which is what a scattering experiment is usually sensitive to) would necessarily smooth itself out. Hence, the average sample structure is expected to rather resemble something seen in Fig. 5.7 than the AFM scan of Fig. 3.3.

However, the island edges at nominal radius are still found to be unrealistically sharp, which might, under certain conditions, lead to recognisable effects on the yet to be implemented scattering structure factor of the island. In order to avoid an abrupt transition from 0 at $r > r_{\mathrm{n}}$ to z_{n} at $r = r_{\mathrm{n}}$, the island height $z(r)$ will be

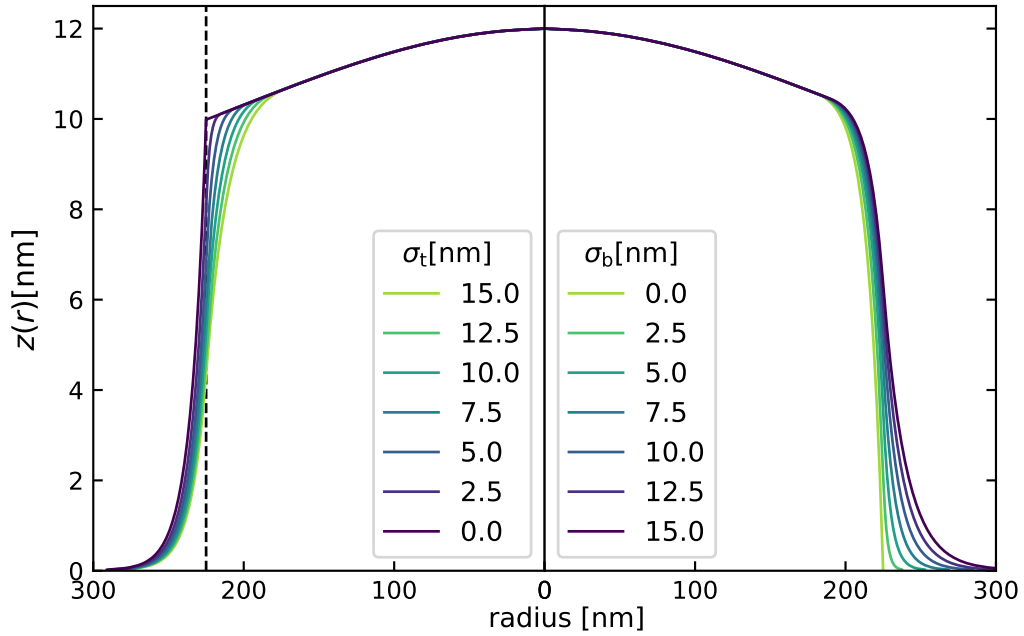

Figure 5.8: The effects of bottom and top shape parameters σ_b and σ_t determining the roundedness of the island sides. The doming has been chosen to be $z_\mathrm{D} = 12\,\mathrm{nm}$ to exemplify the continuous merge of edge function to doming function at $z_\mathrm{crossover} \geq h$.

modelled by a double exponential function in the vicinity of r_n:

$$z(r) = \begin{cases} \alpha t \exp\left(\frac{r_0 - r}{\sigma_\mathrm{b}}\right), & \text{for } z < ta \\ (\alpha t - t)\exp\left(\frac{r - r_0}{\sigma_\mathrm{t}}\right) + b, & \text{otherwise} \end{cases} \tag{5.7}$$

with σ_b and σ_t being shape parameters determining the bottom and top slopes of the function and t being the upper plateau value that the function asymptotically approaches. Similarly, a lower plateau value can be added easily to eq. 5.7, which has here implicitly been set to $b = 0$ and omitted for clarity. Note, however, that the parameter t is not strictly equal to the nominal height h of the island, as this would necessarily lead to an unsmooth transition from the double exponential function determining the island edges to the Pearson VII function defining the top.

As a compromise – because physical realism has been considered more important than parametric consistency – the actual island modelling includes scaling of the plateau value $t > h$ in a way that a smooth transition of double exponential to Pearson VII occurs at a (numerically identified) crossover point $z_\mathrm{crossover}$ as can be seen in Fig. 5.8. This approach ensures a smooth height function $z(r)$ of the island at the expense of an implicit coupling of σ_t to the (parametrically inaccessible)

plateau value t.

Hoping the above approach suffices in providing an island model flexible enough to capture the shape of the actual nano dots presumably similar to what is seen in Fig. 3.3, obvious limitations of its applicability to simulation quickly come to mind; As it is, the model at best provides a way of modelling an island by describing the sharp interface given by the island's surface. However, this approach does not allow for any *chemical variation* of the internal island composition. Here, the island surface is described by it's height at a given radius $z(r)$, but can generally be chosen to be an arbitrary function, being called a *surface cut function*[54]. After choosing a set of the previously discussed shape determining parameters, the only quantity the model provides is a one-dimensional relationship between z and r, which can not be utilised to include any *internal* information of the structure. Nevertheless, it is very likely that oxidation or surface roughness very likely alter the chemical structure at particular points *within* the island, especially when it is identified with a spatial average over a number of islands[68, 212]. The latter distinction is important since the lateral average over the coherently illuminated sample area is the only quantity a scattering experiment of partially coherent radiation is actually sensitive to.

A useful sample model has to contain a spatially fully resolved scattering length density $SLD(\mathbf{r}) = f(\mathbf{r})\rho^{\mathrm{num}}$ describing the scattering potential at any point within an island. For the experiments dealt with in this chapter the latter basically means three things:

1. The final model does not have to provide information about the internal *atomic* structure of the pattern, since the low-angle scattering geometry is not sensitive to atomic length scales found around significantly larger Q values. Hence, it is reasonable to assume a continuous function describing the scattering length density over the spatial extent of the islands.

2. Since the sample internally consists of an amorphous structure anyway, no Bragg reflections would be seen at large Q even if the experiment *were* performed in a corresponding way.

3. It is reasonable to try to exploit the rotational symmetry of the circular islands in a way to simplify the mathematical treatment and computational effort of the simulation.

A straightforward way of extending the model therefore consists in introducing of not only a single, but an arbitrary number of non-intersecting functions $z_i(x, y)$, which allows connecting any local sample property with its spatial position within the structure. More specifically, by utilising the rotational symmetry

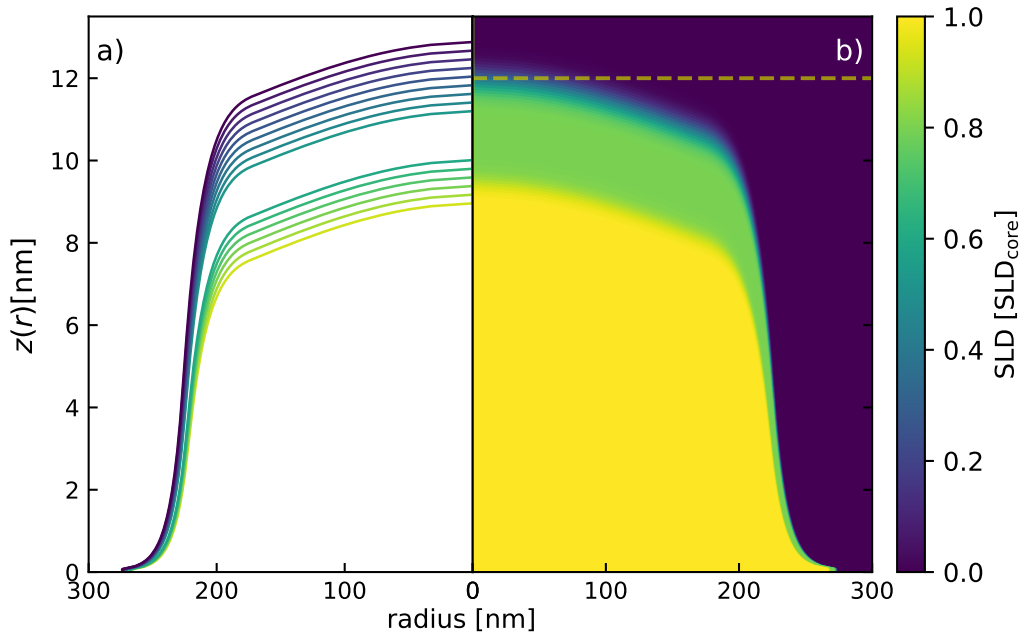

Figure 5.9: Comparison of surface cut functions and SLD profile of an island. In panel a) the island has been modelled by 15 surface cut functions $z_i, i = 0..14$. The z_i are located equally spread over $\pm 3\sigma$ in two clusters around the nominal core and outer shell interfaces, assuming an Error function like diffusive interface width σ. Panel b) color codes the scattering length density of each shell $z_i(r)$, associating all material in between shells i and $i-1$ with a single value f_i. For clarity, the horizontal dashed line marks the nominal height $z_D = 12\,\mathrm{nm}$ of the island, which is naturally smaller than the topmost diffusive shells.

of the sample and demanding $z_i(x, y) = z_i(r)$ a core-shell model of the sample naturally emerges, as seen in Fig. 5.9 a). Here, in an attempt to model island oxidation, the previous function $z(r)$ has been replaced by a set of functions $z_i(r)$, where the doming height z_D and nominal radius r_n change by the same amount $\Delta r_\mathrm{n} = \Delta z_\mathrm{D} = \Delta$ in between any two neighbouring functions z_i and z_{i+1}. Similarly, the set of surface cut functions z_i is easily extensible by functions being centred around $(r = 0, z = z_\mathrm{core} = z_\mathrm{D} - d_\mathrm{ox})$. In the example given in Fig. 5.9, $d_\mathrm{ox} = 2.5\,\mathrm{nm}$ represents the average thickness of a potential oxidation layer surrounding the island, which has been chosen to be larger than physically reasonable for demonstrating purposes only. A thing to be noted here is that the differing scale in the variables r and z exaggerates the oxidation thickness on top, while decreasing the apparent thickness around the edges. In fact, the thickness of the oxidation layer as measured on top of the islands or radially along the sides, in other words along any surface

normal, is identical.

By now applying the convention that a single surface cut function $z_i(r)$ is representative of the material *volume* between $z_i(r)$ and $z_{i-1}(r)$, it now becomes possible to conveniently refer to whole sections of the average island which are chemically identical, implicitly assuming the same chemical gradient normal to any surface normal of the island. In other words, probing the structure along it's surface normal, be it on top or on the sides, always results in an identical SLD profile [1] .

Fig. 5.9 b) represents a visualisation of the chemical structure of a cross section of the island, with the colour coding being proportional to the value of the scattering factors of unoxidised core, oxide shell and the surrounding ambience, respectively. As can be seen, the scattering factors vary smoothly between the shells through means of chemical interdiffusion in between shells. The latter is implemented by assigning each (of the arbitrarily numbered N) surface cut function $z_i(r)$ an *effective fractional scattering factor* $f_{i,j}$ according to *nominal shell* j (of predetermined number J, i.e. three for a system consisting of core, oxide and ambience). In other words, each *shell* i is associated with a contribution of scattering factors $f_{i,j}$ corresponding to *nominal* shell j according to a vertical slice through the island at $r = 0$, with the chemical profile obeying error functions in the form

$$f_{i,j} = f_j\,\varphi_{i,j}(z_\mathrm{D}) = \begin{cases} f_j\,\frac{1}{2}\left(1+\mathrm{erf}\left(\frac{z_i - z_{\mathrm{D},j}}{\sqrt{2}\,\sigma_j}\right)\right), & \text{for } z \le \eta \\ f_j\,\frac{1}{2}\left(1+\mathrm{erf}\left(\frac{z_{\mathrm{D},j-1} - z_i}{\sqrt{2}\,\sigma_{j-1}}\right)\right), & \text{otherwise} \end{cases} \tag{5.8}$$

where η is a weighted average of z_i and z_{i-1} given by

$$\eta = \frac{\sigma_{j+1} z_j + \sigma_j z_{j+1}}{\sigma j + \sigma_{j+1}}. \tag{5.9}$$

Examples of $\varphi_{i,j}$ are seen in Fig. 5.10 a), which shows the chemical fractions at the centre of the island $r = 0$ corresponding to the sample parts being identified as constituting core, oxide shell and ambience, respectively. Note that fractions are only defined where the material composition is *changing* with z by means of chemical diffusion, i.e. in the vicinity of nominal shell interfaces. Afterwards, each scattering length $f_{i,j}$ of shell j is associated with surface cut function $z_i(r)$. Fig. 5.10 b) shows the product of the nominal scattering factor f_j of shell j, i.e. core, oxide and ambience, with the corresponding fractional factors $\varphi_{i,j}$, taking care of the chemical interdiffusion of surface cut function z_i. The *total scattering factor*

[1] Exceptions to this rule are surface profiles of the scattering length density taken closely above the substrate, which, or course, have to correctly merge with the substrate SLD and have to be taken care of separately in the simulation.

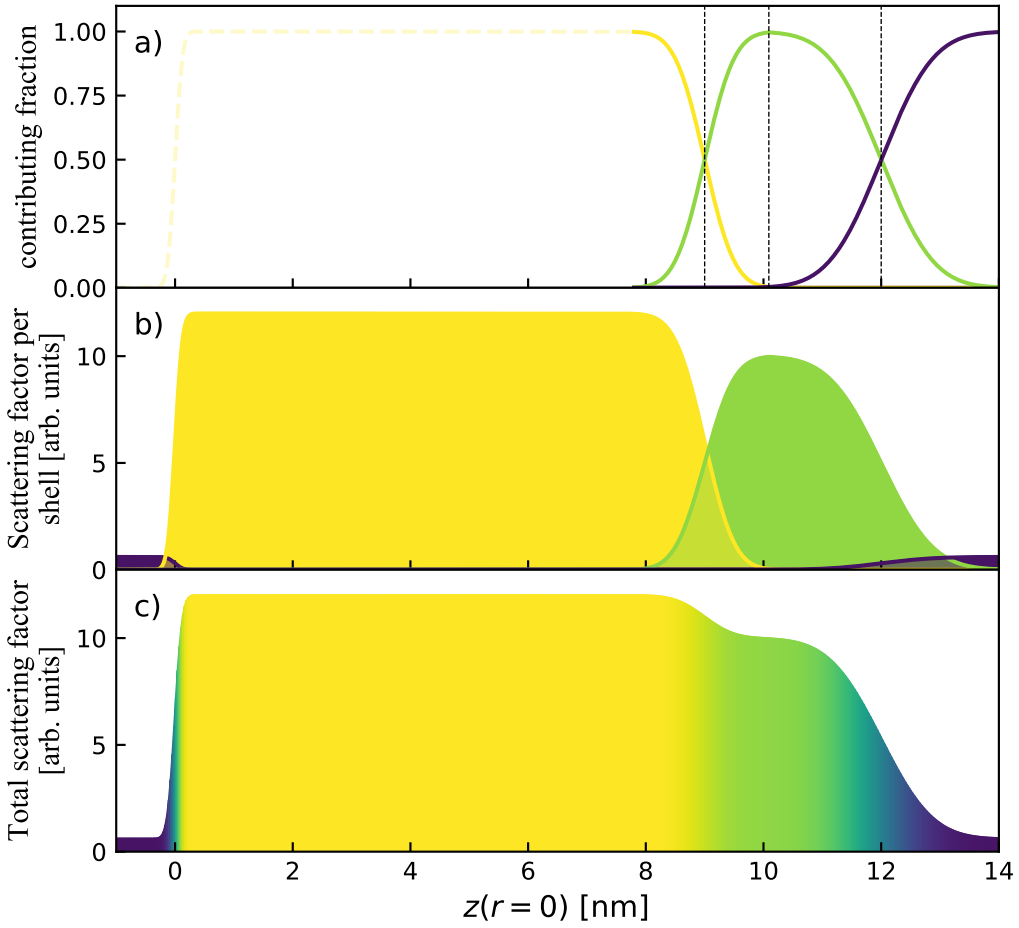

Figure 5.10: Panel a) shows the *fractions* of each *nominal* scattering length density of core, oxide layer and ambience, where the dashed lines mark the nominal height of the non-oxidised core z_{core}, crossover point η and the nominal height of the whole island z_{D}, respectively. Panel b) shows the contribution of each nominal scattering factor at height z, while panel c) shows the weighted *effective* $f(z)$ according to eq. 5.10. In order to effectively calculate the continuous SLD distribution, the $z_i(r = 0)$ are distributed over the diffusive interfaces only, i.e. within the bold lines of panel a).

$f_i(r)$ is then easily calculated by a weighted average of all nominal shells according to

$$f_i(z, r) = \frac{\sum_{j=0}^{J} f_{i,j}(z, r)\, \varphi_{i,j}}{\sum_{j=0}^{J} \varphi_{i,j}} \tag{5.10}$$

where the condition $r = 0$ has been dropped, so that eq. 5.10 allows to calculate the

scattering factor of an arbitrary three dimensional structure, as long as an adequate form of $z_{i,j}(r)$ satisfying rotational symmetry is formulated. Most of the times the denominator of eq. 5.10 will be identically 1, unless more than two φ-functions overlap, which happens when diffusive roughness is large compared to shell thickness. Figure 5.10 c) shows an example of scattering factors calculated according to eq. 5.10 taken at the centre of a domed island.

By taking this one dimensional slice through the island, a profile of scattering factors is obtained, which is similar to the z-profile of a stratified sample. The main difference is that the scattering factor obtained at each value of z through the rotation axis of the island is subsequently associated with a complete *shell* of the structure, instead of only a single z value as is usually sufficient in the case of stratified media. In a way, the approach is not dissimilar to folding a stratified structure over a three dimensional skeleton as is illustrated in Fig. 5.9 b).

5.3 Scattering Framework

This section first presents the particular implementation of calculating the *structure factor* F of the unit cell of a patterned array using this model, i.e. a single patterned island in this case, followed by the description of the diffracted intensity registered in an experiment, under the complicating conditions of an experimental set-up involving an open detector geometry. The theoretical foundations of idealised diffraction of patterned arrays are given in section 2.4, whereas this section deals with the particularities of evaluating the basic equations under the often non-ideal conditions of experimental reality.

5.3.1 Island Structure Factor

Section 5.2 presented a way to independently define shape and chemical structure of a patterned island, giving one possible answer to the previously asked question *"What properties of the real system have to be captured by the model?"*. Hence, it is now time to revisit the second question previously asked, i.e. how the calculation of the scattered signal shall be performed, given all relevant sample properties are defined. Two different approaches of calculating structure factors utilising surface cut functions have been used in this work, both having respective advantages and disadvantages.

The first approach divides the sample into *vertical columns* of varying height, corresponding to the local value of the $N \geq 1 \in \mathbb{Z}$ surface cut functions $s_i(x, y)$. Analytical Fourier transformation of these columns is trivial, and the final

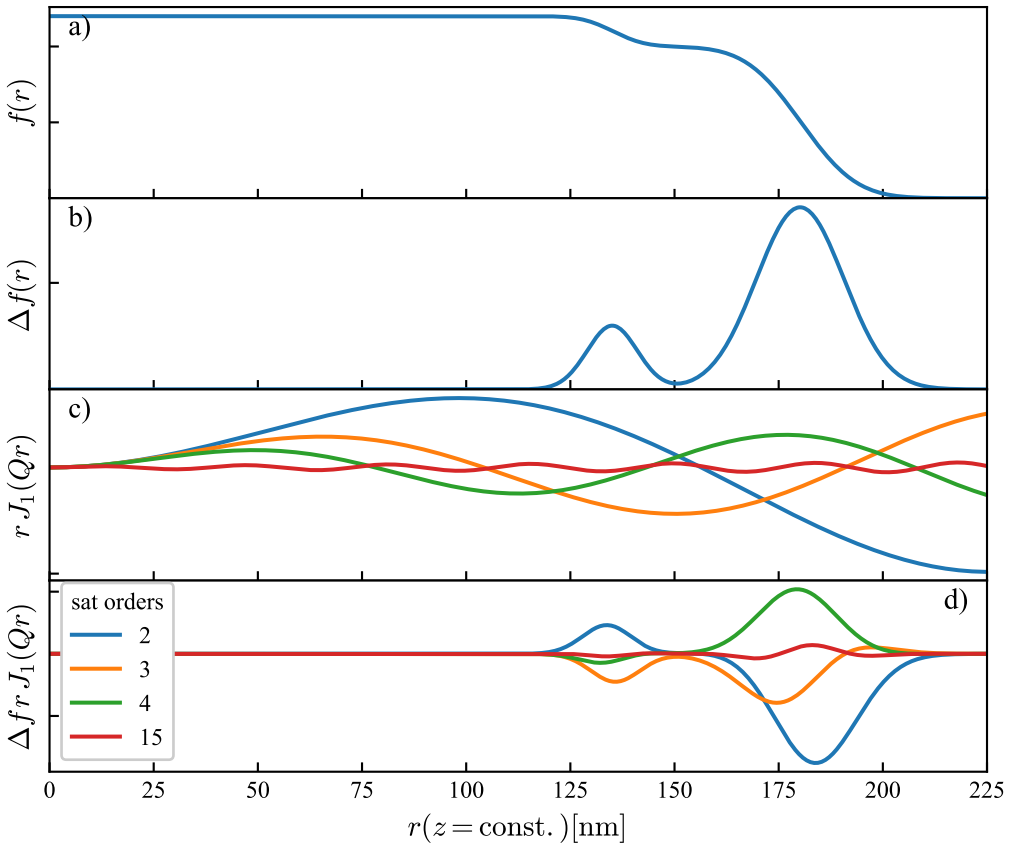

Figure 5.11: Panels a) and b) show the radial distribution of the scattering factors f and Δf at an arbitrarily chosen height z. As can be seen $\Delta f_i = f_i - f_{i+1}$ is zero everywhere apart from in the vicinity of chemically diffused interfaces. Panel c) shows the Fourier transformations of circles of radius r, at positions in reciprocal corresponding to diffraction satellite orders 2, 3, 4 and 15. Panel d) shows the product of $\Delta f(r)$ and the corresponding radial Fourier transformation, again for different satellite orders. The total scattered amplitude of the single slice of the system is given by the sum of each line of panel d), where interfaces may interfere constructively (e.g. 3rd order) or destructively (e.g. 2nd order).

structure amplitude is given by the coherent sum of all columns[2]. The columns are evaluated on an arbitrary Cartesian grid (X, Y), that is large enough to cover the extent of the entire island. Within the kinematic approximation, atoms at position (x, y, z) contribute to the total scattered amplitude at (Q_x, Q_y, Q_z) according to

[2]Note that this strictly corresponds to the high coherence limit as discussed in chapter 4

their scattering length density

$$f(x,y,z)\rho^{\mathrm{num}}(x,y,z)$$

modified by a phase factor

$$\exp(-i(Q_x x + Q_y y + Q_z z)).$$

Hence, keeping fixed a point of the two-dimensional coordinate grid (x,y), the scattered amplitude within the kinematic approximation is calculated according to

$$\begin{aligned} A_z(\mathbf{Q},x,y) &= \mathrm{e}^{i(Q_x x+Q_y y)} \int_{-\infty}^{\infty} f(x,y,z)\mathrm{e}^{-iQ_z z}\,\mathrm{d}z \\ &= -\frac{\mathrm{e}^{i(Q_x x+Q_y y)}}{iQ_z} \sum_{i=1}^{N} \left[f_i(x,y) - f_{i-1}(x,y)\right] \mathrm{e}^{-iQ_z s_i(x,y)} \end{aligned} \tag{5.11}$$

where, by definition, the *lowest* surface cut function represents the substrate at $s_0 \equiv 0$ implying $f_0 \equiv 0$. Hence, the island is "floating" in free space, neglecting the unpatterned substrate. Note that in eq. 5.11 and from now on for the remainder of this section, the atomic number density $\rho^{\mathrm{num}}(\mathbf{r})$ has been implicitly merged with $f(\mathbf{r})$ for notational convenience since both quantities change simultaneously in describing the chemical composition of the island.

The *total scattered amplitude* of one entire island can then be calculated, for instance, by a simple Riemann integral over the Cartesian grid

$$A(\mathbf{Q}) = \sum_{x,y=-\infty}^{\infty} A_z(\mathbf{Q},x,y). \tag{5.12}$$

However, even though the analytic formulation of the z-integration can save a lot of time, the number of points on the x-y-grid is usually very large in order to provide sufficient resolution. Another drawback is reduced compatibility of the integration along columns with the Distorted Wave Born Approximation, the latter requiring the formulation of an undisturbed scattering potential, which is not easy to identify using this approach. Furthermore, the number of calculations scales linearly with the number of surface cut functions s_i, which can furthermore get quite large if modelling of the chemical interdiffusion is found to require high spatial resolution.

The final fitting in chapter 4 has been performed using integration along columns, which was justified by realising that the internal island structure could be dismissed in the case of this particular sample, and only a single surface cut function

was sufficient in order to fit the data. If, on the other hand, the multilayer structure of the sample of chapter 4 *had* to be fitted independently, potentially even including chemical diffusion between the layers, the number of surface cut functions would have very likely overextended the available computational resources. Instead, by fitting the data within GenX[208], the sample's reflectivity was calculated within a different scattering framework, which *did* take into account the average internal depth profile of the sample, however at the cost of not providing any information about the lateral structure of the sample.

The second approach to obtain the structure factor of an island consists in an (at least partly) analytical calculation of the lateral component of the scattering potential within a *horizontal slice* through the island at height z and then obtaining the total scattering amplitude by numerically integrating these potentials over the total height of the sample. This, however, requires that the in-plane structure of the island is of a form which allows analytical formulation of the scattering potential.

In contrast, integration along columns did not rely on *any* closed form expressions, meaning computation of the scattering potential can be performed on a completely numerically defined s_i, a fact which becomes important when simulating more complex (magnetic) structures, which might, for instance, have been obtained from micromagnetic simulations or the like.

Mainly for notational convenience, in the following the sample coordinate system will be expressed in cylindrical coordinates, i.e. $\mathbf{r} = \mathbf{x} + \mathbf{y}$. Then, for the particular case of the rotationally invariant $s_i(r)$ of disk-like islands, every horizontal cross section through $s_i(r)$ at height z results in a set of circles of radii $R_i(z) = s_i^{-1}(r)$, where the superscript denotes the functional inversion operation.

Consequently, calculating the scattered amplitude of a general horizontal slice through an island consisting of an arbitrary number $N \geq 1 \in \mathbb{Z}$ of surface cut functions is given by

$$\begin{aligned} A_{\parallel}(\mathbf{Q}, z) &= \mathrm{e}^{-iq_z z} \int_0^\infty f(\mathbf{r}) \mathrm{e}^{-i\mathbf{Q}_{\parallel}\mathbf{r}} \,\mathrm{d}r \\ &= \mathrm{e}^{-iQ_z z} \sum_{i=0}^{N} f_i \, 2\pi R_i(z) \, J_1(Q_{\parallel} \, R_i(z)) - f_{i+1} 2\pi R_i(z) \, J_1(Q_{\parallel} \, R_i(z)) \\ &= \mathrm{e}^{-iQ_z z} \sum_{i=1}^{N} \Delta f_i \, 2\pi R_i(z) \, J_1(Q \, R_i(z)), \end{aligned} \tag{5.13}$$

where $\Delta f_i = f_i - f_{i+1}$ is the difference of the scattering factors of two neighbouring

shells and the integral has been evaluated using the Fourier transformation of a circle

$$\int_0^R \mathrm{e}^{-iQr}\,\mathrm{d}r = 2\pi R\, J_1(QR) \tag{5.14}$$

where J_1 is the Bessel Function of the first kind of order 1.

In other words, the Fourier transformation of an entire horizontal cross section of an island is replaced by the sum over the Fourier transformation of multiple annuli, each representing an area of constant scattering length density. Furthermore, in order to keep the proper integration limits $R_0 = f_{(0)} \equiv 0$ must hold, and f_{N+1} represents the ambient conditions of the structure, which is equal to zero for vacuum or negligible ambience conditions.

The *total scattered amplitude* in the kinematic single scattering approximation is obtained from first calculating $A_\parallel(\mathbf{Q}, z_m)$ for a sufficiently high number $M \in \mathbb{Z}$ of z values, in essence dividing the sample into M slices, each of known thickness Δz_m. Subsequently, the out-of-plane components are added coherently, considering the correct phase factor ϕ_m along z of each slice

$$A(\mathbf{Q}) = \sum_{m=0}^{M} \phi_m\, A_\parallel(\mathbf{Q}, z_m) \tag{5.15a}$$

$$\phi_m = \int_{z_m}^{z_{m+1}} \mathrm{e}^{iq_z z}\,\mathrm{d}z = \frac{1}{-iq_z}\left(\mathrm{e}^{-iq_z z_{m+1}} - \mathrm{e}^{-iq_z z_m}\right) \tag{5.15b}$$

where z_m correspond to the *lower interfaces* of slice m and z_0 marks the lowest z value of the scattering structure.

The structure the above model describes so far is free floating in space, without any connection to the underlying substrate. This might indeed be a sufficient approximation to the real system *if* only off-specular scattering is considered, since the unpatterned substrate only contributes to the specular intensity. However, if simulating reflectivity data is desired, the substrate necessarily has to be included. Most conveniently, substrate and island amplitudes are calculated separately and coherently summed. If, however, the substrate is modelled simultaneously with the island, two things have to be considered. First, to respect the correct integration limits, the (horizontal) surface cut functions belonging to the substrate $s_{\mathrm{sub}}(z)$ must extend exactly over the entire unit cell, most likely of rectangular shape, in order to ensure a vanishing amplitude contribution at reciprocal lattice points, where satellite reflections occur. Second, care has to be taken to correctly set the integration

limits in terms of s_0 to get the correct phase information. It is often convenient to set $s_0 = -\infty$ and let $f(z_0) = f_{\text{sub}}$ be the scattering factors of the substrate. Since no reflected wave travels within the infinite substrate (see section 2.2.4), the phase factor of the lowest slice the becomes

$$\phi_0 = \frac{1}{-iq_z} \mathrm{e}^{-iq_z z_1}. \tag{5.16}$$

Both approaches described above have been coded and investigated. They generally give reasonable approximations in their own respect, whilst the first approach, integrating along the vertical columns, arguably provides a higher degree of flexibility at the cost of computational efficiency. A further drawback of the first approach is that because the sample is not sliced along a number of z-values, it is not possible to utilise higher order perturbation theory, such as the Distorted Wave Born Approximation (DWBA). The latter might be found necessary for grazing incidence geometries like GISAXS or small angle reflectivity measurements but can often be safely neglected at rocking curves taken at relatively large values of Q_z.

5.3.2 Scattered Intensity

Following the discussion in section 2.4 it is apparent that, given the beam properties are found to coherently illuminate multiple unit cells of the patterned array, the scattered intensity of the sample concentrates within a fan of diffracted x-rays found at planar wavevector transfers corresponding to reciprocal lattice vectors

$$\mathbf{G}_{k,l} = \frac{2\pi}{d_{\text{latt}}}(k\hat{\mathbf{Q}}_x + l\hat{\mathbf{Q}}_x),$$

with $k, l \in \mathbb{Z}$ and d_{latt} being the pitch of the square lattice of the patterned array in real space. The continuous intensity distribution of the GTR along Q_z, given a particular wavevector transfer $\mathbf{Q}_{\|} = \mathbf{G}$, is then given by eq. 2.89.

Fig. 5.12 a) shows the structure factor $F(\mathbf{Q})$ of a test system given by a randomly generated circular domed island, whereas panel b) shows the formation of grating truncation rods. Assuming Gaussian coherence properties of the beam projection onto the sample, each GTR obtains a Gaussian cross section along Q_x, of width $\sigma_{\text{rec}} = \sigma_{\text{real}}^{-1}$, being modulated in intensity along Q_z by $F(\mathbf{Q})$.

As discussed previously in section 4.1.3 the detector resolution function $R(\Delta\alpha_i, \Delta\alpha_f)$ integrates a volume of the scattered intensity in reciprocal space according to its angular acceptance. In particular in an open detector set-up, R can be quite large and span over a significant range of both Q_x and Q_z as was shown

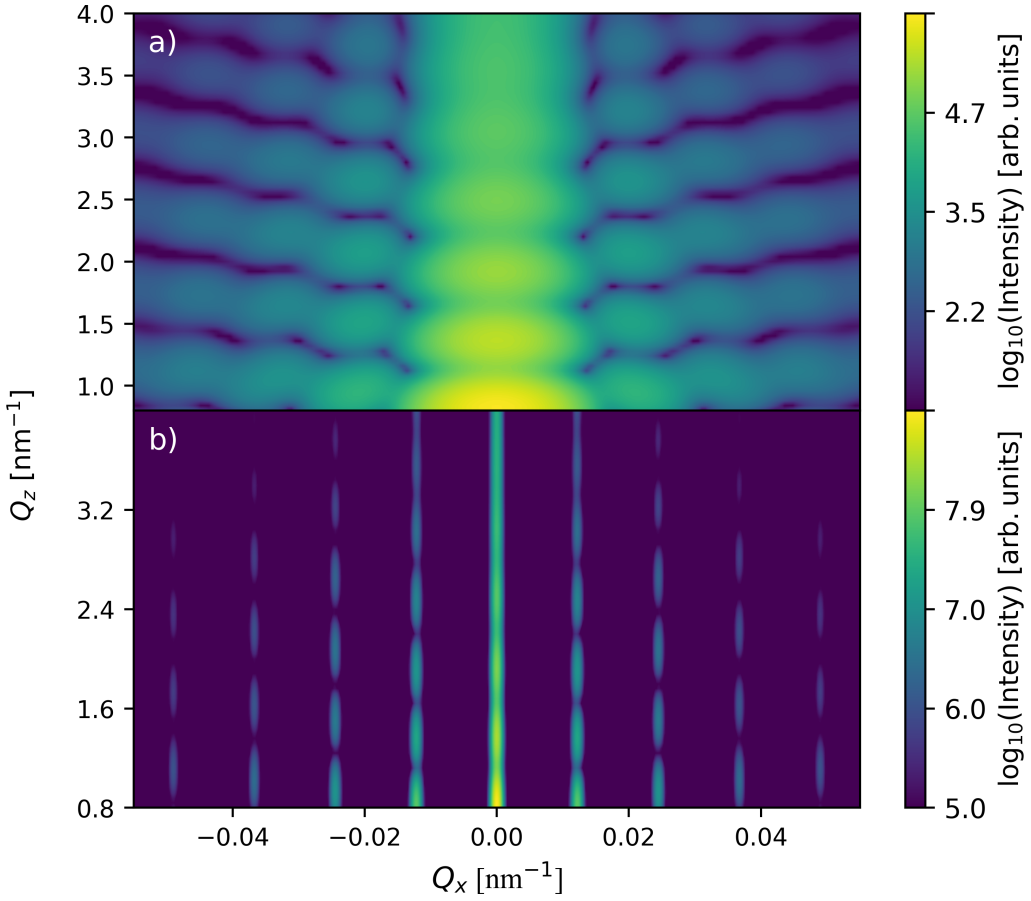

Figure 5.12: Structure factor a), and reciprocal space of a patterned array of domed circular island b). The structure factors of the periodically distributed islands interfere constructively along the grating truncation rods seen in panel b). Parameters used here were for demonstrating purposes: The position of the GTRs corresponds to a lattice pitch of $d = 500\,\mathrm{nm}$ and the width of the (Gaussian) GTR cross section has been chosen to be $\sigma_{\mathrm{rec}} = 0.000\,35\,\mathrm{nm}^{-1}$, corresponding to a real space Gaussian variance along x of $\sigma_{\mathrm{real}} \approx 2.8\,\mu\mathrm{m}$.

in Fig. 4.4. This leads to distinct effects upon the *detected* intensity due to the fact that the diffraction condition is fulfilled across different spatial parts of the detector surface over a significant angular scan range.

In a typical rocking scan experiment the nominal source angle α_i continuously increases from 0 to 2θ, whereas the nominal detector angle α_f continuously decreases by the same amount from 2θ to 0. Hence, upon decreasing α_f the nominal Q_x increases. Similarly, also upon decreasing α_f every GTR is intercepted by the lower part of the detector first, which can easily be shown geometrically to correspond

to a lower Q_z value compared to the top part of the detector as is immediately verifiable from inspection of Fig. 5.13. In consequence, increasing Q_x from left to right along one of the wide satellite peaks as seen in Fig. 5.4 corresponds to a partial scan *upwards* the respective GTR. The latter implies that the sloped peaks can be interpreted as small sections of off-specular reflectivity, with the slope of the peak depending on whether the form factor $F(\mathbf{G}, Q_z)$ happens to increase or decrease along the intersected Q_z range. More specifically, given the nominal α_i and α_f, the part of the detector corresponding to angular offset $\delta^{\mathrm{GTR}}\alpha_f$ is intercepting the GTR can be found from the specific form of the diffraction condition

$$\delta\alpha_f^{\mathrm{GTR}} = \arccos\left(\frac{\mathbf{G}}{k} + \cos\alpha_i\right) - \alpha_f. \tag{5.17}$$

The corresponding Q_z value of the interception point is then given by

$$Q_z^{\mathrm{GTR}} = k(\sin(\alpha_f + \delta\alpha_f) + \sin(\alpha_i)). \tag{5.18}$$

If for a given lattice point $\mathbf{G}$ the angular offset $\delta\alpha_f^{\mathrm{GTR}}$ exceeds the maximum angular offset the detector can accept, i.e. $\left|\delta\alpha_f^{\mathrm{GTR}}\right| > \delta\alpha_f^{\mathrm{det}}$, no part of the detector is fulfilling the diffraction condition, where $\delta\alpha_f^{\mathrm{det}}$ is defined to be the symmetric opening angle of the detector.

Apparently, under open detector geometry $\delta\alpha_f^{\mathrm{det}}$ may get wide enough so that $F(\mathbf{G}, Q_z)$ significantly changes over the total range of intercepted Q_z values of the GTR. Then, approximating the structure factor in the *vicinity* of $\mathbf{G}$ by the nominal structure factor $F(\mathbf{G}, Q_z^{\mathrm{nominal}})$ *at* $\mathbf{G}$ is not justified any more (like it would be when using a narrow detector slit). The latter is obvious if the satellite peaks are wide, as is the case at high detector angles (more pronounced to the left of Fig. 5.4), but the effect is similar at low detector angles. In the latter case the effect is more subtle, since the narrow width of the satellite hides the fact that the detector is actually integrating over a diffracted beam of wide angular divergence, spanning over a large Q_z range.

Technically, at every nominal source- and detector position the total active area of the detector should be mapped to its corresponding area in reciprocal space followed by an integration of the respective intensity distribution. However, in practice it was found that the calculation of the structure factor $F(\mathbf{G}, Q_z^{\mathrm{nominal}})$ constitutes the computational bottleneck of the whole simulation and it is therefore reasonable to limit the number of calculations to the necessary minimum. It is hence advisable to introduce a detector angular offset variable $\Delta\alpha_f^p$, which represents the

angular deviation from the nominal detector angle α_f of the centre of one of a number $P \in \mathbb{Z}$ of subdivided detector areas identified by index p. Subdividing the total detector area into finite units each associated with a *single* Q_z^p value (evaluated at the point of intersecting a given GTR) allows the GTR intensity modulation along Q_z to be determined from the structure factor $F(\mathbf{G}, Q_z^{\text{nominal}})$. In other words, subdividing the detector leads to an approximate increase of the total calculation time of the simulation by factor P.

Most of the time it is found sufficient to divide the detector into $P = 3$ parts. This approximation is valid if the modulation of the GTR intensity over the respective Q_z range is significant enough to be noticed within the experimental angular acceptance of the detector, but low enough to be reasonably modelled by a linear approximation in Q_z.

As a result of the detector integrating over its resolution element R, each detector subunit corresponds to a *real* position in reciprocal space deviating from it's *apparent* (nominal) reciprocal space position at which the intensity is registered in a rocking scan. Correspondingly, the detector subunit associated with a particular $\Delta\alpha_f^p$ maps to a particular set of nominal source- and detector angles α_i^{nom} and α_f^{nom}, i.e. the angles aligned with the *centres* of the source beam and detector. Given the detector subunit at $\Delta\alpha_f^p$ is located at real position in reciprocal space Q_x, the corresponding nominal detector- and source angles can be found geometrically to read

$$\alpha_i^{\text{nom},p}(Q_x) = \frac{Q_x}{k(2\theta + \Delta\alpha_f^p)} + \frac{2\theta + \Delta\alpha_f^p}{2} \tag{5.19a}$$

$$\alpha_f^{\text{nom},p}(Q_x) = 2\theta - \alpha_i^{\text{nom}}(Q_x, p) \tag{5.19b}$$

which allows the calculation of the interception points of a given GTR by detector area p to read

$$Q_z^p(Q_x^{\text{GTR}}) = k\left(\sin[\alpha_f^{\text{nom},p}(Q_x^{\text{GTR}}, p) + \Delta\alpha_f^p] + \sin[\alpha_i^{\text{nom},p}(Q_x^{\text{GTR}}, p)]\right). \tag{5.20}$$

The *apparent* position Q_x^p of the *real* reciprocal space coordinate Q_x as seen in a rocking scan can then be easily calculated according to the standard formula

$$Q_x^p(Q_x^{\text{GTR}}) = k\left(\cos[\alpha_f^{\text{nom},p}(Q_x^{\text{GTR}}, p)] - \cos[\alpha_i^{\text{nom},p}(Q_x^{\text{GTR}}, p)]\right). \tag{5.21}$$

Equivalently, the wavevector transfer $\mathbf{Q}$ of each detector subunit p corre-

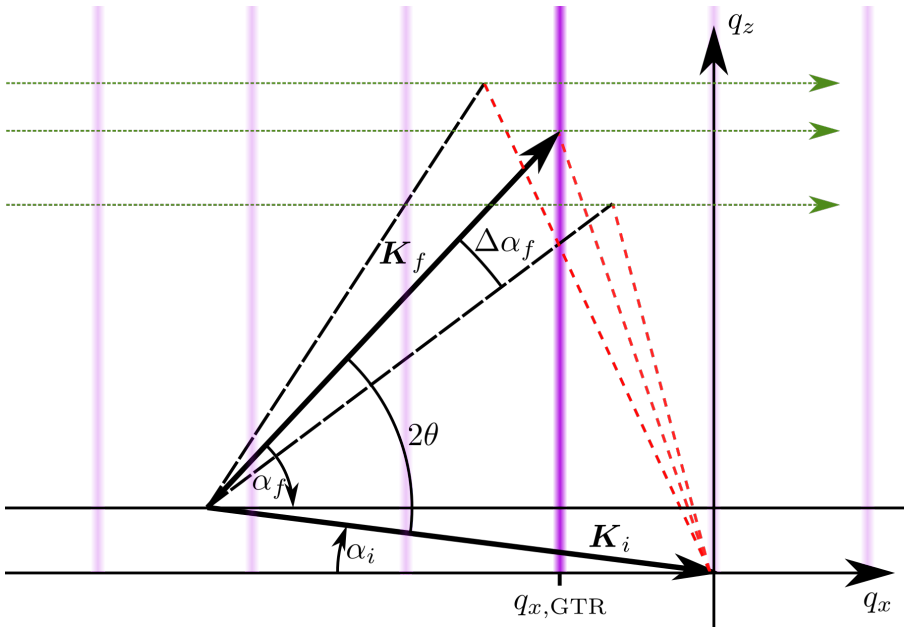

Figure 5.13: Schematic of the experimental geometry as the nominal detector position fulfils the diffraction conditions with a particular GTR. When a rocking scan is performed, (nominal) α_i is continually increasing, while (nominal) $\alpha_f = 2\theta - \alpha_i$ decreases. Upon reducing the detector angle α_f, the lower parts of the detector intercept the GTR first at nominally lower Q_x and Q_z values. The red lines indicate the wavevector transfers $\mathbf{Q}$ of each active part of the detector while the green arrows indicate the (approximately constant) Q_z values associated with each part of the detector and corresponding scan directions.

sponds to only one (nominal) incident angle but varying detector angles given by

$$\alpha_i^p(Q_x) = \alpha_i^{\mathrm{nom},p}(Q_x, p) \tag{5.22a}$$

$$\alpha_f^p(Q_x) = 2\theta - \alpha_i^{\mathrm{nom},p}(Q_x, p) + \Delta\alpha_f^p. \tag{5.22b}$$

In summary, the above equations allow one to predict the angles and reciprocal space positions at which diffracted intensity is registered in an experiment. The latter are offset from their real reciprocal space coordinates because the diffraction condition is fulfilled at different angular offsets accepted by the detector over a range of *nominal* angles α_i and α_f.

Fig. 5.13 shows a schematic of the scattering geometry involving a detector of (exaggeratedly) wide acceptance $\Delta\alpha_f^p$ intercepting a single GTR. From the figure it is clear how parts of the detector corresponding to exit angles $\alpha_f + \Delta\alpha_f^p$ intercept the GTR at differing values of Q_z^p, and (nominal) α_i and α_f.

Since each part of the detector intercepts any GTR exactly once, the corresponding n$^{\text{th}}$ order GTR intensity intercepted by each detector subunit can be approximated by a Gaussian of peak intensity scaled corresponding to eq. 2.89 located at reciprocal space coordinates

$$Q_x^{\mathrm{GTR}} = n\frac{2\pi}{d} \tag{5.23a}$$

$$Q_z^{p,\mathrm{GTR}} = k\left(\sin\alpha_f^p(Q_x^{\mathrm{GTR}}) + \sin\alpha_i^p(Q_x^{\mathrm{GTR}})\right), \tag{5.23b}$$

contributing to the apparent intensity registered at the nominal Q_x.

At any nominal source and detector positions $\alpha_i^{\mathrm{nom},p}$ and $\alpha_f^{\mathrm{nom},p}$, the contribution of intensity from any subunit p of the detector is then given by the integral over the Gaussian cross-section of the GTR within the limits given by the angular acceptance of each subunit

$$\begin{aligned} I^p(\mathbf{Q}) &= I(Q_x^{\mathrm{GTR}}, Q_z^{p,\mathrm{GTR}}) \int_{Q^p_{x,\mathrm{low}}}^{Q^p_{x,\mathrm{high}}} \frac{1}{\sqrt{2\pi}\sigma_{\mathrm{rec}}}\,\mathrm{e}^{\frac{-(Q_x-Q_x^{\mathrm{GTR}})^2}{2\sigma_{\mathrm{rec}}^2}}\,\mathrm{d}Q_x \\ &= \frac{I(Q_x^{\mathrm{GTR}}, Q_z^{p,\mathrm{GTR}})}{2}\left(\mathrm{erf}\left(\frac{Q^p_{x,\mathrm{low}}-Q_x^{\mathrm{GTR}}}{\sqrt{2}\sigma_{\mathrm{rec}}}\right) - \mathrm{erf}\left(\frac{Q^p_{x,\mathrm{low}}-Q_x^{\mathrm{GTR}}}{\sqrt{2}\sigma_{\mathrm{rec}}}\right)\right), \end{aligned} \tag{5.24}$$

where the integration limits $Q^p_{x,\mathrm{low}}$ and $Q^p_{x,\mathrm{high}}$ are calculated corresponding to the $\Delta\alpha_f$ values at the *edges* of the active detector area to read

$$Q^p_{x,\mathrm{low}} = k\,\left(\cos\left(\alpha_f^p + \Delta\alpha_f^p/2\right) - \cos(\alpha_i^p)\right) \tag{5.25a}$$

$$Q^p_{x,\mathrm{high}} = k\,\left(\cos\left(\alpha_f^p - \Delta\alpha_f^p/2\right) - \cos(\alpha_i^p)\right), \tag{5.25b}$$

where $\Delta\alpha_f^p = \Delta\alpha_f/P$, is the angular acceptance of a single detector subunit, corresponding to the total angular acceptance of the detector $\Delta\alpha_f$ and the number of detector subunits $P \in \mathbb{Z}$.

Fig. 5.14 shows a magnified view of the cross-section of a GTR intercepted by a wide detector divided into three subsections. Each active subsection of the detector intercepts the GTR at a different Q_z^p value, leading to the intercepted parts of the GTR to be of varying peak intensity as indicated by the dashed lines.

The obvious problem of the discontinuities at the integration limits seen in Fig. 5.14 can be rectified by subdividing the detector into a larger number of subunits. However, calculating $I(\mathbf{Q})$ for more subdivisions is computationally very costly, since the structure factor at each GTR $F(Q_x^{\mathrm{GTR}}, Q_z^p)$ has to be evaluated

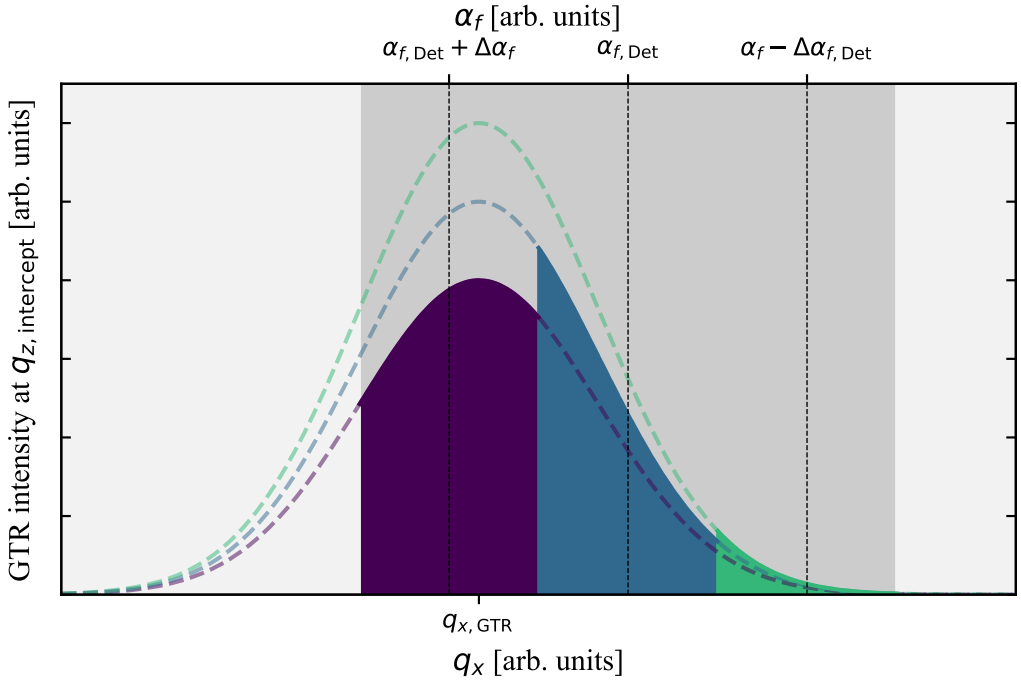

Figure 5.14: Integrated intensity of a wide detector acceptance over an extended GTR., with the detector being divided into three subunits. Since each subunit p is associated with a different Q_z^p value, the associated Gaussian cross-sections of the GTR are of differing peak intensities given by $F(Q_X^{\mathrm{GTR}}, Q_z^p)$, represented by the coloured dashed lines. The dark gray area marks the total Q_x acceptance of the open detector ΔQ_x. The subdivision of the detector area into only three parts leads to obvious discontinuities around the edges of the active subunits.

for an increasing number of only slightly different values of $Q_z^p(Q_x^{\mathrm{GTR}})$, which for many systems may easily require hundreds or thousands of function evaluations each. In consequence, the number of detector subdivisions M required for smooth integration over the simultaneously active area is usually larger than the number P of subdivisions required for a satisfactory approximation of the reciprocal space intensity distribution over the active detector area. Hence, in order to ensure smooth integration over a large number M of detector subunits whilst keeping the total number of function evaluation low, it is often practical to obtain the set of M values $I(Q_x^{\mathrm{GTR}}, Q_z^m)$ from simple, e.g. linear, interpolation of $I(Q_x^{\mathrm{GTR}}, Q_z^p)$, containing $P \gg M$ values.

Finally, the total intensity associated with any nominal q_x value is then found

to read

$$I(Q_x) = \sum_{m=0}^{M} I^m(\mathbf{Q}), \tag{5.26}$$

which is simply the sum of intensities integrated over all subdivisions of the detector, i.e. the sum of the coloured areas seen in figure 5.14.

In the above, no assumptions have been made about relative dimensions of the width of the GTRs and the extent of the detector resolution function R, the integral over which is given by eq. 5.25. Hence, the expression for the simulated intensity is generally valid within both extreme cases of high coherence, in which a very narrow GTR is fully integrated over by only a single detector subunit, as well as the other extreme of the relative width of an GTR with respect to the detector acceptance being so wide that every detector subunit simultaneously intersects only a narrow section of the total width of the GTR in Q_x direction.

In other words, if the width of the detector resolution function R is identified with ΔQ_x, and σ^{GTR} is the width of a GTR, two extreme cases can be distinguished:

1. $\boldsymbol{\Delta Q_x \gg \sigma^{\mathrm{GTR}}}$

   The whole GTR is being integrated over by a single detector subunit, leading to a wide satellite peak. This basically corresponds to the convolution of a rectangular resolution function R with a delta-like GTR. Because of the GTRs Q_z modulation, the intensity varies over the apparent Q_x positions, leading to sloped satellite peaks, as observed on the left hand side of Fig. 5.4.

2. $\boldsymbol{\Delta Q_x \ll \sigma^{\mathrm{GTR}}}$

   If, on the other hand, the projected Q_x detector acceptance is small with respect to the width of the GTR (as can be the case at low detector angles, corresponding to satellite peaks of high, positive order), i.e. $\Delta Q_x < \sigma_{\mathrm{rec}}$, the whole GTR is intercepted simultaneously over the whole cross section of the detector. The resulting intensity is the sum over the intensities of the total intercepted Q_z range, while the shape of the satellite peak effectively corresponds to a convolution of the delta-like detector acceptance ΔQ_x with the cross-section of the GTR. Following from the convolution theorem eq. 2.80, the latter leads to satellite peaks of high positive order to mirror the coherence function of the beam, which is often found to be of a Gaussian shape as observed on the high positive orders seen in Fig. 5.4.

Having defined the range of allowed geometries of the sample as well as the corresponding structure factor $F(\mathbf{Q})$, it is necessary to determine the specific set of

parametric values that best describe the physical sample. A common approach for doing so is by systematic variation of the sample parameters in order to successively approach experimental with simulated data, i.e. fit the data, a process which will be described in detail in the next section.

5.4 Fitting Framework

In this section the framework of fitting simulations to experimental data used in this work is presented. Often, each set of experimental data requires a specifically tailored fitting approach to be reproduced successfully. Hence, the following discussion is strictly true only for the experiments at hand, but can be considered to work as a guideline for approaching similar problems.

The two main aspects determining the success of a fit are the choice of an adequate *figure of merit* (FOM) and the choice of sensible *algorithmic fitting parameters*, which are governing the dynamics of the used fitting procedure as discussed in chapter 3. As opposed to the *model fitting parameters*, which are being optimised to fit experimental data, algorithmic fitting parameters are kept constant over the course of a single fit but might strongly impact how efficient the optimisation progresses, and can therefore be considered as *meta parameters*.

5.4.1 Figure Of Merit

The figure of merit is a function taking the (discrete) experimental- and simulated data, y_i^{exp} and y_i^{sim}, as an argument and returns a single positive number that represents the degree y^{sim} matches y^{exp}, with lower values usually indicating a higher degree of agreement. The abscissa x_i usually refers to the scan direction in reciprocal space. Generally speaking, it is often easy to find a figure of merit that works for a particular fit, but hard to define an *objective* measure of the *quality* of a fit. It is often rather the *perceived* quality by an investigator looking at a specific presentation of the data, that determines if a fit can be considered successful. After all, changing the way the data is presented, e.g. by changing the scale from linear to logarithmic, can dramatically change the perceived quality of the fit.

The fitting algorithm then iteratively adapts the model fitting parameters in an attempt to optimise the FOM, which for most implementations implies minimisation of the FOM, as discussed in more detail in section 3.4.

A particularly simple figure of merit is obtained by simply taking the absolute

difference of y^{exp} and y^{sim}

$$\mathrm{FOM}_{\mathrm{diff}} = \frac{1}{N}\sum_{i}^{N}\left|y_i^{\mathrm{sim}} - y_i^{\mathrm{exp}}\right|, \tag{5.27}$$

where N is the number of datapoints in the set y^{exp}. Despite its simplicity, this figure of merit can indeed be a good choice when fitting a single set of data on a linear scale, which is often found to be the case for rocking curves. However, since high absolute intensities tend to have large absolute differences $y^{\mathrm{exp}} - y^{\mathrm{sim}}$, this approach tends to be drastically more sensitive to minimisation in regions where y^{exp} are large. The latter causes obvious problems if the range of data values spans multiple orders of magnitude, as is often the case for reflectivity measurements. In this case, summing over the logarithm of y^{exp} and y^{sim}

$$\mathrm{FOM}_{\mathrm{log}} = \frac{1}{N}\sum\left|\log y_i^{\mathrm{sim}} - \log y_i^{\mathrm{exp}}\right| \tag{5.28}$$

provides a more symmetric weighting of high and low values.

The simultaneous fitting of multiple datasets of overlapping sets of fitting parameters requires the definition of a global figure of merit, which has to be some combination of the individual FOMs of each dataset. Because of the strictly positive value of the individual FOMs, minimizing the composite FOM also minimises each individual FOM. In a simple form, the global FOM can be provided by summation of all individual FOMs

$$\mathrm{FOM}_{\mathrm{total}} = \frac{1}{M}\sum_{i}^{M}\mathrm{FOM}_i, \tag{5.29}$$

where $\mathrm{FOM}_i \geq 0 \forall i$.

However, eq. 5.29 bears the risk of not being equally sensitive to all constituting terms if, for instance, fits of identical *perceived* deviation from experimental data result in FOMs of differing absolute values. In this case, minimisation of the global $\mathrm{FOM}_{\mathrm{total}}$ will preferentially optimise dataset k providing the highest gain in terms of it's individual figure of merit FOM_k at the expanse of the remaining datasets, so that the quality of the combined fits decreases.

Furthermore, since the probed region of parameter space of the combined system naturally shrinks while the fit is proceeding, it is important that the fits of all datasets progress uniformly in order to prevent misconvergence to local minima. Therefore, when fitting multiple datasets simultaneously, it is important to use *normalised FOMs* for each respective dataset, so that an equal gain in quality of any fit manifests in an equal gain in the FOM. Put differently, the algorithm must

not preferentially minimise with respect to a particular dataset at an earlier stage of the fitting procedure only to have the other datasets "catch up" at a later stage, since, by then, the higher localisation in parameter space might prevent a global optimum to be found.

One example of a normalised FOM is obtained by dividing $\mathrm{FOM_{diff}}$ by the total range of y-values the data points span up

$$\overline{\mathrm{FOM_{diff}}} = \frac{1}{N}\sum_{i}^{N}\frac{\left|y_i^{\mathrm{sim}} - y_i^{\mathrm{exp}}\right|}{\max(y^{\mathrm{exp}}) - \min(y^{\mathrm{exp}})}, \tag{5.30}$$

where $\max(y^{\mathrm{exp}})$ and $\min(y^{\mathrm{exp}})$ are the largest and smallest value of the experimental data, respectively. Each simulated data point using eq. 5.30 contributes to the figure of merit with its *relative* displacement, instead of the absolute displacement of eq. 5.27, therefore resulting in $\overline{\mathrm{FOM_{diff}}}$ being the average relative displacement of simulated and experimental data.

Diffraction data obtained from rocking curves of patterned arrays are characterised by alternating sections of high and low intensity, corresponding to the formation of separate GTRs. Since in the context of this work, no fitting of the diffuse scattering providing the background signal of the data is desired, these sections can (and should) be neglected in determining a figure of merit. In other words, only the GTRs should be considered in the evaluation of the figure of merit. However, generally the peak intensity of GTRs substantially varies between different orders and an implementation like eq. 5.30 is more sensitive to peaks of higher intensities, leading to the fitting algorithm progressing by successively optimising for only the satellite orders which provide the highest gains in the FOM. Naturally, this once again bears the risk that by the time the peaks of highest intensity have been fitted, the algorithm already converged into a local minimum. Note that these fits might actually be *perceived* well, since the most prominent high intensity peaks actually match well in between simulation and experimental data. Generally, fitting low intensity peaks is equally important as fitting high intensity peaks, so a useful figure of merit should weight fitting both as equally important. A possible solution is, instead of evaluating a given dataset as a whole, evaluate the average relative deviation of all individual peaks with respect to their respective height, i.e.

$$\overline{\mathrm{FOM_{peaks}}} = \frac{1}{K}\sum_{k}^{K}\frac{1}{N_k}\sum_{i}^{N}\frac{\left|y_{k,i}^{\mathrm{sim}} - y_{k,i}^{\mathrm{exp}}\right|}{\max(y_k^{\mathrm{exp}}) - \min(y_k^{\mathrm{exp}})}, \tag{5.31}$$

where $y_{k,i}^{\mathrm{sim}}$ and $y_{k,i}^{\mathrm{exp}}$ are the sets of the N_k data points belonging to the $\mathrm{k^{th}}$ satellite

peak, and K is the total number of satellite peaks within the dataset. The figure of merit given by eq. 5.31 weights each satellite equally, disregarding of its peaks intensity, ensuring maximum data sensitivity on probing parameter space.

Finally, *linearisation of data* is another way of changing the presentation of data in a format more convenient for fitting. Since specular reflectivity in particular often spans multiple orders of magnitude in intensity, using a logarithmic figure of merit like eq. 5.28 proves useful in maintaining sensitivity over the whole data range. However, determining the *quality* of the fit is not straightforward, since a significant fraction of the data resides at intensities too low to be perceived well by a human observer, therefore requiring additional analysis not only to perform the fit but also evaluate it's quality. A simple alternative is direct modification of both experimental and simulated data, by rescaling each data point according to a power of the Q_z component of the wavevector transfer

$$\tilde{y} = y \times Q_z^{\gamma}, \tag{5.32}$$

where usually $\gamma \approx 4$, compensating for the Q_z^{-4} scaling of the Fresnel reflectivity[62] according to 2.41.

In practise, it was found empirically that indiscriminately using the $\overline{\mathrm{FOM}_{\mathrm{diff}}}$ function provides best results, mostly because it avoids problems regarding the absolute scale of intensities when simultaneously fitting multiple sets of data. Somewhat contrary to expectation, the $\overline{\mathrm{FOM}_{\mathrm{peaks}}}$ function did rather decrease the quality of the fit. The most likely explanations include the unreliability of low intensity peaks, where noise and background interference are found to be more prevalent. Alternatively, the used island model is likely to not provide sufficient spatial sensitivity in order to reliably fit the high Fourier components found at diffraction peaks of high orders, hence amplifying any model shortcoming and leading the algorithm to compromise the quality of low order peaks in trying to fit the diffraction peaks of higher orders. In the latter case, the decrease of fitting quality is not related to the low intensity of the high order peaks, but to effectively increasing the total range of (sensitively) fitted diffraction peaks.

5.4.2 Meta Optimisation of Algorithmic Fitting Parameters

Most variants of differential evolution offer the choice between multiple *fitting strategies* as well as between three algorithmic parameters, which are the differential weight F of mutants, the crossover probability Cr and population size N.

Both quality and convergence speed of a fit can be highly sensitive to the choice of algorithmic parameters. In fact, when trying to fit the data initially, it was found that long convergence times of the fitting procedure in combination with a huge misconvergence rate significantly hindered the progress of the studies. Not knowing when true convergence has been reached, often spending multiple days on a single fit, with results being hardly reproducible, made classifying any changes in the fitting framework a very tenacious undertaking. It was therefore understood, that finding the most reliable and efficient algorithmic parameters had to be prioritised, if fitting of the experimental data was to be achieved.

However, finding the set of algorithmic parameters most suitable for a problem at hand is far from trivial, although rules of thumb for choosing particular combinations for certain kinds of problems exist[182, 184, 213]. Generally, there will be a trade off in between the robustness of the strategy and convergence speed. But apart from merely requiring to wait longer for a fit to converge, different combinations of algorithmic fitting parameters will also significantly affect the *dynamics* of the algorithm and therefore the quality of the fit and even the probability of a fit converging in the first place.

To find a good set of algorithmic fitting parameters the choice was made to perform a meta-analysis of the fitting problem at hand. Here, the same modelling framework that would later be used in analysing the experimental data was used to create a simplified control system of known solution. The idea is that artificial data are obtained by simulating the control system of known model parameters. The control system should exhibit similar properties as the real system which is meant to be fitted eventually, e.g. by exhibiting similar coupling of parameter, thus ensuring similar fitting dynamics. On the other hand, the total number of parameters can be decreased by neglecting parameters that are not affecting the fitting dynamics in a crucial way. For instance, all effects related to the experimental geometry can be safely discarded, since the latter do not couple to the model parameters determining the spatial shape of the islands.

This way, the time consuming processes of repeated and extended calculation of the structure factor $F(\mathbf{Q})$ as discussed in section 5.3.2 can be reduced to the necessary minimum. Physically this corresponds to neglecting beam divergences $\Delta\alpha_i$ and $\Delta\alpha_f$, eliminating the need for integration over the open detector.

In effect, after eliminating all expendable ballast from the simulation, one is left with the remaining bare skeleton containing the relevant fitting dynamics of the system, which is found to be the calculation of a set of squared structure factors $|F(\mathbf{Q})|^2$ of the island. In other words, the fit consists in simply fitting arrays of

numbers of structure factors corresponding to subsets of the positions in reciprocal space which are similar to the ones probed in experiment. This approach provides the immediate advantages of an increase in simulation time per iteration by up to two orders of magnitude.

More importantly, though, the system has a known solution, which is already proven to be attainable by the specific modelling framework since it has itself been created from within said framework. Without meta-optimisation, and immediately going into fitting true experimental data, it is rather unclear if any problems in attaining good-quality fits reside within the modelling- or fitting framework or both. In contrast, any deviations of the fits to the artificial data are necessarily a result of imperfect fitting dynamics, so that both model parameters and algorithmic parameters can be optimised independently.

The artificial data were created by once allowing all model parameters a random value within reasonable boundaries, therefore fixing a single manifestation of a randomly determined domed island. It was then attempted to recreate the original set of parameters by fitting this system in a chosen subset of the parameters only, while keeping most of the model parameters fixed on their original values. Hence, each population member within the differential evolution framework consisted of a 11-dimensional parameter vector p_i corresponding to the following components

1. Real part of the scattering factor of the oxide shell $\mathrm{Re}(f_{\mathrm{shell}})$
2. Real part of the magnetic contribution to the scattering factor of the magnetic core $\mathrm{Re}(f_{\mathrm{core}}^{\mathrm{mag}})$
3. Diffusion width of the core-shell interface σ^{core}
4. Diffusion width of the shell-vacuum interface σ^{shell}
5. Total height of the island including the dome h_{D}
6. Nominal height of the island excluding the dome h_{n}
7. Offset of the Pearson VII doming function below nominal island height z_{off}
8. Total thickness of the oxidised shell of the island d^{shell}
9. Shape parameter determining upper slope of the side walls σ_{t}
10. Thickness of a SiO_2 capping layer of the substrate d_{SiO_2}
11. Roughness of the SiO_2 capping layer of the substrate σ_{SiO_2}.

Similarly to what would be eventually the case for the experimental data, four artificial datasets obtained from two kinds of reciprocal space scans were fitted simultaneously. Pairs of sum and difference signals of the islands structure factor $F(\mathbf{Q})$ were evaluated along reciprocal space trajectories corresponding to the same rocking curve and specular reflectivity measurement used in the actual experiment as well. However, the number of data points was limited to 15 for the rocking curves and 25 for the reflectivity, distributed uniformly over the total scan range of the experiments. For all fits, the normalised difference figure of merit $\overline{\mathrm{FOM}_{\mathrm{diff}}}$ (eq. 5.30) has been used after linearisation of the reflectivity data as discussed in section 5.4.1.

Then, random combinations from a discrete set of algorithmic parameters were used on performing each fitting procedure. Each fit was technically considered successful if the convergence criterion

$$\sigma_{\mathrm{FOM}} = 0.01 \times \frac{1}{N} \sum_{i=1}^{N} \mathrm{FOM}_i \tag{5.33}$$

was met, i.e. if the standard deviation of the individual FOMs of all population members fell below a certain fraction of it's arithmetic mean. Note that, again, convergence of the algorithm does not necessarily imply convergence into the global optimum. Conversely, if no convergence was obtained after 1500 generations the fit was considered unsuccessful and was aborted. Obviously, exploring the four-dimensional algorithmic parameter space still requires a large number of individual fits, so the allowed values for each parameter were limited to small discrete sets. The respective parameter sets are given by

$$\begin{gathered} strategy = \{best1bin, rand1bin, currenttobest1bin, randtobest1bin\} \\ F = \{0.25, 0.5, 0.75, (0.25, 1.2), (0.5, 1.2), (0.8, 1.8)\} \\ CR = \{0.25, 0.5, 0.75\} \\ N = \{5, 10, 15\} \end{gathered}$$

where tuple notation of the differential weight F indicate dithering and the names of the strategies follow the convention discussed in section 3.4 and Zaharie and Micota [185]. Note that the quoted values for the population correspond to a multiplication factors of the number of open fitting parameters, which means that for the 11 open parameters the real populations were 55, 110, and 165.

rank	Strat	F	Cr	N	E(5%)	E(1%)	E(0.5%)
1	rand1bin	0.25	0.75	15	1773	13434	18098
2	randtobest1bin	0.75	0.75	15	2029	19470	29370
3	currenttobest1bin	(0.5, 1.2)	0.75	10	1542	19475	28102
4	best1bin	(0.5, 1.2)	0.75	15	2053	19926	30160
5	rand1bin	0.25	0.75	10	1288	20868	26522
6	randtobest1bin	(0.5, 1.2)	0.5	10	1683	21175	35835
7	rand1bin	0.5	0.75	10	1496	21323	27856
8	best1bin	(0.5, 1.2)	0.75	10	1502	21629	32297
9	rand1bin	0.25	0.5	10	1390	21929	30303
10	randtobest1bin	0.75	0.5	10	1510	23729	40669
11	randtobest1bin	(0.5, 1.2)	0.75	10	1311	25740	32661
12	randtobest1bin	(0.5, 1.2)	0.75	15	1787	27799	46886
13	rand1bin	0.25	0.5	15	1782	28375	42757
14	currenttobest1bin	(0.8, 1.2)	0.75	10	3457	28490	49258
15	rand1bin	(0.25, 1.2)	0.75	10	2708	28746	41238
55	rand1bin	(0.25, 1.2)	0.5	15	2838	71412	115219
56	rand1bin	(0.5, 1.2)	0.5	10	2506	72890	141733
57	currenttobest1bin	(0.5, 1.2)	0.75	15	2256	77994	96839
58	currenttobest1bin	(0.8, 1.8)	0.25	15	3597	87780	1119525
59	rand1bin	(0.5, 1.2)	0.25	10	3229	90789	-
60	rand1bin	0.75	0.25	10	2783	92950	-
61	rand1bin	(0.25, 1.2)	0.25	10	2039	95099	842270
62	best1bin	(0.8, 1.8)	0.25	15	4059	97185	-
63	rand1bin	0.5	0.25	15	3520	102712	953920
64	rand1bin	(0.5, 1.2)	0.5	15	3795	104362	203890
65	rand1bin	0.75	0.5	15	3975	112605	167565
66	rand1bin	(0.5, 1.2)	0.25	15	4070	122796	-
67	currenttobest1bin	(0.8, 1.8)	0.5	15	4125	124113	1086525
68	rand1bin	(0.25, 1.2)	0.25	15	2816	131642	1573687
69	rand1bin	0.75	0.25	15	4140	132615	1343100

Table 5.1: Summary of values of algorithmic fitting parameters with corresponding number of function evaluations leading to an average deviation of simulated to artificial control data of 5%, 1%, and 0.5%.

This way, a total of 947 fits was performed, each corresponding to one of the 216 possible combinations p_i^{meta} of allowed algorithmic parameter vectors. In order to reduce computational strain, parameter combinations that have been clearly outperformed after six completed fitting procedures have been eliminated from further trials, so that the average number of completed fitting procedures of each combination of algorithmic parameters p^{meta} (including both successful and unsuccessful attempts) was $\bar{N}_{\text{fits}} = 18.6$.

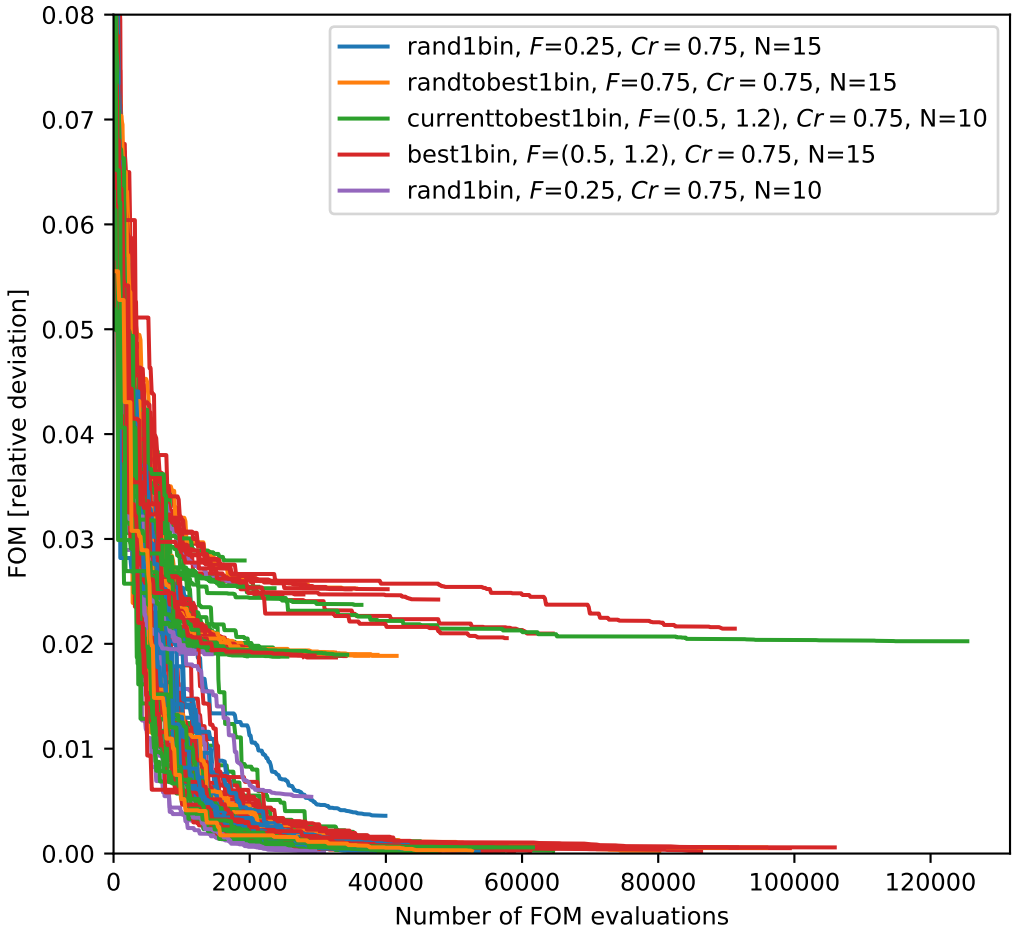

Figure 5.15: The five best performing sets of algorithmic fitting parameters. Misconvergence into one of two local minima is common for the more aggressive fitting strategies.

For each fitting trial the complete evolution of the figure of merit as a function of the total number of FOM evaluations has been tracked, a subset of which can be seen in Fig. 5.15. Noticeably, despite the simplicity of the system and the lack of any kind of experimental noise, misconvergence of the differential evolution algorithm is common and seems to be occurring mainly into two local minima, which are located roughly at $FOM \approx 0.02$. Probably not unsurprisingly these local minima appear to be mainly populated by the *best1bin* and *currenttobest1bin* strategies, which are characterised by their higher convergence aggression coming at the cost of robustness.

Bookkeeping of the FOM history further allows extraction of some useful

statistical properties. For once, fixing a certain *FOM*, the probability $P(FOM)$ of convergence of p_i^{meta} *below* that threshold can be calculated from simple ratios within all simulation runs of the same set of algorithmic parameters. Similarly, $\tilde{E}(FOM)$ is defined as the average number of function evaluations it takes p_i^{meta} to reach a given *FOM* for fits that converge to below said FOM. Hence,

$$E = \frac{\tilde{E}}{P} \tag{5.35}$$

is defined to be the average number of function evaluations it takes p^{meta} to reach a given FOM. The quantity $E(FOM)$ is very useful in evaluation of the performative quality of the algorithmic parameters given by p^{meta}, since it allows deciding which set of algorithmic parameters is most useful for obtaining a fit of a desired quality characterised by a certain figure of merit, including the probability of misconvergence of the procedure.

Table 5.1 presents the 15 best- and worst performing p_i^{meta} of the 69 combinations that made it into the final evaluation, sorted according to the average number of function evaluations $E(1\%)$ it took to obtain 1 percent deviation from the artificial data. Noticeably, both the best and worst performing set of algorithmic parameters are of strategy *rand1bin*. Furthermore, a clear trend is visible for more successful sets p_i^{meta} to obtain a higher crossover probabilities Cr consistent with reported observations[184, 186]. Further, there apparently exists no dominating strategy or differential weights F, although, remarkably, 11 out of the 15 worst performing strategies were *rand1bin*, which is also the overall winning strategy. Moreover, 5 out of the 15 of the best performing and 11 of the 15 worst performing parameter sets were of population factor 15, indicating that the improved covering of parameter space is not generally able to compensate for the increase in number of function evaluations. Again, the best performing strategy contradicts this trend, by also being of population factor 15.

Fig. 5.16 summarises the performance of the five best-performing sets of algorithmic parameters, by plotting the average number of function evaluations as a function of the FOM value to converge below. In particular at low FOM values, the winning candidate is clearly outperforming all its competitors, although the average number of FOM evaluations of all five best performing parameter sets consistently lays within a factor of 2 to each other. However, comparing to table 5.1 it is clear that choosing a still reasonable but less suitable set of algorithmic parameters can easily increase convergence time tenfold.

The main advantage of the winning variant of the *rand1bin* strategy seems to

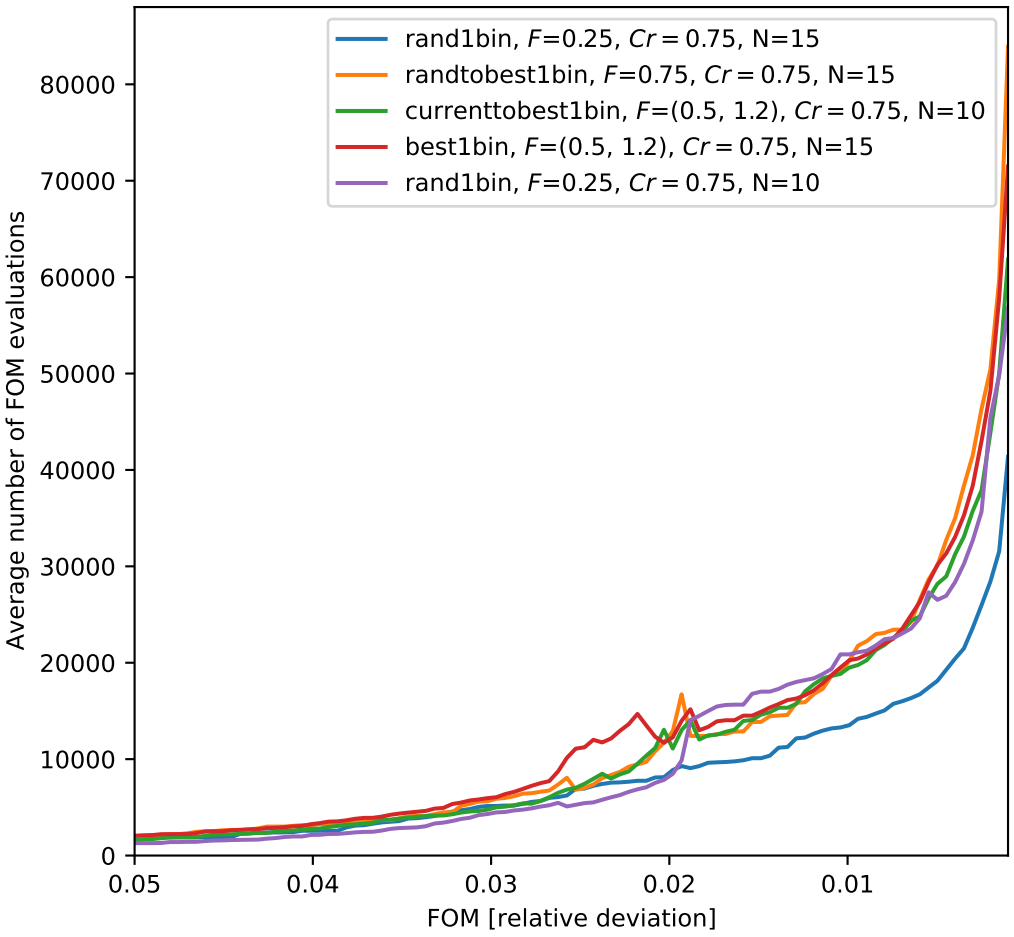

Figure 5.16: Average number of FOM evaluation necessary to converge below a given FOM for the top 5 set of algorithmic parameters. Most implementations perform similarly, although the set corresponding to the blue curve clearly outperforms the remaining sets. The reason is the very high convergence rate, which compensates for the individually slower convergence speed.

be the extremely low misconvergence rate, which is supposedly a consequence of the conservative choice of small differential weight and high population number, which seems to be well able to compensate for the relatively slow convergence speed. Since misconvergence has been found empirically to be a huge concern in fitting the highly coupled model parameters describing the particular domed shape of the patterned

array it was decided to use the winning set of parameters

$$strat = rand1bin$$
$$F = 0.25$$
$$Cr = 0.75$$
$$N = 15$$

for the remainder of this chapter.

5.5 Experimental Results

This section discusses various fits of experimental data which are used to investigate structural, chemical and magnetic sample properties as well as validate the scattering framework as discussed in the preceding sections.

Measurements include both sum- and difference signals taken at opposite polarisation helicities of the circularly polarised x-rays and are hence magnetically sensitive. All fits are restricted to the measurements taken at 30 K, because of the stronger magnetic response at lower temperatures as presented in Fig. 5.4 b) and c). Since only the diffracted intensity of the GTRs is simulated, the sum signal of the rocking curve data has been manually preprocessed by means of subtraction of the continuous background signal provided by the diffuse scattering of the sample. The background signal has been obtained by a common spline fit to points between the GTRs. Background, raw- and corrected data are presented in Fig. 5.17 a).

Furthermore, the sum signal of the specular reflectivity has been linearised by means of multiplying the experimental intensities by Q_z^6, where the exponent was found empirically. As discussed in section 5.4, linearising the data in this way simplifies defining a global figure of merit when simultaneously fitting multiple datasets, as well as serves as a more expressive presentation of the underlying structure within the specular reflectivity.

The difference signals I^- obtained from the rocking curve, as well as the aspect ratio $A.R.$ of the specular reflectivity as seen in Figs. 5.4 b) and 5.5 b) are naturally presented on a linear scale and exhibit no easily distinguishable background signal and were therefore not subjected to additional preprocessing.

The patterned islands were simulated using a core-shell model, implying uniform oxidation of the island surface. The scattering factor of the core $f_{\text{core}} = f_{\text{core}}^{\text{nonmag}} \pm f_{\text{core}}^{\text{mag}}$ were assumed to include a magnetic contribution as discussed in section 2.1.4. Since oxidation is assumed to have rendered the material non-magnetic,

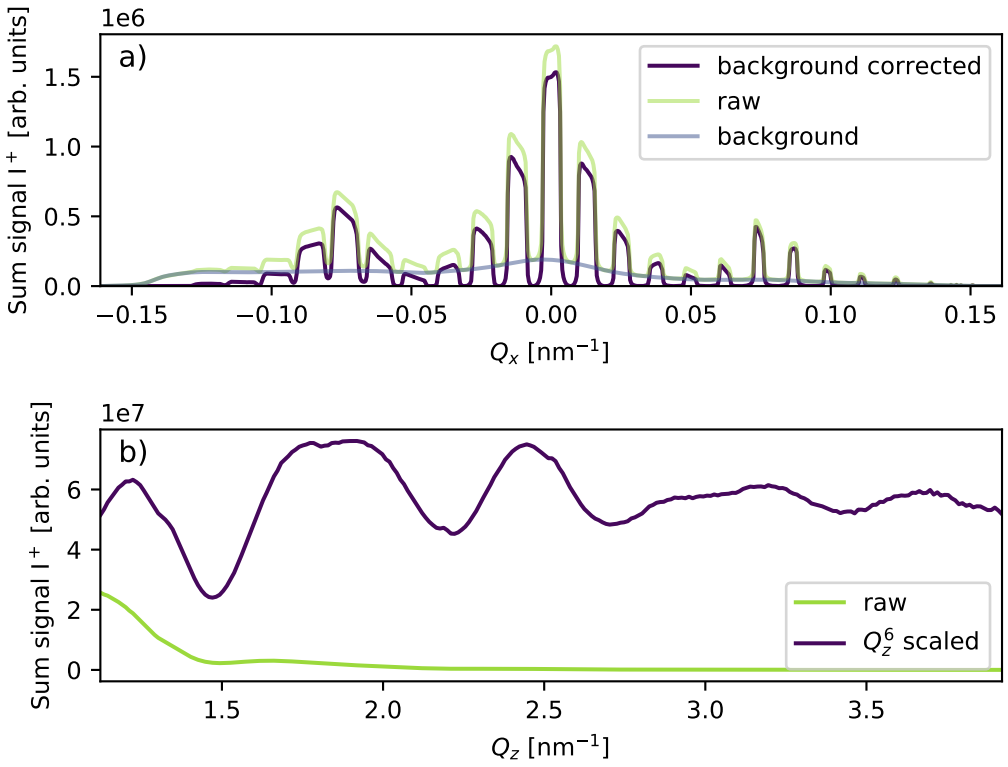

Figure 5.17: Data processing preceding the fit procedure. Panel a) shows the raw data of the sum signal measured at 30 K, the background signal as obtained from spline interpolation between the satellites and the corrected data. Panel b) shows the effect of scaling the sum signal of specular reflectivity taken at 30 K by Q_z^6, which effectively linearises the data. The scaled version exposes a richer structure than the same data on a linear scale, as shown by the green curve, or on logarithmic scale, as shown in Fig. 5.5 b).

the scattering factors f_{shell} of the oxidised shell were consequently assumed to not include a magnetic component.

In all fits, the substrate has been modelled individually by a standard one-dimensional profile of a stratified system. Similar to the nominal shells of the island, the substrate has been divided into nominal layers j, each defined by its lower interface height s_j and corresponding diffusive roughness σ_j^{sub}, as well as it's nominal

scattering length density f_j^{sub}, leading to an SLD profile defined by

$$f_i^{\mathrm{sub}}(z_i) = \frac{\sum_{j=0}^{J} f_j^{\mathrm{sub}}(z_i)\,\varphi_{i,j}(s_j)}{\sum_{j=0}^{J} \varphi_{i,j}}, \tag{5.37}$$

evaluated at each slice i with $\varphi_{i,j}$ being defined analogous to eqs. 5.8 and 5.9. Note that the atomic number density $\rho^{\mathrm{num}}(z_i)$, again, has been implicitly included within $f_i(z_i)$.

Consequently, the substrate SLD can be identified with the ambient SLD, $f_{\mathrm{amb}} = f_i^{\mathrm{sub}}(z_i)$ when evaluating eq. 5.13. Note that here, unlike to earlier discussion, $f_{\mathrm{amb}}(z_i)$ strictly is a function of height z_i, and has hence to be re-evaluated for every sample slice i associated with height z_i.

In other words, above substrate level the scattering factor of the outermost (ambient) shell is equal to zero, while below the nominal substrate level the scattering length density of the islands continuously merges into the substrate's SLD at the same z-value, $f^{\mathrm{sub}}(z_i)$.

5.5.1 Rocking Curves

This section presents the simultaneous fits of the sum and difference signals I^+ and I^- of the rocking curves, while including specular reflectivity into the fits will be implemented in section 5.5.2.

Using the previously discussed approach, calculation of the structure factor was performed by slicing the island into discrete thin layers, each of thickness 0.07 nm. The nominal height of the (flat) islands, as designed by the patterning process, was $h_{\mathrm{n}} = 10\,\mathrm{nm}$ and the model was set up in a way that allowed the spatial structure of the island to continuously morph in between flat- and domed tops. Within the fitting procedure, the domed tops were allowed to vary in their total height h_{d} within reasonable limits, i.e. going up to 20 nm in total, which would imply doubling the total island height with respect to the intended height. Fitting parameters determining the spatial structure of the islands were the shape parameters of the bottom- and top parts of the islands side-walls, σ_{b} and σ_{t}, the nominal height of the island h_{n} on top of which the dome is located, the nominal radius of the island r_{n}, shape determining parameters of the dome, z_{off} and M, and the total height of the island including the dome, h_{d}, all of which have been discussed in section 5.2. Further, the rectangular lattice pitch d_{latt} was included as a fitting parameter, since as the measurement took place at 40 K it was presumed to be

affected by thermal shrinkage.

Since oxidation is assumed to have occurred by uniform diffusion of oxygen normal to the island's surface, the oxide shell is modelled to be of constant thickness d^{shell}. This has been incorporated into the model by coupling the surface cut functions of the oxide shell and magnetic core in a way that nominal radius and height of the core depend on the corresponding values of the shell by

$$r_{\text{n}}^{\text{core}} = r_{\text{n}}^{\text{shell}} - d^{\text{shell}} \tag{5.38a}$$

$$h_{\text{n}}^{\text{core}} = r_{\text{n}}^{\text{shell}} - d^{\text{shell}}. \tag{5.38b}$$

The remaining parameters determining the chemical structure of the sample are the diffusion widths of the core-shell and shell-ambient interfaces, σ^{core} and σ^{shell}, as well as the real and imaginary parts of the scattering factors $\text{Re}(f_{\text{core}}^{\text{nonmag}})$, $\text{Im}(f_{\text{core}}^{\text{nonmag}})$, $\text{Re}(f_{\text{core}}^{\text{mag}})$, $\text{Im}(f_{\text{core}}^{\text{mag}})$, $\text{Re}(f_{\text{shell}})$, and $\text{Im}(f_{\text{shell}})$.

Note that the substrate was included in the sample model, for once because the island pattern extended to below the nominal substrate level because of the surface roughness and secondly because it is required by the DWBA. Hence, the substrate was modelled by an oxidised layer of SiO_2 of thickness d_{SiO_2} located on top of pure Si. The interface roughness of the Si-SiO_2 and SiO_2-island interfaces were given by fitting parameter σ_{Si} and σ_{SiO_2}, while f_{Si} and f_{SiO_2} were taken from standard tabulated values and hence not fitted directly.

Finally, instrumental fitting parameters included the incident intensity I_0, acting as a scaling factor for the simulated intensity, and the source- and detector angular divergences, $\Delta\alpha_i$ and $\Delta\alpha_f$, respectively.

Before proceeding to performing a full fit of the experimental data including all open parameters, some of the previously defined parameters have been possible to be determined in a partial fit involving only a small number of parameters, which allowed the final fit to proceed more efficiently by reducing the dimensionality of parameter space. The parameters determined in this way were the incident beam divergence $\Delta\alpha_i$, the detector acceptance $\Delta\alpha_f$ within the scattering plane, and the lattice pitch d_{latt}, by exploiting their unique effect towards the shape and position of the diffraction peaks. Ignoring their intensity for the moment, every simulated peak ought to match experimental data in both width and side slope. In the experimental data, peaks are looking more rectangular to the left hand side of each rocking curve, while they appear more Gaussian to the right side of the curves. This is a consequence of each diffraction peak being the convolution of the reciprocal coherence function $C(\Delta\alpha_i, \mathbf{Q})$ and the detector resolution function $R(\Delta\alpha_f, \mathbf{Q})$. Generally, it

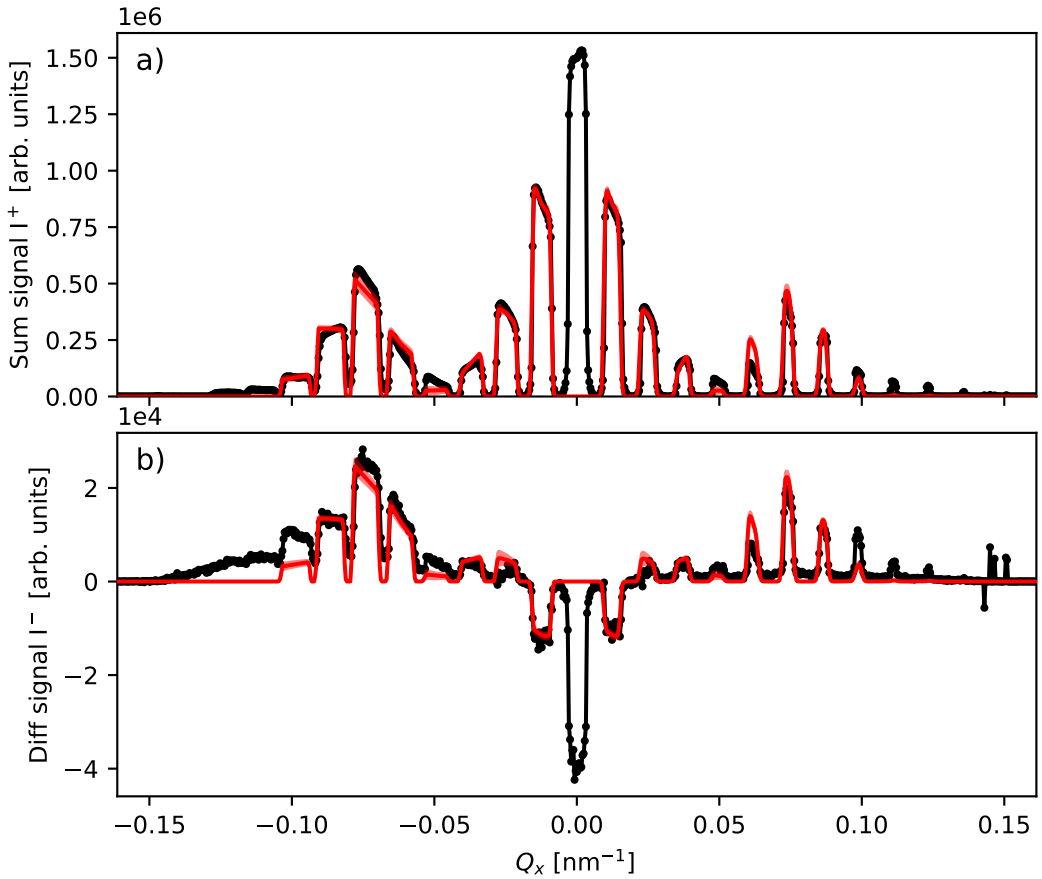

Figure 5.18: Result of repeated simultaneous fits of both sum- and differnece signal as obtained from the rocking curve. The black symbols and line correspond to experimental data, while the red line corresponds to the average of a certain number of simulations. The standard deviations of the simulations is given by the shaded region around the red line, which on most Q_x values is too small to be notices, indicative of the high reproducibility of the fits.

is often legitimate to approximate $C(\Delta\alpha_i, \mathbf{Q})$ by a Gaussian, being more narrow the larger the real space beam coherence is, which is in turn associated with smaller values of $\Delta\alpha_i$. Within the open detector geometry, $R(\Delta\alpha_f, \mathbf{Q})$ is approximated by a box function, being wider the larger $\Delta\alpha_f$ is. Hence, the convolution of the two resembles a box function of smooth edges, with $\Delta\alpha_f$ determining the total width of the peak, while $\Delta\alpha_i$ determines the steepness of the side of the peak, with peaks being sharper the larger the incident beam coherence is. The shape evolution of the peaks over the course of the rocking scan is therefore fully determined by the source- and detector angular divergences, $\Delta\alpha_i$ and $\Delta\alpha_f$. Furthermore, the centre position of each peak is obviously determined by the real space lattice pitch d_{latt}.

To fix values for $\Delta\alpha_i$, $\Delta\alpha_f$, and d_{latt}, first a fit including the full set of parameters was performed, which was aborted once the fit converged to the point at which satellite peaks *roughly* matched experimental peaks in terms of intensity. Subsequently, the fit was restarted but all fitting parameters apart from $\Delta\alpha_i$ and $\Delta\alpha_f$ and d_{latt} were held constant at their interim values. Reducing the dimensionality of the fit significantly sped up the fitting procedure, and despite most peaks not matching experimental data very well, adapting $\Delta\alpha_i$ and $\Delta\alpha_f$ still allowed significant gain using an arbitrary FOM function, simply by matching simulated to experimental peak shapes in terms of their variation in widths as well as the peaks slope around their sides. The values found in this way were

$$d_{\mathrm{latt}} = 509\,\mathrm{nm}$$

corresponding to a 0.77 % reduction to the nominal value of 513 nm due to thermal shrinkage, and

$$\Delta\alpha_i = 0.96\,\mathrm{mrad}$$

$$\Delta\alpha_f = 0.15^{\circ}.$$

Once these three parameters had been eliminated from the fitting process, a full simultaneous fit of the sum- and difference signals of the rocking curves optimising all remaining open parameters has been performed using the $\overline{\mathrm{FOM}_{\mathrm{diff}}}$ for each set of data, the result of which is shown in Fig. 5.18. Sum and difference signal of the rocking scan have been fitted simultaneously, leading to most features of the scan being reproduced both qualitatively and quantitatively. In both fits, the red line represents the mean of 10 simulation runs while the standard deviation of the signal is included as a red shaded area around each simulated value. The fact that the standard deviation is barely visible in the fit is indicative of the high convergence rate and reproducibility of the fitting procedure, suggesting that any remaining (small) deviation between experimental and simulated values are model intrinsic.

Note that in both fits, the zero-order peak has been omitted from the fit because of the potential interference with the reflected x-rays from the unpatterned substrate. Including substrate properties into the model, while certainly possible, adds what was considered to be an unnecessary complication to the fitting procedure, while at the same time providing only very little useful information. After all, the exact shape and chemical composition of the substrate is not considered critically important in determining the structure of the patterned array. These considerations

Parameter name	mean	STD	relative STD [%]
$d_{\mathrm{SiO_2}}$	-1.77	0.43	24
σ_{Si}	0.28	0.2	72
$\sigma_{\mathrm{SiO_2}}$	0.656	0.045	6.9
σ_{b}	1.34	0.48	35
σ_{t}	1.9	1.8	93
h_{n}	8.39	0.39	4.6
r_{n}	227.3	4.7	2.1
z_{off}	1.68	0.33	20
M	4.4	1.9	44
d^{shell}	2.47	0.22	3.6
h_{D}	14.98	0.37	2.5
σ^{core}	0.27	0.095	35
σ^{shell}	0.79	0.16	20
$\mathrm{Re}(f_{\mathrm{core}}^{\mathrm{nonmag}})$	1822	90	5
$\mathrm{Im}(f_{\mathrm{core}}^{\mathrm{nonmag}})$	950	390	41
$\mathrm{Re}(f_{\mathrm{shell}})$	1140	210	18
$\mathrm{Im}(f_{\mathrm{shell}})$	440	200	47
$\mathrm{Re}(f_{\mathrm{core}}^{\mathrm{mag}})$	0.047	9	19000
$\mathrm{Im}(f_{\mathrm{core}}^{\mathrm{mag}})$	-46.4	6.7	14

Table 5.2: List of parameters used to fit simulated to experimental data of sum- and difference signal of the rocking curves.

are discussed in more detail in section 5.5.2, where an attempt of fitting a reflectivity scan of the patterned array is presented.

Table 5.2 presents all fitting parameters in terms of their mean and standard deviation as obtained from a total of 10 simulations. While the fits as seen in Fig. 5.18 show a high degree of conformity as indicated by the very narrow spread of intensities between repeated simulation runs, the standard deviations of many individual parameters are remarkably high. The latter is not necessarily unexpected, since strongly coupled parameters may, in general, be found to highly fluctuate in their respective individual values, yet still lead to highly reproducible fits. The latter is true since the quantity determining the scattered intensity is the factual spatial distribution of scatterers, which are not linked per se to any physical parameters, but which may be obtained from very different combinations of strongly coupled model parameters with no intrinsic meaning in itself.

However, some parameters of particularly low standard standard deviation like the nominal island height h_{n}, the island dome height h_{D}, and the thickness of the oxidised shell d^{shell} are considered to be highly decoupled from the remaining parameters and give valuable information about the spatial structure of the patterned

array.

The unusual intensity modulation for satellite orders ≥ 5 of the rocking curves was surprising, since the structure factor of cylindrical islands is directly proportional to a regular Bessel function of first kind and order 1. Hence, the structure factor $F(\mathbf{Q})$ of the island, acting as the envelope function of the diffraction peaks, was expected to be proportional to the Bessel function, which is rapidly decreasing with increasing $|\mathbf{Q}|$. Scanning electron microscopy images as presented in Fig. 5.1 initially confirmed the cylindrical shape of the islands, so this qualitative deviation from the expected intensity distribution emerged rather surprisingly. Eventually, the AFM measurements presented in Fig. 3.3 revealed the unintended doming of the islands. The unusual modulation can be explained, though, by closer inspection of the structure factor calculation. Considering for the moment only a single surface cut function $s(x, y)$, its scattering length density is described by

$$f(\mathbf{r})\rho^{\mathrm{num}}(\mathbf{r}) = \begin{cases} const. & \text{for } 0 < z \leq s(x,y) \\ 0 & \text{for } z > s(x,y), \end{cases} \tag{5.39}$$

so that in kinematical approximation the island structure factor $F(\mathbf{Q})$ is given by the Fourier transformation of eq. 5.39 to read

$$s(x,y)^{\mathrm{FT}} \propto \iiint s(x,y)\, \mathrm{e}^{-i\mathbf{Qr}}\, \mathrm{d}x\, \mathrm{d}y\, \mathrm{d}z = \iint \mathrm{e}^{-iQ_z s(x,y)} \mathrm{e}^{-\mathbf{iQ}_\parallel \mathbf{r}_\parallel}\, \mathrm{d}x\, \mathrm{d}y. \tag{5.40}$$

In other words, the Fourier transformation of the scattering length density over all three spatial dimensions is equivalent to the two-dimensional in-plane Fourier transformation of the function

$$s(x,y)^{\mathrm{FT_z}} = \exp(-iQ_z s(x,y)). \tag{5.41}$$

Obviously, $s(x,y)^{\mathrm{FT_z}}$ is strongly fluctuating in $\mathbf{r}_\parallel$ if

$$\Delta s = \max(s(x,y)) - \min(s(x,y)) \approx \frac{2\pi}{Q_z}$$

holds for the range of z-values which $s(x, y)$ spans.

Fig. 5.19 shows a comparison of the functions $s(x, y)$ and $s(x, y)^{\mathrm{FT_z}}$ as obtained from the simultaneous fit. The phase of the z-component of the Fourier transformation eq. 5.40 exhibits about three full oscillations on a real-space period

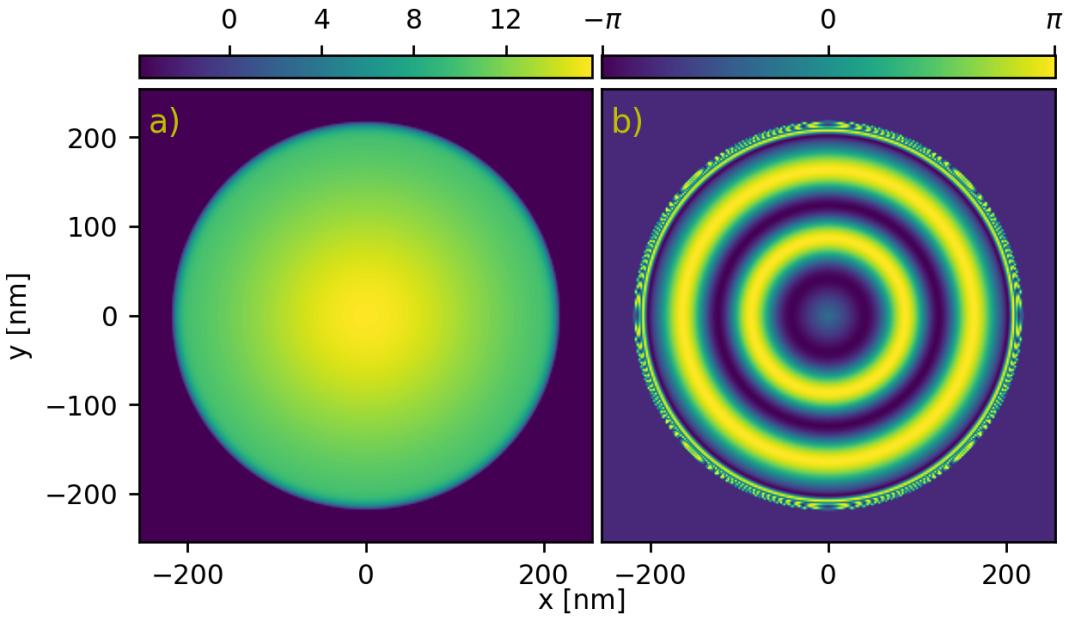

Figure 5.19: Comparison of the surface cut function $s(x, y)$ (panel a) and the z-component of the Fourier transformation $s(x, y)^{\mathrm{FT_z}}$ (panel b). While panel a) exhibits comparatively little structural variation, the periodic nature of the complex exponential function in eq. 5.41 introduces additional oscillatory behaviour rooted within the island's height modulation by means of the doming.

of roughly 60 nm, corresponding to a position in reciprocal space

$$\frac{2\pi}{60\,\mathrm{nm}} \approx 0.1\,\mathrm{nm}^{-1},$$

which is exactly where the unexpected modulation of the diffraction peaks observed in experiment is strongest.

In order to investigate the sensitivity of the fit to individual parameters, Fig. 5.20 presents a number of scans showing the $\overline{\mathrm{FOM}_{\mathrm{diff}}}$ figure of merit, as defined in eq. 5.30, corresponding to the simultaneous fits of the sum- (purple lines) and difference signals (green lines). The scans have been performed on the set of parameters obtained from the fit of the lowest FOM at the end of the optimisation process (although all fits resulted in very similar final FOMs). Each line is obtained from the variation of a single selected parameter while keeping all remaining parameters fixed at their best fitted values. The best value of the parameter under consideration is further indicated by a vertical dashed line. Well defined and deep minima therefore represent high model sensitivity, while flat minima are characteristic for less important parameters.

As a first observation, in all scans the FOMs of both, sum- and difference

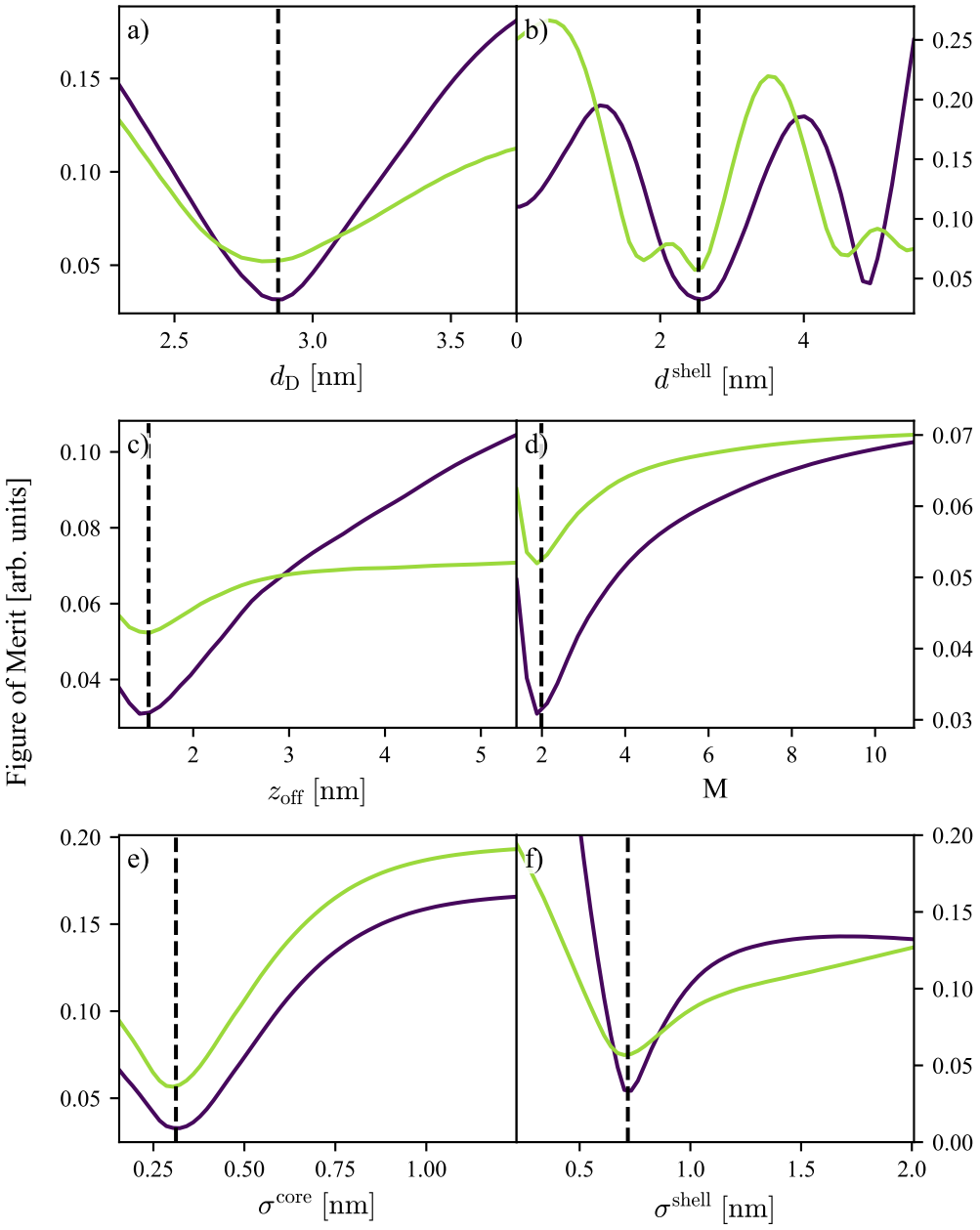

Figure 5.20: Selected parameter scans corresponding to sum signal (purple lines) and difference signal (green lines). Scanned parameters were the thickness of the doming t_D (a), thickness of the oxide shell d_{shell} (b), parameters determining the shape of the dome, z_{off} (c) and M (d), interface roughness between core and shell σ^{core} (e), and surface roughness σ^{shell}. The vertical dashed lines represent the best fitted values. In all cases the $\overline{FOM_{diff}}$ function has been used to evaluate the figure of merit. All involved parameters have been found from simultaneous fitting of the sum and difference signal.

signals, exhibit individual minima aligned at the best parameter values corresponding to the fit. This is a strong indicator that the model captures essential properties of the real system, as the same system obtains identically located minima for different types of measurements, which by no means has to necessarily be the case, even when the fit converged to the global minimum, the latter being a composite of the individual FOM functions for each measurement. In other words, any model will exhibit certain (local and global) minima, but aligned minima are indicative of a single model meeting the requirements of simultaneously fitting multiple measurements, therefore increasing the likelihood of the underlying model being accurate.

Fig. 5.20 a) and b) show parameter scans of the thickness of the dome d_{D} above the nominal island height and the thickness of the oxide layer d^{shell} perpendicular to the island surface. Both scans reveal high absolute change in FOM of all parameters, quickly increasing average deviation of simulated and experimental data from around 5 % to over 15 % for d_{D} and 25 % for d^{shell}. The rapidly increasing FOM upon variation of d^{shell} as well as the apparently highly structured profile of the parameter scan stresses the importance of considering a core-shell structure when fitting both sum and difference signal of the scattered x-rays. If no simultaneous fit of sum- and difference signal had been performed, the algorithm had not been able to differentiate between any of the local minima of the respective FOM function of sum- and difference signal. The alignment of the two individual local minima of sum- and difference signal at the vertical line renders this specific position in parameter space a deep composite minimum, with the latter being calculated from the sum of the individual figures of merit. Despite the parameter space apparently being strongly structured along the d^{shell} dimension, the parameter exhibits a very low relative standard deviation of 3.6 % taken from repeated fitting procedures.

Both z_{off} and M exhibit well defined minima, but because of their supposedly strong coupling in determining the exact shape of the dome, the exact scan profile and best fitted values of z_{off} and M strongly vary in between individual fits (not shown here), which reflects in the high associated errors as seen in table 5.2.

From table 5.2 it follows that the roughness of the interface separating core and oxide shell σ^{core} is consistently lower than the surface roughness of the island surface σ^{shell}, although associated errors on both fitting parameters are relatively large. Despite fluctuating in between individual simulation runs, both σ^{core} and σ^{shell} exhibit well defined minima on the selected simulation run, as seen in Fig. 5.20 e) and f).

In order to further explore the implications of the core-shell model, Fig. 5.21 shows the effect of varying the thickness of the oxide shell, presenting four simula-

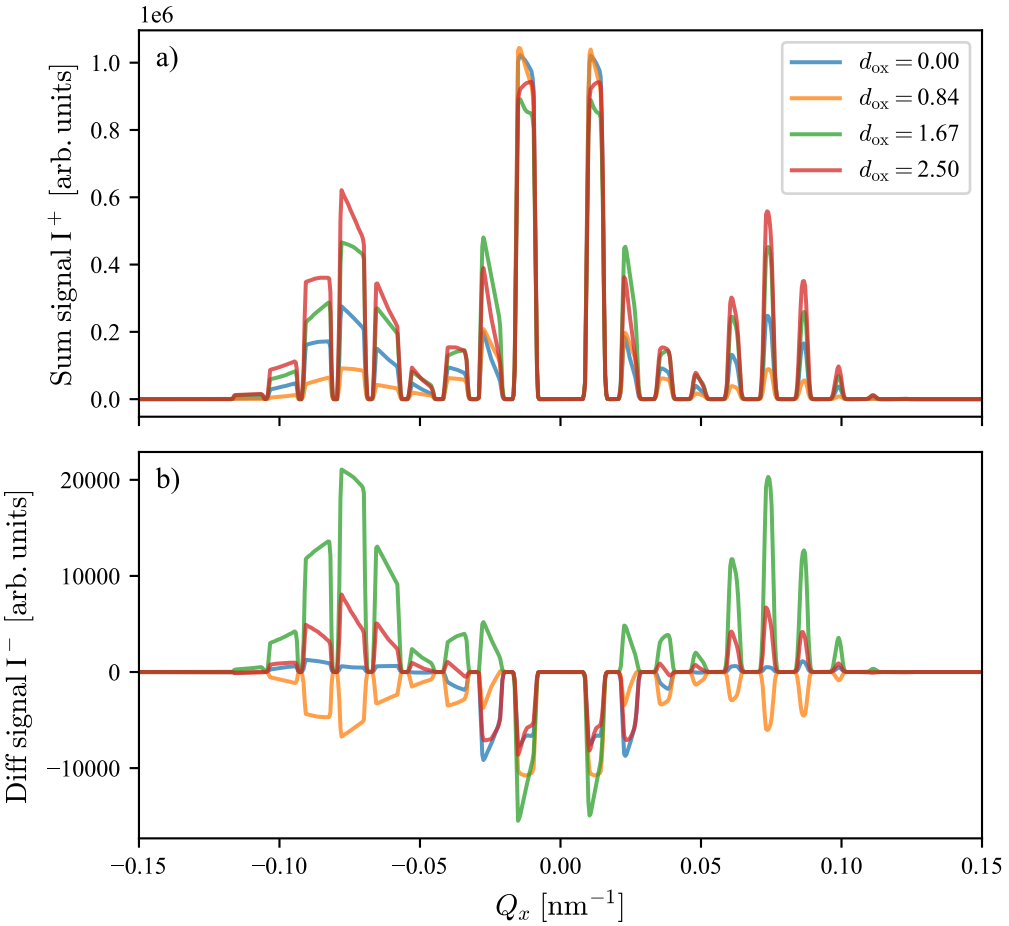

Figure 5.21: Simulations of the effects of varying shell thickness upon the sum- (a) and difference signal (b).

tions spanning the range $d^{\text{shell}} = 0\,\text{nm}$ to $d^{\text{shell}} = 2.5\,\text{nm}$. As can be seen, the effect towards the sum signal is mainly an issue of intensity scaling, as the simulated signal stays qualitatively identical. The difference signal, however, undergoes a massive qualitative transition. At $d^{\text{shell}} = 0\,\text{nm}$ peaks of order ≥ 3 are strongly damped, while at $d^{\text{shell}} = 0.84\,\text{nm}$ distinct peaks develop even for higher order peaks, despite all being negative contrary to the peaks of the experimental data, which change in sign between orders one and two. At $d^{\text{shell}} = 1.67\,\text{nm}$ the experimentally observed pattern emerges, which subsequently gets damped at $d^{\text{shell}} = 2.5\,\text{nm}$. This observation is indicative of the often subtle interplay in between the internal chemical and magnetic structure of the patterned arrays and is exemplary of the high sensitivity of resonant magnetic scattering of patterned arrays.

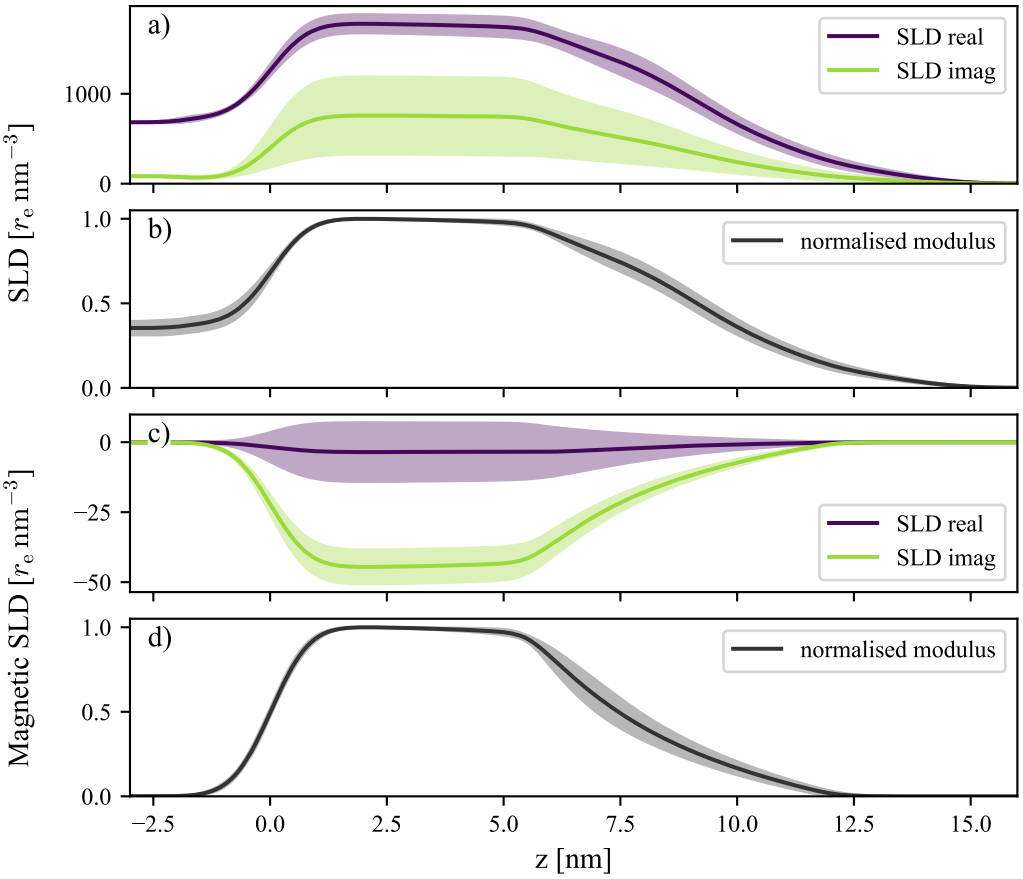

Figure 5.22: Comparison of real- and imaginary parts, and normalised average depth profile of non-magnetic (panels a and b) and magnetic SLD (panels c and d) obtained from simultaneous fitting of sum and difference signal of the rocking curves.

Laterally averaged SLD profiles of the patterned array provide the opportunity to investigate the spatial conformity of the results of repeated fitting procedures. The advantage of reducing the three-dimensional patterned array in this way is that deviations from the mean are easy to grasp visually as seen in Fig. 5.22, which shows a comparison of a number of derived quantities all related to the averaged SLD depth profile. Each line represents mean values, while the surrounding shaded areas indicate the width of one standard deviation. Fig. 5.22 a) shows the real and imaginary components of the SLD. The imaginary part of the SLD shows a huge variability, which is interpreted as a result of the coupling with the incident intensity, acting as a scaling parameter for the simulations. Apparently, the measurements are not critically sensitive to the exact change of phase of the scattered wave associated with the relative amplitude of the real- and imaginary part of the complex

SLD. In other words, the fit is rather sensitive to the modulus of the SLD, which then couples to the global scaling factor of the simulations, therefore allowing some leeway for determining the value of the respective real and imaginary components of the complex SLD. Note that this means that the profile seen in Fig. 5.22 a) and c) are not representative of the uncertainty in determining the true values of the real and imaginary parts of the SLD, but rather exemplify the range of physical systems that all lead to almost indistinguishable scattering intensity distribution, as seen by the tiny deviations of Fig. 5.18.

Fig. 5.22 b) presents the normalisation of the modulus SLD, therefore removing the effect of the actual values of the SLD and reducing the system to a purely geometrical representation. As can be seen, the standard deviation of this representation of the individual fits show a remarkable degree of conformity, each fit essentially tracing the same profile , representing an identical spatial geometry of the patterned array.

Panels c) and d) show the same quantities as discussed above for the magnetic contribution to the SLD. Averaging indicates that the real part of the magnetic contribution to the SLD is fluctuating around zero, while the imaginary part is converging relatively consistently to a value of $\mathrm{Im}(f_{\mathrm{core}}^{\mathrm{mag}}) = -47\,\mathrm{r_e/nm^3} \pm 11\%$.

Note that the general shapes of the non-magnetic and magnetic SLD profiles

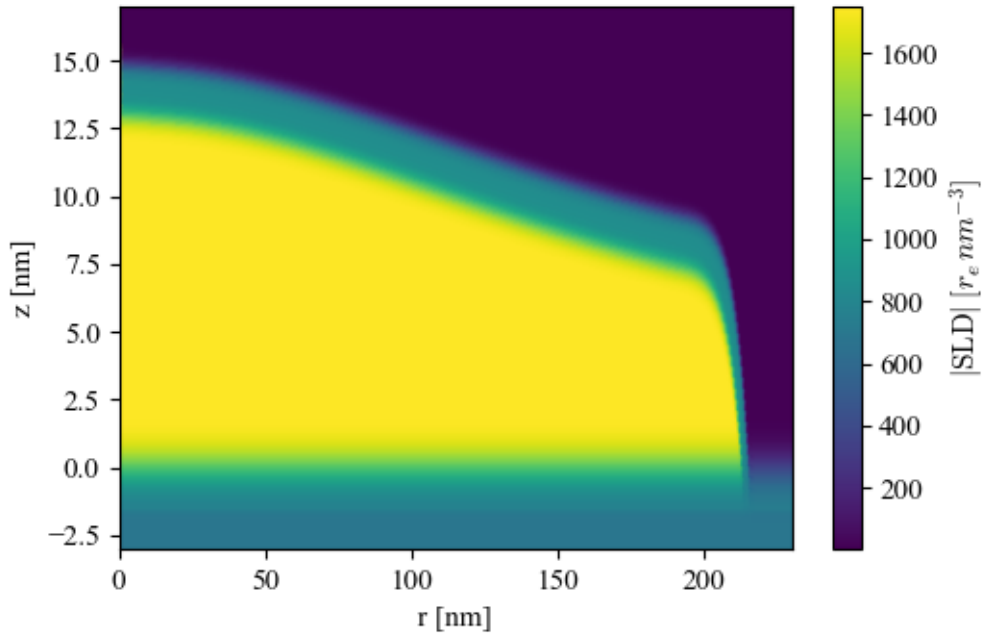

Figure 5.23: Cross section through the island as obtained from the best simultaneous fit of sum- and difference signals obtained form the rocking curve.

differs since the averaged non-magnetic SLD at any given depth z, is affected by the relative weight of the non-oxidised core and oxide-shell SLDs, while the magnetic SLD profile is affected solely by the chemistry and geometry of the non-oxidised core. However, both systems are intricately coupled as discussed at the beginning of this section, so that the high degree of conformity of the non-magnetic SLD, necessarily implied the high conformity seen in the normalised modulus of the magnetic SLD.

Finally, Fig. 5.23 shows a real space cross-section through the island corresponding to the single best fit, with the color coding corresponding to the real part of the SLD. The image gives an idea of both the thickness of the oxide shell as well as the geometrical shape of the island doming. note that since the magnetic SLD is confined to the core, non-magnetic and magnetic SLD of the core overlap within the yellow region of the figure.

5.5.2 Specular Reflectivity

Lateral averaging of the scattering length density according to the sample model discussed in section 5.2 allows the calculation of SLD depth profiles of arbitrary patterned arrays. In conjunction with Parratt's recursive method described in section 2.2.5, this allows for the calculation of the reflectivity of a patterned array using the same sample model that is also used for simulating rocking curves, if the substrate, at least directly below the islands, is included within the sample model. Further, since the reflectivity is expected to be highly sensitive to even slight adjustments of the SLD depth profile, the model was allowed more flexibility by decoupling the surface cut function of the magnetic core from the chemical structure of the island. This implies that the island is still modelled by a chemical core-shell structure, but the distribution of the magnetic SLD is allowed to freely adjust as long as it stays within the chemically defined core. In other words, the chemical- and magnetic structures are now *both* obtaining the full set of parameters describing a general domed structure described in section 5.2.

In practice, taking on the specular condition generally complicates the calculations of x-ray diffraction, which is why, as mentioned earlier, the rocking curve fits presented in section 5.5.1 did not include the zero$^{\text{th}}$ order diffraction peaks. These complications arise because of the potential interference with the reflectivity originating from the inter-element substrate as well as the reflectivity of the substrate in the unpatterned areas of the sample, which may all differ from the substrate directly below the islands, for instance because of etching effects or residuals from the patterning process. Including these effects in the scattering model requires a large number of additional fitting parameters, involving the exact beam shape, projected

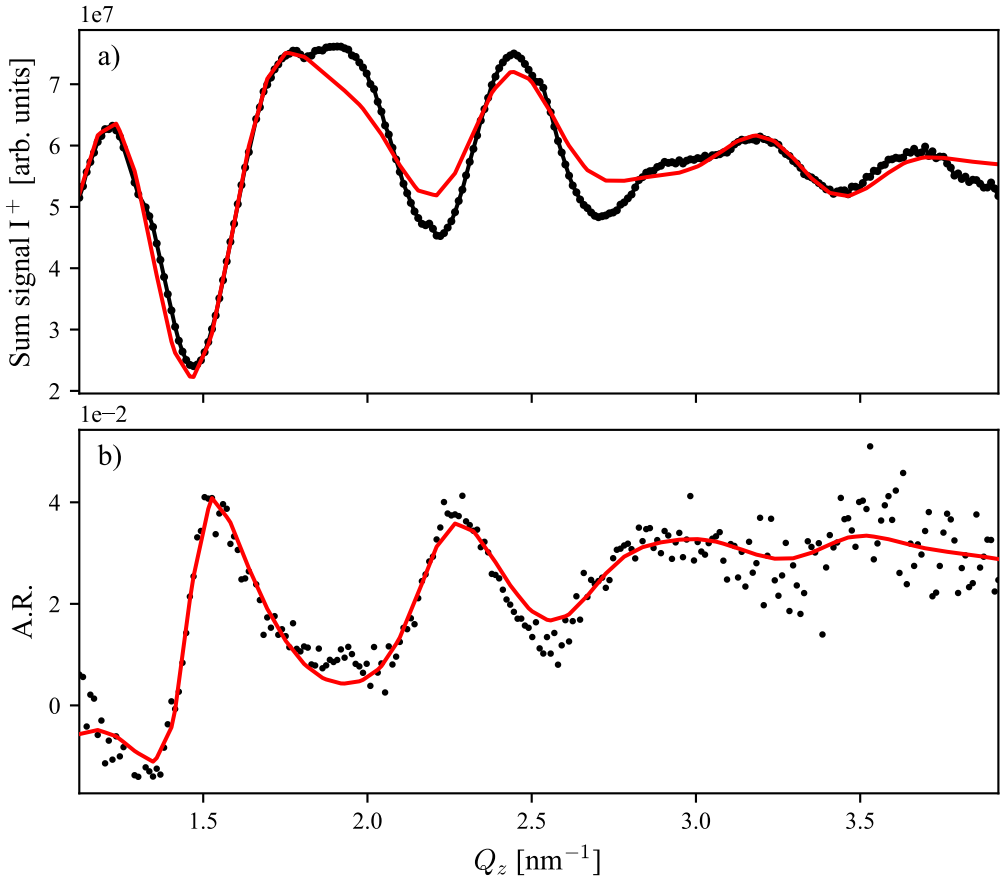

Figure 5.24: Single fit exemplifying the potential consequences of an inadequate sample model. Contributions of the reflectivity of the inter-island substrate are likely to contribute additional intensity at high Q_z that is not considered within the current sample model. Since the model is not able to adequately simulate the reflectivity over the whole range of Q_z, the fit, correspondingly, is of low quality.

footprint, spatial alignment of the beam center with respect to the patterned area, total sample area as well as the patterned area, amongst others. The contributing factors are complicating the modelling framework by introducing correction terms depending on the scattering angles α_i and α_f, as well as significantly increasing optimisation time, while providing only very limited valuable information. It can hence be often found advisable to try to circumvent these complications as much as possible by avoiding experimental conditions under which they might become relevant, i.e. performing reflectivity measurements. The alternative is to instead overburden the model with an disproportional amount of additional fitting parameters, risking overfitting or the emergence of additional fragmentation of the FOM parameter space accompanied by an increased risk of being trapped in local minima.

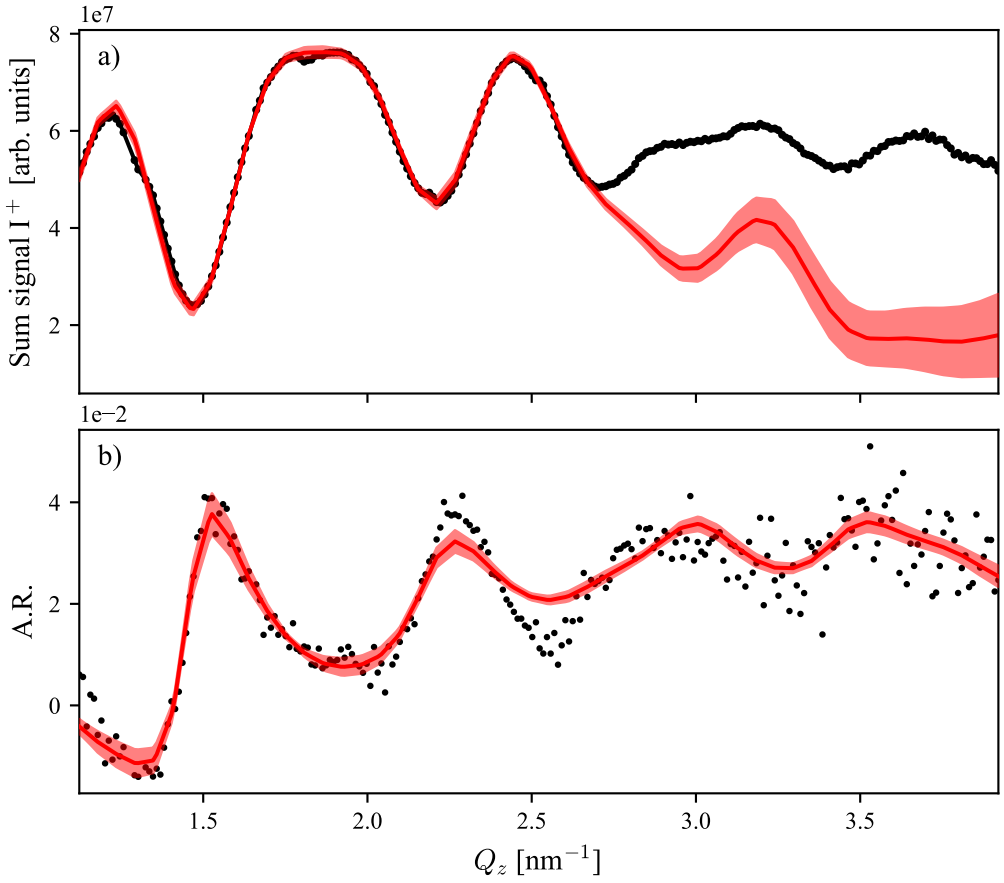

Figure 5.25: Sum signal and asymmetry ratio of the reflectivity measurements after excluding the range $q_z > 2.7\,\mathrm{nm}^{-1}$ from the sum signal. Solid red lines and shaded areas correspond to mean and one standard deviation calculated from 13 individual fits.

The effect of the presumed inadequacy of the model used can be seen in Fig. 5.24, which presents an attempt at simultaneous fitting of the sum signal and the asymmetry ratio in reflectivity geometry. As can be seen, although generally agreeable, especially the fit of the sum signal misses many essential features of the experimental data, which might be indicative of the previously discussed shortcomings of the sample model, i.e. not including the inter-element reflectivity of the substrate. Generally, noticeable interference with the presumably weak reflectivity of the inter-element substrate becomes more likely with increasing wavevector transfer Q_z, which is where the detected intensity is most strongly boosted from the data linearisation process as described in the introductory remarks of section 5.1.

Truncating the fitting range of the sum signal at $Q_z = 2.7\,\mathrm{nm}^{-1}$, the fit is

Parameter name	mean	STD	relative STD [%]
$d_{\mathrm{SiO_2}}$	-0.87	0.32	37
σ_{Si}	0.49	0.16	32
$\sigma_{\mathrm{SiO_2}}$	0.658	0.031	4.7
σ_{b}	1.27	0.49	39
σ_{t}	2.17	0.66	30
h_{n}	8.338	0.069	0.82
z_{off}	3.82	0.58	15
M	8.2	2.2	27
d^{shell}	1.335	0.021	1.2
h_{D}	15.337	0.073	0.48
σ^{core}	0.8	0.16	20
σ^{shell}	0.462	0.083	18
$\mathrm{Re}(f_{\mathrm{core}}^{\mathrm{nonmag}})$	1846	91	4.9
$\mathrm{Im}(f_{\mathrm{core}}^{\mathrm{nonmag}})$	840	180	21
$\mathrm{Re}(f_{\mathrm{shell}})$	1101	79	7.2
$\mathrm{Im}(f_{\mathrm{shell}})$	440	210	48
b^{mag}	0.709	0.084	12
$\sigma_{\mathrm{t}}^{\mathrm{mag}}$	1.06	0.61	57
$\sigma_{\mathrm{b}}^{\mathrm{mag}}$	3.28	0.94	29
$h_{\mathrm{n}}^{\mathrm{mag}}$	7.24	0.32	4.4
$z_{\mathrm{off}}^{\mathrm{mag}}$	5	2.9	57
M^{mag}	8.3	2.9	35
$h_{\mathrm{D}}^{\mathrm{mag}}$	10	1.3	13
$\sigma_{\mathrm{interface}}^{\mathrm{mag}}$	0.85	0.15	18
$\sigma_{\mathrm{bottom}}^{\mathrm{mag}}$	0.563	0.047	8.4
$\mathrm{Re}(f^{\mathrm{mag}})$	-6.2	3.2	52
$\mathrm{Im}(f^{\mathrm{mag}})$	-15.3	2.5	16

Table 5.3: List of parameters used to fit simulated to experimental data of sum- and difference signal of the specular reflectivity.

no longer sensitive to high values of Q_z at which the shortcoming of the model are having the strongest impact, leading to a general improvement of the quality of fits as seen in Fig. 5.25, again utilising the $\overline{\mathrm{FOM}_{\mathrm{diff}}}$ figure of merit. The solid lines again represent the mean as calculated from 13 measurements, while the shaded areas correspond to a width of one standard deviation.

Evidently, within the reduced Q_z range, the sum signals fit almost perfectly, with the intensity dropping significantly for $Q_z > 2.7\,\mathrm{nm}^{-1}$. This generally agrees with the idea of additional intensity arising from inter-island substrate around these wavevector transfers. Interestingly, although relatively well defined in terms of its standard deviation, the fit of the *asymmetry ratio* actually seems to have declined in

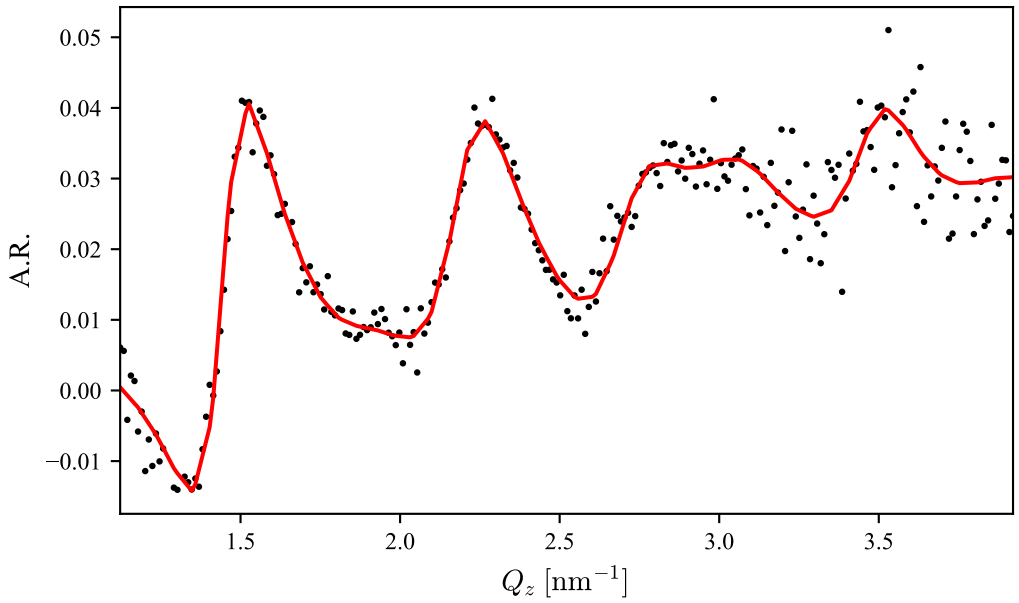

Figure 5.26: Individual fit of the asymmetry ratio using the same model parameters as in the previous fits.

quality upon putting less restraints on the fit of the *sum signal*. For completeness, table 5.3 presents a summary of all used fitting parameters, quoted including the absolute and relative standard deviation.

The still consistently sub-optimal fits of the asymmetry ratio is not intrinsic to the sample model, which can be seen in Fig. 5.26, showing a very agreeable simulation of the A.R., obtained from an individual fit, using the same parameter model as used in the simultaneous fits.

To explore the FOM parameter space further, Fig. 5.27 presents a selected number of parameter scans of the $\overline{\text{FOM}_{\text{diff}}}$ function, with the purple and green lines representing the sum-signal and asymmetry ratio, respectively. As can be seen, in many cases no clearly identifiable individual minima of the two signals emerge, contrasting the well aligned minima of the parameter scans corresponding to the rocking curve fits seen in Fig. 5.20. In fact, in many cases only one of the two signals seems to be sensitive to variation of a given parameter, which is corroborating the hypothesis of a structural weakness of the used fitting model. Also consistent with the presumed importance of substrate reflectivity is the fact that the roughness σ_{SiO_2} and thickness of the d_{SiO_2} of the silicon-oxide substrate-capping-layer is strongly affecting the quality of the fit.

Fig. 5.28 presents a number of SLD profiles obtained from the series of si-

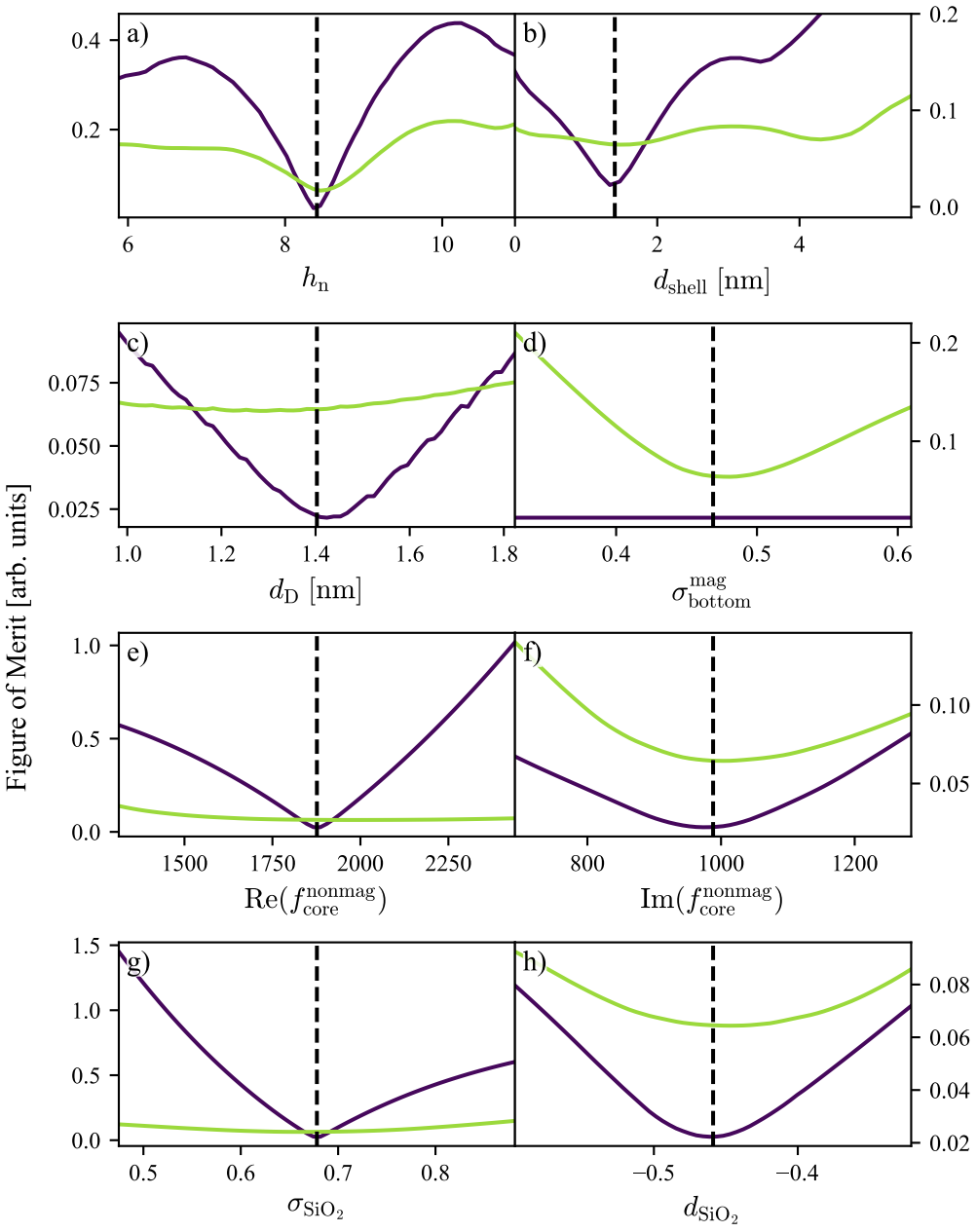

Figure 5.27: Selected parameter scans corresponding to sum signal (purple lines) and asymmetry ratio (green lines). Following the order of the panels, the scanned parameters were the nominal height of the islands, the (chemical) shell thickness, total width of doming, the roughness of the magnetic core above substrate level, real and imaginary scattering factors of the chemical core, and roughness and thickness of the SiO_2 substrate capping layer. The vertical dashed lines represent the best fitted values. In all cases the $\overline{\text{FOM}_{\text{diff}}}$ function has been used to evaluate the figure of merit. All involved parameters have been found from simultaneous fitting of the sum signal and asymmetry ratio.

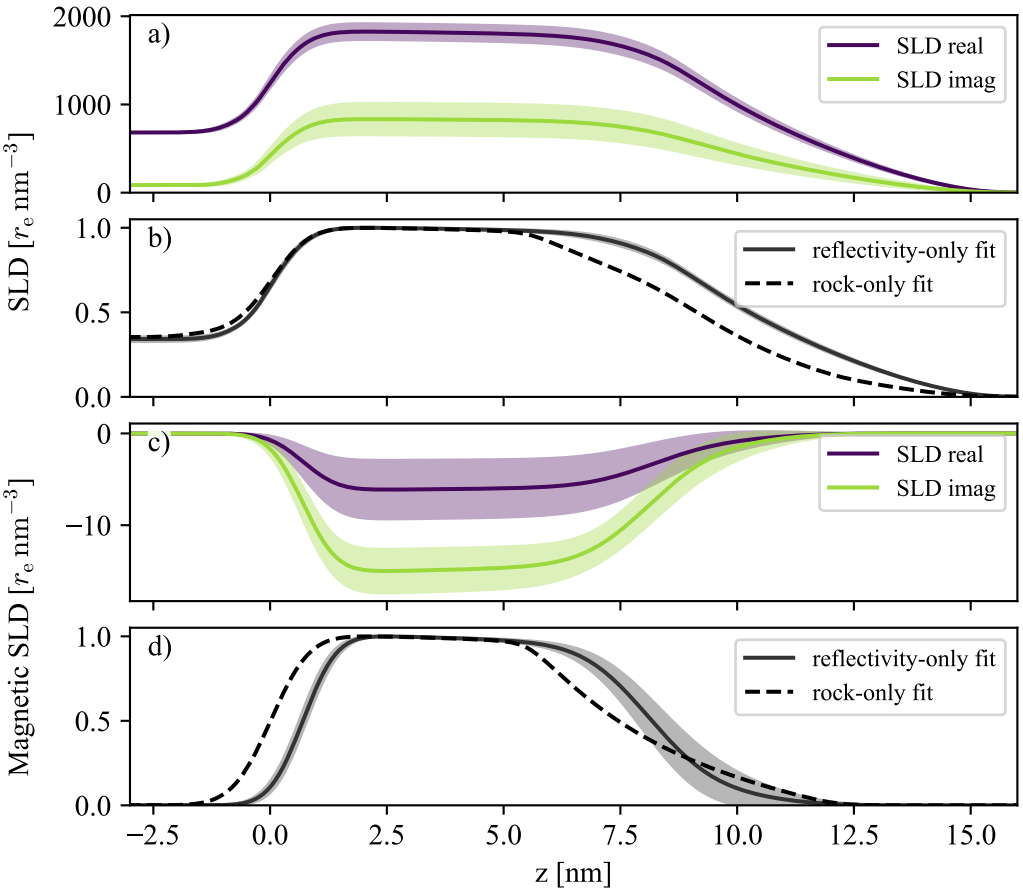

Figure 5.28: Comparison of real- and imaginary parts (panel a), and normalised average depth profile (panel b) of the non-magnetic SLD. The corresponding profiles of the magnetic SLD are presented in panels c) and d). All results (with the exception of the dotted lines in panels b and d) are obtained from simultaneous fitting of sum and difference signal of the reflectivity measurements.

multaneous fits, taking into account only the sum signal and A.R. of the reflectivity measurements. The non-magnetic SLD of panel a) and normalised modulus of the SLD of panel b) are particularly well defined, with error intervals generally being smaller than in case of the SLD profile obtained from the rocking curve measurements presented in Fig. 5.20.

Remarkably, despite originating from scans being either only sensitive to the lateral- *or* the perpendicular sample structure, the SLD profiles of rocking curves and reflectivity measurements show a very high degree of agreement, as indicated by the dotted line in Fig. 5.28 b). Apart from a slight translation of about 1 mm in the z-direction, which is due to the invariance of the scattered signal under z-translation of the dome in the rocking geometry (discussed in more detail in chapter

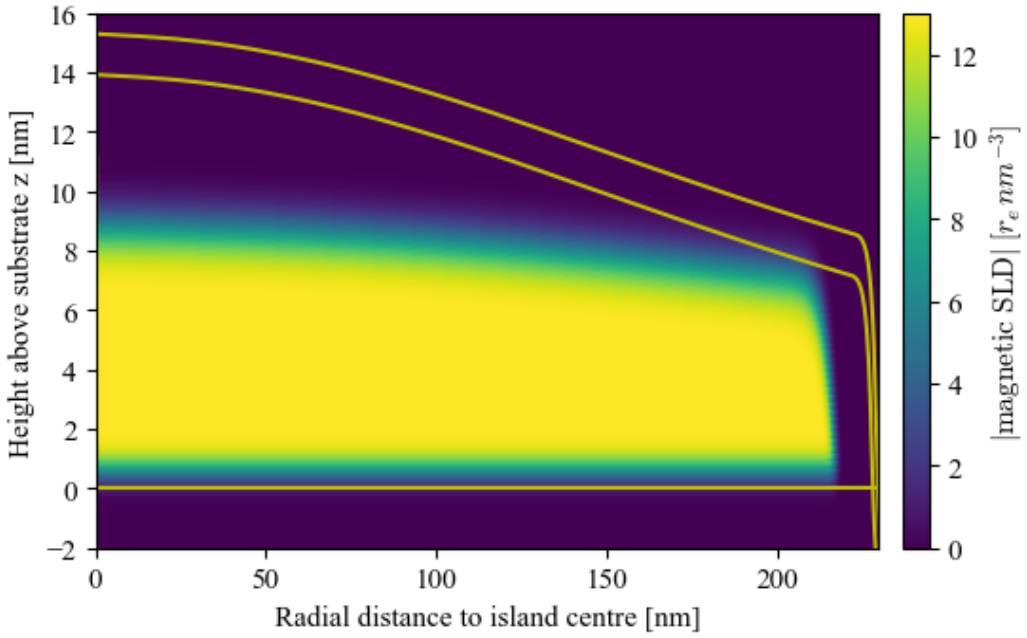

Figure 5.29: Cross section of the island as obtained from fitting the sum signal and asymmetry ratio of the specular reflectivity. The yellow lines indicate the interfaces of the chemical shell and core, and the substrate. Depicted in yellow is the magnetic SLD confined to the chemical core of the island. Doming of the magnetic SLD is significantly reduced compared to the structure obtained from fitting the rocking curves, the latter being enforced by the coupling of chemical and magnetic structure of the core.

4), both profiles look very similar. The latter is indicative that despite the non-optimal quality of the fits, many essential sample properties are still being captures by the sample model. A noticeable exception is the thickness of the oxide shell $d^{\text{shell}} = 1.335\,\text{nm} \pm 1.2\,\%$, deviating from $2.47\,\text{nm} \pm 3.6\,\%$ as found from fitting of the rocking curve data. Because of the previously shown high sensitivity of the rocking curve difference signal, such a strong deviation is surprising, unless the reflectivity signal has a significantly reduced sensitivity towards d^{shell}. Strongly supportive of this hypothesis is the fact that only the reflectivity sum signal is observed to exhibit a minimum at the best fitted value, which is exactly expected if the change in the scans FOM is primarily due to mis-scaling with the (now kept constant) intensity scaling parameter (compare also Fig. 5.21 and the accompanying discussion).

After allowing the model a higher flexibility by decoupling the chemical and magnetic structures, the magnetic SLD profile does now show significant changes with respect to the fits of the rocking curves as seen in Fig. 5.28 d). The differences

mainly manifest in what appears to be a magnetic dead-layer of about 1 nm thickness on the bottom of the island and an almost vanishing doming of the magnetic core as can also be seen in Fig. 5.29.

The total magnetic doming width is strongly reduced down to about 1 nm as opposed to > 6 nm in the more restrictive model used in fitting the rocking curves Finally, Fig. 5.29 presents a radial cross section through an island according to the parameters of fitting series of the lowest total FOM.

5.5.3 Simultaneous Fitting of Rocking Curves and Specular Reflectivity

Because of their complementary information, a simultaneous fit of the rocking curve and specular reflectivity data is expected to provide the most accurate results. The rocking curve data are most sensitive to the lateral structure of the patterned array, but have been seen to be prone to ambiguity regarding the absolute values of the atomic scattering factors and hence local SLD. The reason for this is mainly that only a relatively small range within reciprocal space is being probed by a rocking curve. The issue was in fact unintendedly solved in part by the open detector geometry, that provided additional reciprocal space sensitivity because of the Q_z dependence of the GTR interception points of the detector.

It has further been anticipated that the data obtained by the specular reflectivity could be exploited to further reduce the issue of SLD ambiguity, despite not being eminently sensitive to the lateral structure of the sample. Interestingly, despite the model having provided ample opportunity to deviate, fitting of the specular reflectivity reproduced almost exactly the (three-dimensional) chemical structure of the patterned array as obtained from exclusively fitting the rocking curves, while, contrary to expectation, not having been able to uniquely resolve the values of the SLD. Taking into account the shortcomings of the model in terms of fitting of the specular reflectivity as discussed in section 5.5.1, it is interesting to put a simultaneous fit of all four datasets discussed so far into context with the results of the individual fits of the rocking curves and specular reflectivity.

As can be seen in Fig. 5.30, simultaneous fitting generally provides satisfactory results for each individual set of experimental data indicative of a consistent sample model. The asymmetry ratio of the specular reflectivity is the least well developed, while fitting of the sum signal of the specular reflectivity was again truncated at $Q_z = 2.7\,\mathrm{nm}^{-1}$, for the same reasons as discussed in section 5.5.1.

The result of the simultaneous fit is summarized in table 5.4, presenting the mean and associated standard deviation as obtained from a total of 7 simulation

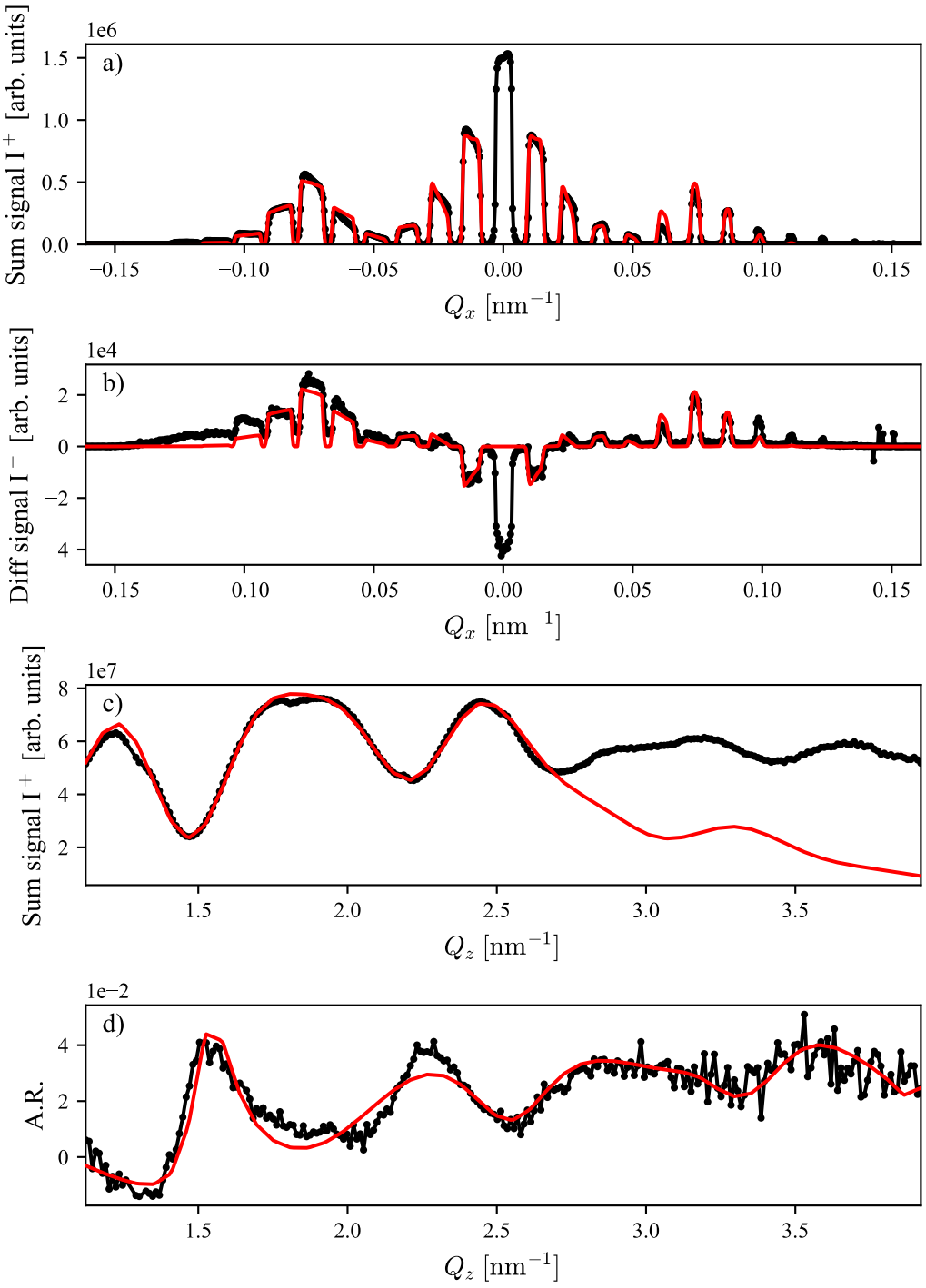

Figure 5.30: Simultaneous fits of the rocking curve sum (a) and difference signal (b), as well as the sum-signal (c) and asymmetry ratio (d) of the specular reflectivity. In all cases, the $\overline{\text{FOM}_{\text{diff}}}$ function has been used to evaluate the figure of merit.

Parameter name	mean	STD	relative STD [%]
σ_{b}	2	0.45	23
σ_{t}	4.6	2.6	56
h_{n}	8.1	0.17	2.1
z_{off}	4.5	1.1	24
M	1.6	0.14	8.7
d^{shell}	2.05	0.15	3.6
h_{D}	14.8	0.34	2.3
σ^{core}	0.05	0.045	89
σ^{shell}	0.49	0.31	63
$\mathrm{Re}(f_{\mathrm{core}}^{\mathrm{nonmag}})$	1930	120	6.2
$\mathrm{Im}(f_{\mathrm{core}}^{\mathrm{nonmag}})$	250	110	45
$\mathrm{Re}(f_{\mathrm{shell}})$	1760	200	11
$\mathrm{Im}(f_{\mathrm{shell}})$	49	10	20
b^{mag}	0.77	0.032	4.2
$\sigma_{\mathrm{t}}^{\mathrm{mag}}$	1.99	0.11	5.7
$\sigma_{\mathrm{b}}^{\mathrm{mag}}$	5	1.6	32
$h_{\mathrm{n}}^{\mathrm{mag}}$	7.38	0.39	5.3
$z_{\mathrm{off}}^{\mathrm{mag}}$	4.4	1.4	31
M^{mag}	1.6	0.2	13
$h_{\mathrm{D}}^{\mathrm{mag}}$	13.38	0.37	2.8
$\sigma_{\mathrm{interface}}^{\mathrm{mag}}$	0.325	0.084	26
$\sigma_{\mathrm{bottom}}^{\mathrm{mag}}$	0.683	0.042	6.1
$\mathrm{Re}(f^{\mathrm{mag}})$	-19	120	640
$\mathrm{Im}(f^{\mathrm{mag}})$	-15	96	660
$d_{\mathrm{SiO_2}}$	-1.64	0.32	19
σ_{Si}	0.261	0.099	38
$\sigma_{\mathrm{SiO_2}}$	0.634	0.022	3.4

Table 5.4: The fitted parameters with associated mean values and standard deviation as taken from 7 simulation runs.

runs. Again, many values exhibit very high uncertainties as a result of parametric coupling. Despite the anticipated compatibility issue of the scattering framework with the specular reflectivity, some parameter are nevertheless remarkably well defined, including the nominal height $h_{\mathrm{n}} = 8.10 \pm 0.17\,\mathrm{nm}$, the thickness of the chemical oxide shell $d^{\mathrm{shell}} = 2.05 \pm 0.15\,\mathrm{nm}$, the total height of the island including the doming $h_{\mathrm{d}} = 14.80 \pm 0.34\,\mathrm{nm}$, the thickness of a magnetic dead-layer directly above the substrate $b^{\mathrm{mag}} = 0.770 \pm 0.032\,\mathrm{nm}$, the nominal height of the magnetic core $h_{\mathrm{n}}^{\mathrm{mag}} = 7.38 \pm 0.39\,\mathrm{nm}$, the width of the (flat) interface separating the magnetic core from the substrate $\sigma_{\mathrm{bottom}}^{\mathrm{mag}} = 0.683 \pm 0.042\,\mathrm{nm}$, and the chemical roughness of the substrate-island interface $\sigma_{\mathrm{SiO_2}} = 0.634 \pm 0.022\,\mathrm{nm}$.

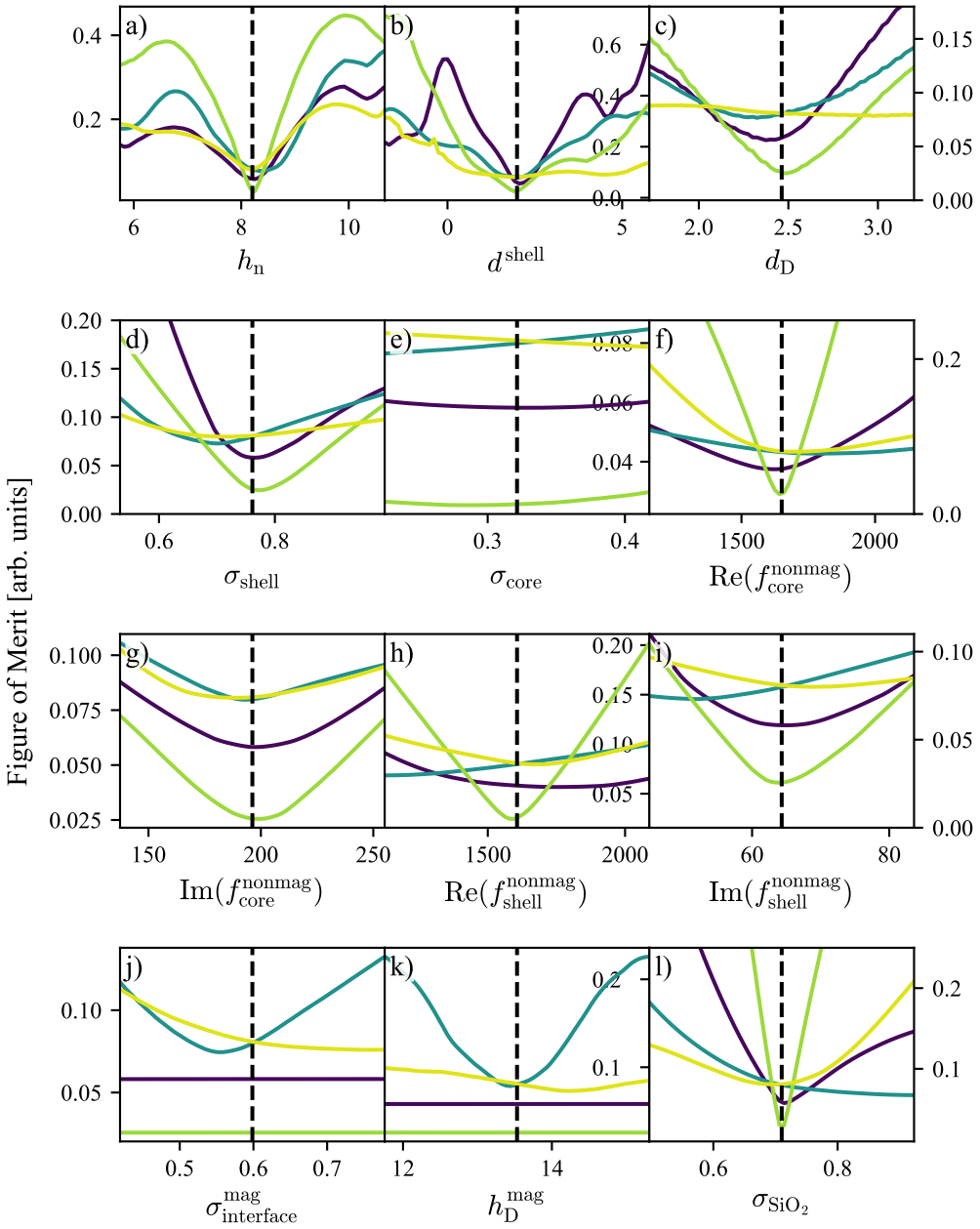

Figure 5.31: Selected parameter scans corresponding to the sum signal (purple) and difference signal (blue) of the rocking curves as well as the sum signal (light green) and asymmetry ratio (yellow) of the specular reflectivity. In all cases the $\overline{\mathrm{FOM}_{\mathrm{diff}}}$ function has been used to evaluate the figure of merit. All involved parameters have been found from simultaneous fitting of all four signals.

Fig. 5.31 shows a number of selected parameter scans, varying a single parameter within $\pm 30\,\%$ of its best fitted value, while keeping all remaining parameters fixed at their fitted values. The purple and blue lines indicate the corresponding FOM of the sum- and difference signal of the rocking curves, while the light green and yellow lines correspond to the sum signal and asymmetry ratio of the specular reflectivity measurement. Panels a) and b) show the variation of the FOM with the nominal height h_{n} and thickness of the chemical oxidation shell d^{shell}, respectively. Despite being highly structured, both scans reveal alignment of all four local minima, indicative of high sensitivity and physical accuracy of the underlying model. Panel c) shows the FOM dependence of the total thickness of the doming d_{d} above the nominal island height, revealing well-aligned minima of both sum signals, while the difference signal of the rocking curve is less pronounced and slightly misaligned. The asymmetry ratio of the specular reflectivity, however, seems to hardly be sensitive towards d_{D}, as the FOM is barely varying and is showing no identifiable minimum within the scanned range.

Despite the problems with fitting the specular reflectivity, the roughness of the island surface σ^{shell} exhibits well defined minima in the two sum signals, with the minima getting progressively ill-defined and misaligned with the difference signal of the rocking curve and asymmetry ratio of the specular reflectivity as can be seen in panel d). Contrary, panel e) shows that the parameter scans of the (chemical) interface width σ^{core} hardly show any variability, which is consistent with the chemical contrast between core and shell being smaller than the contrast between the island and the exterior vacuum, consequently reflecting in a reduced sensitivity of the experimental data towards σ^{core}.

The scattering factor parameters determining the SLD of the core and shell depicted in panels f) to h) remain inconclusive, in that no formation of well defined minima for all four measurements emerges, so that relatively large parameter uncertainties remain as seen in table 5.4. However, in all cases highest sensitivity towards any scattering factor component is exhibited by the sum signal of the specular reflectivity, maintaining the hypothesis that Q_z scans are generally suitable in order to determine the SLD of a patterned array.

The effect of what is presumably a false compromise of the fitting algorithm is seen in Fig. 5.31, where contradicting minima of the two difference signals necessitated the optimiser to choose an intermediate value, therefore minimising the composite FOM. (Obviously, the two sum signals having no magnetic sensitivity leading to the corresponding purple and green lines being flat).

Sensitivity to the magnetic doming is most pronounced for the difference

signal of the rocking curves, as seen in panel k). A very strong sensitivity towards the roughness σ_{SiO_2} of the substrate underlying the islands is observed for the sum signal of the specular reflectivity as seen in panel l). As on scanning σ_{SiO_2}, the asymmetry ratio of the reflectivity signal consistently shows no or only weakly developed minima often misaligned with the remaining curves. This observation matches with the reflectivity A.R. performing worst in the fitting procedure, as seen in Fig. 5.30 d), with the most likely explanation being that the weak magnetic contribution of the scattering is most sensitive to interference with the weak reflectivity of the inter-island substrate, meaning that model inadequacies will in this case have the most noticeable effect, by means of higher disagreement with the remaining (less affected) measurements.

Finally, Fig. 5.32 shows the cross section of the island corresponding to the best set of parameters from the series of simultaneous fits. Again, the solid yellow lines correspond to the interfaces of the chemical core, shell and substrate, while the magnetic core is depicted by the yellow shading. The additional black circles in Fig. 5.32 depict an AFM linescan being representative of the sample. The AFM line-profile agrees well with the SLD profile obtained from data fitting, although the AFM data had to be cleaned by a 4.5 nm height-offset, matching the AFM baseline with the substrate height of 0 nm (compare Fig. 5.2). Note that fitting has been performed to reciprocal space data only (no direct fitting of the spatial SLD profile to AFM data was conducted), yet, the obtained doming geometry resemble the AFM profile remarkably well.

Despite being mostly decoupled from the internal chemical structure, the magnetic core very much aligns with the chemical core, only slightly expanding into the chemical shell on the edges of the islands. The domed structure of the magnetic core is in stark contrast to its much flatter appearance in response of fitting reflectivity data only, as seen in Fig. 5.29. However, the magnetic dead layer seen as a result of exclusive fitting of the reflectivity data is reproduced here, as well, therefore somewhat increasing the confidence in the accuracy of the obtained structure.

Geometrically and chemically, the islands fitted resulting from different combinations of sets of experimental data as seen in Figs. 5.23, 5.29, and 5.32 are virtually identical, again stressing the high reproducibility being associated with high sensitivity towards the experimental data, rendering magnetic x-ray diffraction a reliable tool of resolving the three-dimensional (chemical and magnetic) structure of patterned arrays in even subtle details.

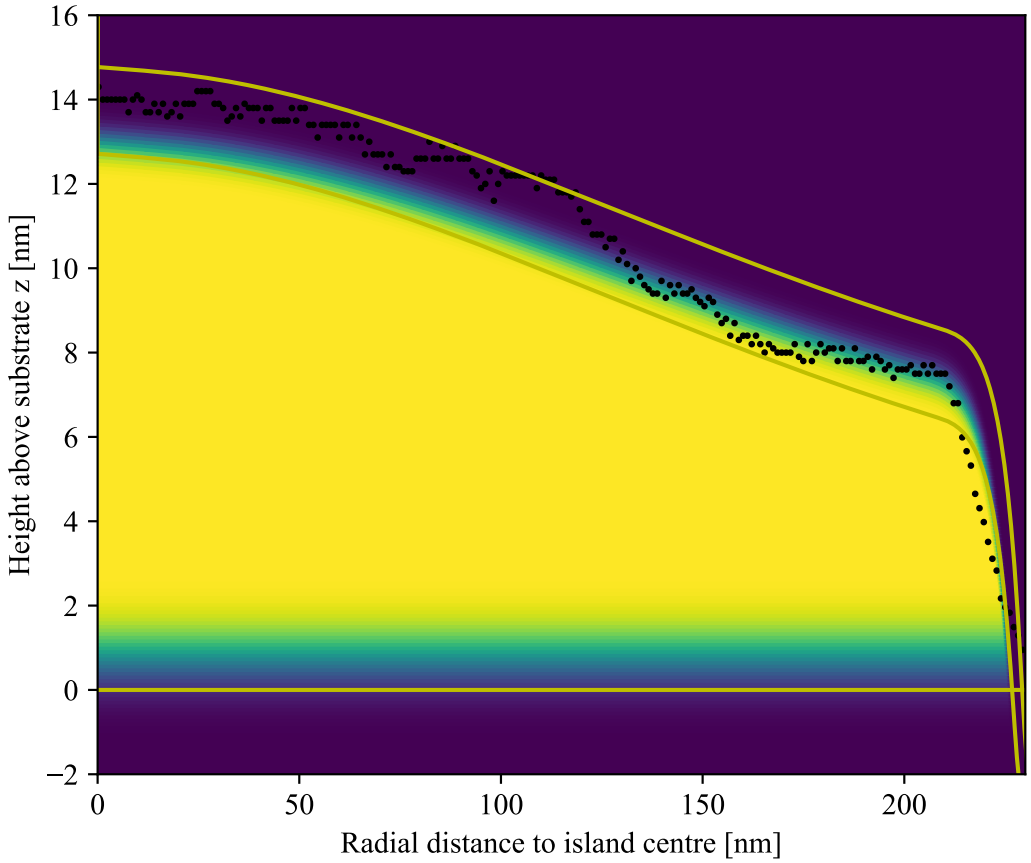

Figure 5.32: Cross section of the island as obtained from fitting the sum and difference signal of the rocking curves as well as the sum signal and asymmetry ratio of the specular reflectivity. The yellow lines indicate the interfaces of the chemical shell, core, and the substrate. Depicted in yellow is the magnetic SLD. Doming of the magnetic SLD is essentially recovering the chemical structure of the core-shell model, despite being provided the opportunity of taking on an arbitrary shape. The black circles depict a (representative) AFM linescan scan of the sample, which has been cleaned by a 4.5 nm height-offset.

5.6 Summary

In this chapter a general scattering x-ray framework for x-ray diffraction from patterned arrays has been developed. The framework covers both resonant- and magnetic x-ray scattering and it has been shown how high sensitivity to both the geometrical, chemical and magnetic structure of the patterned array can be observed in experiment and reproduced by simulation. In a meta-optimisation process, the most efficient algorithmic fitting parameters for the robust fitting of x-ray scattering of patterned arrays have been determined and subsequently utilised in fitting

simulations to experimental data.

It was found that restricting to off-specular scattering generally simplifies the necessary complexity of the model and generally leads to more reliable results. When dealing with stratified media, the effectively one-dimensional nature of the sample means that lateral averaging of the scattering length density is a relatively straightforward and reliably successful approach in determining the sample structure. Contrary, patterned arrays are intrinsically three-dimensional, which drastically complicates the mathematical treatment because of multiple interference effects arising specifically under the specular condition, when substrate reflectivity and the zero$^{\text{th}}$ diffraction order of the pattern superimpose each other. When designing an experiment, it seems therefore advisable to reduce any unnecessary complication by means of avoidance of the specular condition.

Both the sum- and difference signals of magnetically sensitive reflectivity measurements have been successfully reproduced previously, e.g. by Procter [171]. However, data fitting in reflectivity geometry, for instance using the GenX software package, is usually done by creating a somewhat loosely defined SLD depth profile representing the lateral average of the samples SLD. The latter technique is very useful in the case of stratified media, but does hardly allow to draw any conclusions about the actual three dimensional structure of the patterned array. Further, one-dimensional modelling of the sample bears additional risks in that the SLD profiles generated through the fitting process are not bound by any constraints connecting it to the real, three-dimensional physical system. Therefore, the risk of overfitting the experimental data significantly increases, since the likelihood of finding *some* SLD profile whose scattered signal turns out to actually match the experimental data is greatly increased if the SLD profile does not have to *also* obey any constraints ensuring that the SLD profile does actually refer to a physically meaningful representation of the sample.

In contrast, the spatial model proposed in this chapter is directly linked to a well-defined three-dimensional representation of the sample, therefore obeying physically meaningful restriction to the spatial geometry. The latter is true even when fitting laterally insensitive scans like x-ray reflectivity measurements. Consequently, properties like the thickness of the oxidised shell within the core-shell model obtained from fitting reflectivity data, have a direct foundation in the physical reality of the sample, which is in contrast to the relatively obscure lateral average of the SLD, obtained from a one-dimensional model. This advantage comes, however, at the cost of *significantly* increased computational- and simulation-time-effort, associated with the demand of increasing complexity of the underlying model in order to capture

the often very ill-defined geometry of a patterned array. The hardship of fitting experimental data under these conditions stresses the fact that model inadequacies become far more obvious, while being potentially compensated and dismissed when using a more generic formulation of the problem. After all, the information residing in a scattering experiment is always finite, making a thoughtful underlying model extremely important if definitive conclusions are to be drawn.

Perhaps the biggest weakness of the developed framework is its high computational strain, emerging as a natural consequence of the increased dimensionality of the problem. While technically three-dimensional, the rotational symmetry of the islands of the patterned array discussed here allowed reducing the dimensionality from three to two. Nevertheless, even a two-dimensional model might quickly exceed the computational effort by orders of magnitude compared to the one-dimensional problem of calculating the x-ray reflectivity of stratified media . Consequently, having to sit through one to three days of computing time in order to see the effect of changing one of the many aspects of the model was, unfortunately, not uncommon. Hence, parallelised code and making use of centralised computer systems are promising adaptations of the current framework.

Following the earlier discussion, it is advised that future studies of a similar kind rely more heavily on off-specular scattering, avoiding substrate-array interference effects otherwise faced at the specular condition. Furthermore, it appears that future studies require additional information for efficient and uniquely resolved data fitting. These additional information might be obtained by either performing a *set* of rocking scans at various detector angles 2θ. Alternatively, complementary information can be obtained by performing GTR scans along Q_z at multiple values of $\mathbf{Q}_{\parallel} \neq 0$.

An even more promising candidate for an experimental geometry is given by Grazing Incidence Small Angle Scattering (GISAXS), which is fully compatible with the here-developed scattering framework and will be discussed in more detail in chapter 6.

Chapter 6

Laboratory Studies of X-Ray Diffraction of Patterned Arrays in GISAXS Geometry

Performing experiments at synchrotron sources often requires expenses in terms of time-limited access, limited availability and an elaborate proposal process. It is hence desirable to utilise laboratory based x-ray sources, whenever possible. Since lab x-ray sources usually rely on particular electronic transitions (most notably the ubiquitous Cu K-α absorption edge), one obvious drawback of lab based work is the lack of a tunable x-ray energy, negating the utilisation of most resonant scattering effects, including magnetically sensitive measurements. However, lab based sources can still be found very useful in a variety of ways concerning geometric and chemical sample characterisation. Since the x-ray flux of laboratory sources is generally found to be orders of magnitudes lower than modern synchrotron sources, it is often advisable to simultaneously probe as large a volume within reciprocal space as possible in order to maximise the efficiency of a measurement. *Grazing Incidence Small Angle X-Ray Scattering* (GISAXS), in conjunction with a two-dimensional area detector is therefore the obvious experimental geometry to exploit.

Because of the small associated wavevector transfers, GISAXS is a technique commonly employed in investigations of nano- and micro-patterned arrays. Advantages of GISAXS include that the commonly employed two-dimensional CCD detectors allow high spatial resolution and probing of large areas of reciprocal space in single measurements, while ensuring a high dynamic intensity range per pixel. Further, even standard laboratory x-ray sources allow the observation of interesting coherence effects, by tuning the slit size of the aperture of the incident beam,

therefore trading increased coherence against reduced incident radiative flux. However, because of the relatively loosely defined experimental geometry, the scattered intensity generally does not correspond to any well-defined trajectory but usually corresponds to an oblique surface within reciprocal space.

6.1 Experimental Set-Up

The GISAXS experiments were performed in-house using a commercially available Xenocs Xeuss 3.0 machine[214] with a microfocused copper Anode and monochromated Cu K-α. The scattered intensity is captured by a two-dimensional Pilatus 300K CCD detector[215] detector of 487×619 pixels each of 172×172µm size, leading to a total detector area of $83.8 \times 106.5\text{mm}^2$.

The requirements for a standard GISAXS set-up are relatively simple, requiring only that the sample surface can be moved into the centre of the beam (a height adjustment) and a theta axis to define the incident angle. These controls are clearly insufficient to perform the required scattering experiments from patterned arrays for which an additional azimuthal axis is needed. Thus, the Xenocs sample mounting systems was redesigned and engineered. The rotation axis of sample rotation (theta) is centred 87.5 mm from the base of the instrumental theta axis. A manual PR01/M rotation mount from Thorlabs[216] provided the azimuthal axis needed. However, when mounting the sample directly onto this stage there is always a small but unavoidable misalignment of the surface normal $\hat{\mathbf{s}}$ with the principle axis of the rotation stage $\hat{\mathbf{r}}$. This could be corrected through redefining the theta angle value every time ϕ is changed, but is generally found to be tedious, especially when scanning dozens of azimuthal angles. To reduce this, an additional GN2/M dual-axis goniometer (black box with screws on top of the rotation stage seen in Fig. 6.1) was mounted on top of the rotation stage with one of the rotations parallel to theta and the other orthogonal to it in a usual χ direction. This GN2/M was mounted using a PR01A/M adapter plate onto the rotation stage. An additional mounting plate for the sample was designed and manufactured in the departmental workshop to bring the total height of the sample surface up from 76.1 mm to the required 87.5 mm. The additional goniometer enables the alignment of $\hat{\mathbf{s}}$ and $\hat{\mathbf{r}}$ by iterative adjustment of the two goniometer axes until a reflected optical laser beam remains spatially unaltered on rotation of ϕ. Following this, the sample surface is flat with respect to the rotation axis and can then be aligned with respect to the incident beam in the usual way using the diffractometer angle θ and sample heigh z. The incident angle is then defined (to within $\pm 0.005^\circ$) for any azimuthal angle.

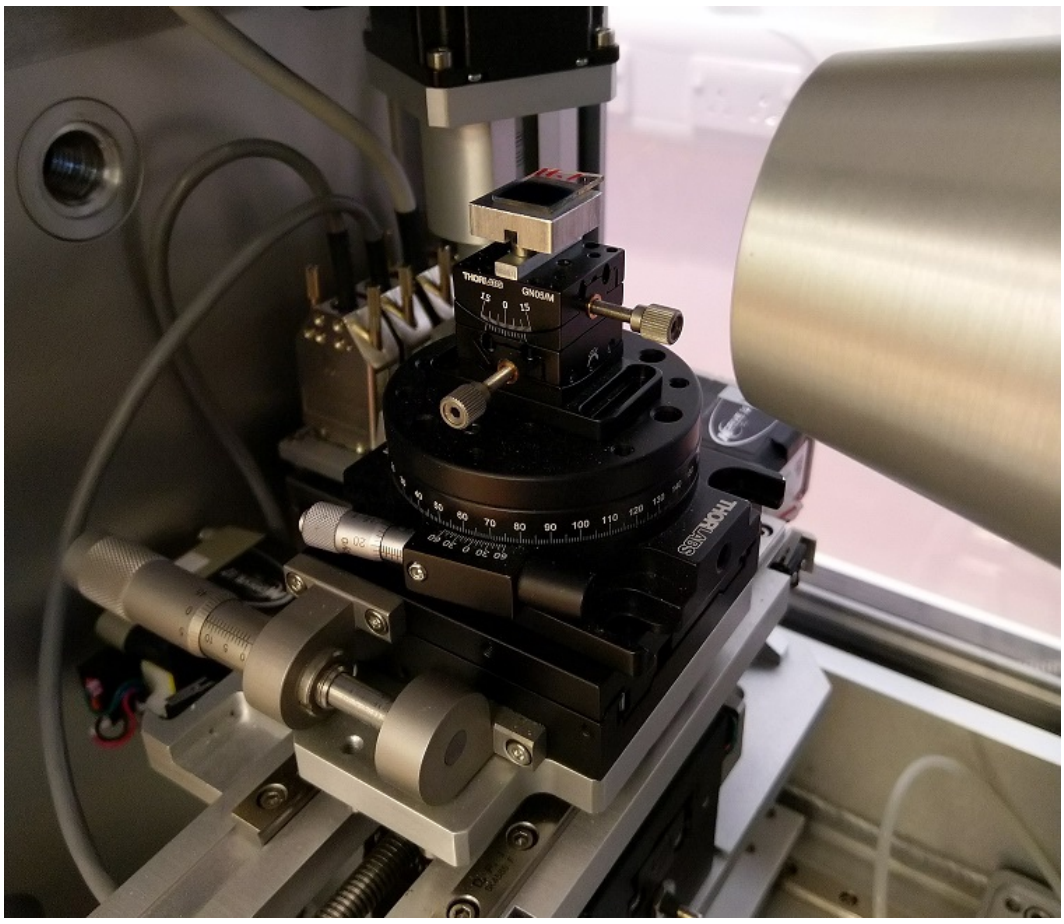

Figure 6.1: The custom rotation stage. Additional to enabling azimuthal sample rotation the two-axis goniometer allows for the alignment of sample normal $\hat{\mathbf{s}}$ with the rotation axis $\hat{\mathbf{r}}$.

The sample studied in this exploratory study consisted of a patterned array of circular disks of radius 250 nm consisting of amorphous FePd located on a square lattice of pitch 513 nm as seen in Fig. 6.2 and similar to the one discussed in chapter 5. In order to utilise the small angle scattering geometry, the detector was placed $D_{\mathrm{sd}} = 2.492\,\mathrm{m}$ away from the sample as verified by a calibration grating. The direct beam transmitted through the sample was covered by a beamstop, and the detector slightly lifted, so it would have been hit by the direct beam approximately at one fifth of its total height, while the detector surface was kept perpendicular to the direct beam.

Assuming normal incidence of the direct beam, the scattering angles in the laboratory frame 2θ and ν can be associated with the corresponding integer pixel positions x and y, with x and y in this context referring to pixel coordinates with

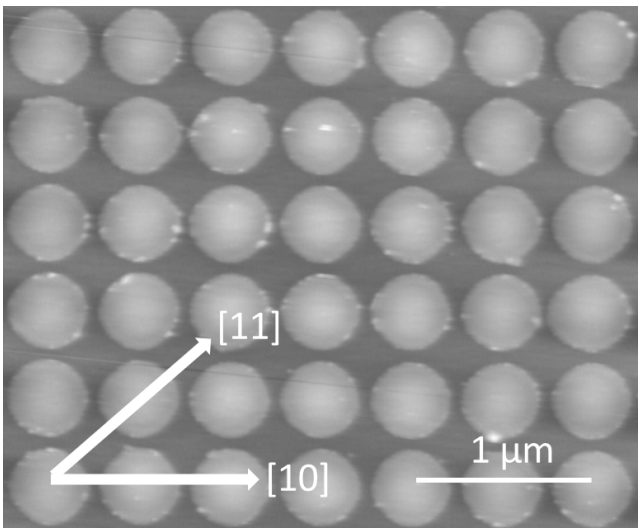

Figure 6.2: Scanning electron microscopy image of the patterned array discussed in this chapter. Published in [77].

respect to the top left corner of the two-dimensional detector array. After determining the position of the direct beam x_0 and y_0, the associated scattering angles are calculated using

$$2\theta = \operatorname{atan}\left(\frac{y - y_0}{\sqrt{(x - x_0)^2 + D_{\mathrm{sd}}^2}}\right) \tag{6.1a}$$

$$\nu = \operatorname{atan}\left(\frac{x - x_0}{D_{\mathrm{sd}}}\right). \tag{6.1b}$$

Therefore, the scattering angle α_f in the sample frame is given by

$$\alpha_f = 2\theta - \theta\cos\nu, \tag{6.2}$$

while ν is identical in both laboratory and sample frame and, of course, $\theta = \alpha_i$.

With all scattering angles known, calculating the wavevector transfers $\mathbf{Q}$ corresponding to each pixel is performed straightforwardly via the well known relationships

$$Q_x = k\left(\cos\alpha_f\cos\nu - \cos\alpha_i\right) \tag{6.3a}$$

$$Q_y = k\,\cos\alpha_f\sin\nu \tag{6.3b}$$

$$Q_z = k\left(\sin\alpha_f + \sin\alpha_i\right). \tag{6.3c}$$

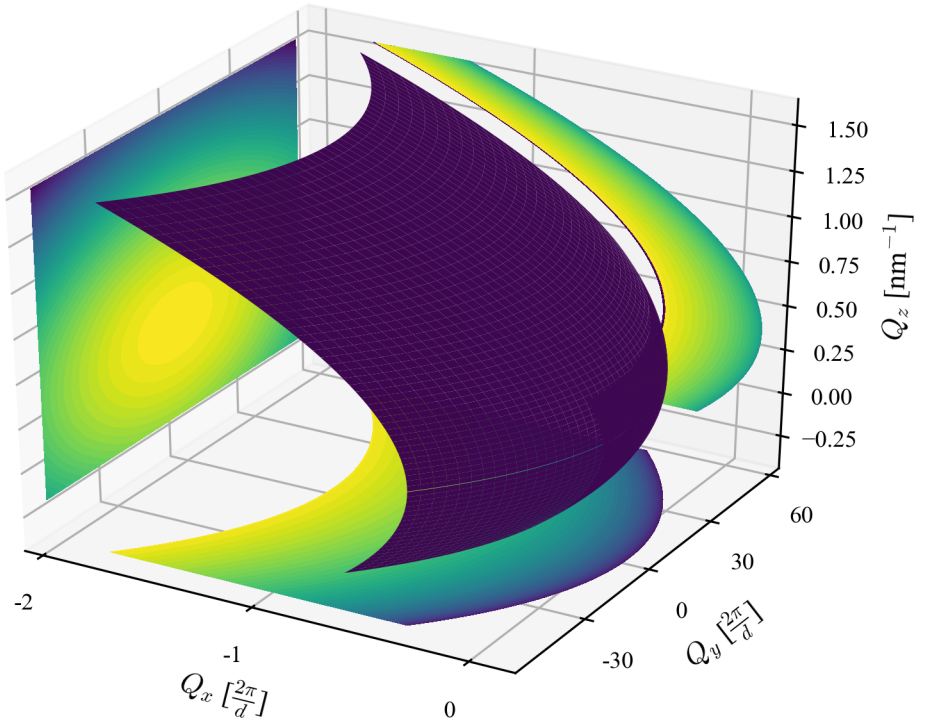

Figure 6.3: Surface in reciprocal space probed by a two-dimensional area detector in GISAXS geometry. The acceptance in Q_y is much wide than in Q_x. Note that units in the Q_x and Q_y direction are measured in reciprocal lattice spacings $2\pi/d_{\text{latt}}$ to stress the different ranges the detector spans within reciprocal space. Also pictured are the projections of the detector window onto the main coordinate planes.

Alternatively, a recent update allows the pixel to **Q** conversion to be performed by using the excellent set of tools provided by the esaProject[217]. Fig. 6.3 shows the detector surface as well as its projection onto the three coordinate planes in reciprocal space, corresponding to an incident angle of $\omega = 0.6°$ and the angular acceptance of the two-dimensional detector area. The projection onto the $Q_y - Q_z-$plane is the only one allowing a unique mapping from angular- to reciprocal space coordinates, while a unique mapping for $Q_y - Q_x$ and $Q_x - Q_z$ projections may be obtained from limiting scattering angles along the lines defined by

$$\alpha_f = 0 \text{ and } \nu = 0.$$

As can be seen, the GISAXS geometry leads to the range of Q_y space probed to be much wider than the range probed in Q_x (compare about three reciprocal lattice

constants in Q_x to about 120 lattice constants in Q_y).

6.2 Influencing perpendicular coherence

Rotating the sample along its azimuth angle ϕ implies the rotation of the Bravais lattice in reciprocal space, leading to varying diffraction patterns of the reciprocal lattice points being intercepted by the detector at any given ϕ. Parallel lattice planes corresponding to particular sets of miller indices hk of the two dimensional reciprocal lattice often appear to be lying on clearly identifiable arcs in Fig. 6.4, which comes as a result of the large discrepancy between the ranges of probed Q_x and Q_y space.

As discussed in section 2.4, the diffraction pattern consists of the product of reciprocal lattice $\text{Ш}(Q_x, Q_y)$ and the rotationally symmetric structure factor $F(\mathbf{Q})$, the latter appearing stripe-like because of the small range of intersected Q_x values. The diminishing intensities towards the top of each image is due to the Q_z dependence of $= F(\mathbf{Q}) = F(Q_x, Q_y, Q_y)$. Whenever ϕ corresponds to a high symmetry direction of low Miller indices, the diffraction pattern aligns in a way to form horizontal arcs of many closely spaced diffraction spots. If the beam coherence along Q_y is too small, individual (widened) GTRs may merge to form a continuous arc, as has been discussed in detail in chapter 4. This continuous intensity distribution can be seen in Fig. 6.4, where at $\phi = 45.1°$ the sample is only very slightly misaligned with respect to the (11)-direction, which is already sufficient to have the GTRs of a lattice plane overlap. Contrasting, in all other panels, the misalignment of the probed lattice planes with respect to the long axis of the coherence function $\tilde{\xi}_\perp$, being in turn normal to the incident beam direction, led to all individual GTRs being clearly separable.

In the grazing incidence geometry, the projected coherence $\xi_\parallel$ onto the sample along the incident beam is almost always sufficient to exceed the lattice constant even of mesoscopic patterned arrays because of the inverse sine relationship stated in eq. 4.7. The beam coherence $\xi_\perp$ perpendicular to the incident beam, however, is generally smaller by up to orders of magnitude. In order to investigate the instrumental capabilities of controlling $\xi_\perp$, multiple GISAXS measurements were performed using varying slit sizes, controlling the width of the beam on the source side, taking values of 1.6 mm, 1.1 mm, 0.6 mm and 0.1 mm. According to the Fraunhofer diffraction integral[86, 194] over the beam aperture, by reducing the slit width the coherence of the radiation behind the aperture is increased.

Measurements were performed in the (11) and (31)-direction, where the sep-

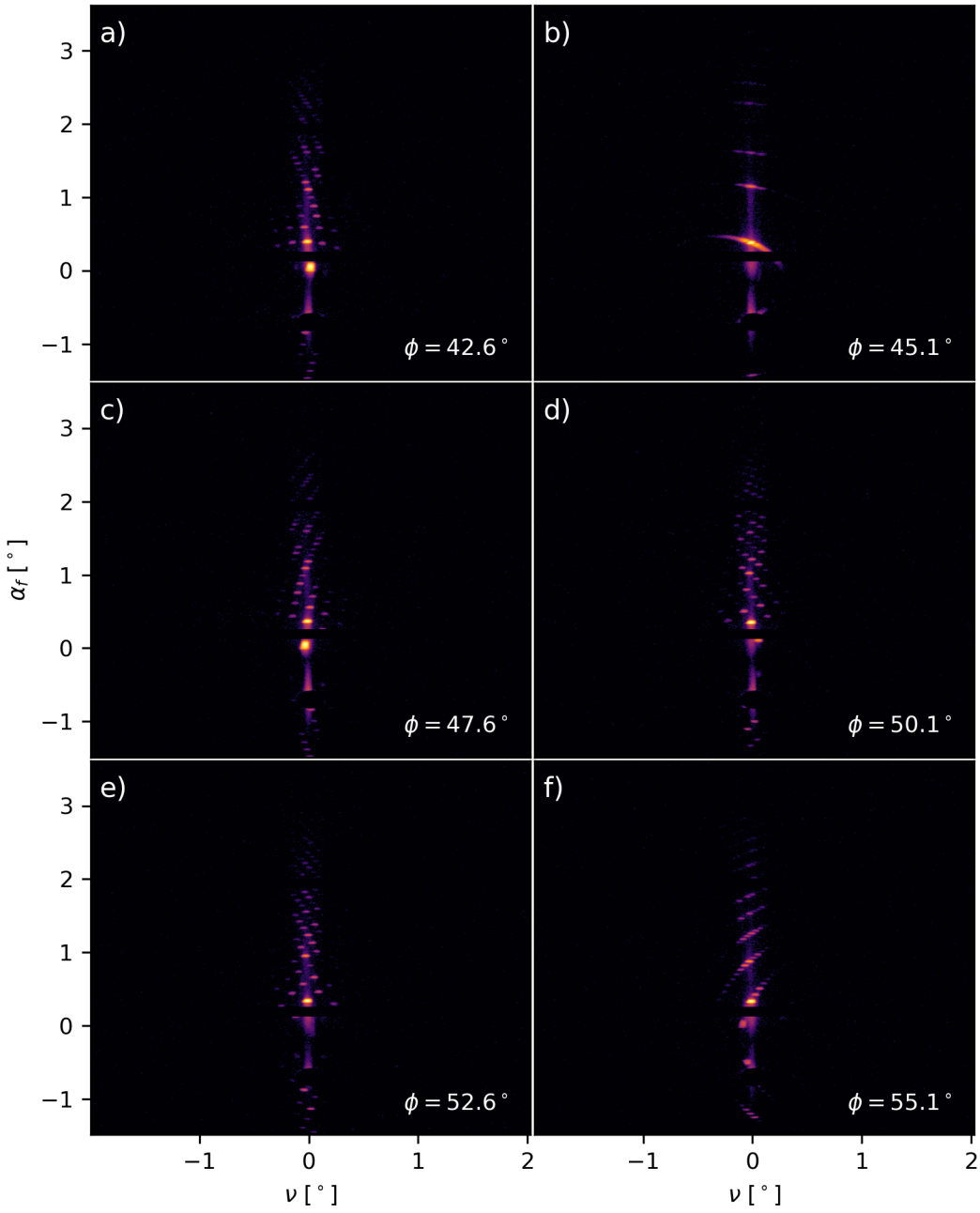

Figure 6.4: GISAXS diffraction patterns at various azimuthal sample angles. Lattice planes appear to lie on arced segments due to the oblique detector geometry. Most of the diffraction peaks to left and right of the purple vertical stripe were fully merged with the diffuse background and are not visible even on a logarithmic scale.

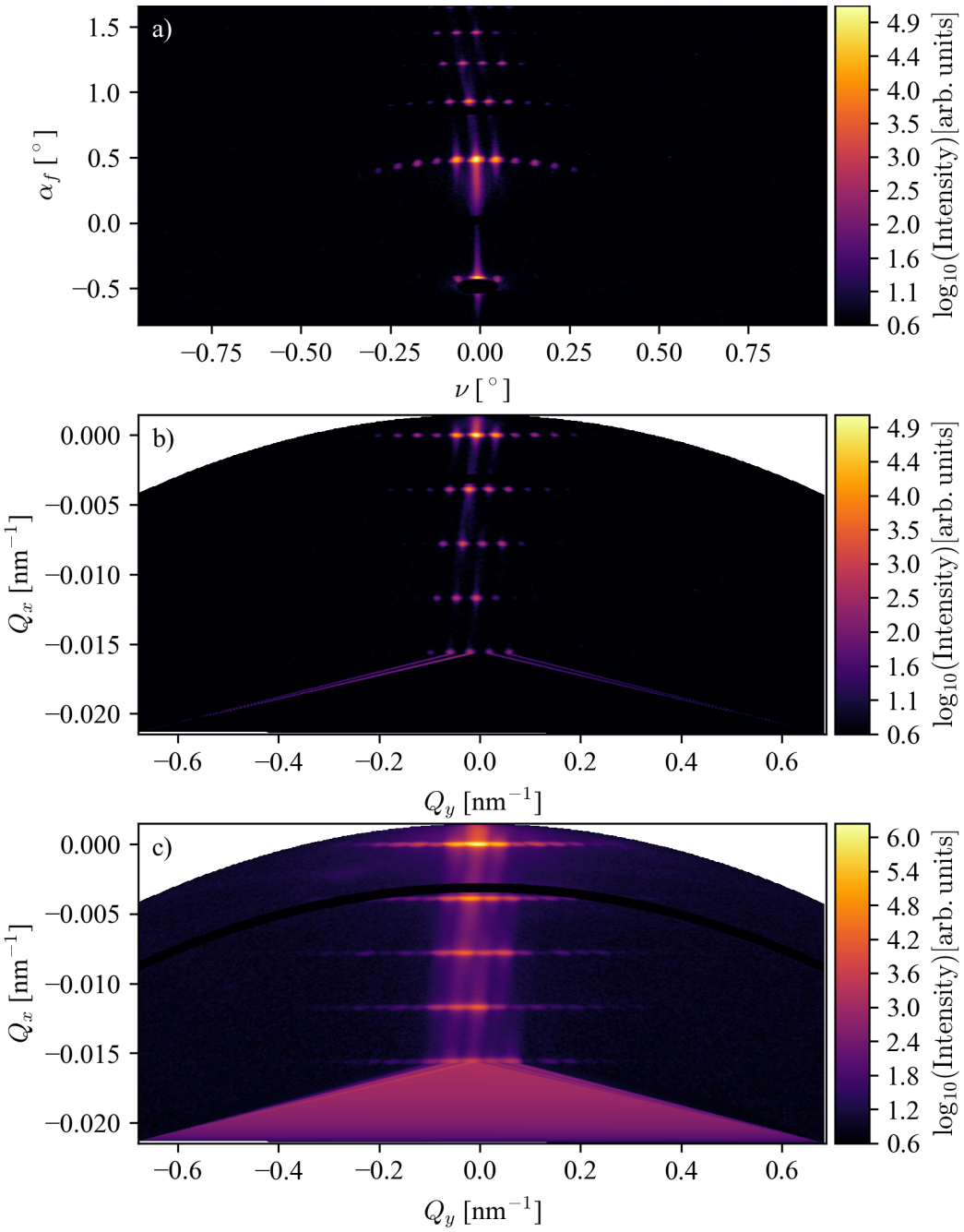

Figure 6.5: The same GISAXS pattern measured along the (31)-direction under low and large beam coherence conditions. Panel a) shows the detected intensity in angular space, while panels b) and c) show representations in $Q_y - Q_x$ space using the narrowest (0.1 mm) and widest (1.6 mm) slit widths. Lattice planes in angular space appear to lie on arced line segments, while appearing on straight lines in the reciprocal space representation, allowing for easy extraction of line scans.

aration of neighbouring GTRs along a single lattice plane was supposed to be of the same order as the width of the coherence function $\tilde{\xi}_{\perp}$, determining in turn the width of each GTR. Fig. 6.5 shows the effect of using either the largest or smallest slit size of 1.6 mm and 0.1 mm, respectively. Using the small slit width clearly increased the beam coherence sufficiently to resolve individual GTRs, whereas in the case of a large slit width the peaks were much less well defined. Expressed in the $Q_y - Q_x$ plane, the reciprocal lattice does not appear distorted any more, which allows for easy line extraction along a particular reciprocal lattice plane. Fig. 6.6 a) and b) shows line scans along lattice planes perpendicular to the (11) and (31) directions, respectively, normalised to their maximum intensity for clarity. The higher distance

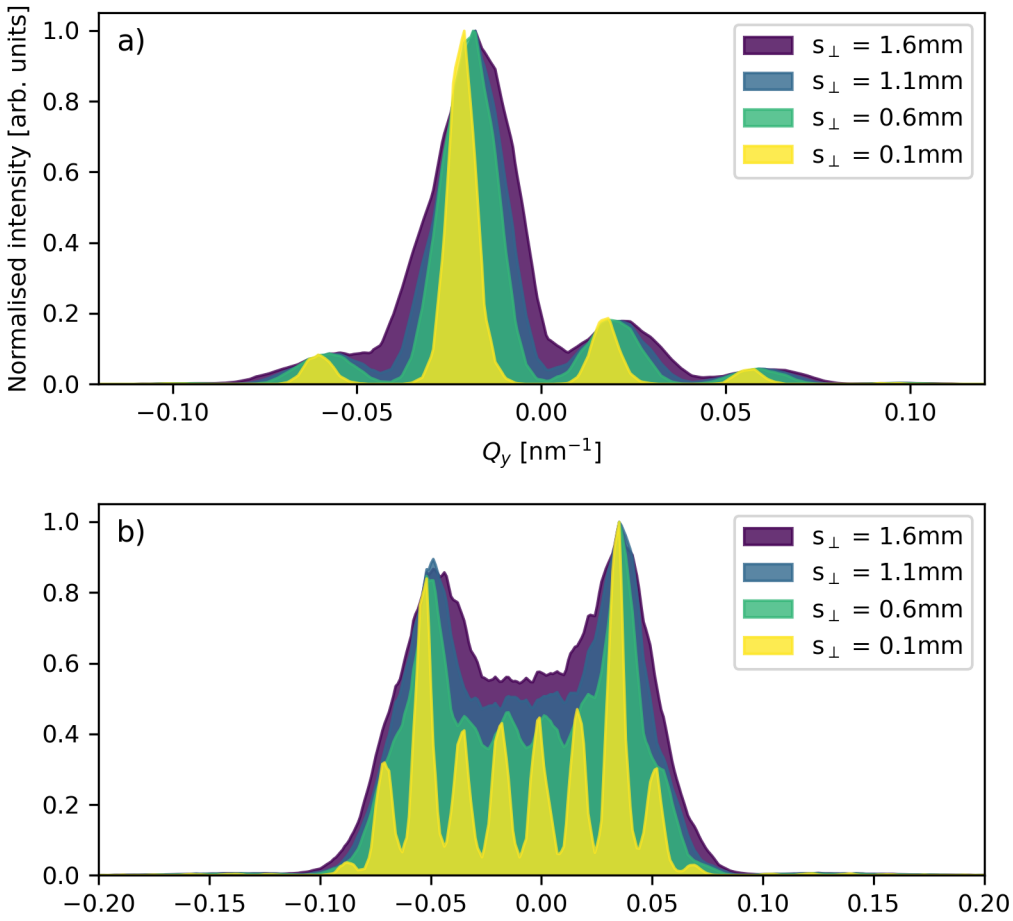

Figure 6.6: Effects of changing beam coherence $\xi_{\perp}$ perpendicular to the incident beam. The figure shows how the diffraction peak widths along the (13) and (11)-lattice planes (panels a) and b), respectively) decrease with decreasing slit width.

amongst GTRs along the (31) planes means that lower beam coherence is sufficient to fully separate individual GTRs. The shorter distance between GTRs along the (11) means that resolving individual peaks requires higher beam coherence. Note that at the very small wavevector transfers, slight misalignments of the slit center and direct beam position resulted in a small offset of the origin of reciprocal space making the two central peaks in panel a) of Fig. 6.6 appear to be of different intensity despite their apparent symmetric location in reciprocal space. In fact, the two central peaks correspond to orders $h = \bar{1}, k = 1$ and $h = \bar{2}, k = \bar{2}$ explaining the apparent asymmetry in peak intensity as a result of differing modulus wavevector transfer Q of all probed peak in Fig. 6.6 a). Fig. 6.6 b), on the other hand, shows a more symmetric distribution of peak intensities, as is expected for the (11)-direction. However, consistent with the observation in panel a), the same offset in Q_y of about $-0.01\,\mathrm{nm}$ is seen again, correcting for which would re-establish the symmetry of all peak *positions*. Note that the slight asymmetry in peak *intensities*, most noticeable at the two peaks of highest intensity, is most likely due to a small angular offset in ϕ. It should again be stressed that, unlike for rocking curves, Q_z is not kept constant over the length of the line scan, which explains the unusual peak intensities in Fig. 6.6 b), since peak modulation in this type of scan is no longer simply given by the planar component of the structure factors $F(\mathbf{Q})$.

Fig. 6.7 a) and b) show Gaussian fits along the Q_x and Q_y directions through the $(\bar{2}\bar{2})$ diffraction spot. Apart from varying intensities due to slit induced flux limitations, all peaks are fitted well by Gaussian cross sections. From the fit the average coherence length along the incident beam was calculated to be

$$\sigma_{\parallel} = 85\,500\,\mathrm{nm} \pm 1.9\% \approx 57 \times d_{\mathrm{latt}}$$

while the coherence lengths perpendicular to the incoming beam where found to be

$$\sigma_{\perp}(1.6\,\mathrm{mm}) = 610\,\mathrm{nm}$$

$$\sigma_{\perp}(1.1\,\mathrm{mm}) = 780\,\mathrm{nm}$$

$$\sigma_{\perp}(0.6\,\mathrm{mm}) = 920\,\mathrm{nm}$$

$$\sigma_{\perp}(0.1\,\mathrm{mm}) = 1670\,\mathrm{nm},$$

which are also presented in Fig. 6.8. The values of $\sigma_{\perp}$ are much better defined than the ones presented in chapter 4, as it was now possible to directly extract $\sigma_{\perp}$ from fitting the *shapes* of separate diffraction peaks, as opposed to the indirect calculation

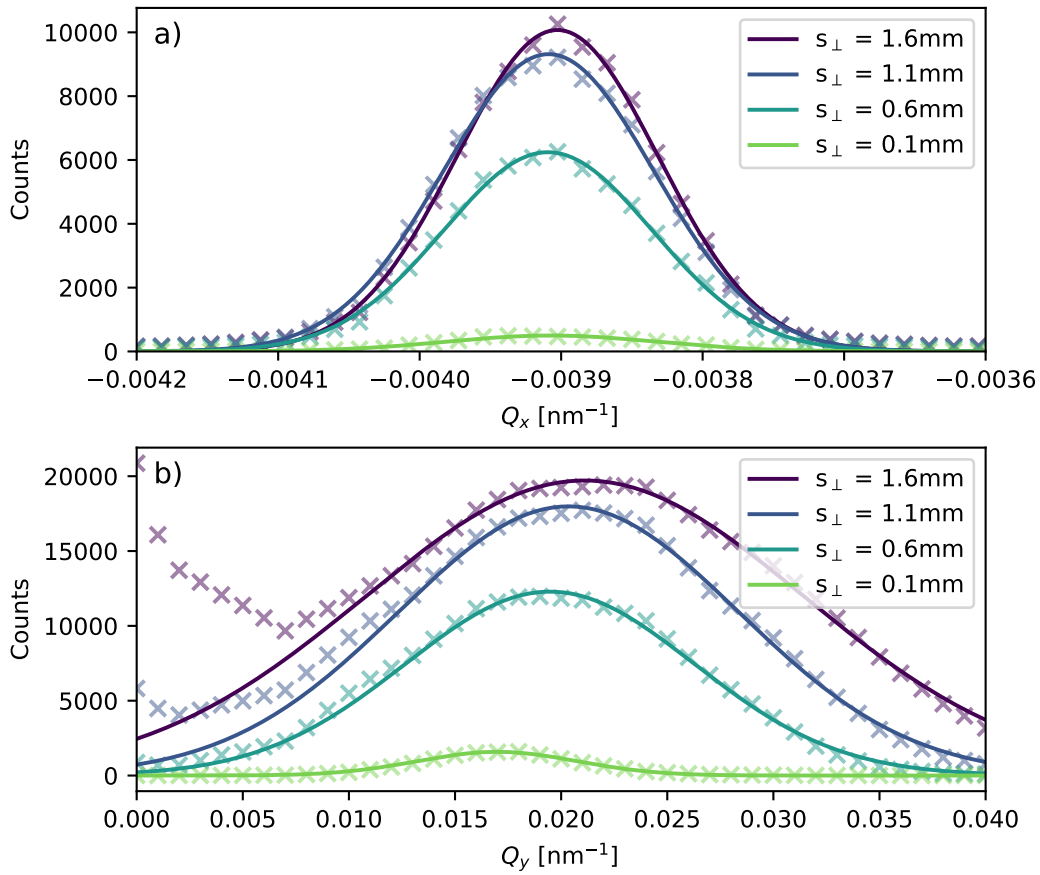

Figure 6.7: Gaussian fits of the $(\bar{2}\bar{2})$ diffraction spot along Q_x (panel a) and Q_y (panel b) directions. The most likely reason for the shift in peak position along Q_y is a slight misalignment of the slit centre from the centre of the beam.

of coherence values obtained from fitting the *intensities* of a set of overlapping diffraction peaks.

Note that the perpendicular coherence is determined solely by the divergence of the beam, which can be easily traded for photon flux by tuning the respective slit sizes of a lab source. In this way, values of perpendicular coherence similar to the synchrotron based measurements presented in chapter 4 can be easily obtained in laboratory based experiments.

6.3 GISAXS fitting protocol

In the previous section the GISAXS geometry has been shown to produce huge numbers of well resolved diffraction spots of patterned arrays of mesoscopic dimensions. Azimuthal rotation of the sample can be used to control the intercepted diffraction

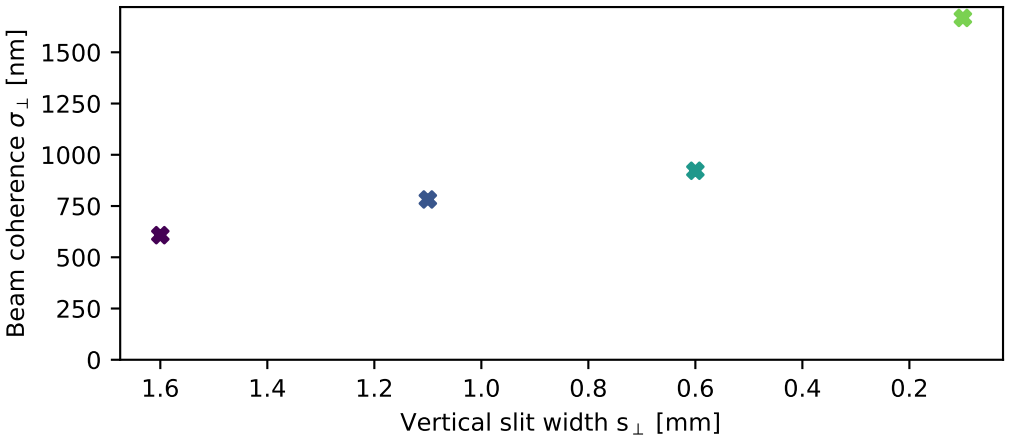

Figure 6.8: Increasing perpendicular coherence as obtained form the Gaussian fits presented in Fig. 6.7 b) as a function of slit width $s_\perp$.

spots and beam coherence can be reliably controlled by adjustment of incidence slits. Furthermore, the previously developed scattering frameworks dealing with low-coherence limiting cases as well as spatial unit cell modelling are fully compatible with the GISAXS geometry. In fact, GISAXS might even be able to circumvent many nuisances of classical rocking curves. For one, the static geometry means that many complicating factors like angle-dependent projected coherence lengths as well as the implicit integration over a changing detector resolution function R do not have to be taken into account. Further, GISAXS measurements allow for the simultaneous integration of wide areas of reciprocal space, whereas step-wise detector integration takes additional orders of magnitude in time.

A promising protocol for fitting of a patterned array to GISAXS measurements consists in taking multiple grazing incidence exposures at varying known values of sample azimuth ϕ and incident angle α_i. After indexing the various diffraction spots, regions of interest (ROIs) are set up to either integrate over or fit an adequate function to it in order to obtain the total scattered intensity. The positions of the ROIs under azimuthal rotation ϕ according to GTR positions Q_x and Q_y in the instrument frame of reciprocal space can be easily found from their position in the sample frame Q'_x and Q'_y due to the rotation matrix

$$\begin{pmatrix} Q_x \\ Q_y \end{pmatrix} = \begin{pmatrix} \cos\phi & \sin\phi \\ -\sin\phi & \cos\phi \end{pmatrix} \begin{pmatrix} Q'_x \\ Q'_y \end{pmatrix}. \tag{6.4}$$

This way, instead of fitting multiple complex curves of various scan types,

many diffraction spots are broken down to single numbers that can be fitted efficiently, since each diffraction spot requires only a single calculation of the structure factor $F(\mathbf{Q})$, corresponding to the Q_z position the detector window intercepts a reciprocal lattice point (k,l), an approach that is widely used in macromolecular crystallography[218, 219]. This protocol appears much more robust, less error prone and computationally light than the previously discussed approaches that required multiple structure factor calculations per diffraction peak, followed by numerical convolution and geometrical corrections, the latter introducing additional fitting parameters and uncertainty to the model.

A proof of the obtainable (good) agreement in between experimental data and a simple simulation is presented in Figs. 6.9 and 6.10. Thanks to its generality, the sample model developed in chapter 5 is fully compatible with the GISAXS geometry. Hence, the sample used here was reconstructed (without being explicitly fitted) using the best model parameters obtained from fitting the (very similar) sample used in chapter 5. Further, values describing the parallel and perpendicular beam coherence, $\sigma_{\parallel}$ and $\sigma_{\perp}$, determined from fitting the diffraction peaks in Fig. 6.7 have been used in order to model the peak shape. Note, however, that unlike most parts of rocking curves, the consistently low scattering angles require utilisation of the DWBA in calculating the structure factor $F(\mathbf{Q})$, implementation of which has been discussed in section 2.4.4.

After adding an empirically determined (constant) diffuse background to the data, the simulations presented in Figs. 6.9 a) and 6.10 a) are found to be almost indistinguishable by eye from the experimental data. Despite the data not having been fitted for reasons of time constrictions, it is apparent that the GISAXS simulation is indeed able to reproduce experimental measurements rather straightforwardly, including most of the experimentally observed diffraction peak modulation. Furthermore, even though the exposure time of each measurement was only about 75 minutes, at least 10 diffraction orders are resolvable at $Q_x = 0$ (topmost row in Figs. 6.9 and 6.10), along the (31)-direction, which corresponds to the covered $\mathbf{Q}$ range being larger than in the rocking curves of chapter 5. This large range in $\mathbf{Q}$ ensures sensitivity to the previously observed enhancement of the islands structure factor coming as a result of island doming, although the exact shape of the modulated structure factor, of course, depends on the x-ray energy E, so that direct comparison of the experimental data is not straightforward.

The major drawback of GISAXS in the context of patterned arrays, however, seems to mainly be a technical issue complicating measurements of magnetic structures which would naturally be of great interest to experimenters studying pat-

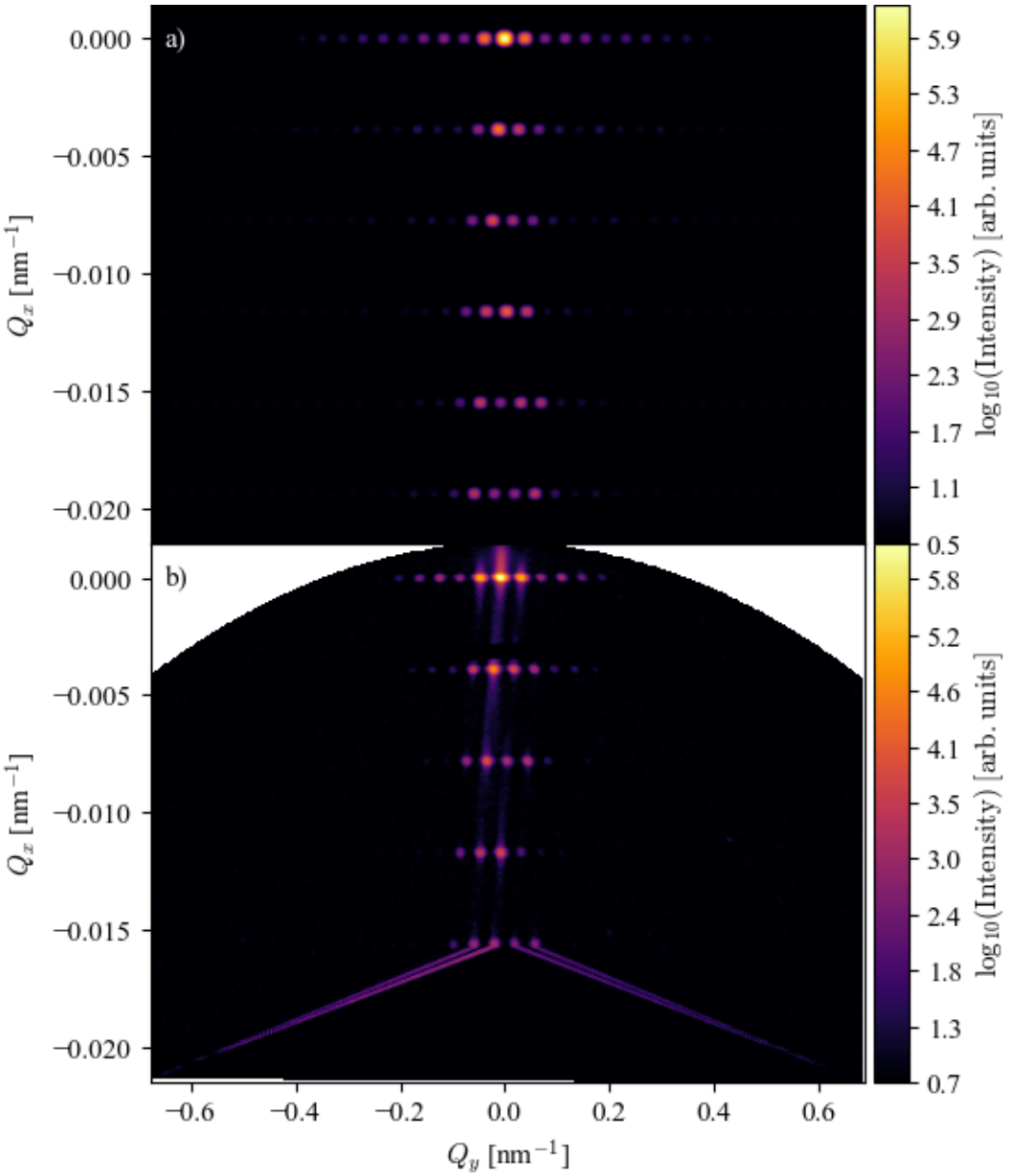

Figure 6.9: Simulation (a) and experimental data (b) of the scattering along the (31)-direction of the patterned array under high coherence conditions corresponding to $\xi_{\parallel} = 1667\,\text{nm}$. Additionally, an empirically found (constant) diffuse background of 2×10^{-6} times the maximum peak intensity of the pattern was added to the simulation.

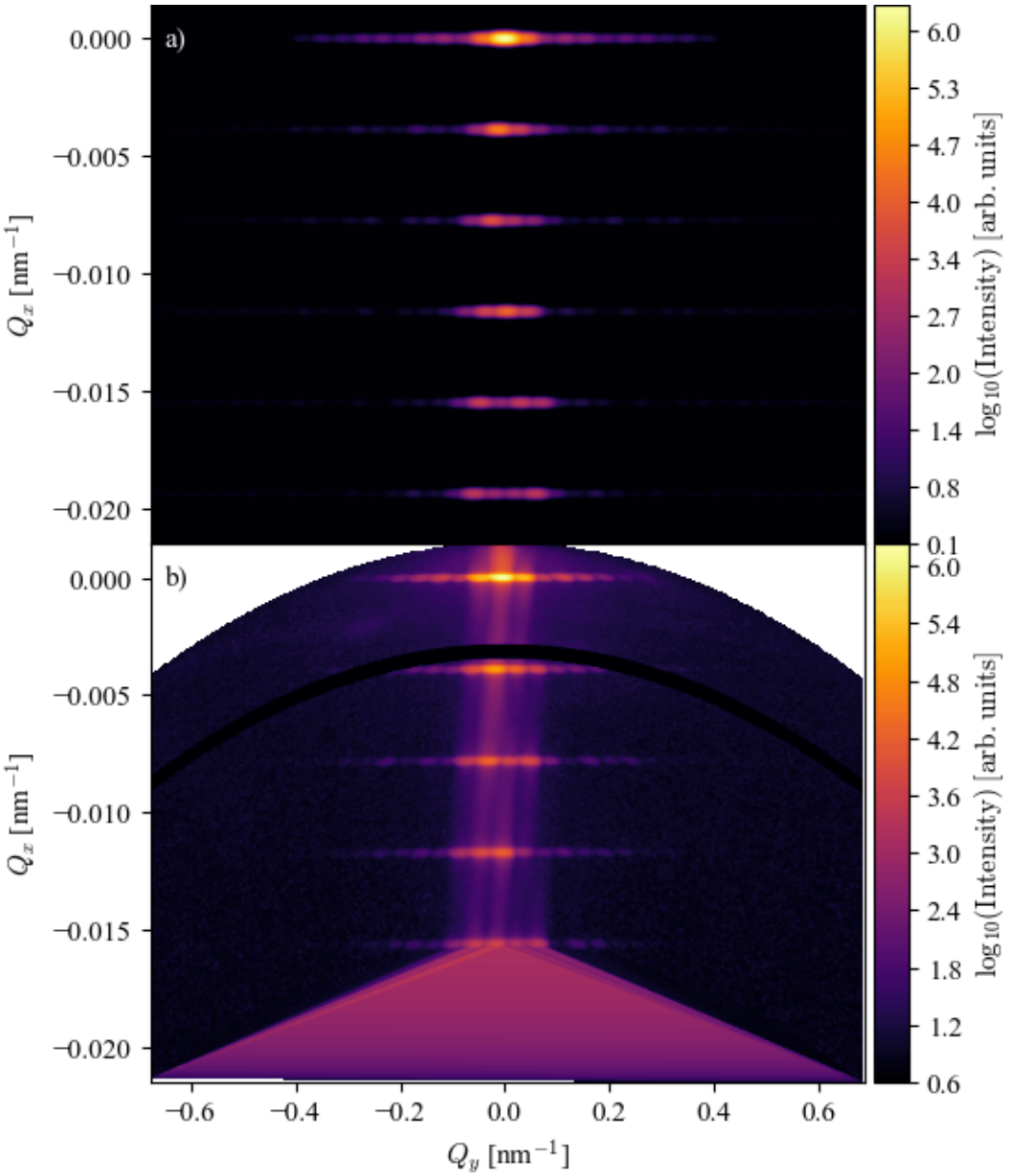

Figure 6.10: Simulation (a) and experimental data (b) of the scattering along the (31)-direction of the patterned array under low coherence conditions corresponding to $\xi_{\parallel} = 607\,\text{nm}$. Additionally, an empirically found (constant) diffuse background of 8×10^{-7} times the maximum peak intensity of the pattern was added to the simulation.

terned arrays. In order to gain magnetic sensitivity towards Palladium, the energy of the synchrotron radiation had to be tuned to just below the Pd L3 edge, which is located at

$$E_{\mathrm{Pd-L3}} = 3.1733\,\mathrm{keV},$$

and falls into the tender x-ray regime. Unfortunately, standard experimental set-ups on most synchrotron beamlines rely on beryllium windows in order to separate the vacuum tube containing the beam from 2D-detectors, preventing the penetration of soft x-rays at these energies. Possible solutions may consist in either using less common custom made vacuum chambers that support usage of large area detectors or to fall back on designing samples of magnetically active material, that obtain adequate absorption edges at energies above roughly 5 keV, at which absorption of the Be windows is significantly reduced.

6.4 Summary

This chapter introduced the GISAXS geometry as an experimental technique in the context of studying patterned arrays. The anisotropic nature of patterned arrays requires making a choice along which direction of the two-dimensional lattice structure of the array a measurement of x-ray scattering is to be performed. In practical considerations, it was discussed how proper alignment of the sample can be maintained if azimuthal rotation of the array is used in order to change the lattice direction of a measurement. It was further shown how a large x-ray beam coherence, $\xi_\perp$, perpendicular to the scattering plane is obtained by confining the beam size by using a sufficiently small aperture slit perpendicular to the scattering plane. Increasing $\xi_\perp$ implies an increasing number of coherently scattering patterned elements. Apart from the higher sensitivity of the x-ray beam probing the patterned array, the increased *coherent* scattering amplitude $A(\mathbf{Q})$ may even compensate for the flux reduction accompanying a narrow aperture of the incident beam, although in the experimental practice of this experiment a factor in registered intensity of ≈ 10 in favour of the open-(1.6 mm) over the closed slit (0.1 mm) was observed, as is apparent from the color scale of Fig. 6.5 as well as from the line scans presented in Fig. 6.7 a) and b). It was demonstrated how, under laboratory conditions, $\xi_\perp$ varied as a function of aperture size, finding that a slit width of 0.1 mm was sufficient to obtain a perpendicular beam coherence (in units of the standard deviation of a Gaussian distribution describing the correlation function of the beam) of more than 1.5 µm, significantly exceeding the lattice constant of the patterned array.

A peculiarity of the small scattering angles of the GISAXS geometry is that

typical area detectors probe an obliquely shaped surface within reciprocal space that is much wider in Q_y (perpendicular to the scattering plane) than along Q_x, again stressing the importance of large $\xi_\perp$. It was shown how the distorted view of reciprocal space provided by the pixelated grid of the area detector, can be transformed into a more familiar view, obtained from projection of the measured intensity onto the Cartesian Q_x-Q_y-plane. The Cartesian representation allows for a simpler analysis of scattering data, for instance by allowing for easier indexing of diffraction peaks. Another advantage lies in the more straightforward definition of regions of interest of a fixed area, surrounding individual diffraction peaks. The latter is required for the proper integration of the total scattered intensity contributing to a given grating truncation rod.

Finally, it was demonstrated how the scattering framework, developed in the earlier chapters, is compatible with the GISAXS geometry, leading to simulations being visually almost indistinguishable from experiment. In more quantitative considerations, it is believed that future studies will produce high quality fits of experimental data, exploiting the high information content obtained from simultaneous analysis of dozens of diffraction peaks a typical GISAXS measurement provides.

Chapter 7

Spatially Resolved Magnetic Vortex States

7.1 Magnetic Vortex States

Formation of magnetic vortex states is a well described phenomenon in magnetic micron- and sub-micron sized disks. A magnetic vortex is characterised by the magnetic moments of all the atoms within the disk forming closed loops around the geometrical vortex core. Most of the magnetic moments are restricted to lie within the plane of the disk, although moments close to the vortex core may exhibit a significant component pointing out of the plane in order to avoid a singularity occurring at the core. Hence, a vortex state is generally characterised by both its chirality, i.e. the sense of rotation of the magnetic moments, and its polarity, i.e. the direction of the out-of-plane component of magnetic moments close to the vortex core. For perfectly symmetric disks the four states defined by these restrictions are energetically equivalent and the vortex state is therefore considered four-fold degenerate. Magnetic vortices are being researched regarding geometrical control[31, 220–222], vortex nucleation mechanism[31, 223, 224], magnetic resonance effects[225–227], magnetisation reversal[26, 77, 228–230], and many more. The most prominent investigation techniques include micromagnetic simulations[27, 28, 227, 231], real-[53, 77, 221, 224, 227] and reciprocal space[28, 31, 53, 97, 232] visualisation.

Given that the sample temperature is below the magnetic ordering temperature $T < T_C$, the total magnetic energy, and hence the magnetic state, of the disk is determined by three energy terms, which are all related to different magnetic interactions:

1. The first type of interaction is of magnetostatic nature, which is related to the

stray field of the disk. The magnetostatic energy[233] of an object is calculated from integrating over the magnetic vector potential

$$E_{\mathrm{ms}} = \frac{\mu_0}{4\pi r^2} \iint \frac{\mathbf{m}(\mathbf{r}) \times (\mathbf{r} - \mathbf{r}')}{|\mathbf{r} - \mathbf{r}'|} \, \mathrm{d}\mathbf{r} \, \mathrm{d}\mathbf{r}' \tag{7.1}$$

of all magnetic moments within the internal magnetic field produced by the entirety of the magnetic moments residing within the body. Integration by parts and application of the divergence theorem on eq. 7.1 leads to the expression for the total magnetostatic energy[27]

$$E_{\mathrm{ms}} = \frac{1}{2} \iint_{\mathrm{mantle}} \frac{\sigma(\mathbf{r})\sigma(\mathbf{r}')}{|\mathbf{r} - \mathbf{r}'|} \, \mathrm{d}\mathbf{S} \, \mathrm{d}\mathbf{S}', \tag{7.2}$$

where $\mathrm{d}\mathbf{S}$ is the outwards-pointing surface normal of the disk, $\sigma(\mathbf{r}) = \mathbf{m}(\mathbf{r}) \cdot \hat{\mathbf{n}}(\mathbf{r})$, and $\mathbf{m}(\mathbf{r})$ and $\hat{\mathbf{n}}(\mathbf{r})$ being the local magnetic moment and surface normal at positional vector $\mathbf{r}$, respectively. Note that eq. 7.2 makes use of the fact that the magnetic field in the bulk of the disk is assumed to be divergence-free, hence ignoring the out-of-plane component of the magnetic moments within the vortex core. Under these assumption, the surface integral of eq. 7.2 is taken over the mantle of the disk only, since $\mathbf{m} \cdot \hat{\mathbf{n}} = 0$ for all moments located on the up- and down faces of the disk.

Since a magnetic vortex minimizes the component of the magnetic moments normal to the surface of both the sides as well as top and bottom of the disk, magnetostatic interaction is the main driving mechanism for the formation of vortex states.

2. The second energy term to consider is the Zeeman energy, which describes the potential energy of magnetic moments within an externally applied magnetic field. It is described by[26]

$$E_{\mathrm{Z}} = -\mu_0 \int \mathbf{m} \cdot \mathbf{H}_{\mathrm{ext}} \, \mathrm{d}\mathbf{V}. \tag{7.3}$$

Obviously, the Zeeman energy is minimized by a co-parallel alignment of the local magnetic moments with the external field $\mathbf{H}_{\mathrm{ext}}$. Therefore, the Zeeman energy is promoting a collinear magnetic state if the externally applied field is sufficiently strong.

3. The last main contributor to the total energy is the exchange energy E_{ex}, mediated by the exchange coupling of magnetic ions[234]. It generally leads

to either parallel or antiparallel alignment of neighbouring magnetic moments even in the absence of externally applied fields. Hence, exchange interaction is the reason for the polarity of vortex states; If the curl of magnetic moments exceeds a critical value close to the vortex core, exchange interaction will locally dominate over magnetostatic interactions and force the magnetic moments into an out-of-plane collinear state, pointing either up or down.

A magnetic vortex will generally be created if the magnetostatic interaction provides the dominant contribution to the overall energy state of the system, which is generally related to three distinct conditions being fulfilled:

1. The disk does not include a strong magnetocrystalline anisotropy, so that the local magnetic moments are provided sufficient flexibility in the choice of their spatial orientation.

2. Similarly, the aspect ratio of radius and thickness of the disk has to be large enough to prevent alignment of the magnetic moments along a shape anisotropy axis of the disks.

3. The thickness of the dots has to exceed a critical value in order to overcome the dominance of exchange coupling at small length scales.

Fig. 7.1 presents a phase diagram visualising the inter-relatedness of disk radius R and thickness T as adopted from [27] summarises the previous discussion.

Without an external magnetic field applied, a rotationally symmetrical disk will exhibit a magnetic vortex located in the centre of the disk. Upon application of an external field, the vortex core shifts perpendicular to H_{ext}. Through this shifting of the vortex core, the Zeeman energy E_{Z} is decreased because the magnetic moments on the far side of the vortex are increasingly aligned with H_{ext}. Simultaneously, keeping most of the magnetic moments aligned within the sample plane minimizes stray fields and keeps the magnetic curl low, therefore accommodating E_{ex}. Hence, the chirality of the magnetic vortex field in its ground state determines the direction the vortex moves so as to ensure that the magnetic moments on the far side of the vortex align with H_{ext}. An example of a simple magnetic vortex with and without an applied field H_{ext} is given in Fig. 7.2 a) and b).

Accounting for the increasing Zeeman energy, the dislocation of the vortex core increases with an increasing amplitude of H_{ext}, a process which is reversible if the vortex core does not annihilate upon reaching the edge of the disk, the latter happening once the external field strength reaches the annihilation field H_{an}. Above

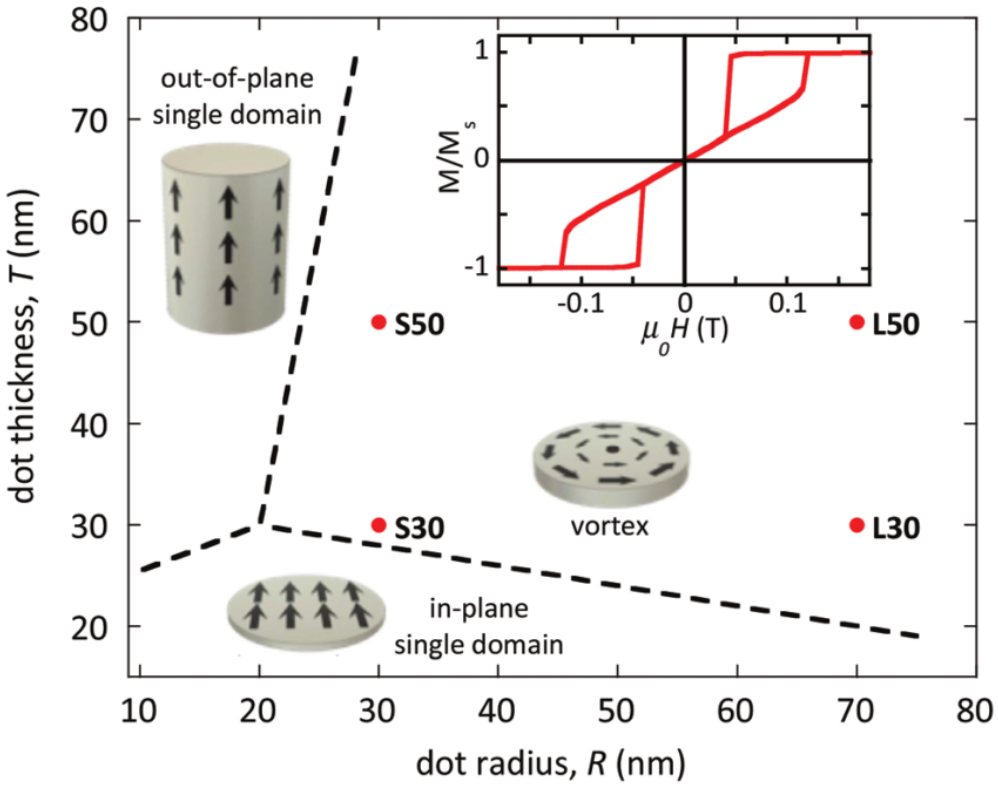

Figure 7.1: Phase diagram of magnetic domain structures of Permalloy nano dots. Adapted from [27].

$|H_{\mathrm{an}}|$ the disk can be considered to be in a collinear state, which is, however, maintained purely by the external field, so that edge effects at the disk perimeter may still prevent it from being uniformly magnetised.

Upon decreasing H_{ext} a vortex will re-appear, albeit below $|H_{\mathrm{an}}|$, at the nucleation field H_{n}. Note, however, that the former provides only a simplified picture of the exact injection mechanism of the vortex. For instance, the two vortex states of opposite chirality nucleating at opposite sides of the disk are energetically degenerate. Hence it is not clear, at which end of the disk a vortex will nucleate, and micromagnetic simulations suggest that, indeed, in general two vortices may nucleate in frequently[223]. If the vortices have traversed far enough towards the centre of the disk, attempting to accommodate the opposite chiralities of the two competing vortices leads to frustration of the magnetic moments located at the centre of the disk since the magnetic moments can not simultaneously be part of both vortices. Either by chance or through geometrical imperfections of the disk, one of the vortices will start to dominate over the other, the latter shrinking and eventually disappearing completely. The remaining vortex core will reach the disks

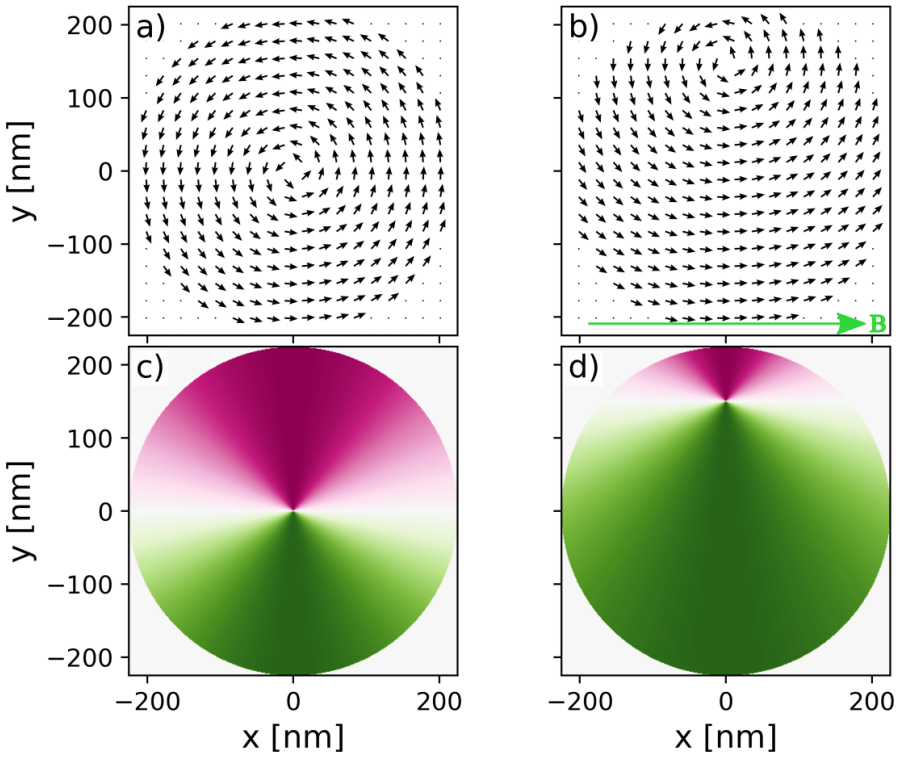

Figure 7.2: Visualisation of simple magnetic vortices using the rigid vortex model discussed in section 7.3.1. Panels a) and b) show the orientation of the local magnetic moments of a vortex of counter-clockwise chirality subjected to no and finite externally applied magnetic field H_{ext}. The shift of the vortex core towards positive y values in panel b) is a consequence of the applied external field H_{ext} pointing in positive x direction, therefore minimising the total Zeeman energy of the disk. Panels c) and d) show the colour coded x-component of the local magnetic moments, which is the quantity the x-rays are sensitive to if impinging along the x-direction.

centre at the (usually very small) coercive field strength H_{c}, from where on the process repeats symmetrically on negative H_{ext}.

Although the process of vortex formation is well understood, many details are still rather elusive. For instance, analytical models for the vortex field generally provide, at most, qualitative agreement with experimental data and are often restricted to small values of H_{ext}[26]. On the other hand, direct measurements of a particular vortex state are generally severely limited, even using the most frequently developed techniques; PEEM-XMCD provides direct space imaging and magnetic contrast, but is restricted to long measurement times and relatively low spatial resolution[30, 235]. SQUID measurements provide information only about the average magnetisation of a sample[27, 31]. Micromagnetic simulations are well known to

be able to reproduce magnetic vortex states, without the need to define an explicit analytical expression describing the field. However, despite micromagnetic results providing a detail rich distribution of magnetic moments[28, 224, 235], comparing these results to experiments is often rather ambiguous and commonly limited to zero T models as incorporating temperature is difficult[236, 237]. For instance, a lack of quantitative agreement between diffraction experiments and simulations using micromagnetic results as an input, render it difficult to decide on the quality of either or both of the micromagnetic results and quality of the simulation framework.

Therefore, the remaining part of this chapter will discuss the sensitivity of resonant x-ray diffraction towards a non-uniform distribution of magnetic moment of circular nano-disks and attempt to further refine the understanding of vortex mediated magnetisation reversal.

7.2 Experimental Observations

To explore the effect of a non-homogeneous magnetic distribution within patterned elements, small angle x-ray resonant scattering experiments have been performed at the 4-ID-D beamline at the Advanced Photon Source (APS), Chicago, USA[211].

The sample is identical to the one discussed in chapter 5 and consists of nano-dots 450 nm in diameter located on a square lattice of pitch 513 nm. The chemical composition of each dot was amorphous $Fe_{13.5}Pd_{86.5}$ and the nominal height of the disks was 10 nm, although it has been shown in the previous chapters how the pre-patterning of the array led to an unintended doming of the islands. A more detailed discussion of the sample properties can be found in chapter 5 and [77] while the patterning procedure is discussed in detail in chapter 3.

Fig. 7.3 shows the difference signal $I_{\text{diff}} = I^+ - I^-$ of two rocking curves taken at opposite helicities of circularly polarised x-rays taken at different external magnetic fields measured at 30 K, while Fig. 7.4 shows the corresponding asymmetry ratio. The detector angle was $2\theta = 8.12°$, corresponding to $Q_z = 2.28\,\text{nm}^{-1}$. The data suggest a distinct modulation of the scattered intensity, depending on the diffraction order and the applied strength of the external field.

In order to increase the magnetically sensitive resonant scattering factors while simultaneously limiting the amount of photon absorption, the x-ray energy was tuned to 3.174 keV, which is located just below the Pd L_3 edge.

Fig. 7.5 and 7.6 show magnetic field loops of the asymmetry ratio taken at temperatures 200 K and 30 K, respectively. At each temperature, measurements were performed at multiple wavevector transfers Q_x corresponding to diffraction

orders $n = Q_x\, d_{\mathrm{latt}}/2\pi$, where $d_{\mathrm{latt}} = 513\,\mathrm{nm}$ is the lattice parameter defining the lattice periodicity of the (10) direction along which the scattering plane was aligned. The diffraction orders measured were -8, -1, 0, and 8.

Each magnetisation loop was measured independently by adjustment of the diffractometer angles to specific values of Q_x followed by scanning the external field, which was applied along the (10) sample direction, therefore aligning with the scattering plane. At each value of H_{ext}, the two intensities I^+ and I^- under reversal of the x-ray helicity were measured, thus enabling the calculation of the asymmetry ratio $A.R.$ under reversal of the x-ray beam helicity as discussed in section 2.1.4.

A qualitative difference between the loops taken at the two temperatures is the formation of a distinct hysteresis found in the 30 K measurement, compared to the field loops measured at 200 K, which lack any hysteresis. This observation has been explained by Östman et al. [77], where it was found from PEEM-XMCD measurements that, in fact, magnetisation reversal by formation of a vortex state occurred at temperatures ranging from 20 K up to room temperature. The formation of a magnetic hysteresis occurs below the bifurcation temperature $T_{\mathrm{e}} \approx 212\,\mathrm{K}$,

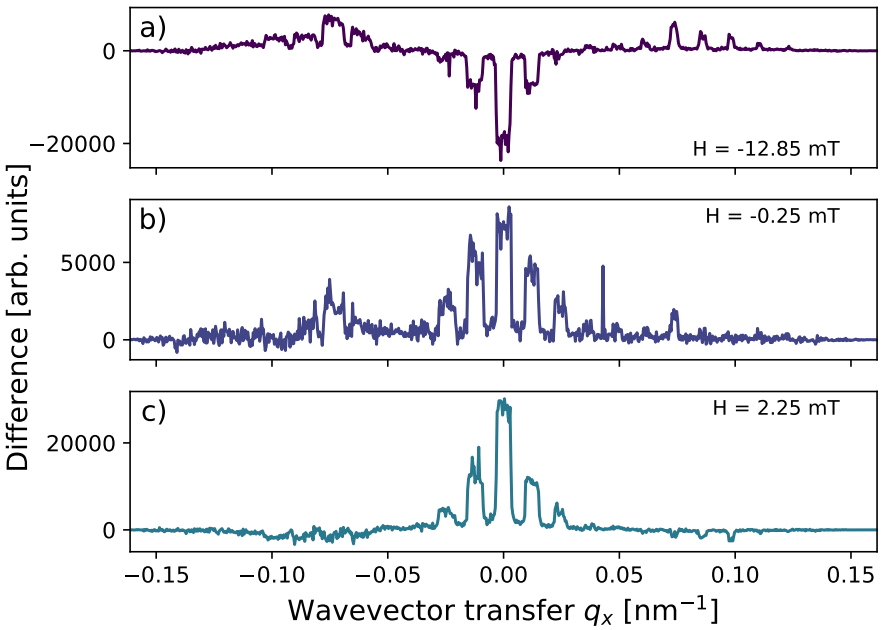

Figure 7.3: Rocking curve difference signal obtained from swapping the x-ray beam helicity, measured at three value of H_{ext} and taken at $E = 3.174\,\mathrm{K}$. Panel a) shows the measured signal at magnetic saturation, panel b) corresponds to magnetic remanence, while panel c) corresponds to a magnetic vortex being dislocated from its ground state in the centre of the disk.

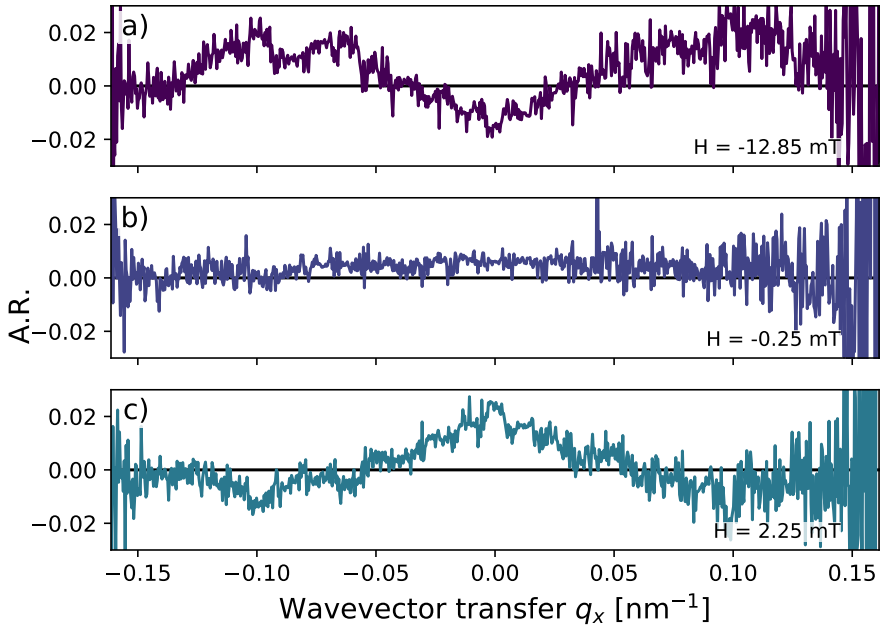

Figure 7.4: Rocking curve asymmetry ratio measured at three value of H_{ext} and taken at $E = 3.174\,\mathrm{K}$. Panel a) shows the measured signal at magnetic saturation, panel b) corresponds to magnetic remanence, while panel c) corresponds to a magnetic vortex being dislocated from its ground state in the centre of the disk.

which marks the point above which the thermal energy $k_{\mathrm{B}}T$ is sufficient to overcome the transition energy $\Delta E(H)$ necessary to reconfigure the distribution of magnetic moments, therefore separating the vortex- and collinear state. Hence, the (apparent) absolute value of the nucleation field H_{n} of a vortex decreases with decreasing temperature, while above T_{e} transitioning from collinear- to vortex state is essentially instantaneous, once the latter becomes energetically favourable.

In other words, at $T < T_{\mathrm{e}}$ and coming from magnetic saturation, the collinear state is maintained deeper into the bistable state on varying H_{ext} as the energy barrier $\Delta E(H_{\mathrm{ext}})$ has to decrease sufficiently in order to be overcome by thermal activation according to the available energy $k_{\mathrm{B}}T$. Therefore, the nucleation field H_{n} is a temperature dependent quantity, which marks the smallest external magnetic field $|H_{\mathrm{ext}}|$ at temperature T at which reconfiguration of the atomic magnetic moments from a collinear- into a vortex state becomes possible within the time-scale of the experiment. However, at $T < T_{\mathrm{e}}$ the equilibrium position of a newly nucleated vortex lies well within the interior of the disk, as opposed to $T > T_{\mathrm{e}}$, where it nucleates at the disk edge. Consequently, this means that at low temperatures the vortex magnetisation $|\mathbf{M}|$ at nucleation is significantly smaller than the magnetisation of

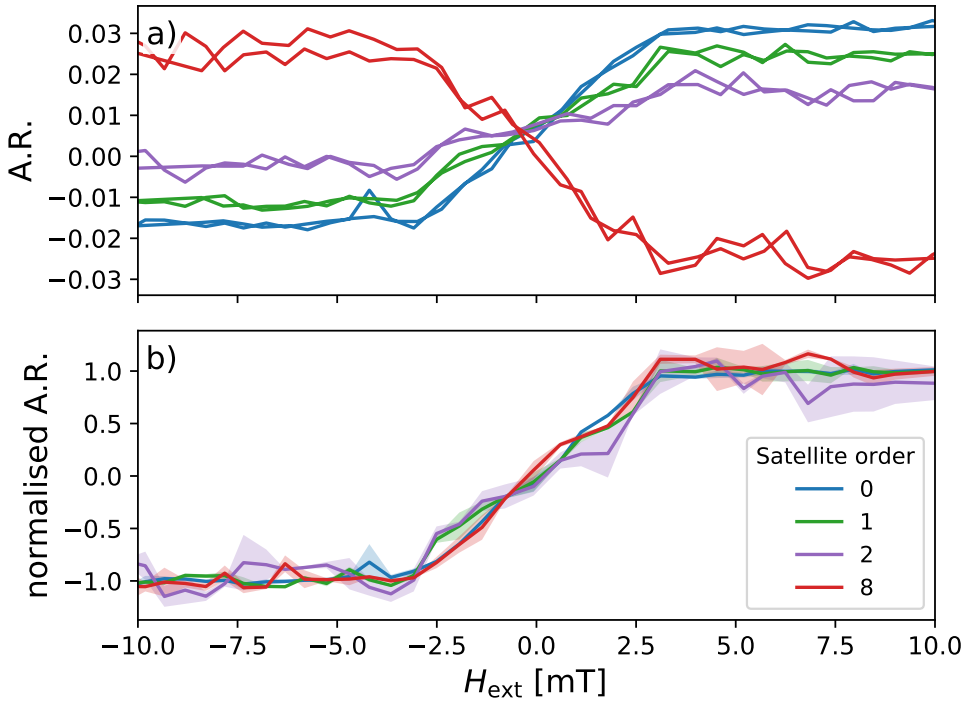

Figure 7.5: *A.R.* taken at multiple satellite orders measured at 200 K. Raw data are presented in panel a), while normalised data are presented in b). Shaded regions indicate the standard deviation obtained from averaging over increasing- and decreasing field branches.

the collinear state, which explains the sharp increase of M around H_n, when the disks transition from collinear- to vortex state.

The effect of performing the experiment at $T > T_e$ can be seen in Fig. 7.5: The magnetisation tracks the same curve along the increasing- and decreasing field branches, indicative of a smooth traversal of magnetic vortices nucleating at the disk edges. Fig. 7.6 presents the opposite case $T < T_e$: The rapid increase of magnetisation at H_n represents the statistical distribution of the magnetic reconfiguration of the individual disks, followed by re-magnetisation via dynamical repositioning and the final annihilation of the vortices according to the applied field H_{ext}. As the thermal energy $k_B T$ is insufficient to immediately nucleate the vortex state once it becomes energetically favourable, the increasing- and decreasing field branches are not identical and a magnetic hysteresis opens up.

Although probing the magnetic structure of a sample occurs only indirectly via the charge-magnetism interference term, a significant advantage of small angle XRMS is the opportunity to measure many Fourier components of the local

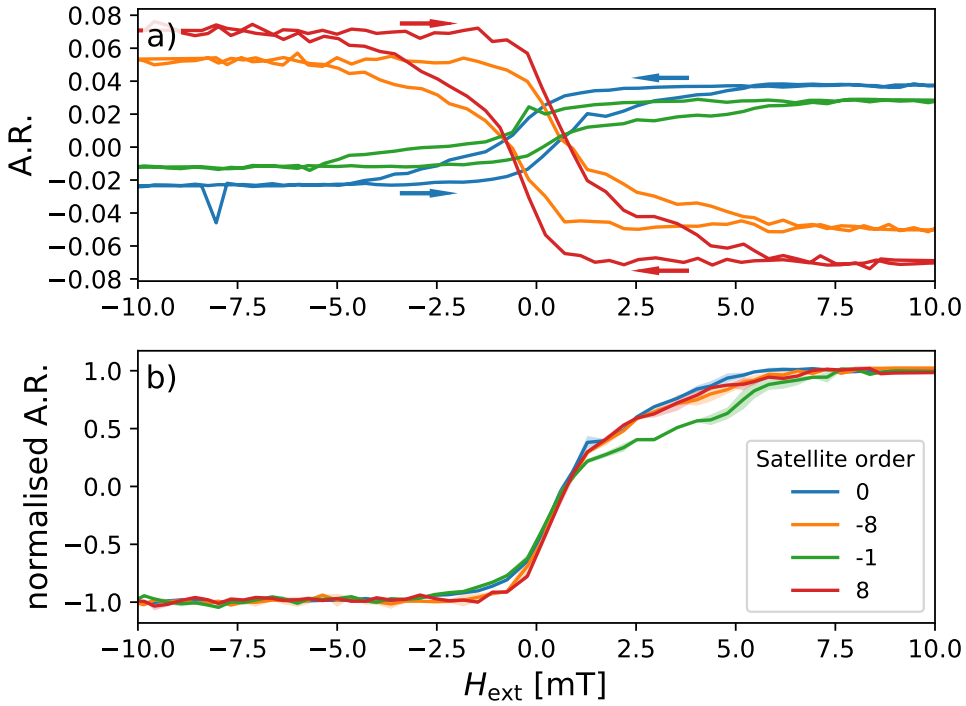

Figure 7.6: *A.R.* taken at multiple satellite orders measured at 30 K. Raw data are presented in panel a), while normalised data are presented in b). Shaded regions indicate the standard deviation obtained from averaging over increasing- and decreasing field branches.

magneto-chemical structure and therefore gain complementary information to techniques like (non-diffractive) MOKE[47, 230, 238] or SQUID measurements[27, 239], which are sensitive to the *average* magnetisation of the sample only. Analogously, the zero$^{\text{th}}$ order reflection in XRMS experiments, i.e. the specular reflection, is directly proportional to the average magnetisation of the sample, as long as $|A_m(\mathbf{Q})| \ll |A_c(\mathbf{Q})|$, i.e. the magnetic scattering amplitude is much smaller than the charge scattering amplitude. However, the sensitivity of higher order Fourier components to the spatial distribution of the electronic charge and magnetic moment allows for the direct evaluation of magnetisation dynamics and, in principal, the comparison of spatial models of a local magnetic structure against experiment. The extraction of higher order Fourier terms still constitutes a lateral averaging over the sample and therefore complements direct space techniques like PEEM-XMCD[77] or MFM-imaging[224, 226].

For easier visual comparison the corresponding field loops have been re-centred to account for small differences in the amount of circular polarisation,

cleaned from obvious statistical outliers, averaged over the increasing and decreasing field branches and finally normalised to ±1 in saturation as seen in Figs. 7.5 b) and 7.6 b). The shaded regions around the average values indicate the standard deviations calculated from the increasing and decreasing branches. The statistical noise level of the 200 K measurement is found to strongly affect the *A.R.* of all scattering orders, so that drawing definitive conclusions is not found to be possible. However, the 30 K measurement shows some clearly resolved differences in between the *A.R.* measured at the 0^{th}, $\text{-}1^{\text{st}}$ and $\pm 8^{\text{th}}$ satellite orders, being subtle but nevertheless significant. On increasing H_{ext} the 0^{th} and $\text{-}1^{\text{st}}$ order the *A.R.* resolvably increases at about $-3\,\text{mT}$, which is the same temperature at which the 200 K appears to be entering the vortex state. Around 0.8 mT the 0^{th} order branch basically mirrors the $\pm 8^{\text{th}}$ order branches, while the $\text{-}1^{\text{st}}$ order crosses the other branches and remains significantly lower than the other branches until the sample reaches magnetic saturation at around 7.5 mT.

The branch splitting provides a direct indication of the sensitivity of the experiment to the magnetic scattering amplitude $A_m(\mathbf{Q})$. It is hence potentially possible to fit simulated to experimental data under some assumption of the distribution of the local magnetic moments $m_x(x, y)$. Furthermore, although much noisier the data taken at 200 K indicates more qualitative differences between the magnetisation reversal process compared to that at 30 K. Obviously, the magnetic configuration of the disks at 200 K and 30 K is expected to vary below $H_{\text{ext}} \approx 0\,\text{mT}$, because of the opening of the hysteresis associated with the thermal activation barrier at the 30 K sample, impacting the switching from the collinear into the vortex state. However, it is clear from comparing Figs. 7.5 and 7.6 that the internal magnetic state of the disks *above* H_{n} also differs significantly at the two temperatures. Despite the higher noise level found at 200 K the *A.R.* found at different diffraction orders does obviously not share the same field dependence. This is most pronouncedly seen when comparing the $+1^{\text{st}}$ and -1^{st} diffraction orders, which are found to be identical after normalisation. While the -1^{st} order is exhibiting a distinct dip at 30 K, the same dip is not present at the $+1^{\text{st}}$ diffraction order measured at 200 K, which is therefore indicative of a qualitative difference in the vortex geometry at the two temperatures.

7.3 Two-Dimensional Modelling of Magnetic Vortices

In order to gain insight into the specific configuration describing a magnetic vortex at a given external field H_{ext}, a model of the vortex has to be applied in calculating

the asymmetry ratio, which is then fitted to the experimental data. Without falling back to micromagnetic simulations[27, 28, 97, 235] an analytical model describing the vortex geometry had to be formulated. It is believed that the exact spatial chemical structure, that has been discussed in depth in chapter 5, is mainly acting as an intensity modulation of the diffraction peaks. Consequently, this modulation is cancelled in the normalised hysteresis loops, which are expected to be primarily sensitive to the internal magnetic structure of the disk, rather than to the exact chemical structure of the island hosting the vortex. It was therefore decided to utilise a purely two-dimensional model of the disk, eliminating as many free parameters as possible.

In order to investigate how different vortex models manifest within the scattered signal, two similar but nevertheless distinct vortex models have been defined. A rigid vortex model and a dynamic model creating an elliptical vortex shape have been employed in order to investigate the ability of the XRMS-technique to resolve spatial magnetic structures. Both models rely on calculating magnetic scattering amplitudes from a specific spatial distribution of the local scattering length density within the sample plane. The charge scattering length density SLD^{ch} is considered to be constant within the whole disk, while the magnetic component of the scattering length density SLD^{mag} depends on the x-component m_x of the local magnetic moment $\mathbf{m}$. SLD^{mag} will thus be proportional to m_x, so that, for simplicity, it is assumed that $|\mathbf{m}| = 1$ holds, allowing the form

$$SLD^{\mathrm{mag}} = m_x \, SLD_0^{\mathrm{mag}} \tag{7.4a}$$

$$SLD_0^{\mathrm{mag}} = \chi \, SLD^{\mathrm{ch}}, \tag{7.4b}$$

where χ is a proportionality factor relating the amplitudes of SLD^{ch} and SLD^{mag}. The magnetic amplitude is considered to be acting only as a small perturbation to the charge amplitude, i.e. either slightly in- or decreasing $|A_{\mathrm{ch}}|$. Since the simulated *A.R.* will be normalised, the only condition required for the magnetic scattering length density is that $SLD^{\mathrm{mag}} \ll SLD^{\mathrm{ch}}$. Hence, in the following the scaling factor relating the scattering amplitudes was fixed to $\chi = 1 \times 10^{-3}$, while it was verified that other values of χ ranging from 0.01 to 1×10^{-5} provided virtually identical results.

7.3.1 Rigid Vortex Model

The rigid vortex model assumes a perfectly circular vortex of magnetic moments distributed symmetrically around a vortex core, y_c, which is free to move along the

y-direction, i.e. perpendicular to the scatting plane and the applied magnetic field H_{ext}. The model is particularly simple, but is generally limited in applicability to small deviations of y_c from the centre of the disk[26]. The local magnetic moments are defined on a two-dimensional grid, representing the lateral coordinates of a single disk. Further, magnetic moments are confined to lie within the boundaries given by the radius R of the disk, i.e. for all radii $\mathbf{r}$ in polar coordinates that obey $r < R$. Under these conditions, for all points (x, y) it holds that

$$r = \sqrt{x^2 + y^2} \tag{7.5a}$$

$$\phi = \arctan\left(\frac{y - y_c}{x}\right) \tag{7.5b}$$

$$m_x = \begin{cases} \mp \sin(\phi) & \text{if } r \leq R \\ 0 & \text{else} \end{cases} \tag{7.5c}$$

$$m_y = \begin{cases} \pm \cos(\phi) & \text{if } r \leq R \\ 0 & \text{else,} \end{cases} \tag{7.5d}$$

with the respective signs in eqs. c) and d) referring to anticlockwise and clockwise chirality.

7.3.2 Elliptical Vortex model

The rigid vortex model is obviously not providing the expected limiting behaviour of merging into a collinear state as the vortex core approaches the edges of the disk. Rather, in order to approximate a collinear magnetic state, the mathematical vortex core has to shift far beyond the edge of the disk therefore rendering local magnetic moments aligned parallel, clearly leading to unphysical behaviour.

In order to overcome this limitation, a model that is believed to be physically more accurate consists of a more dynamic vortex shape, maintaining circular geometry for vortices located in the centre of the disk, while taking on an increasingly elliptical shape when the vortex core is approaching the edge of the disk, finally resembling a linear domain wall just before merging the edge of the disk and annihilating. If the vortex core does reach the edge, the eccentricity of the ellipse shall become infinite, therefore rendering all magnetic moments within the disk to be aligned in a perfectly collinear fashion.

Noting that each magnetic moment has to lie on a single, well defined ellipse centred at a particular value y_c, in order to achieve the limiting behaviour discussed above, the choice was made to couple the long- and short axes, a and b, respectively,

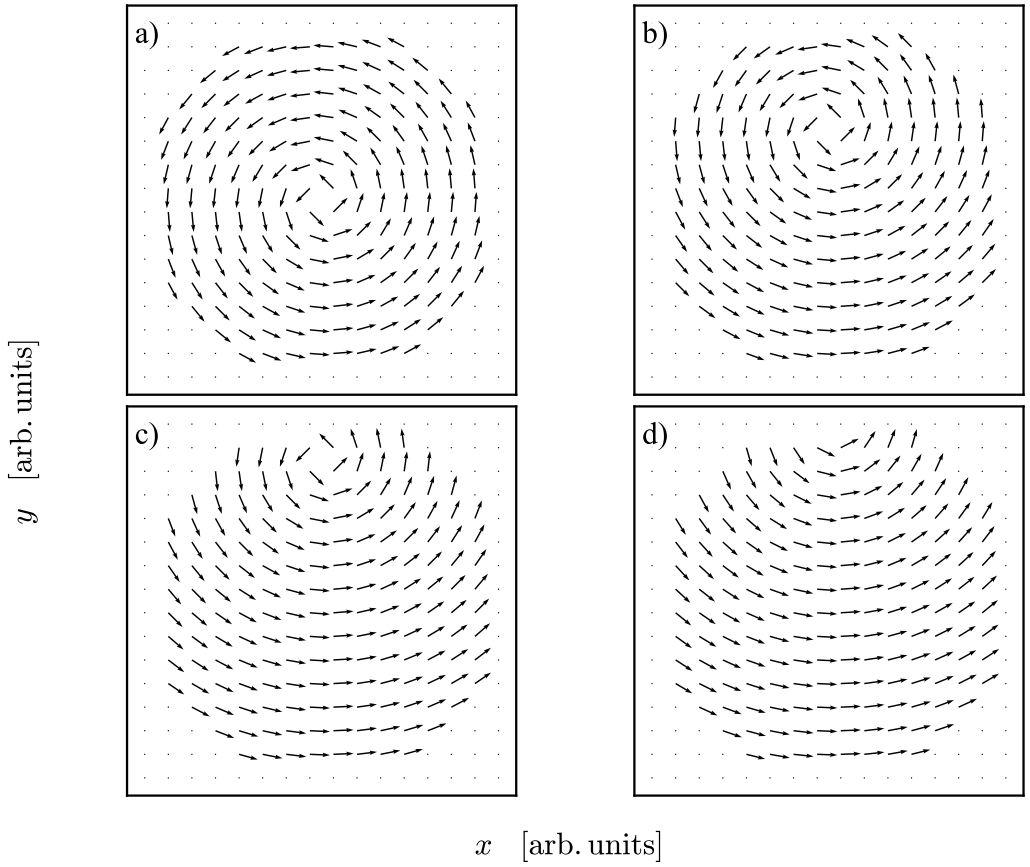

Figure 7.7: Visualisation of the rigid vortex model. Panels a) to d) show the vortices of corresponding y_c values 0, 100, 200, and 250 nm. The vortex keeps its geometry when moving over the disk, leaving behind a non-homogeneous distribution of magnetic moments when the vortex core merges with the disk walls.

of each ellipse by

$$a = \frac{b}{\sqrt{1 - y_c/R}}, \tag{7.6}$$

so that a diverges if y_c approaches the edge of the disk and $a = b$ for $y_c = 0$, i.e. a circular geometry is preserved if the vortex core is located in the middle of the disk. Furthermore, for any point x the corresponding y value of the ellipse defined by a and b is given by

$$y = \pm\frac{b}{a}\sqrt{a^2 - x^2}. \tag{7.7}$$

Rearranging eq. 7.7, inserting eq. 7.6 and including the shift of the vortex core by y_c provides

$$b = \sqrt{(y - y_c)^2 + \frac{x^2(R - y_c)}{R}}, \tag{7.8}$$

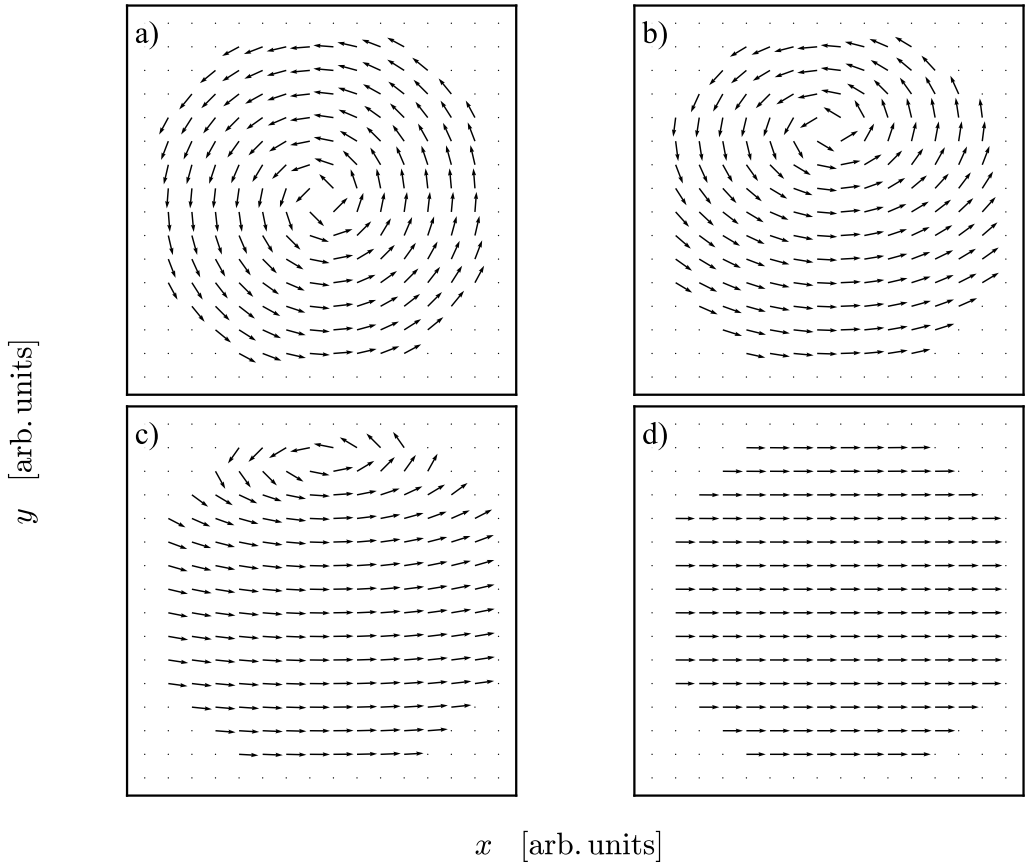

Figure 7.8: Visualisation of the elliptical vortex model. Panels a) to d) show the vortices of corresponding y_c values 0, 100, 200, and 250 nm. Being located in the disk centre, the vortex is perfectly circular, while getting increasing elliptical when approaching the island edges. Once the vortex merges with the edge, its eccentricity diverges to infinity, leading to a fully magnetised disk.

so that it follows

$$\phi = \arctan\left(\frac{xb^2}{-(y-y_c)a^2}\right) \tag{7.9a}$$

$$m_x = \begin{cases} \mp\sin(\phi) & \text{if } r \leq R \\ 0 & \text{else} \end{cases} \tag{7.9b}$$

$$m_y = \begin{cases} \pm\cos(\phi) & \text{if } r \leq R \\ 0 & \text{else} \end{cases}. \tag{7.9c}$$

Fig. 7.8 presents a visualisation of the vortex geometry for a vortex translating along

the y-direction from the centre of the disk to its edge in this elliptical model.

7.3.3 Calculating Scattering Amplitudes

Once the vortex geometry has been defined, the charge- and magnetic scattering amplitudes are calculated numerically via a Riemann sum over the product of the product of the local SLD and the corresponding phase factors according to

$$A^{\mathrm{ch}}(\mathbf{Q}) = \sum_{x,y} SLD^{\mathrm{ch}}(x,y)\, \mathrm{e}^{-i(xQ_x+yQ_y)} \tag{7.10a}$$

$$\begin{aligned} A^{\mathrm{mag}}(\mathbf{Q}) &= \sum_{x,y} SLD^{\mathrm{mag}}(x,y)\, \mathrm{e}^{-i(xQ_x+yQ_y)} \\ &= \sum_{x,y} SLD_0^{\mathrm{mag}}\, m_x(x,y)\, \mathrm{e}^{-i(xQ_x+yQ_y)}. \end{aligned} \tag{7.10b}$$

Once the scattering amplitudes are defined, the scattered intensity is calculated via

$$I^{\pm} = (A^{\mathrm{ch}} \pm A^{\mathrm{mag}})(A^{\mathrm{ch}} \pm A^{\mathrm{mag}})^* \tag{7.11}$$

it is straightforward to calculate the asymmetry ratio according to eq. 2.33.

7.4 Fitting of the Experimental Data

In order to differentiate which vortex model reflects the magnetic structure of the islands more closely, it was decided to fit the asymmetry ratio loops measured at 30 K. Unfortunately, after normalising the data as seen in Fig. 7.6 b), the A.R. of the magnetisation loops looks relatively similar at each measured diffraction order. However, it was still considered insightful to investigate in how far the two vortex models would differ in reproducing the magnetisation loop at the respective diffraction orders.

Note that neither in experiment or in simulating the scattered signal did the chirality of the vortices have to be considered, since restricting to the scattering plane (implying $Q_y = 0$) rendered the scattered signal insensitive to the y component of the scattering phase factor, as can be seen from inspection of eq. 7.10 b). Since the projection onto the x-axis is identical for both vortex chiralities, they both lead to identical scattering amplitudes. Consequently, all simulations of the vortex fields were restricted to anticlockwise chirality for simplicity.

In the absence of a parametrisable expression relating the externally applied field $H_{\mathrm{ext}}$to the vortex core position y_c, the $A.R.$ has to be fitted individually at all

successive values of H_{ext}. However, at each value of H_{ext} the normalised *A.R.* will always be accessible by *some* vortex core position y_c, so that a magnetisation loop corresponding to a specific diffraction order can necessarily be fitted by *any* vortex model. The solution, of course, is to fit the *A.R.* of all experimentally determined diffraction orders simultaneously for each individual value of H_{ext}. This way, a unique value y_c of a vortex is fitted to simultaneously match the corresponding *A.R.* of *all* diffraction orders, therefore adding specificity to the fit. In effect, the quality of the fit is indicative of the resemblance of the used model and the real vortex. As an additional result, y_c is tracked as a function of the (experimental) H_{ext}, allowing to reproduce the traversal of the vortex over the disk. Fig. 7.9 present the results from fitting the two vortex models to the experimental data. Panels a) and b) show the direct fits of the experimentally determined *A.R.* by the rigid and elliptical vortex models, respectively, while panels c) and d) show the corresponding vortex core positions y_c that fit the experimental data best. Both models are able to reproduce the 0^{th} and -8^{th} diffraction orders reasonably well, but the elliptical model is fitting the -1^{st} diffraction order clearly better. In particular, unlike the rigid vortex model, the elliptical vortex fits the dip around 40 mT. Furthermore, in order to fit the data the rigid vortex core had to extent far beyond the disk edge in order to obtain a reasonable collinear state of magnetic moments necessary to obtain the saturation values of ± 1, which constitutes a clearly unphysical behaviour.

In summary, the elliptical vortex model is (not unexpectedly) found to fit the experimental observations better than the naïve rigid vortex, but more importantly, this result shows that XRMS is principally providing sufficient spatial sensitivity to local magnetic moments needed to resolve the internal magnetic structure of patterned elements. Unfortunately, the diffraction orders that the magnetisation loops were performed on turned out to not provide the highest degree of sensitivity towards the underlying vortex geometry, since the Fourier components have to resonate with the characteristic length scales of the vortex geometry. Performing the magnetisation loops on different diffraction orders is therefore believed to provide a higher degree of specificity of experimental data, allowing a more detailed picture of the internal magnetic structure of patterned elements as will be discussed in the following section.

7.5 Proposal for Future Studies

In the previous sections it was demonstrated that XRMS does provide sufficient sensitivity to differentiate internal magnetic states of nano-patterned elements. How-

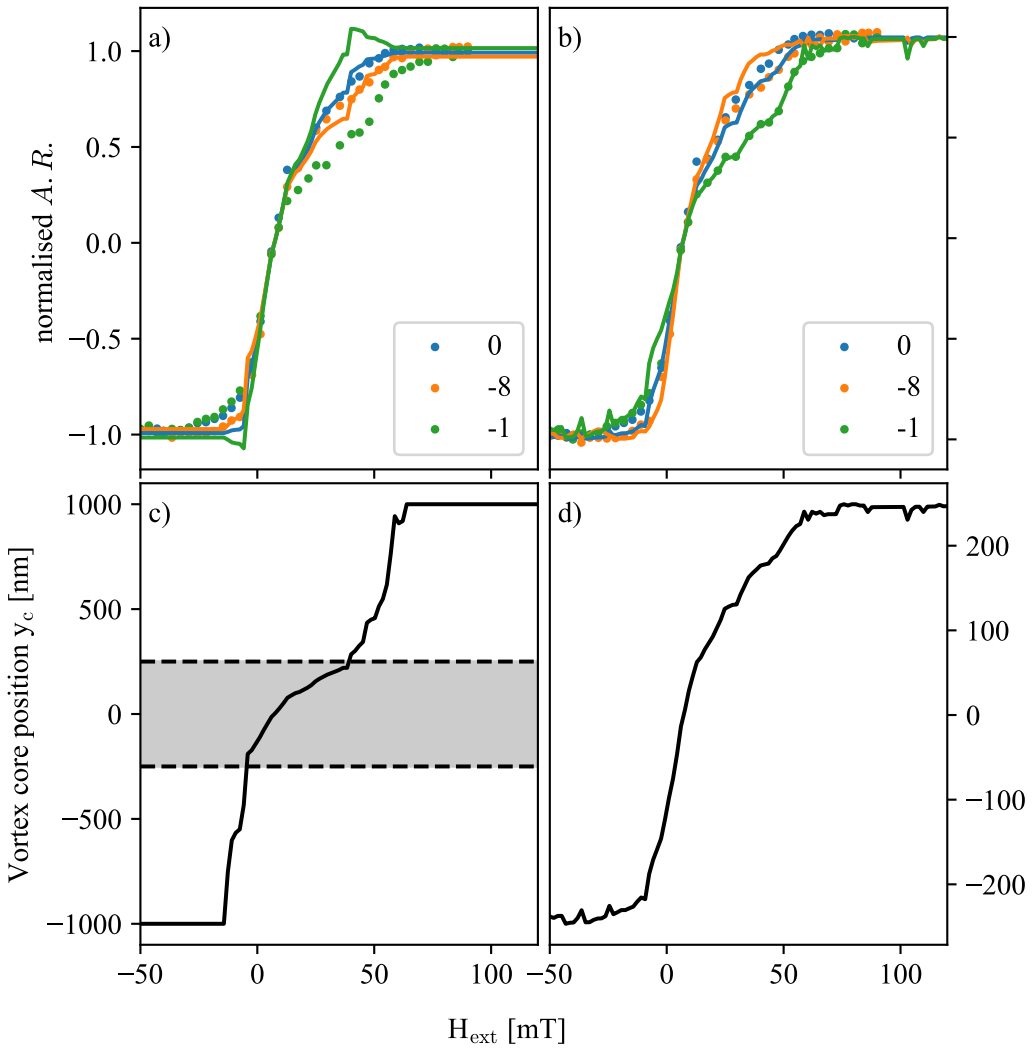

Figure 7.9: Fits (solid lines) and experimental data (symbols) of the normalised asymmetry ratio following a magnetisation loop in panels and corresponding location y_c of the vortex core. Panels a) and c) correspond to the rigid vortex model, while panels b) and d) correspond to the elliptical vortex model. Additionally to the physically unreasonable values of y_c in case of the rigid vortex (the physical dimensions of the disk are indicated by the shaded region in panel c), the elliptical vortex provides a better fit of the experimental data.

ever, it remained unclear whether the choice of the diffraction orders used at which the magnetisation loops were performed on was a good choice from the point of view of maximising the specificity of the experimental data. Since the elliptical vortex has been identified to match closer the experimental observations, the following discussion will be limited to this model.

Fig. 7.10 shows simulations of the asymmetry ratio as a function of the vortex core position y_c. For clarity, Fig. 7.10 a) shows diffraction orders zero to four, while panel b) shows orders five to nine. Obviously, the lower diffraction orders show a much higher degree of variability and therefore provide more specificity towards the exact vortex geometry, while starting with diffraction order five, the $A.R.$ basically lost any distinguishing features and essentially tracks the zero order $A.R.$ again. The zero order diffraction peak measures the average magnetisation of a disk and adding too many Fourier components at high diffraction orders appears to basically restore the magnetisation averaging by probing the disk at a length scale that is too small to provide useful information. On the other hand, the fewer Fourier components of the lower diffraction orders do provide sensitivity length scales relevant for resolving the vortex geometry, and are therefore much more distinct from each other. Because of the relatively little obtained information, it must therefore be considered unfortunate to have performed the experimental measurements on orders 0, -l, and ±8. Keeping

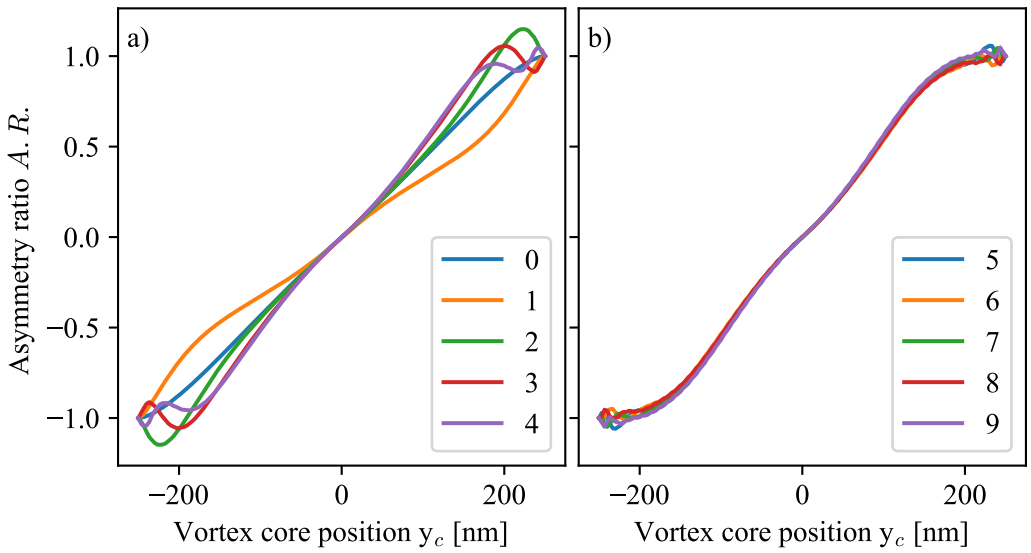

Figure 7.10: Asymmetry ratio of multiple diffraction orders in Q_x, measured within the scattering plane ($Q_y = 0$). The low diffraction orders seen in panel a) are found to exhibit a higher degree of specificity than diffraction orders ≥ 5 seen in panel b).

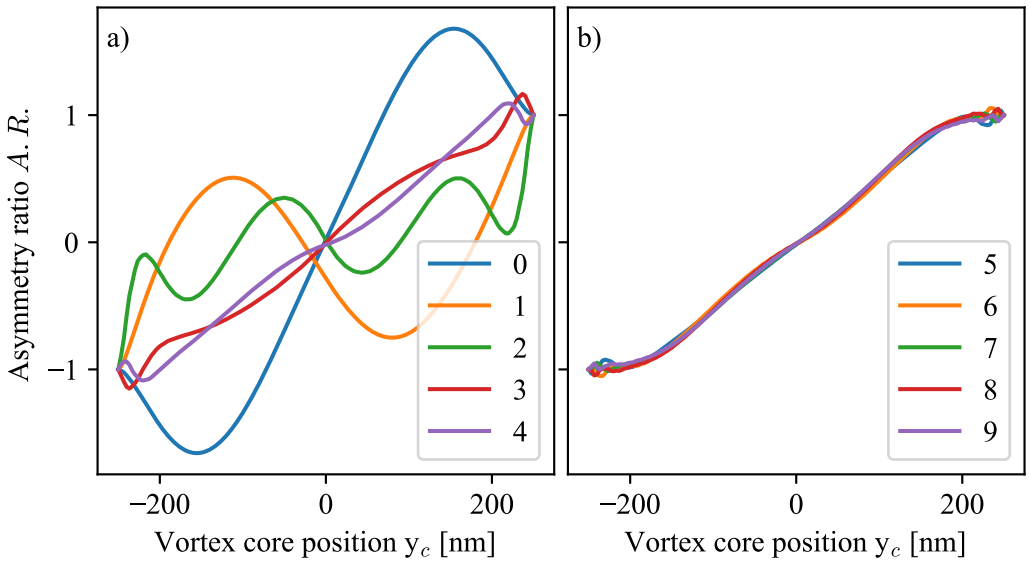

Figure 7.11: Asymmetry ratio of multiple diffraction orders in Q_x, measured out of the scattering plane at the first out-of-plane diffraction order ($Q_y = 1 \times 2\pi/d_{\mathrm{latt}}$). The low diffraction orders seen in panel a) are found to exhibit a higher degree of specificity than diffraction orders ≥ 5 seen in panel b).

in mind the additional complications in interpreting the consequences of the doming of the patterned islands as discussed in chapter 5, identifying the optimal diffraction orders for maximising the information content of the experimental data required extended analysis and could not have been anticipated at the time of the experiment.

The situation is even clearer, when the signal is detected outside of the scattering plane, i.e. Q_y takes on finite values. As seen in Fig. 7.11 a), when measuring multiple diffraction orders in Q_x but fixing the component of the wavevector transfer perpendicular to the scattering plane to the 1$^{\mathrm{st}}$ diffraction order, i.e. $Q_y = 2\pi/d_{\mathrm{latt}}$, the $A.R.$ as obtained form the magnetisation loop shows distinct features, that are found to be highly sensitive to to the exact distribution of magnetic moments, whereas orders ≥ 5 seen in Fig. 7.11 b) are, again, not showing significant sensitivity but are found to essentially reproduce a linear dependency of the $A.R.$ towards scanning the vortex core over the disk. Since it was shown earlier that the detected $A.R.$ was already sufficiently sensitive in order to resolve the rather subtle differences between the 0$^{\mathrm{th}}$ and 1$^{\mathrm{st}}$ diffraction order seen in Fig. 7.10, the immensely amplified relative differences between the first five diffraction orders seen in Fig. 7.11 a) are believed to be resolved well in experiment, while it was shown in chapter 6 that non-zero diffraction orders in Q_y are well resolvable using the GISAXS geometry if

sufficient perpendicular beam coherence is ensured.

Obviously, on finite values of Q_y the degeneracy of the clockwise and anti-clockwise vortex chirality with respect to the $A.R.$ is lifted, so that an equal distribution of both vortex chiralities has to be considered in the subsequent data analysis. Alternatively, asymmetric island geometries that favour one island side for the nucleation of a magnetic vortex[31, 240] might help in avoiding the problem of state degeneracy similar to the approach taken by Lee et al. [28].

7.6 Summary

In this chapter the formation of magnetic vortices within a patterned array of nanoscopic disks was discussed. Magnetically sensitive experiments utilising diffractive XRMS were performed exploiting the energy selectivity of synchrotron radiation. Experimental results, detecting how magnetic vortices affect the asymmetry ratio of rocking curves and magnetisation loops at fixed positions in reciprocal space, indicated a principal sensitivity of the $A.R.$ towards the vortex geometry depending on the detected diffraction order of the array.

Two analytical vortex models were introduced, the first representing a rigid vortex, while the second modelled the vortex in a dynamical way, taking on an increasingly elliptical geometry the closer the vortex core approaches the edge of the patterned elements. Fitting the experimental data using a numerical evaluation of the charge- and magnetism induced scattering factors A^{ch} and A^{mag}, respectively, the elliptical model has been found to reproduce the experimental findings more accurately, although micromagnetic simulations strongly suggest a complex geometry of the distribution of local magnetic moments, particularly around the nucleation and annihilation field values H_{n} and H_{an}.

As an important finding for future studies it was then shown how XRMS measurements at diffraction orders outside the scattering plane are expected to significantly improve the spatial resolution magnetic vortices can be resolved in. To this end, the experimental design should ensure the measurement to non-zero but low diffraction orders in both Q_x and Q_y, since at these orders the sensitivity of the x-rays to the relevant length-scales of magnetic vortices is maximised.

Chapter 8

Conclusion

Over last two decades, lithographically patterned arrays have become increasingly interesting to researchers, specifically with respect to the magnetic interactions between individual patterned nano-islands. However, experiments have often been limited to real-space analysis techniques. Arguably, one of the reasons for the lack of research focussing on quantitative analysis of x-ray scattering of patterned arrays, are the hardship often faced when applying reciprocal space analysis on three-dimensional sample structures of mesoscopic structure sizes. This work provided new insight into x-ray resonant magnetic scattering from patterned arrays. A modelling framework for future application was developed and has been used on specific experimental data, allowing one to resolve spatially the internal chemical- and magnetic structure of individual patterned elements.

Moreover, while it could be argued that diffraction of patterned arrays merely constitutes an extension to classical x-ray diffraction and that theoretical frameworks for dealing with x-ray scattering from patterned arrays already exist, these frameworks have been found to be limited in practical applicability. Traditional theoretical frameworks usually assume the sample model to be formulated in a fully analytical fashion, allowing for the application of certain mathematical operations, like advanced Fourier analysis etc. However, the high spatial sensitivity of resonant x-rays may often be found to render such analytical models too simple, instead requiring numeric modelling to allow for the often ill-defined geometry of real patterned structures. Inclusion of magnetic sensitivity is furthermore rarely considered within the previously developed body of work and is usually limited to comparatively simple cases.

Furthermore, in a very practical way, so far no openly available software packages exist that provide the necessary functionality to perform modelling of pat-

terned arrays as well as fitting experimental data obtained from x-ray scattering. Therefore, a huge amount of time and experience had to be devoted to the development of a scattering framework incorporating all the peculiarities of patterned arrays, while providing a modular structure that avoids the need of re-coding huge parts of the project whenever demands change slightly, such as the introduction of a new kind of scattering geometry. The latter requires restructuring of a very specific part of the underlying computational logic. Without a clearly structured code-base, as the one presented in Fig. 1.1, the high complexity and interrelatedness of different kinds of data can quickly bring a stop to a project or demand many additional hours of working out a particular code design. The structure of the framework developed is believed to allow any investigator to avoid many of the pitfalls and hardships that had to be faced before the empirically proved design eventually emerged.

The studies of chapter 4 focussed on the impact of x-ray coherence. The large lateral dimensions of patterned arrays mean that coherence effects are more likely to be relevant compared to, say, diffraction of atomic lattices. Following the traditional (and often implicit) convention of assuming the beam coherence to be large compared to the structure size of the scattering lattice, effectively renders the beam coherence entering the expression of the scattered intensity as a constant scaling factor, which is usually dropped or incorporated into other scaling factors. However, this is not true under conditions of low beam coherence, i.e. when the projection of the coherently scattering area onto the sample surface is of the order of the array unit cell, either within or perpendicular to the scattering plane. Neglecting coherence effects, the experimentally measured rocking curves could not be reproduced. The reason, as was demonstrated, is that low beam coherence, especially perpendicular to the scattering plane, implies a softening of the diffraction condition from being a two- to essentially a one dimensional problem, leading to a significant widening of grating truncation *rods* into diffraction *planes*. Therefore, most of the experimentally observed diffraction peaks could not be reproduced when neglecting low-coherence effects, specifically because without the widening associated with a low spatial coherence, the well defined positions of the GTRs in reciprocal space never intersected the detector resolution function R. It was further shown how the convolution theorem was used in order to adapt classical diffraction theory to a more generalised form, specifically incorporating arbitrary values of the x-ray beam coherence. Using modifications of Bessel functions to approximate the structure factor $F(\mathbf{Q}_{\|})$ of the circular and elliptical patterned islands, simulation and experiment started to show resemblance of each other. However, only after dropping the (so far very convenient) analytical expression of $F(\mathbf{Q}_{\|})$ in favour of a

computationally much more demanding approach modelling the spatial structure of the island surface on a numerical grid, satisfying agreement between simulation and experiment has been obtained. The results are therefore found to be an important proof of concept, highlighting both the importance of considering beam coherence effects when conducting investigations of patterned arrays as well as the exceptional spatial sensitivity of x-ray diffraction of patterned arrays.

In the studies concerning beam coherence, the relatively simple two-dimensional model of the sample only allowed for simulating rocking curves, which are naturally very insensitive to the depth profile of a patterned array. On the other hand it is exactly these SLD depth profiles that x-ray reflectivity measurements are sensitive to, therefore complementing rocking measurements. The modelling of the SLD depth profile was conducted by using the freely available GenX software package, a tool originally designed for simulating x-ray reflectivity of stratified media. The two very different sample models – the two-dimensional binary representation of the lateral array structure and the one-dimensional SLD depth profile – were fitted individually and provided consistent results. However, it was quickly realised how a unified model of the sample, capturing the three-dimensional structure of patterned elements on a sufficient spatial resolution, would open up the possibilities of fitting arbitrary scans through reciprocal space.

Formulating this three dimensional model is at the core of chapter 5, incorporating the chemical- and magnetic structure of a patterned island. At the same time the model had to be computationally fast enough to be used in a fitting procedure, which often requires hundreds of thousands of simulation cycles. Experimenting with different approaches, the final model was found to consist of a semi-analytical approach, slicing the spatial model of the sample into arbitrarily thin slices parallel to the sample surface. Each horizontal slice then consisted of an arbitrary number of circular "shells", exploiting the rotational symmetry of the islands, with each shell representing the (rotationally invariant) local chemical and magnetic state of the patterned element. Within this approach the sample is essentially disassembled into the superposition of cylindrical sections, the individual scattering amplitudes of which can be calculated analytically, before the total scattering amplitude is calculated numerically from the superposition principle.

Simulation of single measurements was found to be reasonably fast ($< 1\,\mathrm{s}$), yet fitting the highly complex inter-related parameter space turned out to regularly require extended periods of time often found in the range of up to multiple days before parameter convergence. Only after performing a meta-analysis, optimising the algorithmic fitting parameters of the underlying differential evolution framework,

the fitting procedure was found to be of sufficient robustness to ensure avoiding misconvergence of the fit into local minima of the (highly coupled) parameter space. It was possible to determine the chemical structure and distribution of local magnetic moments of the patterned islands in a magnetically saturated state via the simultaneous fitting of a combination of rocking curves and reflectivity data, revealing detailed insights into the (unintentional) domed structure of the patterned islands as well as the oxide layer forming on the surface of the islands, again highlighting the exceptional sensitivity of *x-ray resonant magnetic scattering* (XRMS) in characterising patterned arrays.

Fitting of the experimental data of chapter 5 was somewhat hindered by the limited amount of information found in the finite number of diffraction peaks contained in a single rocking curve measurement. Each diffraction peak essentially provides only a single sampling of the structure factor $F(\mathbf{Q})$, therefore providing only limited insight into the underlying structure of the scattering unit cell. Under these conditions, it has to actually be considered fortunate that the rocking curve measurements have been performed in the open detector geometry, since despite significantly complicating the analysis, the Q_z dependence of $F(\mathbf{Q})$ encoded within the tilt of the diffraction peaks provided additional information about the sample structure. However, the same information could have been obtained more easily by taking additional rocking curve measurements with a detector slit in place.

An alternative to this time-consuming data acquisition process has been found by changing the scattering geometry to *grazing-incidence small-angle x-ray scattering* (GISAXS) measurements, making use of the rapid integration of huge volumes of reciprocal space associated with two-dimensional area detectors. It has been shown in chapter 6 how the previously developed scattering framework is valid for a wide range of scattering geometries, including grazing scattering angles, if the Distorted Wave Born Approximation is employed, mainly in order to incorporate refraction and multiple scattering related to x-rays reflected by the substrate. The immense number of easily obtainable diffraction peaks measured simultaneously by the GISAXS set-up provides a plethora of information to be used in data fitting. As an additional benefit, the rigid scattering geometry of GISAXS significantly simplifies data analysis, as it avoids many of the problems associated with the spatial extent of the patterning in relation to the changing x-ray beam footprint on changing scattering angles.

Finally, chapter 7 presents the basics regarding investigating the internal magnetic structure of individual patterned elements, by utilising the previously observed high resolution of XRMS measurements towards the spatial distribution of

local magnetic moments. X-rays tuned to a magnetically sensitive resonance edge of the island material are known to couple to the local atomic magnetic moment. Therefore, measuring the asymmetry ratio of the scattered signals obtained from flipping the helicity of circularly polarised x-rays, in principal allows one to resolve explicit magnetic states like magnetic vortices that have been observed to constitute a demagnetisation mechanism in nano disk geometries.

Fits of the hysteresis loops considering two competing models of magnetic vortices have been compared, suggesting an elliptical deformation of the otherwise circular magnetic vortices when close to the edges of the circular islands. Unfortunately, the diffraction orders that the experiments were carried out on, did not provide sufficient sensitivity in order to uniquely resolve the magnetic structure, and the analysis therefore had to be kept at a rather basic level. It was, however, shown how even subtle changes of the internal magnetic structure of patterned elements lead to a noticeable impact upon the asymmetry ratio if diffraction orders outside of the scattering plane are being measured. The latter, again, is most easily realisable by turning towards the GISAXS geometry, although it has to be noted that the additional information content comes at the cost of lifting the degeneracy of the vortex chirality with respect to the scattered signal, which constitutes a complication that has to be considered in any subsequent analysis.

In conclusion, this work formulated a general computational framework of x-ray scattering of lithographically patterned arrays of nano- and microscopic dimensions, including the incorporation of a theory of resonant magnetic x-ray scattering. It was shown how x-ray beam coherence affects the scattered signal of patterned arrays and how beam coherence can be controlled in order to obtain a diffracted signal perpendicular to the scattering plane. It became clear how the spatial sensitivity of x-rays can be exploited in order to resolve both the chemical- as well as the magnetic structure of patterned arrays on nm resolution. The results of this work further suggest that future investigations are preferentially to be conducted using the GISAXS geometry, exploiting the high information density, rapid data acquisition time and straightforward analysis procedure, enabling quantitative, element specific, and spatially resolved insights into individual elements of patterned arrays as well as any emergent inter-element structure of interacting magnetic moments.

Bibliography

[1] Mihail Roco, Bert Müller, Ernst Wagner, Gerrit Borchard, Tiziana Di Francesco, Karolina Jurczyk, Urs Braegger, Mieczysław Jurczyk, Cecilia Bartolucci, Oluwatosin Ijabadeniyi, et al. *Nanoscience and Nanotechnology: Advances and Developments in Nano-sized Materials*. Walter de Gruyter GmbH & Co KG, 2018.

[2] Gabor L Hornyak, John J Moore, Harry F Tibbals, and Joydeep Dutta. *Fundamentals of nanotechnology*. CRC press, 2018.

[3] Marc J Madou. *Fundamentals of Microfabrication and Nanotechnology, Three-Volume Set*. CRC Press, 2018.

[4] Jitendra S Sangwai. *Nanotechnology for Energy and Environmental Engineering*. Springer, 2020.

[5] Challa SSR Kumar, Josef Hormes, and Carola Leuschner. *Nanofabrication towards biomedical applications: techniques, tools, applications, and impact*. John Wiley & Sons, 2006.

[6] Volkmar Weissig and Tamer Elbayoumi. *Pharmaceutical Nanotechnology: Basic Protocols*. Springer, 2019.

[7] Mahendra Rai. *Nanotechnology in Skin, Soft Tissue, and Bone Infections*. Springer, 2020.

[8] Alka Dwevedi. *Solutions to Environmental Problems Involving Nanotechnology and Enzyme Technology*. Academic Press, 2018.

[9] Devarajan Thangadurai, Jeyabalan Sangeetha, and Ram Prasad. *Nanotechnology for Food, Agriculture, and Environment*. Springer, 2020.

[10] Zeynep Altintas. *Biosensors and nanotechnology: applications in health care diagnostics*. John Wiley & Sons, 2017.

[11] H. Namatsu, M. Nagase, K. Kurihara, K. Iwadate, T. Furuta, and K. Murase. Fabrication of sub-10-nm silicon lines with minimum fluctuation. *Journal of Vacuum Science and Technology B: Microelectronics and Nanometer Structures*, 13(4):1473–1476, jul 1995. ISSN 0734211X. doi: 10.1116/1.588174.

[12] M. Winzer, M. Kleiber, N. Dix, and R. Wiesendanger. Fabrication of nano-dot- and nano-ring-arrays by nanosphere lithography Rapid communication. *Applied Physics A: Materials Science and Processing*, 63(6):617–619, 1996. ISSN 09478396. doi: 10.1007/bf01567218.

[13] Peter R. Krauss and Stephen Y. Chou. Sub-10 nm imprint lithography and applications. In *Annual Device Research Conference Digest*, pages 90–91. IEEE, 1997. doi: 10.1116/1.589752.

[14] Te Hua Fang, Cheng I. Weng, and Jee Gong Chang. Machining characterization of the nano-lithography process using atomic force microscopy. *Nanotechnology*, 11(3):181–187, sep 2000. ISSN 09574484. doi: 10.1088/0957-4484/11/3/308.

[15] B. Michel, A. Bernard, A. Bietsch, E. Delamarche, M. Geissler, D. Juncker, H. Kind, J. P. Renault, H. Rothuizen, H. Schmid, P. Schmidt-Winkel, R. Stutz, and H. Wolf. Printing meets lithography: Soft approaches to high-resolution printing. *IBM Journal of Research and Development*, 45(5): 697–719, 2001. ISSN 00188646. doi: 10.1147/rd.455.0697. URL `https://www.researchgate.net/publication/224103182`.

[16] Xudong Wang, Christopher J. Summers, and Zhong Lin Wang. Large-scale hexagonal-patterned growth of aligned ZnO nanorods for nano-optoelectronics and nanosensor arrays. *Nano Letters*, 4(3):423–426, 2004. ISSN 15306984. doi: 10.1021/nl035102c.

[17] Ryan van Dommelen, Paola Fanzio, and Luigi Sasso. Surface self-assembly of colloidal crystals for micro- and nano-patterning, jan 2018. ISSN 00018686.

[18] Wei Chen and Haroon Ahmed. Fabrication of 5-7 nm wide etched lines in silicon using 100 keV electron-beam lithography and polymethylmethacrylate resist. *Applied Physics Letters*, 62(13):1499–1501, 1993. ISSN 00036951. doi: 10.1063/1.109609. URL `http://apl.aip.org/apl/copyright.jsp`.

[19] J. A.M. Sondag-Huethorst, H. R.J. Van Helleputte, and L. G.J. Fokkink. Generation of electrochemically deposited metal patterns by means of electron

beam (nano)lithography of self-assembled monolayer resists. *Applied Physics Letters*, 64(3):285–287, 1994. ISSN 00036951. doi: 10.1063/1.111182.

[20] C. Vieu, F. Carcenac, A. Pépin, Y. Chen, M. Mejias, A. Lebib, L. Manin-Ferlazzo, L. Couraud, and H. Launois. Electron beam lithography: Resolution limits and applications. *Applied Surface Science*, 164(1-4):111–117, 2000. ISSN 01694332. doi: 10.1016/S0169-4332(00)00352-4. URL `www.elsevier.nlrlocaterapsusc`.

[21] Ampere A. Tseng, Kuan Chen, Chii D. Chen, and Kung J. Ma. Electron beam lithography in nanoscale fabrication: Recent development. *IEEE Transactions on Electronics Packaging Manufacturing*, 26(2):141–149, 2003. ISSN 1521334X. doi: 10.1109/TEPM.2003.817714.

[22] A. E. Grigorescu and C. W. Hagen. ZResists for sub-20-nm electron beam lithography with a focus on HSQ: State of the art, 2009. ISSN 09574484. URL `http://iopscience.iop.org/0957-4484/20/29/292001`.

[23] M. A. Bruk, E. N. Zhikharev, A. E. Rogozhin, D. R. Streltsov, V. A. Kalnov, S. N. Averkin, and A. V. Spirin. Formation of micro- A nd nanostructures with well-rounded profile by new e-beam lithography principle. *Microelectronic Engineering*, 155:92–96, 2016. ISSN 01679317. doi: 10.1016/j.mee.2016.03.017. URL `https://www.sciencedirect.com/science/article/pii/S0167931716301307`.

[24] Yibo Lin, Bei Yu, Yi Zou, Zhuo Li, Charles J. Alpert, and David Z. Pan. Stitch aware detailed placement for multiple E-beam lithography. *Integration, the VLSI Journal*, 58:47–54, jun 2017. ISSN 01679260. doi: 10.1016/j.vlsi.2017.02.004.

[25] Martin Drost, Fan Tu, Luisa Berger, Christian Preischl, Wencai Zhou, Hartmut Gliemann, Christof Wöll, and Hubertus Marbach. Surface-Anchored Metal-Organic Frameworks as Versatile Resists for Gas-Assisted E-Beam Lithography: Fabrication of Sub-10 Nanometer Structures. *ACS Nano*, 12 (4):3825–3835, apr 2018. ISSN 1936086X. doi: 10.1021/acsnano.8b01071.

[26] K. Yu Guslienko, V. Novosad, Y. Otani, H. Shima, and K. Fukamichi. Field evolution of magnetic vortex state in ferromagnetic disks. *Applied Physics Letters*, 78(24):3848–3850, 2001. ISSN 00036951. doi: 10.1063/1.1377850.

[27] M. Goiriena-Goikoetxea, K. Y. Guslienko, M. Rouco, I. Orue, E. Berganza, M. Jaafar, A. Asenjo, M. L. Fernández-Gubieda, L. Fernández Barquín, and

A. García-Arribas. Magnetization reversal in circular vortex dots of small radius. *Nanoscale*, 9(31):11269–11278, 2017. ISSN 20403372. doi: 10.1039/c7nr02389h.

[28] Min Sang Lee, Andreas Westphalen, Arndt Remhof, Alexandra Schumann, and Harmut Zabel. Extended longitudinal vector and Bragg magneto-optic Kerr effect for the determination of the chirality distribution in magnetic vortices. *Journal of Applied Physics*, 103(9), 2008. ISSN 00218979. doi: 10.1063/1.2919160.

[29] Konstantin Yu Guslienko and Konstantin L. Metlov. Evolution and stability of a magnetic vortex in a small cylindrical ferromagnetic particle under applied field. *Physical Review B - Condensed Matter and Materials Physics*, 63(10): 4, 2001. ISSN 1550235X. doi: 10.1103/PhysRevB.63.100403.

[30] Sven Velten, Robert Streubel, Alan Farhan, Noah Kent, Mi Young Im, Andreas Scholl, Scott Dhuey, Carolin Behncke, Guido Meier, and Peter Fischer. Vortex circulation patterns in planar microdisk arrays. *Applied Physics Letters*, 110(26), 2017. ISSN 00036951. doi: 10.1063/1.4990990.

[31] P. Vavassori, R. Bovolenta, V. Metlushko, and B. Ilic. Vortex rotation control in Permalloy disks with small circular voids. *Journal of Applied Physics*, 99 (5):1–7, 2006. ISSN 00218979. doi: 10.1063/1.2174115.

[32] P. Vavassori, M. Grimsditch, V. Metlushko, N. Zaluzec, and B. Ilic. Magnetoresistance of single magnetic vortices. *Applied Physics Letters*, 86(7): 1–3, 2005. ISSN 00036951. doi: 10.1063/1.1866212. URL `https://www.researchgate.net/publication/239751705`.

[33] Matthew T. Bryan, Thomas Schrefl, Del Atkinson, and Dan A. Allwood. Magnetic domain wall propagation in nanowires under transverse magnetic fields. *Journal of Applied Physics*, 103(7), 2008. ISSN 00218979. doi: 10.1063/1.2887918.

[34] David M. Burn and Del Atkinson. Suppression of Walker breakdown in magnetic domain wall propagation through structural control of spin wave emission. *Applied Physics Letters*, 102(24), 2013. ISSN 00036951. doi: 10.1063/1.4811750.

[35] Ki Suk Lee, Sangkook Choi, and Sang Koog Kim. Radiation of spin waves from magnetic vortex cores by their dynamic motion and annihilation processes.

Applied Physics Letters, 87(19):1–3, 2005. ISSN 00036951. doi: 10.1063/1.2128478.

[36] Carolin Behncke, Christian F. Adolff, Nicolas Lenzing, Max Hänze, Benedikt Schulte, Markus Weigand, Gisela Schütz, and Guido Meier. Spin-wave interference in magnetic vortex stacks. *Communications Physics*, 1(1):1–6, 2018. ISSN 23993650. doi: 10.1038/s42005-018-0052-1. URL `http://dx.doi.org/10.1038/s42005-018-0052-1`.

[37] Seonghoon Woo, Tristan Delaney, and Geoffrey S.D. Beach. Magnetic domain wall depinning assisted by spin wave bursts. *Nature Physics*, 13(5):448–454, 2017. ISSN 17452481. doi: 10.1038/nphys4022.

[38] J. P. Morgan, C. J. Kinane, T. R. Charlton, A. Stein, C. Sánchez-Hanke, D. A. Arena, S. Langridge, and C. H. Marrows. Magnetic hysteresis of an artificial square ice studied by in-plane Bragg xray resonant magnetic scattering. *AIP Advances*, 2(2), 2012. ISSN 21583226. doi: 10.1063/1.4732147.

[39] I. A. Chioar, B. Canals, D. Lacour, M. Hehn, B. Santos Burgos, T. O. Menteş, A. Locatelli, F. Montaigne, and N. Rougemaille. Kinetic pathways to the magnetic charge crystal in artificial dipolar spin ice. *Physical Review B - Condensed Matter and Materials Physics*, 90(22):1–5, 2014. ISSN 1550235X. doi: 10.1103/PhysRevB.90.220407.

[40] Benjamin Canals, Ioan Augustin Chioar, Van Dai Nguyen, Michel Hehn, Daniel Lacour, François Montaigne, Andrea Locatelli, Tevfik Onur Menteş, Benito Santos Burgos, and Nicolas Rougemaille. Fragmentation of magnetism in artificial kagome dipolar spin ice. *Nature Communications*, 7 (May):11446, 2016. ISSN 20411723. doi: 10.1038/ncomms11446. URL `http://www.nature.com/doifinder/10.1038/ncomms11446`.

[41] Vassilios Kapaklis, Unnar B. Arnalds, Alan Farhan, Rajesh V. Chopdekar, Ana Balan, Andreas Scholl, Laura J. Heyderman, and Björgvin Hjörvarsson. Thermal fluctuations in artificial spin ice. *Nature Nanotechnology*, 9(7):514–519, 2014. ISSN 17483395. doi: 10.1038/nnano.2014.104. URL `https://ui.adsabs.harvard.edu/abs/2015APS..MAR.H1133S/abstract`.

[42] Henry Stopfel, Erik Östman, Ioan Augustin Chioar, David Greving, Unnar B. Arnalds, Thomas P.A. Hase, Aaron Stein, Björgvin Hjörvarsson, and Vassilios Kapaklis. Magnetic order and energy-scale hierarchy in artificial spin-

ice structures. *Physical Review B*, 98(1):1–8, 2018. ISSN 24699969. doi: 10.1103/PhysRevB.98.014435.

[43] G Toulouse et al. Theory of the frustration effect in spin glasses: I. *Spin Glass Theory and Beyond: An Introduction to the Replica Method and Its Applications*, 9:99, 1987.

[44] Daniel G. Nocera, Bart M. Bartlett, Daniel Grohol, Dimitris Papoutsakis, and Matthew P. Shores. Spin frustration in 2D kagomé lattices: A problem for inorganic synthetic chemistry. *Chemistry - A European Journal*, 10(16): 3850–3859, aug 2004. ISSN 09476539. doi: 10.1002/chem.200306074. URL `http://doi.wiley.com/10.1002/chem.200306074`.

[45] L. A.S. Mól, W. A. Moura-Melo, and A. R. Pereira. Conditions for free magnetic monopoles in nanoscale square arrays of dipolar spin ice. *Physical Review B - Condensed Matter and Materials Physics*, 82(5):1–6, 2010. ISSN 10980121. doi: 10.1103/PhysRevB.82.054434.

[46] C. Phatak, M. Pan, A. K. Petford-Long, S. Hong, and M. De Graef. Magnetic interactions and reversal of Artificial square spin ices. *New Journal of Physics*, 14, 2012. ISSN 13672630. doi: 10.1088/1367-2630/14/7/075028.

[47] Unnar B. Arnalds, Martina Ahlberg, Matthew S. Brewer, Vassilios Kapaklis, Evangelos Th Papaioannou, Masoud Karimipour, Panagiotis Korelis, Aaron Stein, Sveinn Ólafsson, Thomas P.A. Hase, and Björgvin Hjörvarsson. Thermal transitions in nano-patterned XY-magnets. *Applied Physics Letters*, 105(4):042409, 2014. ISSN 00036951. doi: 10.1063/1.4891479. URL `http://scitation.aip.org/content/aip/journal/apl/105/4/10.1063/1.4891479`.

[48] Oles Sendetskyi, Valerio Scagnoli, Naëmi Leo, Luca Anghinolfi, Aurora Alberca, Jan Lüning, Urs Staub, Peter Michael Derlet, and Laura Jane Heyderman. Continuous magnetic phase transition in artificial square ice. *Physical Review B*, 99(21):28–30, 2019. ISSN 24699969. doi: 10.1103/PhysRevB.99.214430.

[49] Sandra H. Skjærvø, Christopher H. Marrows, Robert L. Stamps, and Laura J. Heyderman. Advances in artificial spin ice. *Nature Reviews Physics*, 2(1): 13–28, 2020. ISSN 25225820. doi: 10.1038/s42254-019-0118-3.

[50] Gerrit van der Laan. Soft X-ray resonant magnetic scattering of magnetic nanostructures. *Comptes Rendus Physique*, 9(5-6):570–584, 2008. ISSN 16310705. doi: 10.1016/j.crhy.2007.06.004.

[51] Carlo Spezzani, Mauro Fabrizioli, Patrizio Candeloro, Enzo Di Fabrizio, Giancarlo Panaccione, and Maurizio Sacchil. Magnetic order in a submicron patterned permalloy film studied by resonant x-ray scattering. *Physical Review B - Condensed Matter and Materials Physics*, 69(22):224412, jun 2004. ISSN 01631829. doi: 10.1103/PhysRevB.69.224412. URL `http://link.aps.org/doi/10.1103/PhysRevB.69.224412`.

[52] J. Perron, L. Anghinolfi, B. Tudu, N. Jaouen, J. M. Tonnerre, M. Sacchi, F. Nolting, J. Lüning, and L. J. Heyderman. Extended reciprocal space observation of artificial spin ice with x-ray resonant magnetic scattering. *Physical Review B - Condensed Matter and Materials Physics*, 88(21):1–7, 2013. ISSN 1550235X. doi: 10.1103/PhysRevB.88.214424.

[53] J. Díaz, P. Gargiani, C. Quirós, C. Redondo, R. Morales, L. M. Álvarez-Prado, J. I. Martín, A. Scholl, S. Ferrer, M. Vélez, and S. M. Valvidares. Chiral asymmetry detected in a 2D array of permalloy square nanomagnets using circularly polarized X-ray resonant magnetic scattering. *Nanotechnology*, 31 (2):1–10, 2020. ISSN 13616528. doi: 10.1088/1361-6528/ab46d7.

[54] M. Tolan, W. Press, F. Brinkop, and J. P. Kotthaus. X-ray diffraction from laterally structured surfaces: Crystal truncation rods. *Journal of Applied Physics*, 75(12):7761–7769, 1994. ISSN 00218979. doi: 10.1063/1.356609. URL `http://scitation.aip.org/content/aip/journal/jap/75/12/10.1063/1.356609`.

[55] A. Gibaud, J. Wang, M. Tolan, G. Vignaud, and S. K. Sinha. An X-ray scattering study of laterally modulated structures: Investigation of coherence and resolution effects with a grating. *Journal de Physique I*, 6(8):1085–1094, 1996. ISSN 11554304. doi: 10.1051/jp1:1996117.

[56] D. R. Lee, Y. S. Chu, Y. Choi, J. C. Lang, G. Srajer, S. K. Sinha, V. Metlushko, and B. Ilic. Characterization of the nanostructures of a lithographically patterned dot array by x-ray pseudo-Kossel lines. *Applied Physics Letters*, 82(6):982–984, 2003. ISSN 00036951. doi: 10.1063/1.1543249. URL `https://doi.org/10.1063/1.1543249`.

[57] D. S. Eastwood, T. P.A. Hase, M. van Kampen, R. Bručas, B. Hjörvarsson, D. Atkinson, and B. K. Tanner. X-ray scattering from two-dimensionally patterned magnetic thin film nanoscale arrays. *Superlattices and Microstructures*, 41(2-3):163–167, feb 2007. ISSN 07496036. doi: 10.1016/j.spmi.2006.06.003. URL `http://linkinghub.elsevier.com/retrieve/pii/S0749603606000498`.

[58] Erich Gamma, Richard Helm, Ralph Johnson, and John Vlissides. *Design Patterns Elements of reusable object-oriented sofware*. Addison Wesley, 2009.

[59] Scipy optimize differential evolution documentation. URL `https://docs.scipy.org/doc/scipy/reference/generated/scipy.optimize.differential_evolution.html`.

[60] Christopher J. Foot et al. *Atomic physics*, volume 7. Oxford University Press, 2005.

[61] B.E. Warren. *X-Ray Diffraction*. Dover Books on Physics. Dover Publications, 2012. ISBN 9780486141619. URL `https://books.google.de/books?id=cA_EAgAAQBAJ`.

[62] Jens Als-Nielsen and Des McMorrow. *Elements of modern X-ray physics*. John Wiley & Sons, 2011.

[63] F. De Bergevin and M. Brunel. Diffraction of X-rays by magnetic materials. I. General formulae and measurements on ferro- and ferrimagnetic compounds. *Acta Crystallographica Section A*, 37(3):314–324, may 1981. ISSN 16005724. doi: 10.1107/S0567739481000739. URL `//scripts.iucr.org/cgi-bin/paper?a19658`.

[64] S.W. Lovesey and S.P. Collins. X-ray scattering and absorption by magnetic materials.(oxford series on synchrotron radiation, no. 1). *J. Synchrotron Radiation*, 5:1181–1182, 1998.

[65] V. Holy, U. Pietsch, and T. Baumbach. *High-Resolution X-Ray Scattering from Thin Films and Multilayers*. Springer Tracts in Modern Physics. Springer Berlin Heidelberg, 2014. ISBN 9783662147429. URL `https://books.google.de/books?id=oRQSswEACAAJ`.

[66] P. P. Kane, Lynn Kissel, R. H. Pratt, and S. C. Roy. Elastic scattering of γ-rays and X-rays by atoms. *Physics Reports*, 140(2):75–159, 1986. ISSN 03701573. doi: 10.1016/0370-1573(86)90018-9.

[67] John C. Henke, Burton L. and Gullikson, Eric M. and Davis. Center for X-Ray Optics. *III-Vs Review*, 18(6):43, 2005. ISSN 09611290. doi: 10.1016/s0961-1290(05)71235-7.

[68] Gilles Renaud, Rémi Lazzari, and Frédéric Leroy. Probing surface and interface morphology with Grazing Incidence Small Angle X-Ray Scattering. *Surface Science Reports*, 64(8):255–380, 2009. ISSN 01675729. doi: 10.1016/j.surfrep.2009.07.002. URL `http://dx.doi.org/10.1016/j.surfrep.2009.07.002`.

[69] J. P. Hill and D. F. Mcmorrow. X-ray resonant exchange scattering: Polarization dependence and correlation functions. *Acta Crystallographica Section A: Foundations of Crystallography*, 52(2):236–244, 1996. ISSN 01087673. doi: 10.1107/S0108767395012670. URL `http://discovery.ucl.ac.uk/136142/`.

[70] J. P. Hannon, G. T. Trammell, M. Blume, and Doon Gibbs. X-ray Resonance Exchange Scattering (XRES). *Hyperfine Interactions*, 50(1-4):477–479, 1989. ISSN 03043834. doi: 10.1007/BF02407679.

[71] K. Chesnel, M. Belakhovsky, S. Landis, J. C. Toussaint, S. P. Collins, G. van der Laan, E. Dudzik, and S. S. Dhesi. X-ray resonant magnetic scattering study of the magnetic coupling in Co/Pt nanolines and its evolution under magnetic field. *Physical Review B - Condensed Matter and Materials Physics*, 66(2):244351–244359, 2002. ISSN 01631829. doi: 10.1103/PhysRevB.66.024435.

[72] C.T. Chantler, K. Olsen, R.A. Dragoset, J. Chang, A.R. Kishore, S.A. Kotochigova, and D.S. Zucker. Detailed tabulation of atomic form factors, photoelectric absorption and scattering cross section, and mass attenuation coefficients for z= 1–92 from e= 1–10 ev to e= 0.4–1.0 mev. *NIST, http://www.nist. gov/pml/data/ffast/index. cfm*, 2005.

[73] Gilles Renaud. Oxide surfaces and metal/oxide interfaces studied by grazing incidence X-ray scattering. *Surface Science Reports*, 32(1-6):5–90, 1998. ISSN 01675729. doi: 10.1016/s0167-5729(98)00005-3.

[74] Matts Björck, Matthew S. Brewer, Unnar B. Arnalds, Erik östman, Martina Ahlberg, Vassilios Kapaklis, Evangelos Th. Papaioannou, Gabriella Andersson, Björgvin Hjörvarsson, and Thomas P. A. Hase. Reflectivity Studies of Magnetic Heterostructures. *Journal of Surfaces and Interfaces of Materials*, 2(1):24–32, mar 2014. ISSN 21647542. doi: 10.1166/

jsim.2014.1032. URL http://openurl.ingenta.com/content/xref?genre=article{&}issn=2164-7542{&}volume=2{&}issue=1{&}spage=24.

[75] Unnar B. Arnalds, Thomas P.A. Hase, Evangelos Th Papaioannou, Hossein Raanaei, Radu Abrudan, Timothy R. Charlton, Sean Langridge, and Björgvin Hjörvarsson. X-ray resonant magnetic scattering from patterned multilayers. *Physical Review B - Condensed Matter and Materials Physics*, 86(6):064426, aug 2012. ISSN 10980121. doi: 10.1103/PhysRevB.86.064426. URL http://link.aps.org/doi/10.1103/PhysRevB.86.064426.

[76] Lev Davidovich Landau, Vladimir B. Berestetskii, Evgenii Mikhailovich Lifshitz, and Lev Petrovich Pitaevskii. *Relativistic quantum theory*. Course of theoretical physics. Pergamon, Oxford, 1971. URL http://cds.cern.ch/record/101813. Trans. from the Russian.

[77] Erik Östman, Unnar B. Arnalds, Emil Melander, Vassilios Kapaklis, Gunnar K. Pálsson, Alexander Y. Saw, Marc A. Verschuuren, Florian Kronast, Evangelos Th. Papaioannou, Charles S. Fadley, and Björgvin Hjörvarsson. Hysteresis-free switching between vortex and collinear magnetic states. *New Journal of Physics*, 16(5):053002, may 2014. ISSN 13672630. doi: 10.1088/1367-2630/16/5/053002. URL http://stacks.iop.org/1367-2630/16/i=5/a=053002?key=crossref.bda3e459f77ec36311c2bd49a39759ae.

[78] M. Abes, D. Atkinson, B. K. Tanner, T. R. Charlton, Sean Langridge, T. P.A. Hase, M. Ali, C. H. Marrows, B. J. Hickey, A. Neudert, R. J. Hicken, D. Arena, S. B. Wilkins, A. Mirone, and S. Lebègue. Spin polarization and exchange coupling of Cu and Mn atoms in paramagnetic CuMn diluted alloys induced by a Co layer. *Physical Review B - Condensed Matter and Materials Physics*, 82(18):6–8, 2010. ISSN 10980121. doi: 10.1103/PhysRevB.82.184412.

[79] Metin Tolan. *X-Ray Scattering from Soft-Matter Thin Films*. Springer-Verlag Berlin Heidelberg, 1999.

[80] J. Daillant and M. Alba. High-resolution x-ray scattering measurements: I. Surfaces. *Reports on Progress in Physics*, 63(10):1725–1777, 2000. ISSN 00344885. doi: 10.1088/0034-4885/63/10/203.

[81] R. Feidenhans'l. Surface structure determination by X-ray diffraction. *Surface Science Reports*, 10(3):105–188, 1989. ISSN 01675729. doi: 10.1016/0167-5729(89)90002-2.

[82] I. Pape, T. P.A. Hase, B. K. Tanner, and M. Wormington. Analysis of grazing incidence X-ray diffuse scatter from Co-Cu multilayers. *Physica B: Condensed Matter*, 253(3-4):278–289, oct 1998. ISSN 09214526. doi: 10.1016/S0921-4526(98)00395-0. URL http://linkinghub.elsevier.com/retrieve/pii/S0921452698003950.

[83] U. Rücker. Scattering under Grazing Incidence from Surfaces and Interfaces. In *Scattering Methods for Condensed Matter Research: Towards Novel Applications at Future Sources - Lecture Notes of the 43rd IFF Spring School 2012*, volume 33, pages D2.1–D2.37. 2012. ISBN 9783893367597.

[84] Petr Mikulik. *X-Ray Reflectivity from Planar and Structured Multilayers*. PhD thesis, L'université Joseph-Fourier, 1997.

[85] N. Bloembergen and P. S. Pershan. Light waves at the boundary of nonlinear media. *Physical Review*, 128(2):606–622, 1962. ISSN 0031899X. doi: 10.1103/PhysRev.128.606.

[86] E. Hecht. *Optics*. Pearson Education, Incorporated, 2017. ISBN 9780133977226. URL https://books.google.de/books?id=ZarLoQEACAAJ.

[87] M. Tolan, W. Press, F. Brinkop, and J. P. Kotthaus. X-ray diffraction from laterally structured surfaces: Total external reflection. *Physical Review B*, 51 (4):2239–2251, 1995. ISSN 01631829. doi: 10.1103/PhysRevB.51.2239.

[88] S. K. Sinha, E. B. Sirota, S. Garoff, and H. B. Stanley. X-ray and neutron scattering from rough surfaces. *Physical Review B*, 38(4):2297–2311, 1988. ISSN 01631829. doi: 10.1103/PhysRevB.38.2297.

[89] L. G. Parratt. Surface studies of solids by total reflection of x-rays. *Phys. Rev.*, 95:359–369, Jul 1954. doi: 10.1103/PhysRev.95.359. URL https://link.aps.org/doi/10.1103/PhysRev.95.359.

[90] V. Holy, T. Baumbach, and U. Pietsch. *High-resolution x-ray scattering from thin films and multilayers*. Springer tracts in modern physics. Springer, Berlin, 1999. URL https://cds.cern.ch/record/445085.

[91] V. Holy, J. Stangl, R. T. Lechner, and G. Springholz. X-ray scattering from periodic arrays of quantum dots. *Journal of Physics Condensed Matter*, 20(45):454215, 2008. ISSN 09538984. doi: 10.1088/0953-8984/20/45/454215. URL http://stacks.iop.org/0953-8984/20/i=45/a=454215?key=crossref.50f1603ff9d368637335b0f76980da8b.

[92] J. Stangl, V. Holý, and G. Bauer. Structural properties of self-organized semiconductor nanostructures. *Reviews of Modern Physics*, 76(3 I):725–783, 2004. ISSN 00346861. doi: 10.1103/RevModPhys.76.725.

[93] Qun Shen, C. Umbach, B. Weselak, and J. Blakely. Lateral correlation in mesoscopic structures on the silicon (001) surface determined by grating x-ray diffuse scattering. *Physical Review B - Condensed Matter and Materials Physics*, 53(8):R4237–R4240, 1996. ISSN 1550235X. doi: 10.1103/PhysRevB.53.R4237.

[94] L. Tapfer, G. C. La Rocca, H. Lage, R. Cingolani, P. Grambow, A. Fischer, D. Heitmann, and K. Ploog. Observation and analysis of quantum wire structures by high-resolution X-ray diffraction. *Surface Science*, 267(1-3):227–231, 1992. ISSN 00396028. doi: 10.1016/0039-6028(92)91126-V.

[95] Qun Shen, C. C. Umbach, B. Weselak, and J. M. Blakely. X-ray diffraction from a coherently illuminated Si(001) grating surface. *Physical Review B*, 48 (24):17967–17971, 1993. ISSN 01631829. doi: 10.1103/PhysRevB.48.17967.

[96] M. Tolan and S. K. Sinha. X-ray scattering with partial coherent radiation: The exact relationship between "resolution" and "coherence". *Physica B: Condensed Matter*, 248(1-4):399–404, 1998. ISSN 09214526. doi: 10.1016/S0921-4526(98)00271-3. URL `http://www.sciencedirect.com/science/article/B6TVH-3W2532C-2F/2/dda9922d983fa631170e4f754f04e4da`.

[97] M. Grimsditch, P. Vavassori, V. Novosad, V. Metlushko, H. Shima, H. Shima, Y. Otani, Y. Otani, and K. Fukamichi. Vortex chirality in an array of ferromagnetic dots. *Physical Review B - Condensed Matter and Materials Physics*, 65(17):1724191–1724194, 2002. ISSN 01631829. doi: 10.1103/PhysRevB.65.172419.

[98] Unnar B. Arnalds, Evangelos Th Papaioannou, Thomas P.A. Hase, Hossein Raanaei, Gabriella Andersson, Timothy R. Charlton, Sean Langridge, and Björgvin Hjörvarsson. Magnetic structure and diffracted magneto-optics of patterned amorphous multilayers. *Physical Review B - Condensed Matter and Materials Physics*, 82(14):144434, oct 2010. ISSN 10980121. doi: 10.1103/PhysRevB.82.144434. URL `http://link.aps.org/doi/10.1103/PhysRevB.82.144434`.

[99] Luiz Carlos De Campos, Carlos Benedicto Ramos Parente, and Vera Lucia Mazzocchi. Determination of the β-quartz hexagonal cell parameters from a

00.1 neutron multiple diffraction Umweganregung pattern measured at 1003 K. *Journal of Applied Crystallography*, 43(6):1488–1494, 2010. ISSN 00218898. doi: 10.1107/S0021889810037969.

[100] Marius Grundmann, Michael Scheibe, Michael Lorenz, Jürgen Bläsing, and Alois Krost. X-ray multiple diffraction of ZnO substrates and heteroepitaxial thin films. *Physica Status Solidi (B) Basic Research*, 251(4):850–863, apr 2014. ISSN 15213951. doi: 10.1002/pssb.201350297. URL `http://doi.wiley.com/10.1002/pssb.201350297`.

[101] M. Jergel, P. Mikulík, E. Majková, Š Luby, R. Senderák, E. Pinčík, M. Brunel, P. Hudek, I. Kostič, and A. Konečníková. Structural characterization of lamellar multilayer gratings by X-ray reflectivity and scanning electron microscopy. *Journal of Physics D: Applied Physics*, 32(10 A):A220–A223, 1999. ISSN 00223727. doi: 10.1088/0022-3727/32/10A/343.

[102] B. K. Tanner, T. P.A. Hase, J. Clarke, I. Pape, A. Li-Bassi, and B. D. Fulthorpe. High resolution X-ray scattering from nanotechnology materials. *Applied Surface Science*, 182(3-4):202–208, oct 2001. ISSN 01694332. doi: 10.1016/S0169-4332(01)00424-X. URL `http://linkinghub.elsevier.com/retrieve/pii/S016943320100424X`.

[103] T. Hase, I. Pape, B. Tanner, H. Dürr, E. Dudzik, and G. van der Laan. Soft-x-ray resonant magnetic diffuse scattering from strongly coupled Cu/Co multilayers. *Physical Review B - Condensed Matter and Materials Physics*, 61 (6):R3792–R3795, 2000. ISSN 1550235X. doi: 10.1103/PhysRevB.61.R3792.

[104] V. Holý and T. Baumbach. Nonspecular x-ray reflection from rough multilayers. *Physical Review B*, 49(15):10668–10676, 1994. ISSN 01631829. doi: 10.1103/PhysRevB.49.10668.

[105] H. Zabel. X-ray and neutron reflectivity analysis of thin films and superlattices. *Applied Physics A Solids and Surfaces*, 58(3):159–168, 1994. ISSN 07217250. doi: 10.1007/BF00324371. URL `http://link.springer.com/article/10.1007/BF00324371`.

[106] Jens Als-Nielsen, Didier Jacquemain, Kristian Kjaer, Franck Leveiller, Meir Lahav, and Leslie Leiserowitz. Principles and applications of grazing incidence X-ray and neutron scattering from ordered molecular monolayers at the air-water interface. *Physics Reports*, 246(5):251–313, 1994. ISSN 03701573. doi: 10.1016/0370-1573(94)90046-9.

[107] G. K. Wertheim, M. A. Butler, K. W. West, and D. N.E. Buchanan. Determination of the Gaussian and Lorentzian content of experimental line shapes. *Review of Scientific Instruments*, 45(11):1369–1371, 1974. ISSN 00346748. doi: 10.1063/1.1686503.

[108] Helmut Schift and Anders Kristensen. Nanoimprint lithography. *Springer Handbooks*, 14(6):113–142, nov 2017. ISSN 25228706. doi: 10.1007/978-3-662-54357-3_5. URL http://scitation.aip.org/content/avs/journal/jvstb/14/6/10.1116/1.588605.

[109] L. J. Heyderman, H. H. Solak, C. David, D. Atkinson, R. P. Cowburn, and F. Nolting. Arrays of nanoscale magnetic dots: Fabrication by x-ray interference lithography and characterization. *Applied Physics Letters*, 85 (21):4989–4991, nov 2004. ISSN 00036951. doi: 10.1063/1.1821649. URL http://aip.scitation.org/doi/10.1063/1.1821649.

[110] Byron D. Gates, Qiaobing Xu, Michael Stewart, Declan Ryan, C. Grant Willson, and George M. Whitesides. New approaches to nanofabrication: Molding, printing, and other techniques. *Chemical Reviews*, 105(4):1171–1196, apr 2005. ISSN 00092665. doi: 10.1021/cr030076o. URL https://pubs.acs.org/doi/full/10.1021/cr030076o.

[111] John A Rogers and Hong H Lee. *Unconventional nanopatterning techniques and applications*. John Wiley & Sons, 2008.

[112] In Roel Gronheid and Paul Nealey, editors, *Directed Self-assembly of Block Co-polymers for Nano-manufacturing*, Woodhead Publishing Series in Electronic and Optical Materials, page iv. Woodhead Publishing, 2015. ISBN 978-0-08-100250-6. doi: https://doi.org/10.1016/B978-0-08-100250-6.09992-2. URL http://www.sciencedirect.com/science/article/pii/B9780081002506099922.

[113] Mitsuhiro Terakawa. *Femtosecond Laser Direct Writing*. 2018. ISBN 978-981-13-0097-4. doi: 10.1007/978-981-13-0098-1_14. URL http://link.springer.com/10.1007/978-981-13-0098-1.

[114] Yao Lin, Alexander Böker, Jinbo He, Kevin Sill, Hongqi Xiang, Clarissa Abetz, Xuefa Li, Jin Wang, Todd Emrick, Su Long, Qian Wang, Anna Balazs, and Thomas P. Russell. Self-directed self-assembly of nanoparticle/copolymer mixtures. *Nature*, 434(7029):55–59, 2005. ISSN 00280836.

doi: 10.1038/nature03310. URL http://www.nature.com/nature/journal/v434/n7029/abs/nature03310.html.

[115] David Eastwood. *Durham E-Theses Grazing Incidence X-ray Scattering from Magnetic Thin Films and Nanostructures*. PhD thesis, 2009.

[116] D. Mishra, M. J. Benitez, O. Petracic, G. A. Badini Confalonieri, P. Szary, F. Brüssing, K. Theis-Bröhl, A. Devishvili, A. Vorobiev, O. Konovalov, M. Paulus, C. Sternemann, B. P. Toperverg, and H. Zabel. Self-assembled iron oxide nanoparticle multilayer: X-ray and polarized neutron reflectivity. *Nanotechnology*, 23(5):055707, feb 2012. ISSN 09574484. doi: 10.1088/0957-4484/23/5/055707. URL http://www.ncbi.nlm.nih.gov/pubmed/22236964http://iopscience.iop.org/0957-4484/23/5/055707/article/.

[117] Vassilios Kapaklis, Unnar B. Arnalds, Adam Harman-Clarke, Evangelos Th. Papaioannou, Masoud Karimipour, Panagiotis Korelis, Andrea Taroni, Peter C.W. Holdsworth, Steven T. Bramwell, and Björgvin Hjörvarsson. Melting artificial spin ice. *New Journal of Physics*, 14, 2012. ISSN 13672630. doi: 10.1088/1367-2630/14/3/035009.

[118] Unnar B. Arnalds, Alan Farhan, Rajesh V. Chopdekar, Vassilios Kapaklis, Ana Balan, Evangelos Th Papaioannou, Martina Ahlberg, Frithjof Nolting, Laura J. Heyderman, and Björgvin Hjörvarsson. Thermalized ground state of artificial kagome spin ice building blocks. *Applied Physics Letters*, 101(11), 2012. ISSN 00036951. doi: 10.1063/1.4751844.

[119] S. Swann. Magnetron sputtering. *Physics in Technology*, 19(2):67–75, 1988. ISSN 03054624. doi: 10.1088/0305-4624/19/2/304. URL http://iopscience.iop.org/0305-4624/19/2/304.

[120] Vincent S. Smentkowski. Trends in sputtering, may 2000. ISSN 00796816.

[121] P. J. Kelly and R. D. Arnell. Magnetron sputtering: A review of recent developments and applications, mar 2000. ISSN 0042207X.

[122] John R. Arthur. Molecular beam epitaxy. *Surface Science*, 500(1-3):189–217, mar 2002. ISSN 00396028. doi: 10.1016/S0039-6028(01)01525-4.

[123] Leroy L Chang and Klaus Ploog. *Molecular beam epitaxy and heterostructures*, volume 87. Springer Science & Business Media, 2012.

[124] C. J. Lawrence. The mechanics of spin coating of polymer films. *Physics of Fluids*, 31(10):2786–2795, oct 1988. ISSN 10897666. doi: 10.1063/1.866986. URL https://aip.scitation.org/doi/10.1063/1.866986.

[125] Niranjan Sahu, B. Parija, and S. Panigrahi. Fundamental understanding and modeling of spin coating process: A review. Technical Report 4, 2009.

[126] Krishna Seshan. *Handbook of thin film deposition processes and techniques*. William Andrew, 2001.

[127] Longjian Xue and Yanchun Han. Pattern formation by dewetting of polymer thin film. *Progress in Polymer Science (Oxford)*, 36(2):269–293, 2011. ISSN 00796700. doi: 10.1016/j.progpolymsci.2010.07.004. URL http://linkinghub.elsevier.com/retrieve/pii/S0079670010000675.

[128] Richard C. Jaeger. Film deposition: Introduction to microelectronic fabrication. *Upper Saddle Rivers: Prentice Hall*, 83, 2002.

[129] W. Patrick Mccray. MBE deserves a place in the history books. *Nature Nanotechnology*, 2(5):259–261, 2007. ISSN 17483395. doi: 10.1038/nnano.2007.121.

[130] Ioan-Augustin Chioar. *Artificial Kagome Spin Networks - From Short-Range Degeneracy towards Long-Range Dipolar Order*. PhD thesis, 2015. URL http://www.theses.fr/2015GREAY033/document.

[131] Sangmoo Jeong, Liangbing Hu, Hye Ryoung Lee, Erik Garnett, Jang Wook Choi, and Yi Cui. Fast and scalable printing of large area monolayer nanoparticles for nanotexturing applications. *Nano Letters*, 10(8):2989–2994, aug 2010. ISSN 15306984. doi: 10.1021/nl101432r. URL http://www.ncbi.nlm.nih.gov/pubmed/20698612.

[132] K. S. Usha, R. Sivakumar, C. Sanjeeviraja, Vasant Sathe, V. Ganesan, and T. Y. Wang. Improved electrochromic performance of a radio frequency magnetron sputtered NiO thin film with high optical switching speed. *RSC Advances*, 6(83):79668–79680, aug 2016. ISSN 20462069. doi: 10.1039/c5ra27099e. URL https://pubs.rsc.org/en/content/articlehtml/2016/ra/c5ra27099ehttps://pubs.rsc.org/en/content/articlelanding/2016/ra/c5ra27099e.

[133] Lakshmi Kolipaka and Stefan Vajda. High-pressure and reactive gas magnetron sputtering. *Gas-Phase Synthesis of Nanoparticles*, 2017.

[134] R. A. Procter, F. Magnus, G. Andersson, C. Sánchez-Hanke, B. Hjörvarsson, and T. P.A. Hase. Magnetic leverage effects in amorphous SmCo/CoAlZr heterostructures. *Applied Physics Letters*, 107(6):062403, 2015. ISSN 00036951. doi: 10.1063/1.4928632. URL http://scitation.aip.org/content/aip/journal/apl/107/6/10.1063/1.4928632.

[135] E. Benes. Improved quartz crystal microbalance technique. *Journal of Applied Physics*, 56(3):608–626, aug 1984. ISSN 00218979. doi: 10.1063/1.333990. URL http://aip.scitation.org/doi/10.1063/1.333990.

[136] Dunbar P. Birnie. A model for drying control cosolvent selection for spin-coating uniformity: The thin film. *Langmuir*, 29(29):9072–9078, jul 2013. ISSN 07437463. doi: 10.1021/la401106z. URL http://www.ncbi.nlm.nih.gov/pubmed/23808408.

[137] D. Mishra, D. Greving, G. A. Badini Confalonieri, J. Perlich, B. P. Toperverg, H. Zabel, and O. Petracic. Growth modes of nanoparticle superlattice thin films. *Nanotechnology*, 25(20):205602, may 2014. ISSN 13616528. doi: 10.1088/0957-4484/25/20/205602. URL http://www.ncbi.nlm.nih.gov/pubmed/24785547.

[138] Aaron R. Halpern, Naoya Nishi, Jia Wen, Fan Yang, Chengxiang Xiang, Reginald M. Penner, and Robert M. Corn. Characterization of electrodeposited gold and palladium nanowire gratings with optical diffraction measurements. *Analytical Chemistry*, 81(14):5585–5592, 2009. ISSN 00032700. doi: 10.1021/ac900938t. URL https://pubs.acs.org/sharingguidelines.

[139] Yugang Sun and John A. Rogers. Fabricating semiconductor nano/microwires and transfer printing ordered arrays of them onto plastic substrates. *Nano Letters*, 4(10):1953–1959, 2004. ISSN 15306984. doi: 10.1021/nl048835l.

[140] Seiji Samukawa. Ultimate top-down etching processes for future nanoscale devices: Advanced neutral-beam etching. *Japanese Journal of Applied Physics, Part 1: Regular Papers and Short Notes and Review Papers*, 45(4 A):2395–2407, 2006. ISSN 00214922. doi: 10.1143/JJAP.45.2395. URL https://www.researchgate.net/publication/239054516.

[141] Leonhard Grill, Matthew Dyer, Leif Lafferentz, Mats Persson, Maike V. Peters, and Stefan Hecht. Nano-architectures by covalent assembly of molecular building blocks. *Nature Nanotechnology*, 2(11):687–691, 2007.

ISSN 17483395. doi: 10.1038/nnano.2007.346. URL www.nature.com/naturenanotechnology.

[142] Katsuhiko Ariga, Jonathan P. Hill, and Qingmin Ji. Layer-by-layer assembly as a versatile bottom-up nanofabrication technique for exploratory research and realistic application. *Physical Chemistry Chemical Physics*, 9(19):2319–2340, 2007. ISSN 14639076. doi: 10.1039/b700410a. URL https://pubs.rsc.org/en/content/articlehtml/2007/cp/b700410a.

[143] Kyle J.M. Bishop, Christopher E. Wilmer, Siowling Soh, and Bartosz A. Grzybowski. Nanoscale forces and their uses in self-assembly. *Small*, 5(14):1600–1630, jul 2009. ISSN 16136810. doi: 10.1002/smll.200900358. URL http://www.ncbi.nlm.nih.gov/pubmed/19517482.

[144] Vitor R. Manfrinato, Aaron Stein, Lihua Zhang, Chang Yong Nam, Kevin G. Yager, Eric A. Stach, and Charles T. Black. Aberration-Corrected Electron Beam Lithography at the One Nanometer Length Scale. *Nano Letters*, 17(8):4562–4567, aug 2017. ISSN 15306992. doi: 10.1021/acs.nanolett.7b00514. URL https://pubs.acs.org/doi/abs/10.1021/acs.nanolett.7b00514.

[145] Vitor R. Manfrinato, Fernando E. Camino, Aaron Stein, Lihua Zhang, Ming Lu, Eric A. Stach, and Charles T. Black. Patterning Si at the 1 nm Length Scale with Aberration-Corrected Electron-Beam Lithography: Tuning of Plasmonic Properties by Design. *Advanced Functional Materials*, 29(52):1903429, dec 2019. ISSN 16163028. doi: 10.1002/adfm.201903429. URL https://onlinelibrary.wiley.com/doi/abs/10.1002/adfm.201903429.

[146] John N. Randall, James H. G. Owen, Joseph Lake, and Ehud Fuchs. Next generation of extreme-resolution electron beam lithography. *Journal of Vacuum Science & Technology B*, 37(6):061605, nov 2019. ISSN 2166-2746. doi: 10.1116/1.5119392. URL http://avs.scitation.org/doi/10.1116/1.5119392.

[147] R. P. Seisyan. Nanolithography in microelectronics: A review, aug 2011. ISSN 10637842. URL https://link.springer.com/article/10.1134/S1063784211080214.

[148] John T. Fourkas. Nanoscale photolithography with visible light. *Journal of Physical Chemistry Letters*, 1(8):1221–1227, apr 2010. ISSN 19487185. doi: 10.1021/jz1002082. URL https://pubs.acs.org/doi/abs/10.1021/jz1002082.

[149] Aurélie Pierret, Mora Hocevar, Silke L. Diedenhofen, Rienk E. Algra, E. Vlieg, Eugene C. Timmering, Marc A. Verschuuren, George W.G. Immink, Marcel A. Verheijen, and Erik P.A.M. Bakkers. Generic nano-imprint process for fabrication of nanowire arrays. *Nanotechnology*, 21(6):65305, 2010. ISSN 09574484. doi: 10.1088/0957-4484/21/6/065305. URL `http://www.ncbi.nlm.nih.gov/pubmed/20057022`.

[150] Alee N. Broers, A. C.F. Hoole Andrew, and Joseph M. Ryan. Electron beam lithography - Resolution limits. *Microelectronic Engineering*, 32(1-4 SPEC. ISS.):131–142, sep 1996. ISSN 01679317. doi: 10.1016/0167-9317(95)00368-1.

[151] Yifang Chen. Nanofabrication by electron beam lithography and its applications: A review, mar 2015. ISSN 01679317.

[152] Harry Sewell and Jan Mulkens. Materials for optical lithography tool application. *Annual Review of Materials Research*, 39(1):127–153, 2009. ISSN 15317331. doi: 10.1146/annurev-matsci-082908-145309. URL `www.annualreviews.org`.

[153] L. A. Giannuzzi and F. A. Stevie. A review of focused ion beam milling techniques for TEM specimen preparation. *Micron*, 30(3):197–204, 1999. ISSN 09684328. doi: 10.1016/S0968-4328(99)00005-0.

[154] P. Atkinson, S. P. Bremner, D. Anderson, G. A.C. Jones, and D. A. Ritchie. Molecular beam epitaxial growth of site-controlled InAs quantum dots on prepatterned GaAs substrates. *Microelectronics Journal*, 37(12):1436–1439, dec 2006. ISSN 00262692. doi: 10.1016/j.mejo.2006.05.003.

[155] Paola Atkinson, Oliver G. Schmidt, Stephen P. Bremner, and David A. Ritchie. Formation and ordering of epitaxial quantum dots, oct 2008. ISSN 16310705.

[156] T. H.P. Chang. Proximity Effect in Electron-Beam Lithography. In *J Vac Sci Technol*, volume 12, pages 1271–1275. American Vacuum SocietyAVS, nov 1975. doi: 10.1116/1.568515. URL `http://avs.scitation.org/doi/10.1116/1.568515`.

[157] Eunsung Soe, Bo Kyung Choi, and Ohyun Kim. Determination of proximity effect parameters and the shape bias parameter in electron beam lithography. *Microelectronic Engineering*, 53(1):305–308, jun 2000. ISSN 01679317. doi: 10.1016/S0167-9317(00)00320-8.

[158] Rachel K. Smith, Penelope A. Lewis, and Paul S. Weiss. Patterning self-assembled monolayers. *Progress in Surface Science*, 75(1-2):1–68, 2004. ISSN 00796816. doi: 10.1016/j.progsurf.2003.12.001.

[159] T. H.P. Chang. Proximity Effect in Electron-Beam Lithography. In *J Vac Sci Technol*, volume 12, pages 1271–1275, 1975. doi: 10.1116/1.568515.

[160] R. Van Grieken and A. Markowicz. *Handbook of X-ray Spectrometry*. 2001. URL `https://books.google.com/books?hl=en{&}lr={&}id=10qyDwAAQBAJ{&}oi=fnd{&}pg=PP1{&}dq=Handbook+of+x-ray+spectrometry{&}ots=5d19iRvt85{&}sig=QtvvgmvyoG4gXWoRUN08dwWmiSQ`.

[161] Herman Winick and Arthur Bienenstock. *Synchrotron Radiation Research.*, volume 28. 1978. doi: 10.1146/annurev.ns.28.120178.000341. URL `https://books.google.com/books?hl=en{&}lr={&}id=uvgICAAAQBAJ{&}oi=fnd{&}pg=PA1{&}dq=synchrotron{&}ots=JL41WXEbVi{&}sig={_}EtBVUs9h8FsTJVP5Q0qqbNA8I0`.

[162] European Synchrotron Radiation Facility (ESRF). URL `https://www.esrf.eu/home/UsersAndScience/Accelerators/parameters.html`.

[163] Advanced Photon Source (APS), instrument parameters, . URL `https://ops.aps.anl.gov/SRparameters/SRparameters.html`.

[164] R. Kompfner. On the operation of the travelling wave tube at low level. *Journal of the British Institution of Radio Engineers*, 10(8):283–289, aug 1950. doi: 10.1049/jbire.1950.0028.

[165] A. K. Sinha, R. Verma, R. K. Gupta, L. Kumar, S. N. Joshi, P. K. Jain, and B. N. Basu. Simplified tape model of arbitrarily-loaded helical slow-wave structures of a travelling-wave tube. *IEE Proceedings H: Microwaves, Antennas and Propagation*, 139(4):347–350, 1992. ISSN 0950107X. doi: 10.1049/ip-h-2.1992.0062.

[166] ESRF - x-ray oriented programs 2.4. URL `http://www.esrf.eu/Instrumentation/software/data-analysis/xop2.4`.

[167] Shigemi Sasaki, Taihei Shimada, Ken ichi Yanagida, Hideki Kobayashi, and Yoshikazu Miyahara. First observation of undulator radiation from APPLE-1. *Nuclear Inst. and Methods in Physics Research, A*, 347(1-3):87–91, aug 1994. ISSN 01689002. doi: 10.1016/0168-9002(94)91860-0.

[168] J. Bahrdt, W. Frentrup, A. Gaupp, M. Scheer, and G. Wuestefeld. Active shimming of the dynamic multipoles of the BESSY UE112 apple undulator. *EPAC 2008 - Contributions to the Proceedings*, 2(2):2222–2224, 2008. URL https://www.researchgate.net/publication/242223510.

[169] Hongchang Wang, Peter Bencok, Paul Steadman, Emily Longhi, Jingtao Zhu, and Zhanshan Wang. Complete polarization analysis of an APPLE II undulator using a soft X-ray polarimeter. *Journal of Synchrotron Radiation*, 19(6): 944–948, nov 2012. ISSN 09090495. doi: 10.1107/S0909049512034851.

[170] Fuhao Ji, Rui Chang, Qiaogen Zhou, Wei Zhang, Mao Ye, Shigemi Sasaki, and Shan Qiao. Design and performance of the APPLE-Knot undulator. *Journal of Synchrotron Radiation*, 22(Pt 4):901–907, jul 2015. ISSN 16005775. doi: 10.1107/S1600577515006062. URL /pmc/articles/PMC4489533/?report=abstracthttps://www.ncbi.nlm.nih.gov/pmc/articles/PMC4489533/.

[171] Rachael Procter. *Resonant X-ray Scattering from Magnetic Multilayers and Patterned Arrays*. PhD thesis, University of Warwick, 2017. URL https://pugwash.lib.warwick.ac.uk/record=b3141983~S15.

[172] Xmas beamline details. URL https://warwick.ac.uk/fac/cross_fac/xmas/xmasbeamline/description/.

[173] Marc Lemonnier, Odile Collet, Claude Depautex, Jean Marc Esteva, and Denis Raoux. High vacuum two crystal soft X-ray monochromator. *Nuclear Instruments and Methods*, 152(1):109–111, jun 1978. ISSN 0029554X. doi: 10.1016/0029-554X(78)90246-X.

[174] P. L. Cowan, J. B. Hastings, T. Jach, and J. P. Kirkland. A UHV compatible two-crystal monochromator for synchrotron radiation. *Nuclear Instruments and Methods In Physics Research*, 208(1-3):349–353, apr 1983. ISSN 01675087. doi: 10.1016/0167-5087(83)91148-1.

[175] K. J.S. Sawhney and R. V. Nandedkar. Imaging characteristics of toroidal and ellipsoidal mirrors for synchrotron radiation source Indus-1. *Pramana: Journal of Physics*, 39(2):177–180, 1992. ISSN 09737111. doi: 10.1007/BF02857506.

[176] Takehiko Ishii, Osamu Aita, Kouichi Ichikawa, and Takasi Sagawa. Use of a Toroidal Mirror in the Soft X-Ray Optical System. *Japanese Journal of Applied Physics*, 10(5):637–642, may 1971. ISSN 0021-4922. doi: 10.1143/jjap.10.637.

[177] Ph Sainctavit, J. Petiau, A. Manceau, R. Rivallant, M. Belakhovsky, and G. Renaud. A two mirror device for harmonic rejection. *Nuclear Inst. and Methods in Physics Research, A*, 273(1):423–428, dec 1988. ISSN 01689002. doi: 10.1016/0168-9002(88)90845-5.

[178] F. Yuan, X. Song, W. Xiangjun, J. Zheng, G. Songqi, C. Ming, H. Yuying, and Y. Xiaohan. The development of a harmonic rejection mirror on XAFS beamline at Shanghai Synchrotron Radiation Facility. *Diamond Light Source Proceedings*, 1(MEDSI-6), 2010. doi: 10.1017/s2044820110000766.

[179] Kouhei Okitsu, Yoshinori Ueji, Kiminori Sato, and Yoshiyuki Amemiya. X-ray double phase retarders to compensate for off-axis aberration. *Journal of Synchrotron Radiation*, 8(1):33–37, 2001. ISSN 09090495. doi: 10.1107/S0909049500019567.

[180] Elias Vlieg. Integrated Intensities Using a Six-Circle Surface X-ray Diffractometer. *Journal of Applied Crystallography*, 30(5):532–543, 1997. ISSN 00218898. doi: 10.1107/S0021889897002537.

[181] Rainer Storn and Kenneth Price. Differential Evolution - A Simple and Efficient Heuristic for Global Optimization over Continuous Spaces. *Journal of Global Optimization*, 11(4):341–359, 1997. ISSN 09255001. doi: 10.1023/A:1008202821328.

[182] F. Peñuñuri, C. Cab, O. Carvente, M. A. Zambrano-Arjona, and J. A. Tapia. A study of the Classical Differential Evolution control parameters. *Swarm and Evolutionary Computation*, 26:86–96, 2016. ISSN 22106502. doi: 10.1016/j.swevo.2015.08.003. URL `http://dx.doi.org/10.1016/j.swevo.2015.08.003`.

[183] Deepak Dawar and Simone A. Ludwig. Differential evolution with dither and annealed scale factor. *IEEE SSCI 2014 - 2014 IEEE Symposium Series on Computational Intelligence - SDE 2014: 2014 IEEE Symposium on Differential Evolution, Proceedings*, 2015. doi: 10.1109/SDE.2014.7031528.

[184] Jani Rönkkönen, Saku Kukkonen, and Kenneth V. Price. Real-parameter optimization with differential evolution. *2005 IEEE Congress on Evolutionary Computation, IEEE CEC 2005. Proceedings*, 1:506–513, 2005. doi: 10.1109/cec.2005.1554725.

[185] Daniela Zaharie and Flavia Micota. Revisiting the analysis of population variance in Differential Evolution algorithms. *2017 IEEE Congress on Evolutionary Computation, CEC 2017 - Proceedings*, (i):1811–1818, 2017. doi: 10.1109/CEC.2017.7969521.

[186] Swagatam Das and Ponnuthurai Nagaratnam Suganthan. Differential evolution: A survey of the state-of-the-art. *IEEE Transactions on Evolutionary Computation*, 15(1):4–31, 2011. ISSN 1089778X. doi: 10.1109/TEVC.2010.2059031.

[187] Kenneth Price, Rainer M. Storn, and Jouni A. Lampinen. *Differential Evolution*. Natural Computing Series. Springer-Verlag, Berlin/Heidelberg, 2005. ISBN 3-540-20950-6. doi: 10.1007/3-540-31306-0. URL `http://scholar.google.com/scholar?hl=en{&}btnG=Search{&}q=intitle:No+Title{#}0http://www.springerlink.com/index/10.1007/3-540-31306-0`.

[188] Swagatam Das, Amit Konar, and Uday K. Chakraborty. Two improved differential evolution schemes for faster global search. *GECCO 2005 - Genetic and Evolutionary Computation Conference*, pages 991–998, 2005. doi: 10.1145/1068009.1068177.

[189] Matts Björck. Fitting with differential evolution: An introduction and evaluation. *Journal of Applied Crystallography*, 44(6):1198–1204, 2011. ISSN 00218898. doi: 10.1107/S0021889811041446.

[190] Daniela Zaharie. Influence of crossover on the behavior of Differential Evolution Algorithms. *Applied Soft Computing Journal*, 9(3):1126–1138, 2009. ISSN 15684946. doi: 10.1016/j.asoc.2009.02.012.

[191] James Montgomery. Differential evolution: Difference vectors and movement in solution space. *2009 IEEE Congress on Evolutionary Computation, CEC 2009*, pages 2833–2840, 2009. doi: 10.1109/CEC.2009.4983298.

[192] Anthony E. Siegman. Lasers university science books. *Mill Valley, CA*, 37 (208):169, 1986.

[193] R Gordon Gould. The LASER, light amplification by stimulated emission of radiation. In *The Ann Arbor conference on optical pumping, the University of Michigan*, volume 15, page 92, 1959.

[194] Geoffrey Brooker. *Modern classical optics*, volume 8. Oxford University Press, 2003.

[195] Andrej Singer and Ivan A. Vartanyants. Coherence properties of focused X-ray beams at high-brilliance synchrotron sources. *Journal of Synchrotron Radiation*, 21(1):5–15, 2014. ISSN 09090495. doi: 10.1107/S1600577513023850.

[196] Leonard Mandel and Emil Wolf. *Optical coherence and quantum optics*. Cambridge university press, 1995.

[197] Albert C. Thompson, Douglas Vaughan, David Attwood, Erik Gullikson, Malcolm Howells, Jeffrey Kortright, Arthur Robinson, and James Underwood. *X-ray data booklet*, volume 8. Lawrence Berkeley National Laboratory, University of California Berkeley, CA, 2001.

[198] Bruno Dorner and Andrew R. Wildes. Some considerations on resolution and coherence length in reflectometry. *Langmuir*, 19(19):7823–7828, sep 2003. ISSN 07437463. doi: 10.1021/la026949b. URL `http://pubs.acs.org/doi/abs/10.1021/la026949b`.

[199] S. Sinha and M. Tolan. Effects of partial coherence on the scattering of x rays by matter. *Physical Review B - Condensed Matter and Materials Physics*, 57 (5):2740–2758, feb 1998. ISSN 1550235X. doi: 10.1103/PhysRevB.57.2740. URL `http://link.aps.org/doi/10.1103/PhysRevB.57.2740`.

[200] Tadashi Matsushita and H. Hashizume. X-ray monochromators. *Handbook on Synchrotron Radiation*, 1:261–314, 1983.

[201] Wim H. De Jeu, Joseph D. Shindler, and Elisabeth A.L. Mol. The Resolution Function in Diffuse X-ray Reflectivity. *Journal of Applied Crystallography*, 29 PART 5(5):511–515, 1996. ISSN 00218898. doi: 10.1107/s0021889896001550.

[202] Ariel Caticha and S. Caticha-Ellis. Dynamical theory of x-ray diffraction at Bragg angles near 2. *Physical Review B*, 25(2):971–983, 1982. ISSN 01631829. doi: 10.1103/PhysRevB.25.971.

[203] R. Høier and K. Marthinsen. Effective structure factors in many-beam X-ray diffraction – use of the second Bethe approximation. *Acta Crystallographica Section A*, 39(6):854–860, 1983. ISSN 16005724. doi: 10.1107/S0108767383001725.

[204] Science and technology facilities council. URL `https://stfc.ukri.org/`.

[205] Micro And Nanotechnology Centre. URL https://stfc.ukri.org/about-us/where-we-work/rutherford-appleton-laboratory/micro-and-nano-technology-centre/.

[206] National Synchrotron Light Source II (NSLS). URL https://www.bnl.gov/ps/.

[207] Nico M. Temme. *Special functions: An introduction to the classical functions of mathematical physics*. John Wiley & Sons, 2011.

[208] Matts Björck and Gabriella Andersson. GenX: An extensible X-ray reflectivity refinement program utilizing differential evolution. *Journal of Applied Crystallography*, 40(6):1174–1178, 2007. ISSN 00218898. doi: 10.1107/S0021889807045086.

[209] Martin Pärnaste, Moreno Marcellini, Erik Holmström, Nicolas Bock, Jonas Fransson, Olle Eriksson, and Björgvin Hjörvarsson. Dimensionality crossover in the induced magnetization of pd layers. *Journal of Physics: Condensed Matter*, 19(24), 2007. doi: 10.1088/0953-8984/19/24/246213.

[210] Evangelos Th Papaioannou, Vassilios Kapaklis, Andrea Taroni, Moreno Marcellini, and Björgvin Hjörvarsson. Dimensionality and confinement effects in δ-doped Pd(Fe) layers. *Journal of Physics Condensed Matter*, 22(23), 2010. ISSN 09538984. doi: 10.1088/0953-8984/22/23/236004.

[211] Advanced Photon Source (APS), . URL https://www.aps.anl.gov/.

[212] I. A. Vartanyants, I. K. Robinson, J. D. Onken, M. A. Pfeifer, G. J. Williams, F. Pfeiffer, H. Metzger, Z. Zhong, and G. Bauer. Coherent x-ray diffraction from quantum dots. *Physical Review B - Condensed Matter and Materials Physics*, 71(24), 2005. ISSN 10980121. doi: 10.1103/PhysRevB.71.245302.

[213] Meh Pedersen. Good Parameters for Differential Evolution. *Evolution*, pages 1–10, 2010. URL http://www.hvass-labs.org/people/magnus/publications/pedersen10good-de.pdf.

[214] Xenocs Xeuss 3.0 Laboratory Beamline. URL http://www.xenocs.com/products/xeuss-3-0/.

[215] Pilatus 300K Hybrid Photon Counting Detector. URL https://www.dectris.com/products/pilatus3/pilatus3-r-for-laboratory/pilatus3-r-300k/.

[216] Thorlabs. URL https://www.thorlabs.com/.

[217] esa project. URL https://warwick.ac.uk/fac/cross_fac/xmas/other_projects/esaproject/.

[218] Bernhard Rupp. *Biomolecular crystallography: principles, practice, and application to structural biology*. Garland Science, 2009.

[219] Alexander McPherson. *Introduction to macromolecular crystallography*. John Wiley & Sons, 2011.

[220] B. Van Waeyenberge, A. Puzic, H. Stoll, K. W. Chou, T. Tyliszczak, R. Hertel, M. Fähnle, H. Brückl, K. Rott, G. Reiss, I. Neudecker, D. Weiss, C. H. Back, and G. Schütz. Magnetic vortex core reversal by excitation with short bursts of an alternating field. *Nature*, 444(7118):461–464, 2006. ISSN 14764687. doi: 10.1038/nature05240.

[221] Keisuke Yamada, Shinya Kasai, Yoshinobu Nakatani, Kensuke Kobayashi, Hiroshi Kohno, André Thiaville, and Teruo Ono. Electrical switching of the vortex core in a magnetic disk. *Nature Materials*, 6(4):270–273, 2007. ISSN 14764660. doi: 10.1038/nmat1867.

[222] Sangkook Choi, Ki Suk Lee, Konstantin Yu Guslienko, and Sang Koog Kim. Strong radiation of spin waves by core reversal of a magnetic vortex and their wave behaviors in magnetic nanowire waveguides. *Physical Review Letters*, 98 (8):98–101, 2007. ISSN 00319007. doi: 10.1103/PhysRevLett.98.087205.

[223] Marek Vaňatka, Michal Urbánek, Roman Jíra, Lukáš Flajšman, Meena Dhankhar, Mi Young Im, Jan Michalička, Vojtěch Uhlíř, and Tomáš Šikola. Magnetic vortex nucleation modes in static magnetic fields. *AIP Advances*, 7 (10), 2017. ISSN 21583226. doi: 10.1063/1.5006235.

[224] Vedat Karakas, Aisha Gokce, Ali Taha Habiboglu, Sevdenur Arpaci, Kaan Ozbozduman, Ibrahim Cinar, Cenk Yanik, Riccardo Tomasello, Silvia Tacchi, Giulio Siracusano, Mario Carpentieri, Giovanni Finocchio, Thomas Hauet, and Ozhan Ozatay. Observation of Magnetic Radial Vortex Nucleation in a Multilayer Stack with Tunable Anisotropy. *Scientific Reports*, 8(1):1–10, 2018. ISSN 20452322. doi: 10.1038/s41598-018-25392-x. URL http://dx.doi.org/10.1038/s41598-018-25392-x.

[225] L. Giovannini, F. Montoncello, F. Nizzoli, G. Gubbiotti, G. Carlotti, T. Okuno, T. Shinjo, and M. Grimsditch. Spin excitations of nanometric

cylindrical dots in vortex and saturated magnetic states. *Physical Review B - Condensed Matter and Materials Physics*, 70(17):1–4, 2004. ISSN 01631829. doi: 10.1103/PhysRevB.70.172404.

[226] V. Novosad, F. Y. Fradin, P. E. Roy, K. S. Buchanan, K. Yu Guslienko, and S. D. Bader. Magnetic vortex resonance in patterned ferromagnetic dots. *Physical Review B - Condensed Matter and Materials Physics*, 72(2):1–5, 2005. ISSN 10980121. doi: 10.1103/PhysRevB.72.024455.

[227] Q. F. Xiao, J. Rudge, B. C. Choi, Y. K. Hong, and G. Donohoe. Dynamics of vortex core switching in ferromagnetic nanodisks. *Applied Physics Letters*, 89 (26):78–81, 2006. ISSN 00036951. doi: 10.1063/1.2424673.

[228] V. Novosad, K. Yu Guslienko, H. Shima, Y. Otani, K. Fukamichi, N. Kikuchi, O. Kitakami, and Y. Shimada. Nucleation and annihilation of magnetic vortices in sub-micron permalloy dots. *IEEE Transactions on Magnetics*, 37(4 I): 2088–2090, 2001. ISSN 00189464. doi: 10.1109/20.951062.

[229] K. Yu Guslienko, W. Scholz, R. W. Chantrell, and V. Novosad. Vortex-state oscillations in soft magnetic cylindrical dots. *Physical Review B - Condensed Matter and Materials Physics*, 71(14):1–8, 2005. ISSN 10980121. doi: 10.1103/PhysRevB.71.144407.

[230] F. Carace, P. Vavassori, G. Gubbiotti, S. Tacchi, M. Madami, G. Carlotti, and T. Okuno. Magnetization reversal process in elliptical Permalloy nanodots. *Thin Solid Films*, 515(2 SPEC. ISS.):727–730, 2006. ISSN 00406090. doi: 10.1016/j.tsf.2005.12.178.

[231] Jonathan Kin Ha, Riccardo Hertel, and J. Kirschner. Micromagnetic study of magnetic configurations in submicron permalloy disks. *Physical Review B - Condensed Matter and Materials Physics*, 67(22):1–9, 2003. ISSN 1550235X. doi: 10.1103/PhysRevB.67.224432.

[232] Junya Shibata and Yoshichika Otani. Magnetic vortex dynamics in a two-dimensional square lattice of ferromagnetic nanodisks. *Physical Review B - Condensed Matter and Materials Physics*, 70(1):2–5, 2004. ISSN 01631829. doi: 10.1103/PhysRevB.70.012404.

[233] Robert M. White and Bradford Bayne. *Quantum theory of magnetism*, volume 1. Springer, 1983.

[234] David J. Griffiths and Darrell F. Schroeter. *Introduction to quantum mechanics*. Cambridge University Press, 2018.

[235] Jimmy J. Kan, Marko V. Lubarda, Keith T. Chan, Vojtěch Uhlíř, Andreas Scholl, Vitaliy Lomakin, and Eric E. Fullerton. Periodic chiral magnetic domains in single-crystal nickel nanowires. *Physical Review Materials*, 2(6): 064406, 2018. ISSN 24759953. doi: 10.1103/PhysRevMaterials.2.064406. URL `https://link.aps.org/doi/10.1103/PhysRevMaterials.2.064406`.

[236] G. M. Wysin and W. Figueiredo. Thermal vortex dynamics in thin circular ferromagnetic nanodisks. *Physical Review B - Condensed Matter and Materials Physics*, 86(10):1–16, 2012. ISSN 10980121. doi: 10.1103/PhysRevB.86.104421.

[237] G. M. Wysin. Vortex dynamics in thin elliptic ferromagnetic nanodisks. *Low Temperature Physics*, 41(10):788–800, 2015. ISSN 1063777X. doi: 10.1063/1.4932353. URL `http://dx.doi.org/10.1063/1.4932353`.

[238] P. Vavassori, V. Metlushko, R. M. Osgood, M. Grimsditch, U. Welp, G. Crabtree, Wenjun Fan, S. R.J. Brueck, B. Ilic, and P. J. Hesketh. Magnetic information in the light diffracted by a negative dot array of fe. *Physical Review B - Condensed Matter and Materials Physics*, 59(9):6337–6343, 1999. ISSN 1550235X. doi: 10.1103/PhysRevB.59.6337.

[239] M. J. Benitez, D. Mishra, P. Szary, G. A. Badini Confalonieri, M. Feyen, A. H. Lu, L. Agudo, G. Eggeler, O. Petracic, and H. Zabel. Structural and magnetic characterization of self-assembled iron oxide nanoparticle arrays. *Journal of Physics Condensed Matter*, 23(12):126003, mar 2011. ISSN 09538984. doi: 10.1088/0953-8984/23/12/126003. URL `http://www.ncbi.nlm.nih.gov/pubmed/21378441`.

[240] F. Giesen, J. Podbielski, B. Botters, and D. Grundler. Vortex circulation control in large arrays of asymmetric magnetic rings. *Physical Review B - Condensed Matter and Materials Physics*, 75(18):1–4, 2007. ISSN 10980121. doi: 10.1103/PhysRevB.75.184428.